Fundamental Studies of Polyelectrolyte Multilayer Films: Optical, Mechanical, and Lithographic Property Control

by

ADAM JOHN NOLTE

Bachelor of Science, Chemical Engineering
University of Missouri-Rolla, Rolla, Missouri, 2001

Submitted to the Department of Materials Science and Engineering
in partial fulfillment of the requirements for the degree of

DOCTOR OF PHILOSOPHY IN MATERIALS SCIENCE AND ENGINEERING
at the
MASSACHUSETTS INSTITUTE OF TECHNOLOGY

FEBRUARY 2007

Signature of Author:_____
Department of Materials Science and Engineering
November 21st, 2006

Certified by:_____
Michael F. Rubner
TDK Professor of Materials Science and Engineering
Thesis Advisor

Certified by:_____
Robert E. Cohen
St. Laurent Professor of Chemical Engineering
Thesis Co-Advisor

Accepted by:_____
Samuel M. Allen
POSCO Professor of Physical Metallurgy
Chair, Departmental Committee on Graduate Students

Fundamental Studies of Polyelectrolyte Multilayer Films: Optical, Mechanical, and Lithographic Property Control

by

Adam John Nolte

Submitted to the Department of Materials Science and Engineering
on November 21st, 2006 in partial fulfillment of the
requirements for the degree of Doctor of Philosophy in
Materials Science and Engineering

ABSTRACT

Polyelectrolyte multilayers (PEMs) are a versatile type of thin film that is created via layer-by-layer assembly of positively and negatively charged polymers from aqueous solutions. Precise control of the PEM thickness, chemical functionality, and molecular architecture is made possible by changing the polyelectrolytes and assembly conditions during film growth, allowing films to be designed with properties suitable for a given application. This thesis elucidates the intra-film structure and interactions of PEMs through the use of optical, mechanical, and chemical techniques.

PEM rugate filters, wherein the refractive index varies through the depth of the film in a continuous, periodic fashion, were constructed by confining silver nanoparticle growth to layers of nanometer-scale thickness. The ability to construct such structures is shown to be dependent on the ability to precisely control the concentration of metal-binding carboxylic acid groups throughout the depth of the film. Software to enable the computation design and optical simulation of these and similar structures was developed.

A buckling instability technique was used to probe the Young's modulus of PEM assemblies as a function of polyelectrolyte type, assembly pH, and the relative humidity of the ambient environment. In particular, a two-plate methodology was developed to allow testing on a broad array of multilayer films, and an experimental apparatus was constructed to allow in situ modulus measurements of PEM films under controlled humidity conditions. These techniques are used to elucidate the strong effects that polyelectrolyte type, assembly pH, and the ambient humidity can have on the stiffness of PEM films.

The controlled removal of material from assembled PEMs was accomplished via etching of films in solutions of increasing ionic strength. The properties of etched films and process dynamics point to evidence of a polydispersity-enabled phenomenon driven by dissolution of polyelectrolyte complexes containing chains of disproportionate molecular weight. Kinetic and equilibrium data are presented that support this hypothesis.

Beyond elucidation of the underlying mechanisms governing molecular interactions within PEMs, possible practical applications for the particular PEM assemblies described in this thesis are discussed, including conformable interference filters and buckling-enabled patterning.

Thesis Supervisors: Michael F. Rubner, TDK Professor of Materials Science and Engineering

Robert E. Cohen, St. Laurent Professor of Chemical Engineering

Acknowledgements

I am deeply indebted to a number of people for making this thesis a reality. I first thank my advisors, Michael Rubner and Robert Cohen, for their individual and collaborative efforts to guide and shape my research and professional development during my time at MIT. I consider myself extremely lucky to have had not only the resources and guidance from two of the best scientists at MIT, but also the benefits that have emerged from the synergistic pairing of their two research groups on a number of exciting projects. I also would like to thank my other committee members, Krystyn Van Vliet and Yoel Fink. In particular, I thank Krystyn for discussions about mechanics and for her helpful assistance with preparing my final presentation, and Yoel for discussions and advice on my rugate filter work.

In addition to my committee, I thank John Joannopoulos from the Physics Department at MIT and Chris Stafford from NIST for helpful discussions during various phases of my research.

To my colleagues from the Rubner and Cohen groups I owe a particular debt of gratitude for all they have taught me through our numerous interactions and friendships both inside and outside of the lab. In particular, I would like to thank: Tom Wang, Hartmut Rudmann, Jeri'Ann Hiller, Jeff Abes, Yot Boontongkong, Yonathan Thio, Ed Kopesky, Prem Pavoor, Roger Aronow, Heejae Kim, Michelle Poliskie, Mike Berg, Jeeyoung Choi, Jonas Mendelsohn, Nobuaki Takane, Sung Yun Yang, Daeyeon Lee, Koji Itano, Aleks White, Toshi Takasaki, Hyunku Ahn, Lei Zhai, Zhizhong Wu, Xiaoxia Sheng, Jimmy Li, Zhi Li, Fevzi Çebeci, Javier Bravo, Ryan "thanks for the food" Bennett, Ben Wang, Sharon Soong, Andy Miller, Solar Olugebefola, Jenny Lichter, Zek Gemici, Al Swiston, Gary Chia, Erik Williamson, Marisa Beppu, Giovanna Machado, and Ray Turner. I also thank Nicole Zacharia and Jodie Lutkenhaus of the Hammond group for helpful discussions, as well as Joe Walish of the Thomas group for collaborative assistance on a number of projects.

Although I have learned much from all of my research colleagues at MIT, a couple of individuals stand out for having been extremely helpful and supportive during my time here. I would like to specifically thank Tom Wang for showing me the ropes at MIT, and training me in the ways of PEM nanoparticle chemistry and TEM characterization. To Daeyeon Lee goes an enormous "thank you" for everything from teaching me about colloid chemistry to trading babysitting duty with our kids. I would also like to acknowledge Daeyeon's expert ability to spot hot papers as soon as they hit the press (or the Internet, as the case may be). Daeyeon was the first to spot the paper on buckling of polymer films and realize its potential for testing PEMs. I am proud to count him as a collaborator and friend.

I am extremely grateful for my collaborations with guest researchers from outside of the Institute, including Hannah Sevian, Sean Muller, and Kristen Cacciatore through the RET program of the CMSE. I also had the pleasure of advising a few excellent CMSE/MPC summer interns through the years: Paul Albertus (University of Michigan), Evan Hindman (Stanford University), and Neil Treat (University of Southern Mississippi). I thank them, as well as my UROP students from MIT, Dalton Cheng and Leah Dancy, for hard work and significant contributions in the lab.

Students at MIT have a significant arsenal of scientific equipment at their disposal—I thank the CMSE Shared Experimental Facilities and the MIT Institute for Soldier Nanotechnologies for providing the equipment I needed to accomplish my research. In particular, I thank Libby Shaw, Tim McClure, Mike Frongillo, and Taras Gorishnyy for training me on the various instruments and sharing their expert advice on obtaining the best possible measurements. I also thank the MRSEC program of NSF for generously providing the funding for my research.

I thank Jess Landry, Susan Rosevear, Jei Lee Freeman, Danielle Delgado, Stephanie Hansen, Carrie Casado, and Karyn Jones for their administrative assistance and for being great resources for the student in need. I thank Kathy Farrell, Angelita Mireles, and Stephanie Bright from the DMSE office for their time spent explaining to me the intricate ins and outs of the DMSE doctoral process.

Despite their meager budget, graduate students at MIT seldom go hungry. Thanks to MIT and my advisors for the countless free lunches and dinners, as well as the endless supply of Flavia coffee. I would also like to thank Peet's Coffee & Tea for keeping me caffeinated and making the best coffee known to man.

I will treasure more than anything else the friendships that have arisen as a result of my time spent at MIT. I would like to mention a few people in particular: my fellow CMSE/MPC alumni, Brad Peterson and Pat Underhill, as well as Curran Crawford for being a great roommate through my first semester, Joe Walish, for always taking the time for a cup of coffee (and being almost as distractible as me), Daeyeon Lee, Terry and Ann Orlando, and Elizabeth Basha. Thank you to Bob and Gloria Legvold for many a fun dinner in Winchester and on the Cape. A huge hug goes out to the Huffs of Cranston, RI, who are and always will be our "family away from home." Many thanks also go to the godparents of our children, Steve and Bridget Englebretson and Joe and Jenn Kushner, for their loving friendship and exemplary Christian witness.

I thank the MIT Tech Catholic Community and the Oblates of the Virgin Mary for providing many opportunities to attend Mass and help me grow in the Faith. In this regard, I also would like to thank the guys at Elmbrook and Chestnut Hill, and the local members of Teams of Our Lady for their friendship and witness. To God be all the thanks and glory.

Last but certainly not least, I acknowledge the love and support of my family. To my parents, Jim and Denise Nolte, I offer my loving thanks for bringing me up and patiently answering all the numbing questions of an extremely inquisitive child. I thank my sisters, Laurie and Sara, for their love and for tolerating an often annoying big brother. I also thank my grandparents John and Frances Nolte for their support and encouragement, and also my Grandma Reese who taught me about finding the truly important things in life.

Finally, I thank my wife, Suzanne, and my children, John Paul and Adelaide, for their love and understanding through late nights, early mornings, and crazy research schedules. I love you with all of my heart.

This thesis is dedicated to Mary, who has stuck with me through thick and thin. *Totus Tuus*.

Table of Contents

List of Figures

List of Tables

Chapter 1
Introduction

1.1 Thin Film Materials

Many of the most important recent advances in field of Materials Science have been in the field of thin films. In modern science, the study of thin films is ubiquitous, reflecting a diversity of important scientific and technological applications, for which the ability to produce, pattern, and measure materials at the nanoscale is often critical. The manufacture and study of thin film materials have enabled advances in a number of important fields, including:[1-9]

1. Semiconductor processing and the development of integrated circuits, where advances in thin film processing have enabled the development of modern microprocessors, computers, and storage media,

2. Optical filters such as antireflection coatings and distributed Bragg reflectors, where careful design and manufacturing have led to the creation of devices such as vertical-cavity surface-emitting lasers (VCSELs), dielectric mirrors, and photonic crystals,

3. Protective thin films designed to decrease wear, prevent contact damage, and protect the underlying substrate from chemical or thermal degradation, and

4. Coatings aimed at promoting or inhibiting the attachment of biological molecules and cells, killing infectious organisms, or decreasing friction or wear in artificial implants.

The use of thin films for a given application can be motivated by a number of factors. In many cases, their use stems from a desire to modify only the surface of an object while preserving the bulk properties of the underlying material. Such is the case, for example, when an anti-fog coating is applied to a mirror, or a non-stick coating to a frying pan. In some instances, the nanoscale thickness of the film is necessitated by physical principles;

e.g., an optical interference filter must be structured on the order of the wavelength of light if it is to be effective.[10] Even thinner films may be required for other possibly desirable properties to manifest, such as quantum confinement effects.[11] In other cases, such as with the ever-shrinking characteristic dimensions of integrated circuits and memory devices, a major motivational factor has been the desire to enable increasing amounts of computational power or information storage potential.

In many of the applications for thin films mentioned thus far, refractory materials have traditionally been used due to their superior electronic and optical properties, as well as their resistance to damage and wear. Organic materials, however, have shown increasing promise for applications where only decades ago their use would be thought impossible. This is true, for example, in the case of polymer electronics and organic light-emitting diodes (OLEDs).[12] Far from being just a novel alternative to inorganic materials, "soft material" thin films possess some distinct property advantages that are important in a number of applications. These advantages include:

1. Ease of processability—soft materials are more compliant and are able to be processed at relatively lower temperatures,

2. Cost effectiveness—the ease of manufacturing and the ready availability of many polymeric materials in particular make them cost-effective,

3. Flexibility and conformability—greater compliancy and higher toughness allows for the construction of films on deformable and non-planar substrate topologies, and

4. Stimuli responsiveness—soft materials are often able to change their dimension, as well as their optical, electrical, or other properties in response to environmental stimuli.

Thus, thin films composed of organic "soft materials" possess some distinct materials property advantages. Often, however, success in a given application demands precise spatial

control over the film composition and structure in order to create structures with enhanced functional properties as well as in creating optical, electrical and mechanical effects not possible in homogeneous films. Layer-by-layer (LbL) assembly is a technique particularly well-suited for the task of building such structures. As will be demonstrated in this thesis, nanoscale control over the composition of LbL-assembled polyelectrolyte multilayer (PEM) film materials is a critical requirement for successful optical, mechanical, and lithographic property control in these systems. In the following section, LbL assembly PEMs will be discussed in more detail.

1.2 Layer-by-Layer Assembly and Polyelectrolyte Multilayer Films

1.2.1 Background Information on Layer-by-Layer Assembly and Polyelectrolytes

The concept of constructing thin films via alternating deposition of two oppositely charged species is generally attributed to R. K. Iler, who introduced the concept of creating layers of oppositely charged colloidal particles, and suggested that this methodology could be applied to other oppositely charged species.[13] Interestingly, Iler's original ideas lay more or less dormant until the early 1990's, when Gero Decher and co-workers introduced the concept of creating multilayers of oppositely charged polymers—thus introducing the concept of a "polyelectrolyte multilayer" (PEM).[14-17]

The field of PEM research has expanded greatly since Decher's original findings, which reported on the deposition of fully ionized PEMs onto planar substrates. Subsequent major contributions to the field have included the assembly of PEMs on non-planar (including colloidal) substrates,[18, 19] the substitution of charged particles or other species in place of one or both polymers,[20-31] and the assembly of PEMs through hydrogen bonding, as opposed to electrostatic, interactions.[32-36] Another important development in the field of PEM research has been the creation of films using so-called "weak" polyelectrolytes, which allow one to control the degree on ionization of each polyelectrolyte during film assembly.[37, 38] As will be discussed in more detail below, control over the degree of ionization of the polyelectrolytes during assembly permits the construction of films with different types of

architecture and chemical functionalities, which in turns leads to a variety of functional possibilities for the resulting PEMs.

Polyelectrolytes are polymer molecules containing water-ionizable moieties along the molecular backbone. Polyelectrolytes are generally classified as strong or weak; a polyelectrolyte is said to be "strong" when it is fully ionized over a wide range of solution pH. "Weak" polyelectrolytes, on the other hand, exhibit pH-dependent ionization behavior in solution.[37] The ionization behavior of a weak polyelectrolyte is often described in terms of the pK_a; this parameter denotes the pH value at which exactly half of the ionizable groups on the polyelectrolyte are dissociated. Figure 1.1 shows the structure of three polyelectrolytes used to assemble the PEMs explored as part of this research.

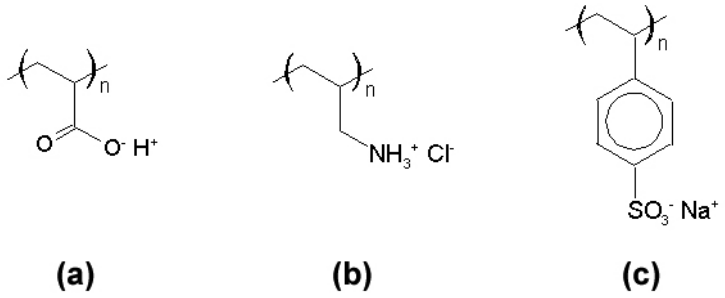

Figure 1.1. The chemical structure of three common polyelectrolytes. (a) Poly(acrylic acid) (PAA), (b) poly(allylamine hydrochloride) (PAH), and (c) poly(sodium 4-styrene sulfonate) (PSS). PAA and PAH are weak polyelectrolytes with pK_a values in solution of ≈ 6.5 and 8.8, respectively.[39] PSS is a strong polyelectrolyte as is fully charged over a wide range of solution pH.

Poly(acrylic acid) (PAA) (Figure 1.1a) is a weak polyacid that was used in conjunction with the weak polycation poly(allylamine hydrochloride) (PAH) (Figure 1.1b) to form polyelectrolyte multilayers with structures and functionalities dependent upon the pH of the deposition solutions. PAH can alternatively be deposited with poly(sodium 4-styrene sulfonate) (PSS) (Figure 1.1c, a strong polyanion). In all cases discussed in this thesis, multilayers formed from PAH and PSS were assembled at a low solution pH where both polymers were fully charged. The importance of this fact will be discussed below at greater length. Solution values of the pK_a for PAA and PAH have been given in a recent publication

as 6.5 and 8.8, respectively.[39] It should be noted that the pK_a of weak polyelectrolytes has been observed to shift dramatically when the polymers are assembled into a multilayer film. PAA, for example, becomes much more acidic when incorporated into a multilayer film with PAH, with its pK_a shifting to a value close to 3.[39]

For this research, PAA was used in its acid form, while salt forms of both PAH and PSS were employed in the construction of multilayer films (see Figure 1.1). Because such low concentrations of polymer were prepared for the deposition solutions (0.01 M by repeat unit), the presence of the salt ions accompanying PAH and PSS was not accounted for when reporting the ionic strength of the polyelectrolyte solutions.

1.2.2 Polyelectrolyte Multilayer Film Assembly

The usual way of carrying out PEM deposition is by dipping a substrate back and forth between aqueous solutions of a polycation and a polyanion, with rinse steps following the adsorption of each polyelectrolyte. Techniques such as spray-coating[40, 41] or roll-to-roll processing[42, 43] have also been explored and are of considerable technical interest, particularly for speeding up or streamlining the process of LbL deposition; however, most fundamental research on PEMs continues to focus on films assembled by the traditional solution dipping technique.

A PEM begins with the first polymer adsorption step onto the substrate. When glass, silicon, or other similar materials are employed, a negative charge is generally present on the substrate, so that deposition begins with the polycation. Each adsorption step of polyelectrolyte results in reversal of the substrate surface charge due to adsorption of the oppositely charged polymer species from solution. A "bilayer" is defined as one layer of polycation deposition followed by one layer of polyanion deposition. PEMs are built up by repeatedly cycling the bilayer formation process.

Adsorption is driven by electrostatic interactions of the solution polymer with the oppositely charged film surface; however, the energetic favorability of these bond interactions is not the primary driving force for PEM formation. Although electrostatic bond

formation between the positively and negatively charged repeat units of the polyelectrolytes may be enthalpically favored, the adsorption process is mainly entropically driven.[44] This can be understood by considering that for the small entropic penalty involved in the adsorption of one polyelectrolyte chain to the surface of the PEM, there is a large gain in entropy from the release of multiple counter ions into solution with the formation of ionic crosslinks between the PEM surface and the adsorbing chain.

Once a polyelectrolyte film is assembled, it generally possesses a resistance to dissolution in aqueous solutions of moderate ionic strength. As will be discussed in more detail in Chapter 6, solutions of sufficient ionic strength can compromise the electrostatic crosslinks in a PEM and cause dissolution of the film. A similar erosive effect can also be obtained by treating a PEM at extreme pH conditions.[45]

1.2.3 Polyelectrolyte Multilayer Nomenclature

To describe the molecular design of a polyelectrolyte film, the following common convention of representing the film is used:

Equation 1.1

$$(\text{"}Polymer\ 1\text{"}\,x\,/\,\text{"}Polymer\ 2\text{"}\,y)_z$$

where *Polymer 1* and *Polymer 2* are the abbreviations of the two polyelectrolytes forming the film. Typically, *Polymer 1* refers to the polycation, which is usually the first polyelectrolyte deposited on the substrate (see Section 1.2.2). The variables *x* and *y* denote the pH values of the deposition solutions containing *Polymer 1* and *Polymer 2*, respectively. Finally, *z* represents the number of bilayers deposited to form the PEM. A whole number value for *z* means that the film has been capped with the deposition of Polymer 2. A half-integer *z* value means that after the deposition of *z* bilayers, an additional layer of *Polymer 1* has been adsorbed. For example, say a certain dip consists of 10 bilayers of PAH (solution pH = 7.5) and PAA (solution pH = 3.5), with an additional PAH adsorption step to complete the film. This PEM would be represented as $(PAH7.5/PAA3.5)_{10.5}$. Alternatively, consider a

film composed of 6 bilayers of PAH and PAA, followed by 15 bilayers of PAH and PSS, with all dipping solutions maintained at a pH of 3.0. This film would then be represented as $(PAH3.0/PAA3.0)_6(PAH3.0/PSS3.0)_{15}$.

1.2.4 The Effects of Deposition pH and Post-Assembly Polyelectrolyte Multilayer Modification

As previously mentioned, the properties of a polyelectrolyte film and its behavior under different environmental conditions can depend dramatically on the pH of the polymer solutions during assembly of the film when weak polyelectrolytes are used. Changing the ionization of a polyelectrolyte changes the chemical functionality of the molecule; it is thus reasonable to expect that these changes might manifest themselves in the assembled film. The effects of deposition pH on the properties of multilayers of PAH and PAA have been well-studied in previous publications.[37, 38, 46, 47] The film architecture and functionality obtained by depositing multilayers of PAH and PAA under three common assembly conditions are depicted schematically in Figure 1.2.

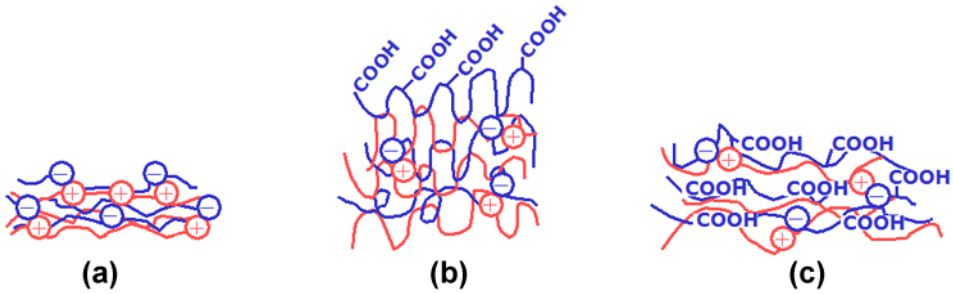

Figure 1.2. Schematic diagram of the film architecture upon assembly of multilayers of PAH (red chains) and PAA (blue chains). Films are depicted at various deposition pH values: (a) (PAH6.5/PAA6.5), (b) (PAH7.5/PAA3.5), and (c) (PAH3.0/PAA3.0).[47]

Figure 1.2 underscores the important effects caused by deposition pH in multilayers of PAH and PAA. In Figure 1.2a, a (PAH6.5/PAA6.5) film is depicted. Film assembly at this intermediate pH value results in more or less fully charged polymer chains and complete ionic crosslinking of the PEM, resulting in very flat chain conformations and a very low bilayer thickness increment. In Figure 1.2b, the structure of a (PAH7.5/PAA3.5) film is depicted. In this case, each polyelectrolyte is deposited at a solution pH where it is only

partially ionized, leading to the formation of chain loops due to the longer average distance between electrostatic crosslinks. As a result, these multilayers have very large bilayer thickness increments. Finally, Figure 1.2c depicts a (PAH3.0/PAA3.0) film. When the assembly pH of both polyelectrolyte baths is kept low, films of intermediate film thickness are formed that are rich in free carboxylic acid groups.

The control over the functionality and structure of a PEM allows the film to be utilized as a template for subsequent chemical reactions. Such processes are particularly interesting when they lead to the growth of an additional inorganic phase, transforming the PEM into a nanocomposite film. For example, the incorporation of various types of metal, oxide, and semiconductor nanoparticles,[48-51] molecules for sol-gel chemistry,[52-55] and the addition of catalysts for electroless plating[56, 57] have all been demonstrated. In addition to these additive types of chemistries, the presence of specific functionalities at certain pH assembly conditions also can allow for porosity phase transitions within the film that are triggered at certain solution conditions, such as low pH. Micro and nanoporous phase transitions have been demonstrated,[45] and these can have a variety of applications, including bio-resistant surfaces,[47] antireflection films,[58] sensing optical devices,[59] and superhydrophobic coatings.[60, 61]

The above-mentioned post-assembly film modifications can be divided into two distinct classes. The first is *additive* modification, where materials (e.g. nanoparticles, electrolessly plated metal) are being grown or deposited within the film. In the second case, voids are being created in the PEM structure as the film increases in volume and becomes pocketed with air. Even with no net material loss, the average density of the film decreases in such cases, so there is a sense in which porosity transitions can be viewed as *subtractive* techniques. It is interesting to note that both types of film modification lead to changes in the refractive index of the film that can be controlled to create useful optical coatings.[58, 59, 62, 63] Furthermore, by changing the polyelectrolyte system being used during the dipping process, such changes in the film refractive index can be confined to very precise regions of the film; this topic will be the focus of Chapter 2, where the creation of complex refractive index gradients is accomplished through the templated growth of silver nanoparticles.

The idea of incorporating metal nanoparticles into polyelectrolyte systems was inspired from earlier work that had been done on incorporating nanoparticles into specific domains of block copolymer films.[64-66] In both the block copolymers and PEMs, free carboxylic acid groups serve as exchange sites for metal cations which enter the film from either a solution or vapor phase. Subsequent exposure to a reducing atmosphere results in the growth of nanoparticles distributed throughout the carboxylic acid-containing regions of the film. In certain cases, such as when the film is exposed to pressurized hydrogen gas, the carboxylic acid protons are regenerated during reduction, and multiple loading-reduction cycles can be accomplished. Figure 1.3 presents a schematic of the nanoparticle growth progress in a (PAH/PAA) film that has been assembled at low pH conditions (as in Figure 1.2c). In Figure 1.3b the creation of silver nanoparticles via aqueous exchange of silver ions and reduction in hydrogen gas is assumed, which is the method that was employed to create the films discussed in Chapter 2.

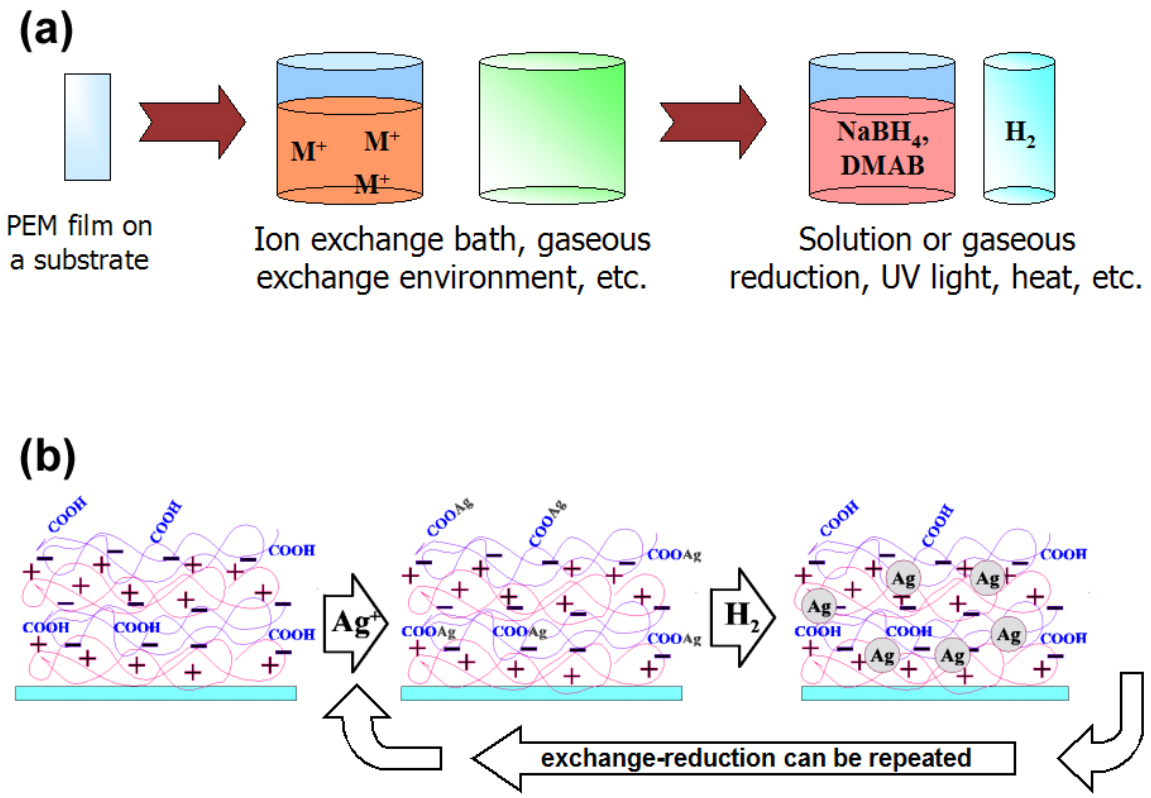

Figure 1.3. In situ synthesis of silver nanoparticles by ion exchange and reduction. (a) The generalized nanoreactor scheme is illustrated. (b) The synthesis of silver nanoparticles in multilayers rich in free carboxylic acid groups is depicted. Silver ions are exchanged onto acid groups via a salt bath. Reduction is carried out in a hydrogen gas atmosphere, which also results in the regeneration of the acid groups so that the exchange process can be cycled multiple times.

When polyelectrolyte films are prepared with the intention of templating nanoparticle growth, care must be taken to build the film at a pH such that many free carboxylic acid groups will remain for the ion-exchange reaction. Thus, it becomes necessary to adjust the PAA bath to a low pH—typically between 2.5 and 3.0. The solution of polycation is usually kept at a low pH as well—previous work has shown these systems to generate reproducible thicknesses on the order of a few nanometers per bilayer.[38] This is important, as bilayers that are too thin are impractical for constructing films with useful optical properties (micron-scale total thicknesses), while those that are too thick generally have undesirable surface roughness, preventing the creation of smooth, planar refractive index domains and enhancing diffuse scattering, leading to poor optical interference filters. As will be discussed in more detail in Chapter 2, optical interference effects depend upon the localization of regions of

different refractive index with thicknesses on the order of the wavelength of light. In this research, the growth of silver nanoparticles in selected regions of PEM films leads to the requisite index contrast.

1.2.5 Optical Properties of Silver Nanoparticles*

The optical properties of metallic nanoparticles have been studied for almost a century, and there seems to be no foreseeable decrease of research interest in this field.[67] Nanoparticle incorporation in a polymer film modifies the refractive index of the structure due to the unique size-dependent properties of metals at the nanoscale. It is well known that bulk conductors are opaque to a large range of the electromagnetic spectrum (including the visible and near-IR regions) due to damping of the impinging wave by conduction electrons inside the material.[68] Because of their small size, metallic nanoparticles do not possess the same extinction properties of bulk metals; instead, their absorption response is generally concentrated in a narrow peak at the surface plasmon (SP) frequency. At this frequency there exists a resonance of the conduction electrons in the particle—where this resonance appears depends not only on the type of metal, but also its shape, size, and the optical properties of the surrounding medium.[67]

Because the SP absorption is confined to a fairly narrow region of the electromagnetic spectrum, useful optical properties (i.e. a higher real part of the refractive index) can still be obtained from the nanocomposite by working in a region sufficiently removed from the SP frequency. A study analyzing the change in refractive index for PEM-silver nanocomposites has confirmed a high refractive index for silver nanocomposites with small extinction coefficients in the red and near-IR parts of the electromagnetic spectrum.[62] As a result of the high absorbance of PEM-silver nanocomposites in the shorter wavelength part of the visible spectrum, the work presented in Chapter 2 of this thesis focuses on the design of an optical filter with a reflectance band in the near-IR portion of the electromagnetic spectrum. It should be noted, however, that in certain cases the absorption of blue and UV light might

* This section provides only a brief overview of this topic. For a more detailed summary see Reference 63. Wang, T. C. Polyelectrolyte Multilayers as Nanostructured Templates for Inorganic Synthesis. *Doctoral Thesis*, Massachusetts Institute of Technology, Cambridge, MA, 2002.

be a desired part of the application. This could be true, for example, if there was concern that higher-energy photons could pose a health risk or damage a sensitive piece of equipment. In these cases, the absorption properties of silver nanoparticles could prove an advantage.

1.3 Thesis Scope

This thesis describes three distinct but closely interrelated areas of fundamental research on the properties of PEM films. Chapter 2 demonstrates how a careful choice of polyelectrolytes and dipping conditions can lead to very precise control of the distribution of silver nanoparticles being grown inside of a heterostructured PEM film. The focus on spatial control of gradients in material properties, in this case the refractive index, permits the construction of a PEM rugate filter, which is a special type of interference filter with optimized spectral properties.

Chapter 3, Chapter 4, and Chapter 5 present the detailed results from studies of the Young's modulus of PEM films grown at various assembly conditions, and the subsequent mechanical response of the films to changes in the ambient environment.

Finally, Chapter 6 examines lithographic etching of PEM assemblies in solutions of salt. This phenomenon is shown to be controllable and reproducible, and to depend heavily upon the individual properties of the polyelectrolytes comprising the PEM, as well as the strength of the chemical interactions binding the assembly together.

These topics are related by their focus on the study and practical application of the chemical functionality and internal interactions present in PEM films. Through careful control of these interactions, PEMs can be designed with unique material properties for a variety of useful applications.

Chapter 2
Polyelectrolyte Multilayer Rugate Filters*

2.1 Introduction

Optically tunable materials that are capable of efficiently reflecting light of specific wavelengths form the basis of a wide range of existing optical filters and have recently enabled the development of a host of emerging technologies such as vertical-cavity surface-emitting lasers (VCSELs),[2] dense wavelength division multiplexers (DWDM),[3] and dielectric coaxial communication fibers.[70] In all cases, these materials exclude light via optical interference effects that are promoted by their spatially periodic arrangement of regions of high and low refractive index.[71] Simply changing the length-scale and index contrast of these periodic structures, in turn, varies their spectral features. The fabrication of such structures from polymeric materials offers the additional possibility of making deformation-tunable dielectric mirrors, as well as environmentally responsive devices suitable for use as chemical or biological sensors.[72, 73]

Unlike their inorganic counterparts, the fabrication of large area, conformal optical coatings from polymeric materials with precisely controlled periodic structures of relevant length-scales remains a significant technical challenge. This chapter will discuss the basics of optical interference filters and the motivation for creating such filters from polyelectrolyte multilayers. Previous research in this area will be discussed, as well as the results of this thesis research involving a computer-controlled method for designing and constructing advanced metallodielectric mirrors through the layer-by-layer (LbL) deposition of polyelectrolytes from aqueous solutions, followed by in situ nanoreactor chemistry. The precise control afforded by this process not only enables the production of novel optical coatings, but could also be of general interest to those seeking methods for the spatially selective synthesis and arrangement of materials at the nanoscale.

* This chapter is reproduced in part with permission from Reference 69: Nolte, A. J.; Rubner, M. F.; Cohen, R. E., Creating effective refractive index gradients within polyelectrolyte multilayer films: Molecularly assembled rugate filters. *Langmuir* **2004,** 20, (8), 3304-3310.

2.2 Background and Motivation

2.2.1 Review of Optical Interference Filter Basics

An optical interference filter is a structure that has domains of high refractive index and low refractive index material, the length-scales of which are on the order of the wavelength of light. The simplest example is perhaps the quarter-wave antireflection (AR) coating, which is constructed by depositing a thin film with thickness d and refractive index n onto a substrate with refractive index n_s. The coating is generally designed so that:

Equation 2.1

$$d = \frac{\lambda_0}{4 \cdot n}$$

where λ_0 is the wavelength at which the reflectance is desired to be a minimum.[10] The condition imposed by Equation 2.1 is known as the quarter-wave condition, and d is commonly referred to as the quarter-wave optical thickness. Such coatings are capable of complete reflection suppression when n obeys the relationship:

Equation 2.2

$$n = \sqrt{n_0 \cdot n_s}$$

where n_0 is the index of refraction of the ambient medium (usually air, $n_0 = 1$). A schematic illustration of a quarter-wave AR coating and its simulated response are depicted in Figure 2.1.

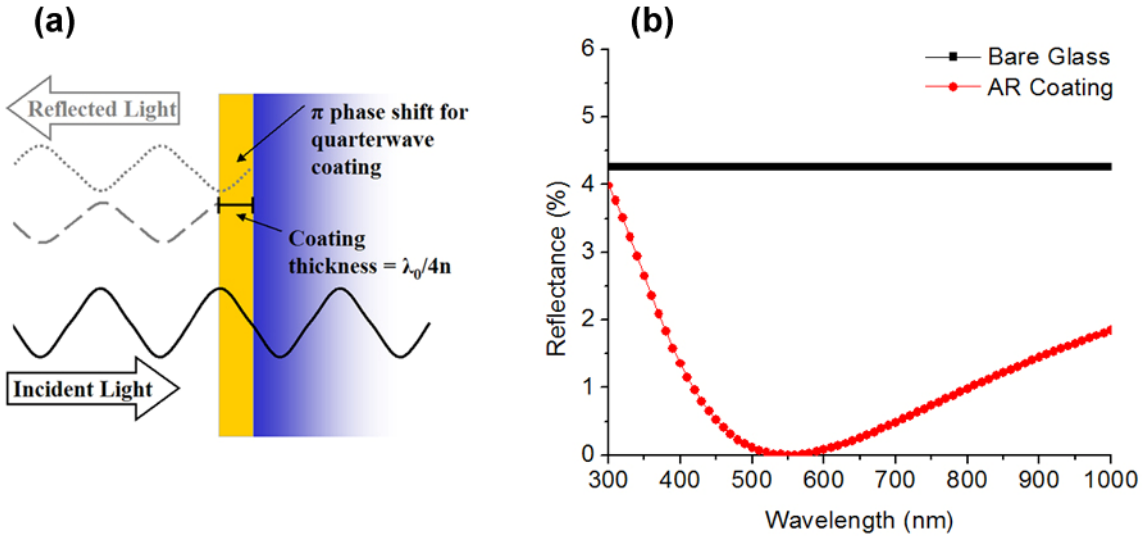

Figure 2.1 A quarter-wave AR coating. (a) A coating with a quarterwave optical thickness induces deconstructive interference in reflecting light, leading to decreased reflectance at the design wavelength, as illustrated by the reflectance simulation (b). The coating was designed with $n = 1.23$ and $\lambda_0 = 550$ nm. The substrate is glass (semi-infinite, $n = 1.52$).

Figure 2.1a illustrates the principle behind AR behavior in a quarter-wave coating. Destructive interference of reflected light is maximized at λ_0, leading to the suppressed reflection spectrum depicted in Figure 2.1b. At other wavelengths in the spectrum the quarter-wave coating actually can lead to constructive interference of reflected light, causing a higher reflectance. This principle illustrates the importance of designing the coating correctly using Equation 2.1.

The same principles of constructive and deconstructive interference of light can be employed to create more complex coatings that incorporate multiple planar regions of different refractive indices. Such coatings can often possess many advantages—gradients in the refractive index of a film, for example, can lead to broadband AR behavior.[58] When a repeating pattern of high and low index domains appear within a film, a 1-D photonic crystal results.[74] These materials are capable of efficiently reflecting light of specific wavelengths via optical interference effects that are promoted by their spatially periodic arrangement of regions of high and low refractive index.[71] Simply changing the length-scale and index contrast of these periodic structures, in turn, varies their spectral features. The simplest of

these structures is the quarter-wave Bragg reflector that has the ability to reflect nearly 100% of incident radiation within a certain wavelength range, thereby avoiding the losses of a few percent inherent in metallic reflectors.

In a quarter-wave Bragg reflector, alternating layers, possessing the quarter-wave optical thickness of a certain wavelength λ_0 (see Equation 2.1), cause constructive and destructive interference of incident light. The interference effects yield a reflectance band at λ_0 with reflectance side bands at higher and lower wavelengths. A 4.5 period quarter-wave Bragg reflector with alternating regions of refractive index $n_H = 2.0$ and $n_L = 1.55$ and its simulated optical response is depicted in Figure 2.2.

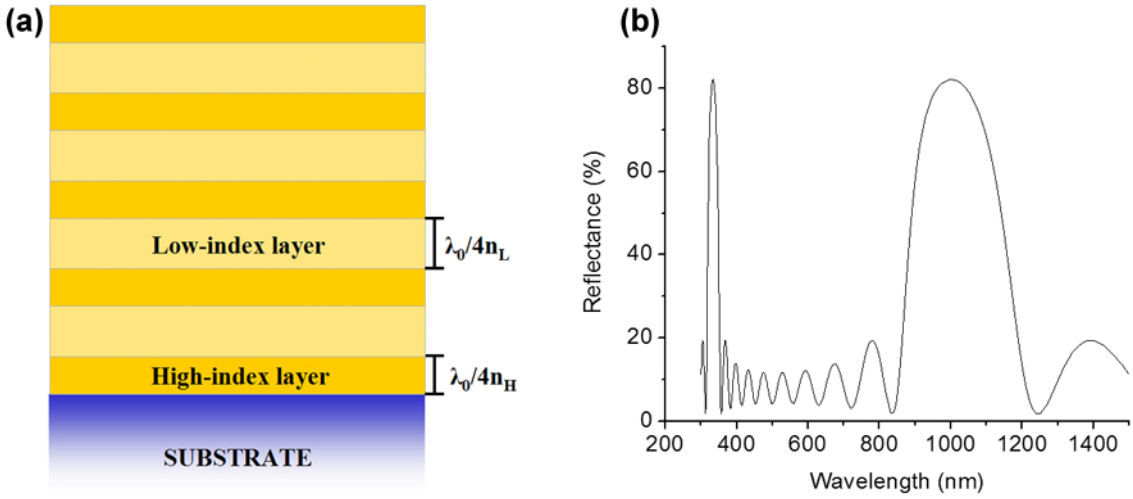

Figure 2.2. A quarter-wave Bragg reflector. (a) Illustration of a 4.5 period quarter-wave Bragg reflector. Such designs give a broad reflectance peak centered at λ_0, as shown in the by the reflectance simulation (b). This coating was designed with $n_H = 2.0$ and $n_L = 1.55$. The substrate is glass (semi-infinite, $n = 1.52$).

Figure 2.2 illustrates some of the common features in the optical response of Bragg reflectors, including the wide 1st-order reflection band centered at λ_0 (in Figure 2.2, $\lambda_0 = 1000$ nm). In addition, higher-order bands are present in the reflection profiles of these structures—one can be seen in Figure 2.2 at 333 nm. Reflection side bands are also present, which, although they do not indicate a complete photonic band gap and thus do not near

100% rejection of incident light, nevertheless manage to reflect a good portion (here 10-20%) of the incident light.

Other types of optical interference filters can be built using variations on the Bragg design—a typical example is the Fabry-Perot filter. Fabry-Perot filters, which are also sometimes known as etalons, are based on the principle that a cavity sandwiched between two mirrors can allow transmission of light in a very narrow frequency range while rejecting transmission of other frequencies.[68] Consequently, these structures are useful for isolating particular wavelengths of light and are common components in modern optical components, such as DWDMs.[3] The mirrors surrounding the cavity in a Fabry-Perot etalon can be constructed from any partially reflecting material, including Bragg reflectors. Tuning the cavity size between the two reflectors in turn varies the location of the narrow transmission window introduced by the cavity. Fabry-Perot filters are commonly seen where an extra half-wave cavity has been introduced between two quarter-wave Bragg reflectors. The spectral response of such filters is very similar to that of a comparable Bragg filter, except that now a narrow transmission window is opened directly in the middle of the primary rejection (reflection) band. Figure 2.3 illustrates a Fabry-Perot filter constructed based on a Bragg reflector design with an added half-wave cavity and gives its simulated optical response.

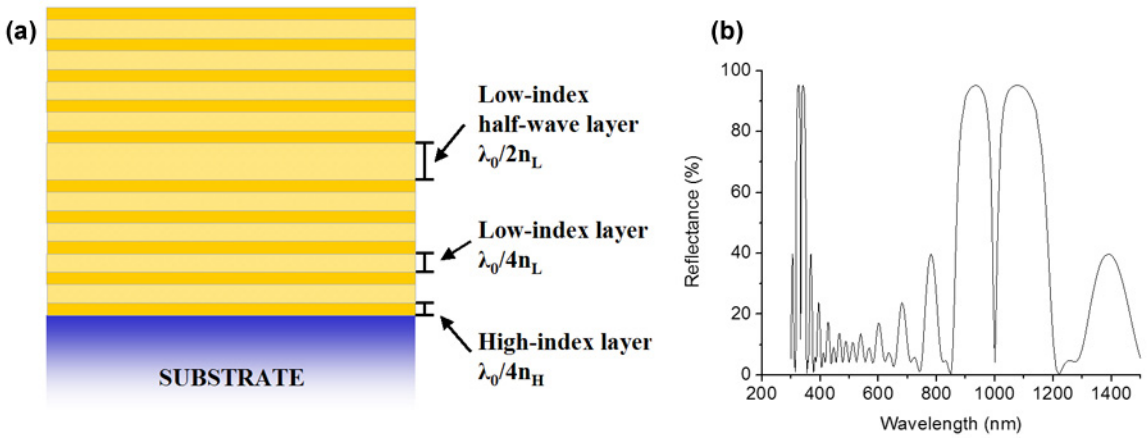

Figure 2.3. A Fabry-Perot filter. (a) Illustration of a Fabry-Perot filter constructed by inserting a half-wave low-index layer between two 4.5 period quarter-wave Bragg reflectors. Such designs give a broad reflectance peak with a very thin transmission window located at λ_0, as shown in the by the reflectance simulation (b). This coating was designed with $n_H = 2.0$ and $n_L = 1.55$. The substrate is glass (semi-infinite, $n = 1.52$).

2.2.2 Optical Filters from Polyelectrolyte Multilayers: Previous Work

Having now covered the basic principles of optical interference filters, this section will present a more specific discussion of optical filters constructed using PEMs. Optical filters constructed using PEMs can offer a number of advantages over traditional coatings, which are usually prepared using deposition techniques such as sputtering or evaporation. PEM processes require dipping into relatively mild aqueous solutions, and thus are very environmentally friendly. Polyelectrolytes are also amenable to deposition on many different substrate materials, and they can be deposited conformably on large-area curved or flexible surfaces. With PEMs, for example, it would be possible to create a conformable optical interference filter on the inside of a tube or surrounding a colloidal particle. This would be very difficult if not impossible to accomplish using more traditional inorganic deposition techniques, which generally require flat substrates, and only allow for reliable film deposition in a straight line of sight from the sputtering target or evaporation source. In addition, because they are composed of polymers, PEMs are less stiff than the refractory oxides and semiconductors such as Si, MgF_2, SiO_2, and TiO_2, which are often used for interference filter construction. In addition to their increased conformability and compliancy, the ability of

PEMs to soften and swell when exposed to ambient moisture makes them ideal candidates for environmentally responsive materials and sensors.[59, 62]

A considerable amount of work has been done investigating the potential of PEMs for optical interference filters. As explained above, AR coatings generally require a thin film of material with a refractive index between the incident medium (usually air, $n = 1$) and the substrate. Because PEMs have refractive indices on the order of 1.5, very similar to many other polymer and glass substrates, pockets of air must be incorporated into the PEM matrix to lower the refractive index of the film. These pockets must comprise a considerable amount of the film volume, but yet remain on average much smaller than the wavelength of light to avoid diffuse scattering.[58] Two basic strategies to create such coatings have emerged thus far. The first employs the acid-driven porosity transformations introduced in Section 1.2.4 and pioneered by Hiller et al. to create single-layer and stepwise-graded index coatings from films of (PAH8.5/PAA3.5).[58] Subsequent to these initial findings, other researchers have examined ways to accelerate the construction of such coatings[75] and assemble them non-rigid substrates, such as thin sheets of polyethylene terephthalate (PET).[42]

The second approach to LbL-based AR coatings involves the deposition of charged colloidal particles in place of one or both polyelectrolytes.[76-83] The void spaces between the particles lead to a coating which is composed of $\approx$ 50% air by volume, with the exact amount of void space depending upon the size of the nanoparticles, number of deposited layers, and the assembly conditions. Because of the larger bilayer thicknesses associated with depositing colloidal particles, one sacrifices a certain degree of control over the precise thickness of such coatings. The absence of a porosity transitions also precludes large adjustments in the refractive index for a deposited film. Nevertheless, these coatings exhibit many other advantages over their non-colloidal counterparts, including mechanical stability and the possibility of superhydrophilic or superhydrophobic behavior.[78]

More complex PEM-templated interference filter designs have been pursued by Wang[62] and Zhai.[59] In the latter case, porosity transitions in the (PAH8.5/PAA3.5) system were

confined by regions consisting of (PAH4.0/PSS4.0) multilayers. It was found that while (PAH/PSS) regions would not undergo porosity transitions upon treatment, regions of the film consisting of (PAH/PAA) could still undergo transition. Post-treatment films thus consisted of alternating regions of (PAH/PSS) multilayers (high index) and porous (PAH/PAA) multilayers (low index), creating a Bragg-style interference filter. These filters exhibited high reflectances, cyclical behavior (from environmentally-induced pore closing and opening), and vapor sensing capabilities.

Wang, on the other hand, pioneered the creation of Bragg filters[62] and Fabry-Perot etalons[63] through the use of PEM in-situ nanoreactor chemistry (see Section 1.2.4). In this case, films were created with regions of (PAH3.0/PAA3.0) multilayers alternating with regions of (PAH3.0/PSS3.0). PAA-containing regions templated silver nanoparticle growth, which served to increase the local effective refractive index of those regions. Extensive work was conducted to study the amount of silver incorporated as a function of the number of exchange-reduction cycles,[51] as well as the magnitude of the resulting refractive index change.[62]

2.2.3 Rugate Interference Filters

The standard Bragg reflector and variations on its design, such as the Fabry-Perot etalon, are adequate for most applications. Certain applications may call for more control of the spectral features than these structures can give, however. The need, for example, to have a high degree of control over the widths and positions of the transmission or rejection bands, or to eliminate the side bands from a Bragg reflection peak, has motivated the development of rugate filters, in which the refractive index varies through the film in a smooth, sinusoidal fashion.[10, 84]

Optical filters in which the refractive index is allowed to vary continuously through the film in a *periodic* fashion are referred to as rugate filters. The term *gradient-index* is usually reserved for filters possessing a graded, non-periodic index design. Rugate filters and their design have been a popular topic in the literature for the past few decades.[85-123] Greenewalt et al. reported that these structures can be found in nature, such as in the case of the

hummingbird wing,[124] but efforts to design and create man-made rugate filters appear to have begun in earnest with the work of Delano.[125] Since his original efforts, rugate design methods based on Fourier transform techniques have spurred increasing theoretical and experimental research, but creating the requisite continuous index gradients within the film continues to be a challenging problem. Physical vapor deposition (PVD) methods that control the relative deposition rates of at least two different materials are capable of creating smooth index gradients. These and other approaches such as silicon etching,[72, 126] glancing angle deposition (GLAD),[127] stepwise-grading[128, 129] have been examined in the literature,[89, 91-93, 119, 128, 129] but they remain fairly complicated techniques, generally requiring feedback control systems with detailed rugate computer models[92] and expensive deposition equipment. In addition, researchers must face all of the problems associated with co-evaporation of compounds, including differences in evaporation temperatures, rates, and miscibility between compounds, and/or the problem of precisely determining the relative mixing ratios of pure material to generate a desired refractive index.

In an effort to circumvent the difficulties associated with constructing continuous index profiles, many researchers have examined the problem of approximating continuous refractive index profiles with thin, homogeneous layers.[93, 128, 129] This approach, which basically consists of building a piecewise continuous approximation to the original continuous profile, demands a large number of compatible materials with many different, closely spaced, refractive indices. Because it would not always practical or even possible to find such a group of materials, scientists soon began examining the question of whether one could reconstruct a continuous refractive index material using only a low index and a high index material.

Herpin[130] seems to have first demonstrated that for a single film of any thickness with refractive index n, there exists (at one wavelength) an equivalent symmetrical thin film combination built from materials with refractive indices n_L and n_H, such that $n_L < n < n_H$. Epstein[131] and Berning[132] expanded the original work to demonstrate applications to filter design, and Southwell[122] went on to generalize the concept. Southwell's algorithm generates a non-dispersive equivalent film that approximates an arbitrary gradient-index

profile *n(x)* (*x* being distance into a film measured from the incident interface) with thin, alternating low and high refractive index layers, which need not be symmetric, as was required with earlier approaches. The refractive indices, n_L and n_H, again must be chosen such that for all *x*, $n_L < n(x) < n_H$. Light traversing a film with such layers "sees" an effectively continuous index profile, provided the layer thicknesses are much less than the wavelength of light. The combination of high index and low index layers approximating a continuous index profile is referred to as a digital equivalent, and rugate filters designed and built in this fashion are known as digitized rugates.

Southwell's algorithm for generating digital equivalents is relatively straightforward. First, divide the coating into layers thin enough that the average refractive index change over a layer is not too great. Next, replace each of these layers with an equivalent low-high index pair whose thicknesses are found using the equations:[122]

Equation 2.3

$$t_H = \frac{N^2 - n_L^2}{n_H^2 - n_L^2} \cdot T \qquad t_L = T - t_H$$

where *N* and *T* are the average index and the thickness of the layer one wishes to represent with the low-high index pair, n_L and n_H are the indices of the low and high index materials available, and t_L and t_H are the necessary thicknesses of the low and high index regions to achieve spectral equivalence with the continuous index film. Exactly how thin t_L and t_H are will of course depend on the number of equivalent layers one has chosen to approximate the continuous design, but Southwell indicates that for accurate duplication of the original index profile one should guarantee that $N \cdot T << \lambda$.

Southwell's method can be nicely demonstrated using the example of an AR coating with a continuous quintic index profile. Quintic index profiles are of some interest, as they have been shown to lead to near-optimal broadband AR behavior if appropriately designed.[120] Consider the case where one wishes to continuously grade the refractive index with a quintic profile from a low (n_L) to a high (n_H) (substrate-matched) value to create, for example, a

broadband AR coating for an air-glass interface. A possible quintic equation that could be used to accomplish this gradation in index would be:

Equation 2.4

$$n(t) = n_L + (n_H - n_L) \cdot (10\chi^3 - 15\chi^4 + 6\chi^5)$$

where $n(\chi)$ denotes the index as a function of distance in a direction orthogonal to the plane of the film, and χ, the normalized distance into the film, varies from 0 at the air-coating interface to 1 at the interface between the coating and the substrate. In addition, Equation 2.4 satisfies the condition that both the first and second derivatives are continuous (equal to zero) at the air and substrate interfaces.[120]* Consider a coating of thickness 0.5 μm with $n_L = 1.1$ and $n_H = 1.5$. The continuous index profile of the AR coating defined by Equation 2.4 is shown graphically in Figure 2.4a, and the stepwise approximation for a film divided into 10 sections is depicted in Figure 2.4b. Figure 2.4c displays the digital design predicted by Equation 2.3, where only two materials (of refractive indices $n_L = 1.1$ and $n_H = 1.5$) are incorporated in thin regions of variable thickness. The simulated responses for the continuous, stepwise, and digital films display very close agreement; they are shown together in Figure 2.4d.

* This is true only if $n_L = n_0$ and $n_H = n_s$. For the particular coating described here, there is a discontinuity in the refractive index and the first derivative at the interface between air ($n_0 = 1$) and the coating ($n_L = 1.1$).

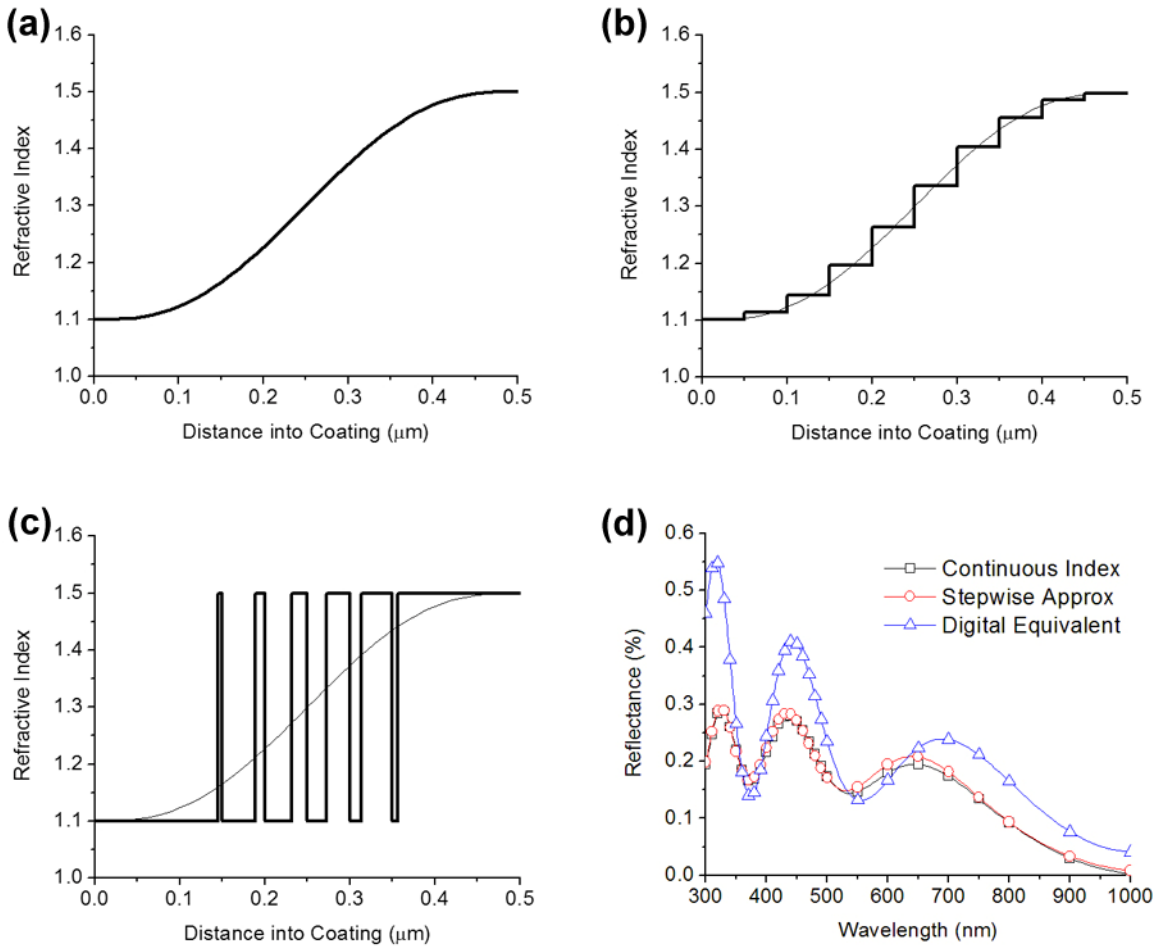

Figure 2.4. Various approaches to creating a quintic AR coating. The continuous index profile (a) can be approximated by a stepwise-constant refractive index profile (b), but 10 different index materials are required. A simpler approach would be to create a digital design using only two materials of index $n_L = 1.1$ and $n_H = 1.5$, utilizing Equation 2.3 to calculate the correct thickness of each region (c). The simulated reflectance profile for each coating is displayed in (d). The digital equivalent coating shows a maximum difference from the continuous index coating of only 0.25% over the tested range. Two very thin slabs each of high and low index material where removed from the digital equivalent profile in (c) before graphing due to unrealistically small thickness values (< 5 nm).

Thus, the design problem of a digitized rugate filter is no more difficult than that of a continuous-index structure—it simply requires the extra steps of discretizing the index profile and calculating the thicknesses of many smaller high-low index layers, an easy task for any computer. The construction problem, however, becomes much easier, assuming one has access to a technique capable of depositing many ultrathin layers of material with

nanoscale control over their thicknesses. Some have demonstrated the feasibility of this technique with inorganic materials,[90, 123] and at least one group has demonstrated its utility in the deposition of organic interference filters via Langmuir-Blodgett deposition[133, 134]—it is, however, especially suited to the nanoscale control offered by the PEM process.

2.3 Experimental Details

PAH (M_w = 70 000), PSS (sodium form, M_w = 70 000), and silver(I) acetate were obtained from Sigma-Aldrich (St. Louis, MO). PAA (25% aq. solution, M_w = 90 000) was obtained from Polysciences (Warrington, PA). Hydrogen gas (grade 4.7) was obtained from BOC Gases (Murray Hill, NJ). All chemicals were used without further purification. All solutions and rinse baths were prepared using de-ionized water (>18 MΩ·cm, Millipore Milli-Q). All polymer solutions were prepared at a concentration of 10^{-2} M (by repeat unit), and the silver acetate solution was prepared at a concentration of 5 mM. An additional 0.1 M NaCl was added to the PAH and PSS solutions used to construct (PAH/PSS) bilayer regions. All solutions were adjusted to a pH of 3.0 using 1.0 M HCl.

Polyelectrolyte multilayer films were assembled onto pre-cleaned glass and polystyrene substrates using an automated Zeiss HMS slide stainer. (PAH/PAA) and (PAH/PSS) bilayers were formed by first immersing the substrate in the polycation for 3 min, followed by 3 rinse steps in Milli-Q water (1 min, 1 min, 1 min). The substrates were then immersed in the polyanion for 3 min and rinsed in the same manner. The above process was repeated to generate the desired number of bilayers. Fresh rinse solutions were introduced approximately every 20 bilayers, and fresh polymer solutions approximately every 75 bilayers.

A computer was used to transform the continuous index profile into a blueprint for the construction of a PEM film. Following the calculation of digital equivalent layer thicknesses,[122] experimental data were used to determine the requisite number, order, and type of polyelectrolyte bilayers to deposit. First, the continuous rugate profile was discretized into individual slabs of thickness T, and the average refractive index over the slab thickness, N, was calculated. T was picked to minimize the number of discretization steps

(here 75) while ensuring that $N \cdot T << \lambda$ to maintain a good approximation of the original rugate profile. Each of the slabs of thickness T and index N were then replaced with a unique high-low index layer pair of calculated thicknesses using Equation 2.3.

In order to quantify the non-linear deposition behavior of (PAH/PSS) on underlying layers of (PAH/PAA), an increasing number of (PAH/PSS) bilayers were deposited on top of a 10 bilayer (PAH/PAA) platform. Profilometry was performed at regular intervals during the deposition of the (PAH/PSS) bilayers to determine the incremental thickness attributed to each bilayer of (PAH/PSS) (see Figure 2.7).

A computer was used to assemble the above deposition data into a plan for constructing the digital rugate filter, calculating the exact number and order of (PAH/PAA) and (PAH/PSS) bilayers to deposit. The resulting design contained 136 regions of alternating index: 68 high index (PAH/PAA) domains, and 68 low index (PAH/PSS) domains. The number of bilayers in each domain varied, but in all 645 bilayers were deposited—215 of (PAH/PAA), and 430 of (PAH/PSS). The thinnest and thickest planned domain sizes were 3.0 nm and 64 nm, respectively.

The silver nanoparticle synthesis was accomplished by immersing an assembled film in silver acetate solution for 1 hr, followed by a 10 min rinse in Milli-Q water, and then blow-drying with filtered air. The films were reduced in a hydrogen atmosphere (2 atm, room temperature) for 24 hrs. The nanoparticle synthesis was cycled the desired number of times to increase the silver concentration (refractive index) of the silver-containing regions of the film.[62, 63]

Transmission and near-normal (7°) reflectance measurements were performed using a Varian Cary 5E spectrophotometer on a film assembled onto a glass substrate. Because the PEM technique leads to the construction of films on both sides of the glass, the film was removed from one side before measurement by swabbing with 1M HCl. Theoretical reflectance responses were calculated in MATLAB® using the matrix method (see Section A.1) with previously obtained refractive index data.[62]

Samples were prepared for cross-sectional TEM by room temperature ultramicrotomy (diamond knife, 70-80 nm thick film sections) on films assembled on polystyrene slides after 3 silver exchange-reduction cycles. TEM imagining was performed using a JEOL 200CX operated at 200 kV. Film thickness and surface roughness were examined using a Tencor P10 profilometer on a film assembled on a polystyrene substrate (the same sample was used for both profilometry and TEM analysis). A step was created for profilometry by removing part of the film with a cotton swap dipped in 1.0 M HCL. Thickness and RMS roughness measurements were taken near the same part of the substrate from which the sample for TEM was obtained.

2.4 Results and Discussion

2.4.1 Digital Rugate Design

A rugate filter having a linearly apodized 6.5 period sinusoidal refractive index profile was chosen for construction (see Section E.1.2 for the exact functional form). Apodization is the process by which the original index profile is modulated with an envelope function to fine-tune the spectral response. Such profiles can produce high, narrow reflectance peaks while suppressing side band reflections that would otherwise appear in a Bragg-like design.[108]

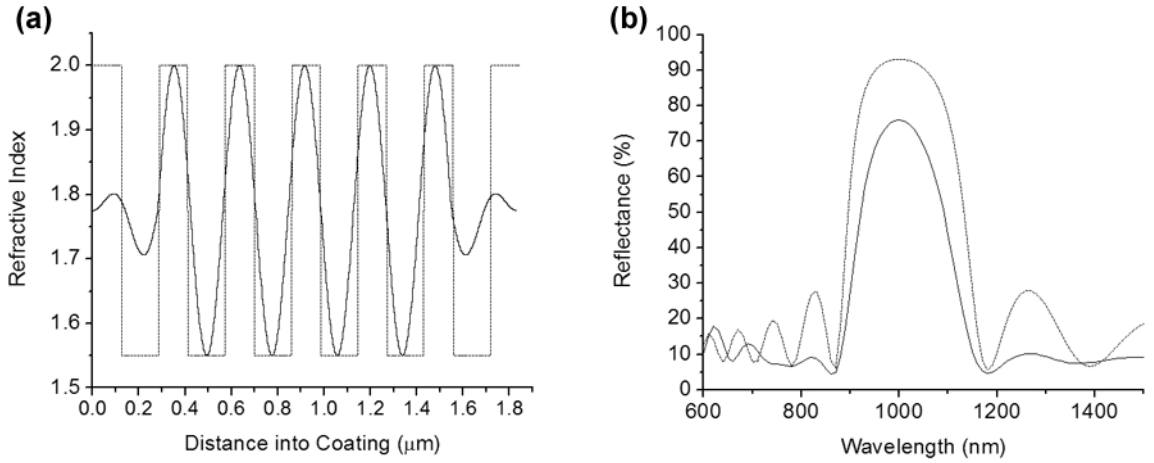

Figure 2.5. Bragg and rugate structures with their corresponding calculated reflection behavior. The index profiles (a) for the Bragg reflector (dotted line) and the rugate structure (solid line) are shown with the corresponding theoretical reflectance curves (b), calculated using the matrix method (see Section A.1)

The simulated spectral profiles in Figure 2.5 demonstrate the side band reflectance suppression of the apodized rugate over the traditional Bragg structure. Simulations of these structures were performed assuming non-dispersive indices and light incident in air from the film side of a structure deposited on a glass (n = 1.52) substrate. The high and low refractive index values represent the values of polymer layers that contain and do not contain silver nanoparticles, respectively. For the purpose of the calculations in Figure 2.5 these values were assumed frequency-independent, but other simulations in this chapter take the dispersive behavior of the silver-containing regions into account. In this design, the index oscillates between extrema of n_L = 1.55 and n_H = 2.00 and the filter's periodic structure is designed to reflect strongly in a band centered at 1000 nm. The selected index values represent the index of the unmodified (PAH/PSS) regions and the nanoparticle-containing (PAH/PAA) regions, respectively. The rugate profile of Figure 2.5a was discretized into 75 regions, as this number ensured that $N \cdot T << \lambda$ and provided good agreement between the simulated responses of the 75-region device and the theoretically smooth rugate (see Section A.2). After choosing the number of discretization steps, thicknesses of the high index and low index regions of the equivalent digitized rugate structure were calculated using Equation 2.3. The results of this calculation are shown in Figure 2.6 for two periods of the continuous index profile.

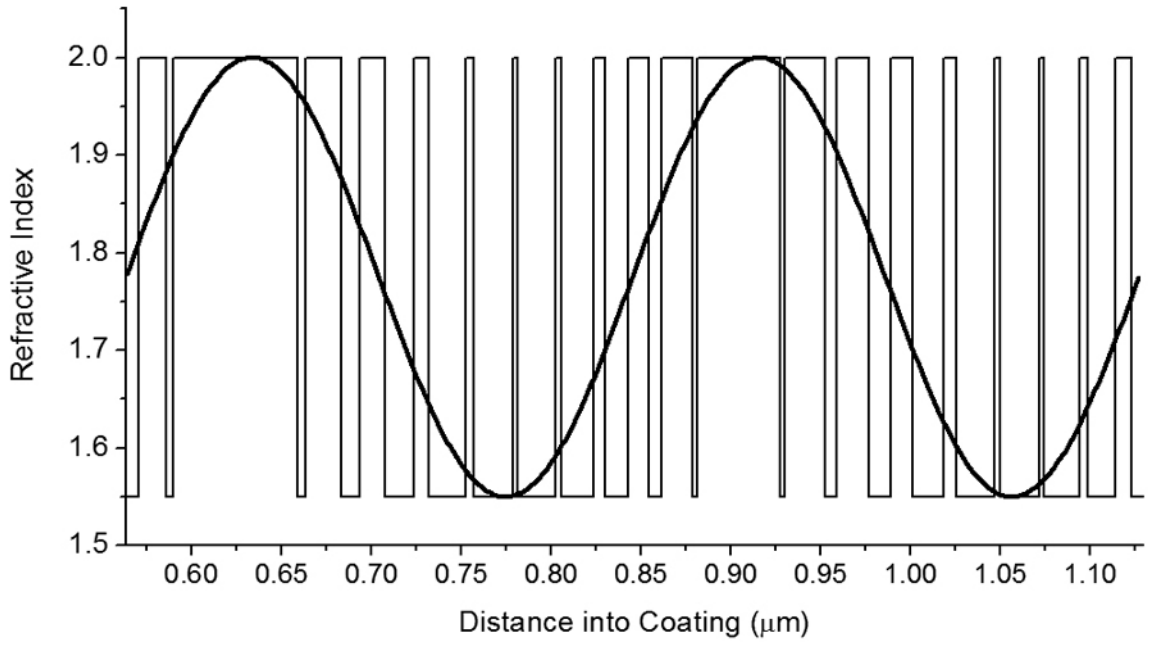

Figure 2.6. Rugate digital equivalent. Two periods of the original rugate profile from Figure 2.5a (bold line) are shown against the index profile of the digital equivalent, which consists of slabs of only high index and low index material.

2.4.2 (PAH/PSS) Growth Study

Construction of the high index regions in the digital equivalent structure of Figure 2.6 was accomplished using the polyelectrolytes poly(allylamine hydrochloride) (PAH) and poly(acrylic acid) (PAA). These polymers have a pH-dependent degree of ionization in solution that permits tuning of the chemical and structural properties of the resulting multilayers. All polymers in this study were deposited at a pH of 3.0, which, for the (PAH/PAA) multilayers, yields a high density of free carboxylic acid groups.[51] The free carboxylic acid groups in the (PAH/PAA) bilayers bind silver via ion exchange upon immersion of the film in a silver salt solution. Reduction with hydrogen leads to the formation of zero-valent silver nanoparticles and regeneration of the free acid groups, allowing repeated cycling of the nanoparticle synthesis.

The low index regions of the film were built using PAH and poly(styrene sulfonate) (PSS). Regions of the multilayer film containing (PAH/PSS) layers had no binding sites for silver cations, and therefore did not support the synthesis of metal nanoparticles by the process

outlined above.[50] Building a heterostructured film containing both (PAH/PAA) and (PAH/PSS) multilayer regions enabled confinement of nanoparticle growth to only those planar regions of the film containing (PAH/PAA) multilayers.

Control of the thickness and spacing of the nanoparticle-containing domains required knowledge of the deposition behavior of both the (PAH/PAA) and the (PAH/PSS) multilayers. In general, weak polyelectrolyte systems such as (PAH/PAA) have been shown to increase linearly in thickness with the number of bilayers deposited.[38] The (PAH/PSS) system, fully charged at a pH of 3.0, displays somewhat different behavior when deposited on the underlying weakly charged (PAH/PAA) platform. The first few bilayers of (PAH/PSS) will tend to deposit at approximately the same thickness per bilayer as the underlying (PAH/PAA) layers, but the incremental thickness due to further (PAH/PSS) bilayers will be considerably smaller.[50] The success of digitized rugate construction relies on the precise thickness control of many thin layers. Studies to quantify this phenomenon were therefore performed.

The incremental thickness of (PAH/PSS) bilayers on an underlying (PAH/PAA) platform is shown in Figure 2.7 for 2 min and 5 min dipping times, respectively. All polymer solutions were adjusted before dipping to pH 3.0 with 1.0 M HCl. The solutions used to dip the (PAH/PSS) bilayers contained an additional 1 M NaCl. The film thickness becomes linear in the number of (PAH/PSS) bilayers deposited after an initial growth regime where the film thickness increases at a higher rate.

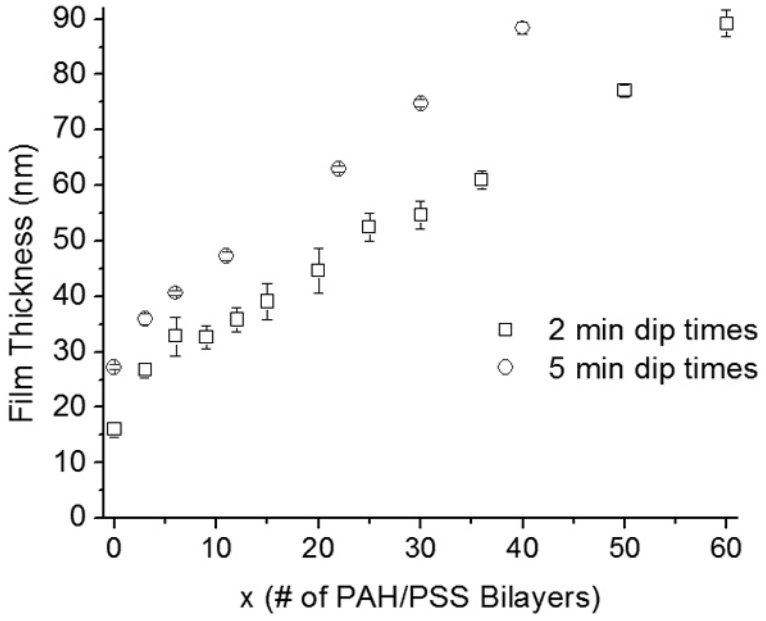

Figure 2.7. Incremental film thickness vs number of (PAH3.0/PSS3.0) bilayers deposited on an underlying 10 bilayer (PAH/PAA) platform for 2 min and 5 min dipping times. Film structures can be represented as: $(PAH3.0/PAA3.0)_{10}(PAH3.0/PSS3.0)_x$.

Based on a qualitative examination of these figures, the polymer growth for purposes of the digital design algorithm was modeled as two linear regions. The first region incorporated the growth behavior of the first 3-6 bilayers of (PAH/PSS) growing on the (PAH/PAA) platform. The second region was comprised of all remaining data. Least-squares regression was performed on each data set. The growth rates obtained from this analysis are outlined in Table 2.1.

Dipping Time (min)	Region 1 Initial growth rate (nm/bilayer)	Region 2 Final growth rate (nm/bilayer)
2	2.8	1.1
3	*2.8*	*1.2*
5	2.9	1.4

Table 2.1. Growth rate of (PAH/PSS) bilayers on a (PAH/PAA) platform for various dip times. The values at a dipping time of 3 mins were interpolated from the known values at 2 and 5 min dipping times.

The thickness increment of the first 2 to 3 (PAH/PSS) layers on an underlying weak polyelectrolyte platform was 2.8 nm/bilayer, with further layers depositing at an incremental thickness of 1.2 nm/bilayer. Based on the values in Table 2.1, bilayer growth information was interpolated to 3 min dipping times (italics in Table 2.1). This information was then used for design of the rugate digital equivalent as detailed in the following section.

2.4.3 Digital Rugate Construction

After the initial selection of a continuous index profile, the digital design and PEM dip planning was completed by computer, and construction of the rugate filter was accomplished by an automated slide dipping system. This scheme is outlined graphically in Figure 2.8.

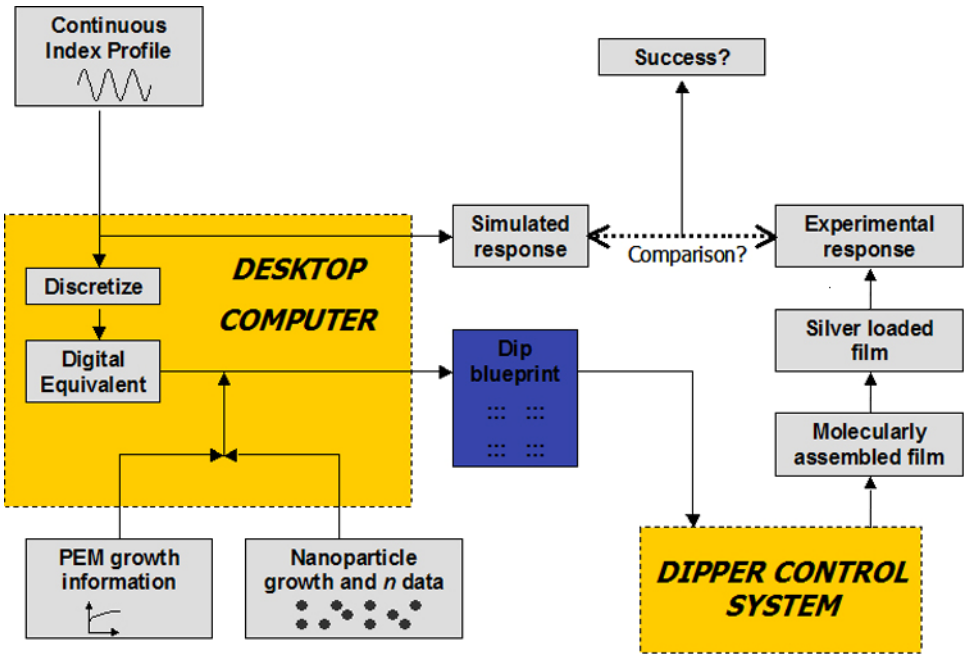

Figure 2.8. Building a digital rugate.

Figure 2.8 can be summarized as follows: the initial continuous rugate profile was first entered into a computer in functional form. Discretization was chosen at 75 steps, followed by digitization according to the method of Southwell. The latter step utilized experimentally measured polyelectrolyte deposition information (see Table 2.1) as well as silver

nanocomposite region expansion and refractive index data,[51, 62] to produce a blueprint for the construction of a polyelectrolyte multilayer film. This blueprint, which detailed the exact number and order of polymer layers to deposit, was then entered into a computer that controlled an automated Zeiss slide stainer, which then deposited the necessary sequence of layers to create a digitized rugate template. The assembled film was then loaded with silver ions from solution and reduced in a hydrogen atmosphere to yield the completed filter, whose optical and structural properties were then characterized and compared to the theoretical response of the planned design.

2.4.4 Digital Rugate Characterization

The near-normal incident reflection and transmission properties of the rugate filter were analyzed using a Varian Cary 5E spectrophotometer, and are detailed in Figure 2.9. A single reflectance band with minimal side bands was observed to grow and shift spectrally over the course of successive silver exchange-reduction cycles, from R_{max}=26.5% at 732 nm after 1 cycle, to R_{max}=75.1% at 924 nm after 5 cycles (Figure 2.9a). The growth of the reflectance band is expected because of the increasing index contrast between the silver-containing and non-silver-containing polymer domains. This index effect is also partly responsible for the spectral shift of the band to higher wavelengths, as is the increasing thickness of the silver-containing domains with the increasing concentration of nanoparticles. Due to the apodized rugate profile, side band reflectances are suppressed at or below 10% after 5 silver exchange-reduction cycles over the entire observed spectral range. The surface plasmon absorbance[67] of the silver nanoparticles is responsible for the reflectance feature near 500 nm, as well as the rapid decrease in the transmittance of the filter at shorter wavelengths due to absorbance (Figure 2.9b).

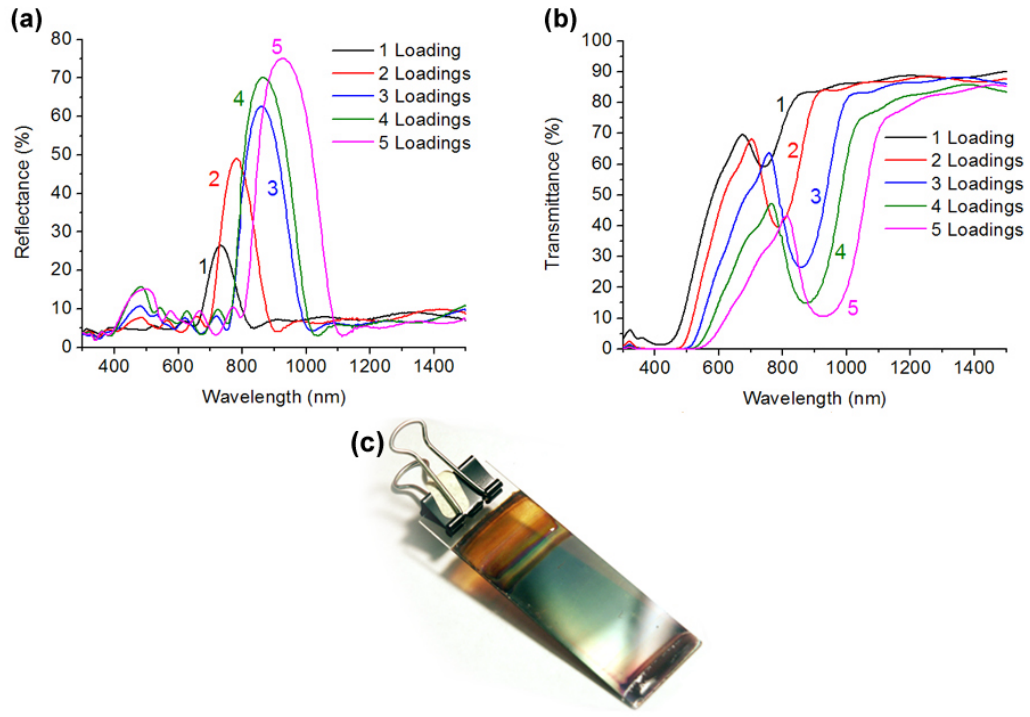

Figure 2.9. Reflectance (a) and transmittance (b) of a PEM-templated digitized rugate. A photograph of the rugate film on which these measurements were performed is shown in (c). Numbers shown by the curves indicate the number of silver nanoparticle exchange-reduction cycles. The reflectance feature near 500 nm that grows but does not shift with increasing silver loading is due to the silver nanoparticle surface plasmon,[67] not to an interference effect. The photograph was taken following 5 exchange-reduction cycles.

Cross-sectional TEM was performed to characterize the structure of the rugate filter (Figure 2.10). Well-defined (PAH/PAA) domains containing silver nanoparticles (dark regions) are clearly visible between multilayer regions containing (PAH/PSS). The images confirm consistent and precise thickness control among the 136 total high index and low index domains within the film, even at the length-scale of a few nanometers—approximately the same size as the diameter of the nanoparticles themselves. In order to further quantify information about the rugate structure, a 2-D Fourier transform was performed on the grayscale image in Figure 2.10a, yielding a spectrum, the central part of which is shown in the inset of Figure 2.11.

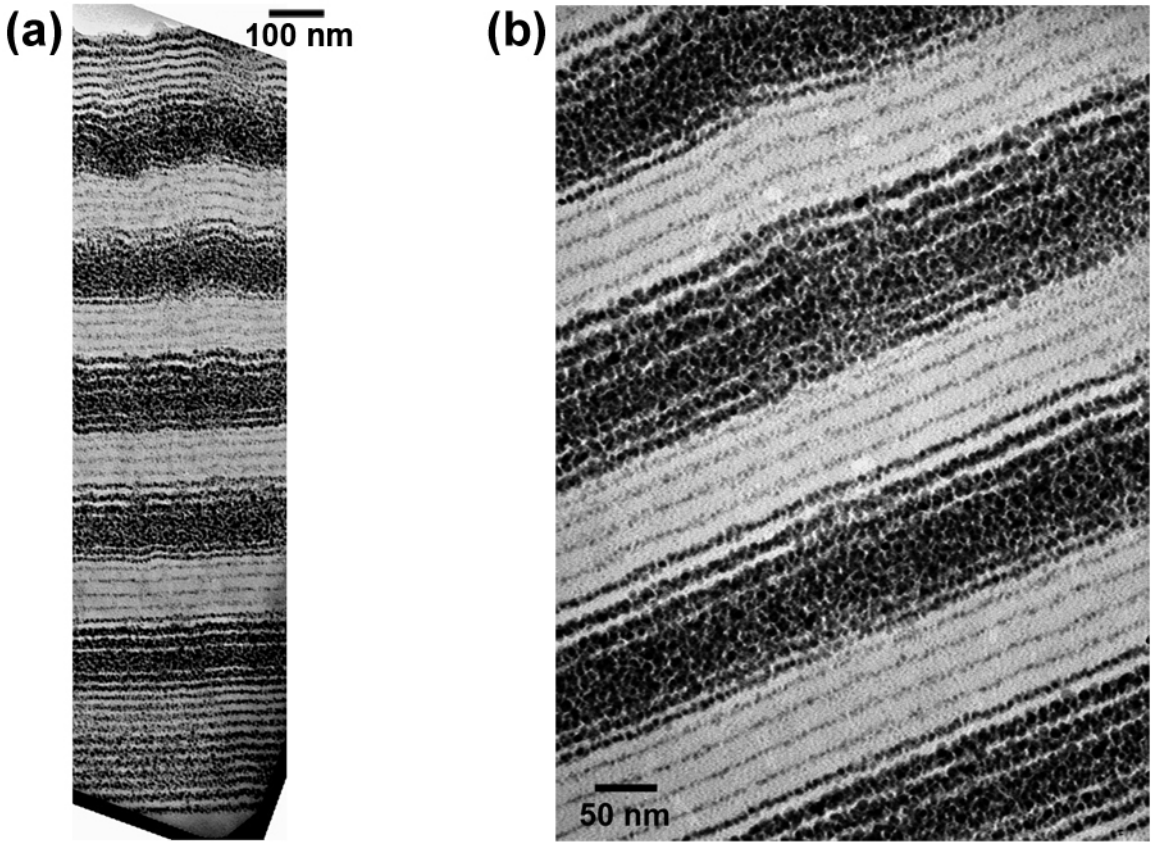

Figure 2.10. Cross-sectional TEM images of a PEM-templated digitized rugate. The sample was deposited on a polystyrene substrate, which can be seen at the very bottom of (a). Undulations in the film were likely introduced during sample preparation by ultramicrotomy, which also caused delamination of the last 10 high-index and low-index regions of the composite on the air side of the film. Profilometry on the same sample shows an average RMS surface roughness of 9.3 nm ± 2.1 nm.

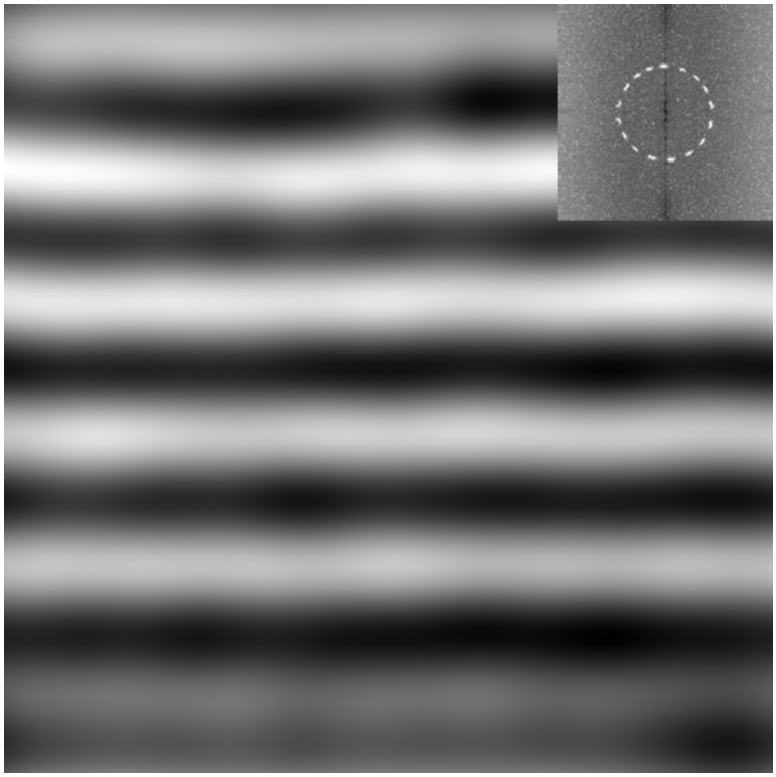

Figure 2.11. The Fourier transform of the TEM image (inset) reveals information about the periodicity of the structure. High frequency filtering (passing only frequencies inside the dotted circle of radius 5.1 μm^{-1}) masks the sharp index discontinuities apparent in the image of the digital rugate so that an inverse transform reveals the smooth sinusoidal periodicity of the original continuous profile.

The Fourier spectrum displayed strong intensity peaks along the vertical axis, indicating a dominant spatial frequency of 4.3 μm^{-1}. Direct measurement of the total film thickness from the electron micrograph shown in Figure 2.10a was not possible due to delamination of the last 10 high-index and low-index regions during ultramicrotomy. The spatial frequency value of 4.3 μm^{-1}, however, if interpreted as an average period length for the sinusoidal index variations within the film displayed in Figure 2.10a, implies that the overall length-scale of the experimental structure is $\approx$ 82% of the original design. Computer simulations of the optical response of the theoretical structure lead to similar conclusions. The anticipated spectral response of the digitized rugate filter was calculated using the matrix method (see Section A.1) and is shown in Figure 2.12, along with the experimentally measured data (at 3 silver exchange-reduction cycles). A notable blue-shift of the experimental response is evident, which can be accounted for by uniformly compressing the theoretical structure

length to 84% of its original value. The resulting corrected simulation shows excellent agreement with the data obtained by experiment. The results of profilometry performed on the same filter corroborate these findings as well. A total film thickness of 1.52 ± .01 μm was obtained, a value ≈ 83% of the expected result.

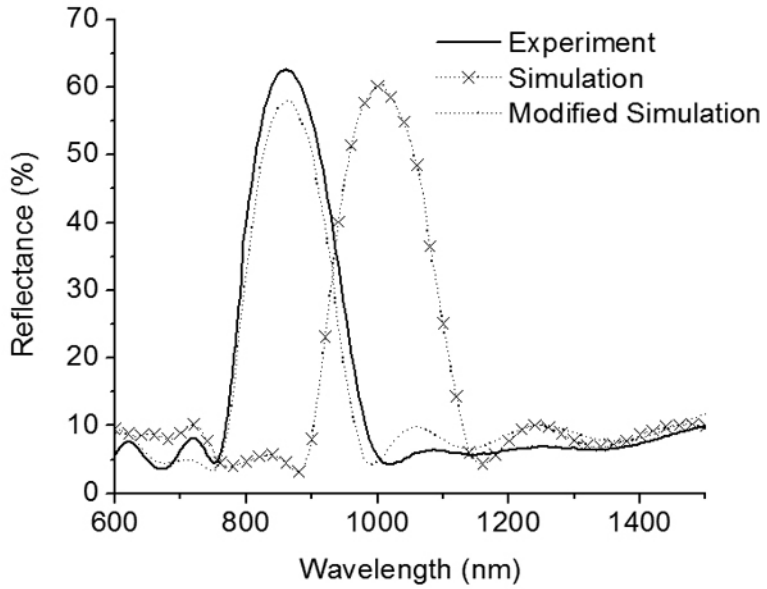

Figure 2.12. Digital rugate reflectance response. Experimental data is shown along with the computer-simulated theoretical model (three silver exchange-reduction cycles). The simulation results of a film whose theoretical structure has been uniformly compressed by 84% (modified simulation) show very close agreement with experiment.

2.5 Conclusions

This work confirms that layer-by-layer deposition can be used successfully to create polymer films with precisely confined planar domains of a specific chemical functionality. This is in contrast to recent studies that have demonstrated significant long-range chain diffusion within multilayers of certain systems.[135, 136] In addition, the creation of a multilayer film such as the one presented here subjects the material to a complex processing cycle of swelling, de-swelling, and chemical ion-exchange. As proof of the remarkable resiliency of the films to such treatment, the same sample was used for all optical characterization results presented in this chapter, and after repeated cycling of nanoparticle growth it still demonstrated consistent nanometer-scale arrangement over a total film

thickness on the order of micrometers. Despite the long processing times required to create precisely-tailored nanocomposite films of micron-scale thickness, the layer-by-layer technique remains very appealing due to the low cost and ease of production. The constructed filter was slightly thinner than anticipated, pointing to an error in the PEM deposition data input to the computer design algorithm. With further investigation such deviations of experiment from theory will no doubt be reduced. Though there is potential application for these devices as advanced conformable optical filters, the choice of silver nanoparticles as an index enhancer may preclude their use at visible wavelengths due to the strong absorbance from the silver surface plasmon (see Figure 2.9b). Such behavior is undesirable to those seeking high transmission in the visible range at shorter wavelengths, but could conceivably prove useful for anyone desiring a high-frequency cutoff for low-power applications. The PEM-templating technology, however, is not limited to the use of silver. The addition of different metals or semiconductors,[48, 50, 57] as well as the possibility of performing templated sol-gel chemistry,[52] are exciting topics for future exploration.

Possible uses of devices of this type as chemical or biological sensors have been suggested in the literature,[72, 73] and changing photonic effects upon swelling of similar systems in solution have already been observed.[62] In addition, organic vapor sensing with porosity-templated PEM Bragg filters has been demonstrated.[59] Other possible applications resulting from the construction of these filters from soft, hydrophilic materials could include deformation-tunable photonic devices, as well as pH- or humidity-sensitive optical devices. It should also be noted that the creation of composition gradients in thin films is an important topic whose interest extends far beyond the field of optical engineering. Although here the spatial selectivity afforded by polyelectrolyte multilayer synthesis has been used to create a digitized rugate filter, there could also be potential application for this technology in any field where one wishes to precisely control the structural features of thin polymer films at the single nanometer length-scale. Grading the modulus within a polymer composite, for example, can have beneficial effects on the mechanical properties, such as increased resistance to contact damage.[4] In addition, the use of aqueous-based, PEM-templated synthesis for the construction of rugate filters not only enables the inexpensive and

straightforward production of graded nanocomposite films, but it opens the possibility for their construction on the surfaces of colloids, the insides of tubes, and on a wide variety of other substrate materials and morphologies—feats that may be difficult or impossible by traditional means. This work suggests that the polyelectrolyte layer-by-layer technique may be an easy and affordable way to approach these and other challenges facing the development of nanoscale processing with organic materials.

Having discussed the process for creating PEM films with graded property profiles through carefully controlled construction techniques, the following several chapters will focus on how one can measure the Young's modulus of PEM films. The Young's modulus is an important mechanical property parameter that can be an important determinate in predicting the durability of a functional coating, and is also expected to yield insights into the structure and bonding properties of various layer-by-layer assemblies.

Chapter 3
Young's Modulus Measurements on Polyelectrolyte Multilayer Films via Strain-Induced Elastic Buckling Instabilities*

3.1 Introduction

Polyelectrolyte multilayer deposition has become increasingly popular as a means of creating thin polymer films with a wide range of physical properties and potential applications, making the mechanical strength and stability of these films an important factor in evaluating the practicality of their use. This is especially true, for example, in the biomaterials area, where the mechanical properties of a surface have been shown to dramatically affect the attachment and growth of cells.[7, 138] Though a number of different techniques have been pursued in the literature,[7, 27, 29, 138-167] PEMs continue to present a considerable challenge for those wishing to investigate their mechanical stiffness, as they usually exist only as ultrathin films. Previous attempts to measure the modulus of PEMs, for example, have required assembly of films into hollow capsules followed by mechanical-[141, 142, 153-158, 167] or chemical-driven[146, 147, 152, 166] probing of the capsule stiffness, or have utilized specialized equipment that typically requires films to be of micron-scale thickness, as in the case of nanoindentation.[7, 138, 143, 144, 159-162] Not all multilayer systems have proven amenable to microcapsule assembly,[9] however, and building films microns thick can be prohibitively time consuming with certain polyelectrolyte systems that may exhibit thickness increments of less than 1 nm/bilayer.[38]

The following three chapters discuss the use of a buckling-based technique termed "strain-induced elastic buckling instability for mechanical measurements", or SIEBIMM for short.[168] The current chapter will introduce the basic technique, and demonstrate how it has been used to measure the modulus of (PAH/PSS) assemblies in both the wet and dry states, while Chapter 4 and Chapter 5 will cover further development of the SIEBIMM technique and measurement of PEM mechanical properties as a function of the ambient humidity. It is

* This chapter is reproduced in part with permission from Reference 137: Nolte, A. J.; Rubner, M. F.; Cohen, R. E., Determining the young's modulus of polyelectrolyte multilayer films via stress-induced mechanical buckling instabilities. *Macromolecules* **2005,** 38, (13), 5367-5370. Copyright 2005 American Chemical Society.

shown that SIEBIMM is a simple and easy to implement method that solves many of the problems associated with previous attempts to measure the modulus of these materials.

3.2 Background and Motivation

3.2.1 Motivation for the Mechanical Characterization of Polyelectrolyte Multilayers

Many important motivating factors drive the mechanical study of PEM films. Many studies have explored the possibility of using PEM-coated surfaces to control the attachment and function of certain cells.[7-9, 47, 138, 143, 162, 169-185] Control of the cytophilicity or cytophobicity of such coatings has been shown to be linked in part to the stiffness of the PEM in the culture environment.[47] These results are consistent with recent biological studies that have confirmed that the mechanical properties of a substrate can affect the adhesion, movement, and function of cells.[174] Because the crosslink density of PEMs, and hence their moduli, can be easily controlled by the assembly conditions[38] or other post-assembly chemistries,[8] these materials represent promising candidates for biosurface modification schemes. A method of easily measuring the stiffness of (potentially ultrathin) PEM coatings could significant aid quantitative study of these phenomena.

PEMs have also been proposed for use as tribological coatings on orthopedic implants.[5, 161] Preliminary studies have indicated that PEMs may serve to reduce wear at interfaces in, for example, artificial joint implants, and that PEMs may also be able to reduce friction at such interfaces. Further study of the abrasion resistance of PEMs will also be important for other PEM applications where regular mechanical contact with the coating might be expected, such as with PEM antireflection coatings.

In addition to the above considerations, study of the mechanical properties of PEMs may yield important insights into the intrafilm structure and bonding interactions. Of particular interest is the effect of the degree of electrostatic crosslinking on the PEM modulus; this parameter can be varied (in weak polyelectrolyte systems) by careful control of the pH conditions during assembly.[38] Other studies have found that electrostatic crosslinks in hydrated films can be mediated post-assembly by the ionic strength of the solution.[167, 186-192]

Study of these phenomena via mechanical properties measurements should provide an important window into internal film dynamics, paving the way towards a better understanding of how PEMs behave in various environments, as well as revealing their strengths and weaknesses for various surface engineering applications.

3.2.2 Literature Review of Previous Work

This section will present a brief review of previous literature aimed at measuring the elastic modulus of PEM assemblies, with a focus on the techniques and their relative advantages and disadvantages; the reader is referred to Section 3.4.3 (especially Table 3.2) for a summary of numerical results that have been reported for the various techniques.

Because polyelectrolytes are inherently thin film materials for which no bulk analogue exists, mechanical property characterization is a challenging task. Hsieh and McCarthy seem to have been the first to report attempts to measure the modulus of PEMs (comprising PAH and PSS multilayers) by conducting tensile tests on PEM-coated Lycra yarns.[148, 149] This was a relatively straightforward approach that was able to obtain modulus estimates within an order or magnitude, but the accuracy of their analysis suffered from the lack of an appropriate method to obtain the exact PEM film thickness due to the cylindrical topology of the substrate.

Nanoindentation is the controlled indentation of a film or substrate surface with a small probe.[193] Knowledge of the force exerted as a function of indentation distance can allow calculation of the mechanical properties of the material. This technique is arguably the most popular technique for thin film mechanical property characterization, but difficulties in extending the technique to PEMs remain. One challenge involves the need to build films to minimum depths of hundreds of nanometers in order to avoid substrate influences on the calculated film modulus, which can be prohibitively time consuming for systems with very low bilayer growth increments. By depositing sufficiently high number of bilayers, Pavoor et al. was able to find the Young's modulus for (PAH/PAA) multilayers deposited at various assembly conditions using the technique.[160] Richert et al. have examined highly swollen

networks of crosslinked PEMs using colloidal probe AFM,[162] and most recently, Thompson et al. have demonstrated nanoindentation of PEM assemblies in the hydrated state.[7, 138]

Microcapsule manipulation has been perhaps the most popular method to date for measuring the mechanical properties of PEMs. PEM microcapsules are formed from the assembly of PEMs onto micron-scale colloids, followed by the dissolution of the colloidal substrate to leave a hollow PEM shell. Gao et al. were the first to demonstrate Young's modulus measurements on PEM microcapsules.[146] Their technique involved observing the osmotic-driven collapse of microcapsules in solutions of polymer for which the capsule wall was impermeable. The modulus of the capsule was extracted from the known capsule wall thickness and the average osmotic pressure at which the capsules began to collapse (invaginate). Vinogradova et al. used a similar technique to extract the wall modulus of osmotically swollen PEM microcapsules.[152, 166] With Lulevich, they also demonstrated the deformation of immobilized PEM microcapsules with modified AFM cantilevers for PEM modulus measurements,[154-158] a technique that was combined with reflection interference contrast microscopy and used by Fery, Dubreuil, and Heuvingh et al.[141, 142, 145, 167] The major contribution of the latter researchers was to demonstrate work in a deformation regime where assumptions about permeability of the capsule wall could be effectively eliminated. This step greatly improved the confidence in the accuracy of PEM modulus values obtained via capsule deformation, where before measurements on the same system resulted in a spread of reported moduli over a range of three orders of magnitude (see Table 3.2). While PEM microcapsule deformation techniques have certainly improved since their first inception, they remain technologically difficult to employ and rely on various assumptions about the mechanical behavior of the capsule membrane. Two relatively recent review articles[145, 165] cover development of these techniques and their relative advantages and disadvantages in more detail.

Another technique that has recently emerged in the literature is the tensile testing of free-standing films. Mamedov et al.[27] and Tang et al.[29] have recently demonstrated this technique on free-standing films of PEM-carbon nanotube and PEM-clay composite films, respectively. Jaber et al. used a very similar technique to measure the tensile modulus of

PDAC/PSS layers in solution at various salt concentrations, and has recently demonstrated dynamic mechanical testing of PEMs using a similar technique.[194, 195] Tensile-testing of free-standing films, however conceptually straightforward, still presents considerable difficulties for PEM researchers. Films generally need to be grown to large thicknesses to survive peeling from a low surface energy substrate such as Teflon, and peeled films must then be mounted and tested in a specially designed apparatus. PEM modulus values can also be extracted from free-standing films via a bulging test, as demonstrated by Jiang et al. for PEM membranes assembled using spin-assisted LbL assembly.[150, 151] This method also requires freeing the film from the assembly substrate, generally by use of a dissolvable sacrificial substance between the substrate and the PEM.

Despite the many novel approaches that have been followed by previous researchers, elucidation of PEM mechanical properties has, until only recently, remained a challenging problem. The following section will introduce the SIEBIMM technique, which has proven remarkably well-suited to the task of measuring the Young's modulus of PEM films.

3.2.3 Description of the SIEBIMM Technique and Derivation of the Buckling Equation

SIEBIMM analysis exploits the fact that a thin, higher modulus material bonded to a semi-infinite, lower modulus substrate will buckle when subjected to compressive planar forces in order to relieve the strain energy in the system. To minimize this energy, buckling takes place at a characteristic wavelength, λ, given by:[168, 196]

Equation 3.1

$$\lambda = 2\pi d \cdot \left(\frac{E_f \left(1 - \nu_s^2\right)}{3E_s \left(1 - \nu_f^2\right)} \right)^{1/3}$$

where d is the film thickness, and E_f, ν_f, E_s, and ν_s are the Young's moduli and Poisson's ratios of the film and substrate, respectively. This phenomenon is represented graphically in Figure 3.1.

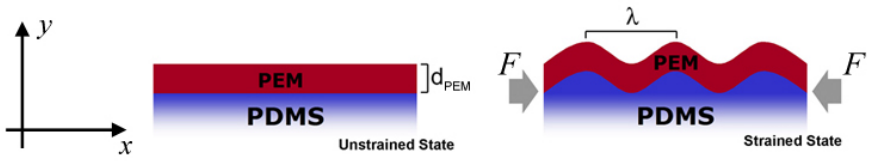

Figure 3.1. Schematic of PEM film deposited on a PDMS substrate. The left panel shows a film of thickness d_{PEM} deposited on a thick (assumed semi-infinite) substrate. The right panel illustrates the formation of a buckling instability of wavelength λ with compression of the system.

The derivation of Equation 3.1 is relatively straightforward and can be obtained from the equation describing the bending of a rigid plate on an elastic foundation:*

Equation 3.2

$$\overline{E}_{PEM} \cdot I_{PEM} \cdot \frac{d^4 y}{dx^4} + F \cdot \frac{d^2 y}{dx^2} + ky = 0$$

where E_{PEM} is the Young's modulus of the PEM film, x is the distance along the direction of buckling, y is the displacement orthogonal to the plane of the film, and I_{PEM} represents the second moment of area of the PEM film (with width w) about its neutral bending axis, which for the case of a uniform film with thickness d_{PEM} is found at the midpoint:

Equation 3.3

$$I_{PEM} = \frac{w \cdot d_{PEM}^3}{12}.$$

The overbar on a Young's modulus denotes a *plane strain modulus*, which accounts for the planar geometry of the film and is taken for any material as:

* The derivation of the buckling equation in this section follows a similar methodology to the work of Volynskii. See, for example, Reference 196.Volynskii, A. L.; Bazhenov, S.; Lebedeva, O. V.; Bakeev, N. F., Mechanical buckling instability of thin coatings deposited on soft polymer substrates. *Journal of Materials Science* **2000,** 35, (3), 547-554.

Equation 3.4

$$\overline{E} = \frac{E}{\left(1-\nu^2\right)}$$

where v is the Poisson's ratio of the material with Young's modulus E. The quantity F is the longitudinal compressive force applied to induce buckling (as depicted in Figure 3.1), and k is known as the Winkler modulus of half-space, which is the modulus of resistance to a displacement y into the substrate:[197]

Equation 3.5

$$k = \overline{E}_{PDMS} \cdot \pi \frac{w}{\lambda}$$

where E_{PDMS} is the Young's modulus of the PDMS substrate, and λ is the wavelength of the buckling deformation. The expression for the Winkler modulus is derived according to an assumed deformation profile for the buckling film. In the case of Equation 3.5, a sinusoidal profile with wavelength λ is assumed:

Equation 3.6

$$y = A \cdot \sin\left(\frac{2\pi}{\lambda} x\right)$$

where A is the amplitude of the buckling deformation. By combining Equation 3.2, Equation 3.3, Equation 3.5, and Equation 3.6, one can obtain an expression for the stress in the film:

Equation 3.7

$$\sigma = \frac{F}{w \cdot d_{PEM}} = \overline{E}_{PEM} \cdot I_{PEM} \cdot \left(\frac{4\pi^2}{w d_{PEM} \lambda^2} + \frac{\overline{E}_s \cdot \lambda}{4\pi d_{PEM} \cdot \overline{E}_{PEM} \cdot I_{PEM}} \right).$$

The quantity σ in Equation 3.7 is positive for all values of lambda. Equation 3.7 can be rewritten in a dimensionless form:

Equation 3.8

$$\Sigma = \frac{\pi^2}{3} \cdot \Lambda^{-2} + \frac{1}{4\pi} \cdot \Lambda$$

by taking Σ, the dimensionless stress, and Λ, the dimensionless wavelength, as:

Equation 3.9

$$\Sigma = \frac{\sigma}{\sqrt[3]{\overline{E}_{PEM} \cdot \overline{E}_{PDMS}^{2}}} \qquad \Lambda = \sqrt[3]{\frac{\overline{E}_{PDMS}}{\overline{E}_{PEM} \cdot d_{PEM}^{3}}} \cdot \lambda \, .$$

The plot of Equation 3.8 is given in Figure 3.2.

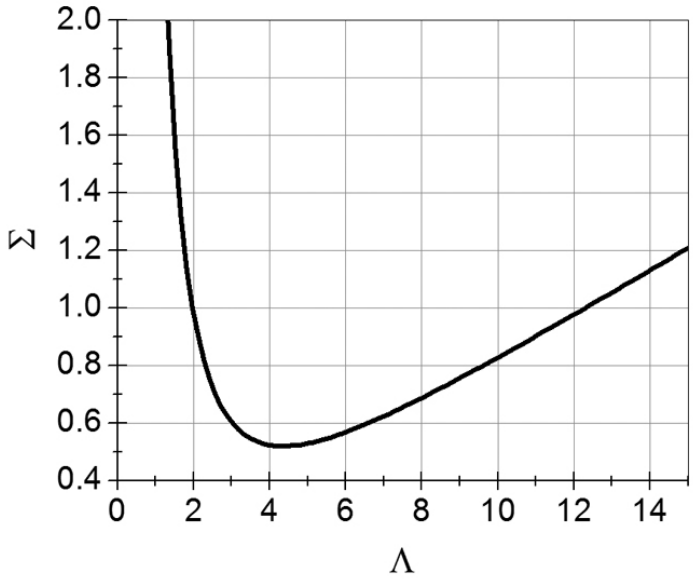

Figure 3.2. Plot of the dimensionless stress (Σ) vs dimensionless wavelength (Λ).

Figure 3.2 demonstrates that a minimum in Σ can be found at $\Lambda \approx 4$. The exact value can be shown to be $2\pi/3^{1/3}$ by differentiating Equation 3.8 and setting $d\Sigma/d\Lambda = 0$. Plugging $\Lambda = 2\pi/3^{1/3}$ into Equation 3.9 and solving for λ yields Equation 3.1. The critical stress value for

onset of buckling ($\Sigma \approx$ 0.5 in Figure 3.2) is found to be $\Sigma = (3^{2/3})/4$ by taking $\Lambda = 2\pi/3^{1/3}$ and combining Equation 3.8 and Equation 3.9. For stresses below this value, the film and substrate will simply compress elastically in the *x* direction.

Equation 3.1 is commonly rewritten to solve for the film modulus:

Equation 3.10

$$\frac{E_{PEM}}{1-\nu_{PEM}^2} = 3 \cdot \frac{E_{PDMS}}{1-\nu_{PDMS}^2}\left(\frac{\lambda}{2\pi d_{PEM}}\right)^3 .$$

It is important to note that the applied stress does not appear in Equation 3.10. The buckling transition is a critical phenomenon, and the wavelength is therefore expected to be strain-independent in the limit of small deformations. This consideration is a major advantage for the SIEBIMM technique, as Young's modulus measurements conducting using other methods almost always require force-displacement measurements, which can be extremely challenging to carry out on very small scales. In practice, some researchers have reported slight decreases in the expected buckling wavelength for high strains (10%);[198] it should be noted that the strains in this study were only a few percent, and were therefore assumed to not measurably change the buckling wavelength from its critical value. The Poisson's ratios for the film and substrate are typically assumed to be 0.33, in the case of glassy polymeric films, and 0.5 for the rubbery substrate.[168] In the work that follows, a value of 0.33 is assumed for dry-state PEMs, and a value of 0.5 for PEMs in the wet state.

The experimental details of how the quantities in Equation 3.10 are found in order to calculate the Young's modulus of the PEM are given in the following section and summarized in Figure 3.3.

3.3 Experimental Details

PDMS (Sylgard 184, Dow Corning) was prepared by mixing the crosslinker and base compound in a 1:10 w/w ratio. The mixture was cast into a tray to a thickness of $\approx$ 3 mm, and allowed to de-gas at atmospheric conditions for 45 min – 1 hr, after which it was baked

at atmospheric pressure for 45 min at 80°C. After cooling to room temperature, the PDMS was cut into 2 cm × 6 cm pieces.

PAH (M_w = 70 000, Sigma-Aldrich) and PSS (sodium form, M_w = 70 000, Sigma-Aldrich) were used without further purification to create polymer solutions of 0.01 M concentration by repeat unit. In addition, 0.1 M NaCl (Mallinckrodt Chemicals) was added to each polyelectrolyte solution as previously described. Milli-Q deionized water (Millipore) with a resistivity of 18.2 MΩ·cm was used for all procedures and preparations. Solutions were adjusted to the appropriate pH with 1.0 M HCl or NaOH immediately prior to PEM assembly.

Assembly of PEMs onto PDMS was performed by an automated programmable slide stainer (HMS slide stainer, Zeiss). Substrates were first immersed in the polycation (PAH) for 15 min, followed by three 1 min rinse steps. The samples were then immersed in the polyanion (PSS) for 15 min, followed again by three 1 min rinses. This process was cycled until the desired number of bilayers were deposited. If more than 10 bilayers were deposited, the immersion time in the polyelectrolyte baths was decreased to 5 min for the 11^{th} and all subsequent bilayers. Following the completion of PEM assembly, samples were allowed to air dry. Samples were stored in air at ambient conditions and tested within a few days of PEM assembly.

Modulus measurements were obtained by applying planar compressive strains (1-2%) on each sample with a pair of tweezers while taking photographs of the buckled surface with an optical microscope (Axioplan 2, Zeiss). Optical micrographs were subjected to Fourier analysis (see Appendix C) to determine the average wavelength of buckling. Spectroscopic ellipsometry (M-2000D, J.A. Woollam Co.) was performed in order to obtain PEM thickness values (see Section 3.4.1 for more information on this technique). During dry-state experiments, the relative humidity was in the range of 20-32%. Compression testing (Model Z010, Zwick/Roell) of ½" diameter cylindrical samples cut from the PDMS substrates was performed to find the Young's modulus of the substrate (E_{PDMS}). Samples were compressed at a strain rate of $\approx$ 0.02 sec^{-1} and the modulus values were taken as the slopes of the stress-

strain curves in the linear, small strain portions of the data. The results from testing at least 8 different samples were averaged to yield E_{PDMS} for a particular batch of PDMS.

Young's modulus values were calculated using Equation 3.10. As mentioned previously, a Poisson's ratio of 0.33 was assumed for dry-state multilayers, and a value of 0.5 was assumed for wet-state multilayers and the elastomeric PDMS substrate. All error bars in this chapter were calculated by propagation of the uncertainties in the PEM thicknesses, the buckling wavelengths, and the Young's modulus of the PDMS substrate.[199, 200]

The experimental procedure for using SIEBIMM to measure the Young's modulus of PEMs is represented graphically in Figure 3.3.

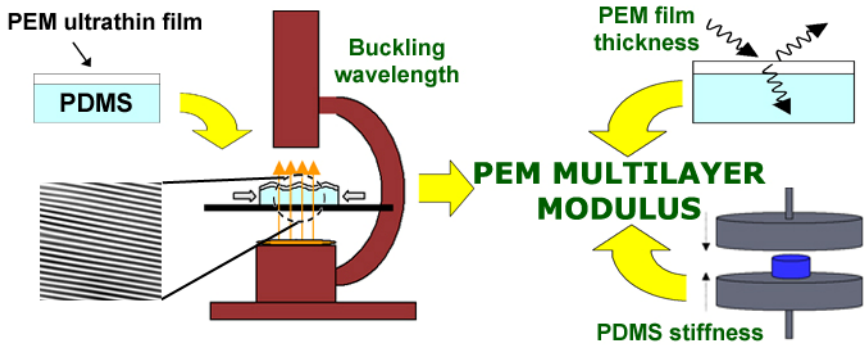

Figure 3.3. Graphical scheme summarizing SIEBIMM testing of PEM films. Films are photographed in the optical microscope while subjected to lateral compression to determine the buckling wavelength. The PEM film thickness is determined via spectroscopic ellipsometry, and the PDMS stiffness is obtained through compression testing.

3.4 Results and Discussion

3.4.1 PEM Thickness Determination via Spectroscopic Ellipsometry

In order to determine the modulus of the PEM films, a method of accurately measuring the PEM film thickness was required. Although ellipsometry is typically used with highly reflective substrates such as silicon, a measurement method was developed whereby spectroscopic (multiple wavelength) ellipsometry was performed directly on the PEM-coated PDMS system. The significant refractive index mismatch between the PEMs ($n \approx 1.55$) and

PDMS ($n \approx$ 1.41) allowed calculation of the film thickness through modeling of the ellipsometric data.

An uncoated piece of PDMS was first scanned in the ellipsometer (M-2000D, J. A. Woollam Co., Inc.). The data were fitted to a Cauchy model (an excellent fit was obtained) and saved in a custom material file. The Cauchy model assumes that the real part of the refractive index, n_R, can be described by:[68]

Equation 3.11

$$n_R(\lambda) = A + \frac{B}{\lambda^2} + \frac{C}{\lambda^4}$$

where A, B, and C are constants, and λ is the wavelength of light. The imaginary part of the refractive index was modeled assuming Urbach absorption:[201]

Equation 3.12

$$n_I(\lambda) = \alpha \cdot \exp\left[12400 \cdot \beta \cdot \left(\frac{1}{\lambda} - \frac{1}{\gamma}\right)\right]$$

where α is known as the amplitude coefficient, β as the exponent coefficient, and γ as the band edge. Table 3.1 gives these parameters as measured for PDMS prepared as described in Section 3.3. The optical parameters for a few representative PEM systems are also provided.

Material	A	B (μm^2)	C (μm^4)	α	β (nm)	γ (nm)	n_R (555 nm)
PDMS	1.401	$2.923 \cdot 10^{-3}$	$1.225 \cdot 10^{-4}$	$2.527 \cdot 10^{-3}$	0.4793	400	1.412
(PAH3.0/PSS3.0)	1.551	$2.634 \cdot 10^{-3}$	$5.862 \cdot 10^{-4}$	--	--	--	1.566
(PAH7.5/PAA3.5)	1.526	$7.257 \cdot 10^{-3}$	--	--	--	--	1.550
(PAH2.5/PAA2.5)	1.492	$7.202 \cdot 10^{-3}$	--	--	--	--	1.515

Table 3.1. Typical optical parameters for PDMS and representative PEM systems. PEM optical parameters were obtained at room temperature and 36% relative humidity by scanning films assembled on PDMS substrates. Blank cells indicate that the parameter was not used in the model to obtain a fit to the ellipsometer data. (PAH3.0/PSS3.0), (PAH7.5/PAA3.5), and (PAH2.5/PAA2.5) multilayer films for this study were assembled to 75, 10.5, and 20 bilayers in thickness, respectively. The final column in the table displays the real refractive index calculated using *A*, *B*, and *C* for each system.

After obtaining the optical parameters shown in Table 3.1 for the bare PDMS substrate, samples of PEM-coated PDMS were then scanned. The resulting experimental data were fitted to a multilayer model consisting of:

1. The underlying PDMS substrate whose optical properties were previously characterized,

2. The PEM film, represented by a Cauchy material model of unknown thickness, and

3. A surface roughness layer of unknown thickness, which consisted of an effective medium of 50% of the ambient medium and 50% PEM film. The ambient medium was usually air ($n \approx 1$), except in the case of solution-state in-situ ellipsometry, where it was water ($n \approx 1.33$).

After scanning, the data were fit to the multilayer model described above by varying the thickness and Cauchy parameters of the PEM (see Equation 3.11 and Equation 3.12), as well as the thickness of the surface roughness layer (usually on the order of 1 nm). The best-fit thickness of the PEM film was then reported—the thickness of the surface roughness layer

was assumed to be indicative of the roughness of the air-PEM or water-PEM interface, and was not included in the reported PEM thickness values.

In-situ ellipsometry refers to the technique of performing ellipsometry on a sample while it is immersed in an environment other than air—typically an aqueous solution. This is accomplished by placing the sample and fluid inside of a cell that has angled windows to permit the entry and exit of the incident and reflected beams.

3.4.2 Determination of the Young's Modulus of (PAH/PSS) via SIEBIMM

In all, 25 samples created in three separate batches with different numbers of bilayers were assembled in order to evaluate the SIEBIMM method at a variety of film thicknesses. The thickness vs number of bilayers plot generated from these samples is displayed in Figure 3.4.

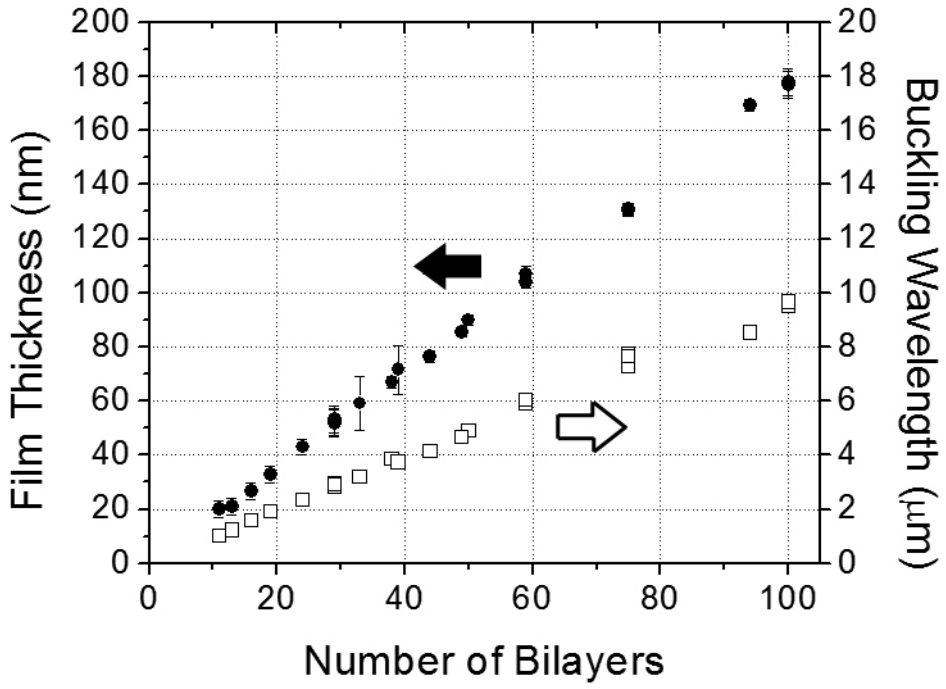

Figure 3.4. Film thickness and buckling wavelength of (PAH/PSS) films vs number of bilayers deposited on PDMS. Thicknesses were determined by spectroscopic ellipsometry, and buckling wavelengths were determined through Fourier analysis of optical microscope images (see Appendix C).

A linear regression performed on the data indicated a thickness increment of 1.76 nm/bilayer with an *R*-squared value of 0.999. These results show that (PAH/PSS) multilayers exhibit a reproducible, linear growth profile on PDMS over the entire range of thicknesses (11 to 100 bilayers) that were tested. The thickness increment reported here is slightly higher than previous results obtained by growing (PAH/PSS) multilayers on weak polyelectrolyte platforms on glass substrates (see Figure 2.7).

When subjected to a lateral strain, all films exhibited uniform buckling over the entire sample surface, except for regions where the occasional crack would locally relax planar stresses. The buckling wavelength was observed to increase linearly with thickness (see Figure 3.4), as would be expected from Equation 3.1 for a PEM Young's modulus which does not change with increasing film thickness. Figure 3.5 shows the Young's modulus measured using the SIEBIMM method for films with different numbers of bilayers. Also shown is an optical microscopy image of a film undergoing buckling (inset).

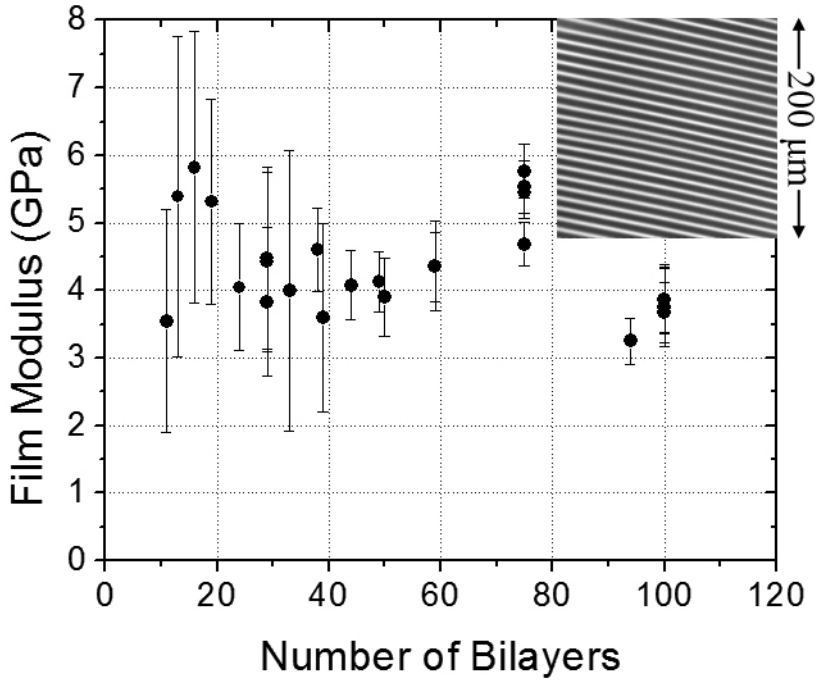

Figure 3.5. Young's modulus vs number of bilayers for (PAH/PSS) films. Error bars indicate the estimated measurement error. Larger errors are associated with films containing < 40 bilayers. The inset image is an optical micrograph (200 μm square) of a 100 bilayer film undergoing buckling.

The modulus values of films ranging from 20 nm (11 bilayers) to 180 nm (100 bilayers) thick were measured, and error bars were calculated by propagation of the uncertainties in the PEM thicknesses, the buckling wavelengths, and the Young's modulus of the PDMS substrate. Averaging the data yields a value of 4.4 ± 0.7 GPa for the Young's modulus of (PAH/PSS) multilayers.

The accuracy of the SIEBIMM technique is limited primarily by measurements of the PEM film thickness. This is especially true for very thin films, where the data indicate higher uncertainties for films less than ≈ 70 nm (40 bilayers) thick. Despite such uncertainties, SIEBIMM proved to be remarkably sensitive to the PEM modulus, even in very thin films. This was evidenced in two additional batches of samples that were prepared, which were identical to the previous samples except that the PDMS substrates had been soaked in DI water for ≈ 6 hrs before beginning multilayer deposition. The modulus values determined from these samples are displayed in Figure 3.6.

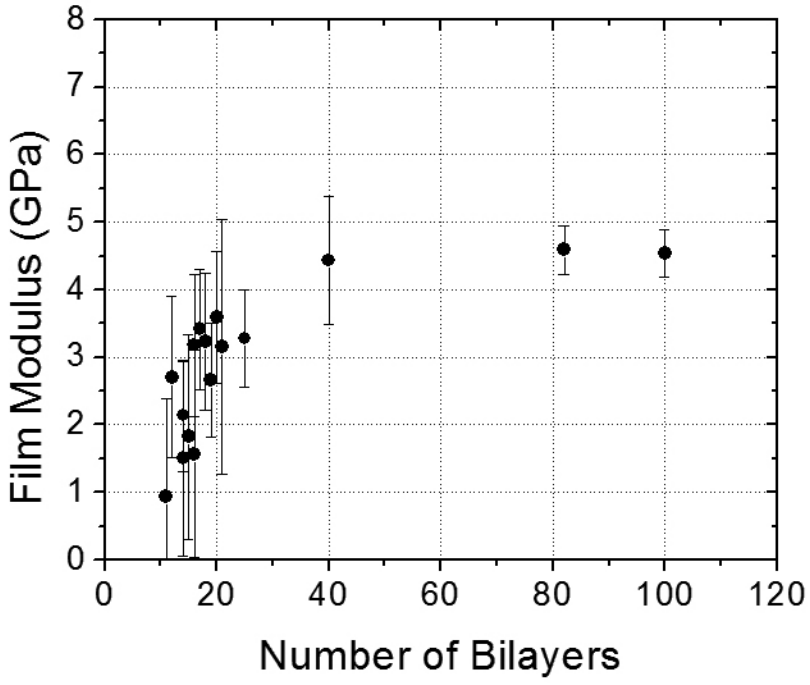

Figure 3.6. The effect of substrate treatment on the Young's modulus of (PAH/PSS) films. PDMS substrates were treated by soaking in DI water for ≈ 6 hrs prior to multilayer deposition.

The PEM films deposited on the water-treated PDMS show lower modulus values at small bilayer numbers. The modulus then rises rapidly with increasing film thickness, eventually reaching a plateau at 4.5 GPa, essentially the same modulus value observed for PEMs on untreated PDMS. Correspondingly, the bilayer thickness increment was observed to be only 1.56 nm/bilayer for films with less than 40 bilayers, with an *R*-squared value of 0.823 indicating less linearity in the data. Soaking the PDMS in water most likely causes surface reconstruction, allowing the initial adsorbing layers to adopt a different chain configuration compared to what is obtained without pretreatment in water. As more bilayers are deposited, the effect of the substrate treatment on the growth behavior diminishes, and the mechanical properties of the thin region of initially adsorbed layers are less influential in determining the overall film properties. These observations are consistent with the notion that in the region near the substrate, a PEM film can possess physical properties and growth behavior different from that of the interior region of the film.[202] The above observations lead to two important conclusions: First, SIEBIMM measurements are sensitive enough to respond to the modulus difference resulting from substrate-dependent morphologies in PEM films. Second, films must be built to an adequate thickness to avoid measuring a modulus influenced by substrate-induced effects in very thin films, as well as to minimize film thickness measuring errors. For the (PAH/PSS) system on PDMS as explored here, building films thicker than 70 nm is recommended.

Given the potential of PEMs for use as biomaterials (see Section 3.2.1) an important question was whether SIEBIMM could be used to measure the wet-state modulus of PEM assemblies. For this task two samples assembled on untreated PDMS were utilized. Samples were immersed in either DI water or a 1 M solution of NaCl and allowed to equilibrate for ≈ 1 hr before testing. Upon compression, buckling was observed over the entire sample surface, and the images obtained looked similar to films buckling in the dry state (see inset, Figure 3.5), except for a decrease in contrast as a result of the smaller refractive index difference between the sample and the water environment. It was thus concluded that the PEM films remained well bonded to the PDMS in solution, as achieving the buckling state relies upon good adhesion of the film to the substrate. In-situ spectroscopic ellipsometry (see

Section 3.4.1) was performed to determine the PEM wet-state thicknesses. After wet-state measurements, the samples were dried and the modulus values were re-measured. The results are shown in Figure 3.7.

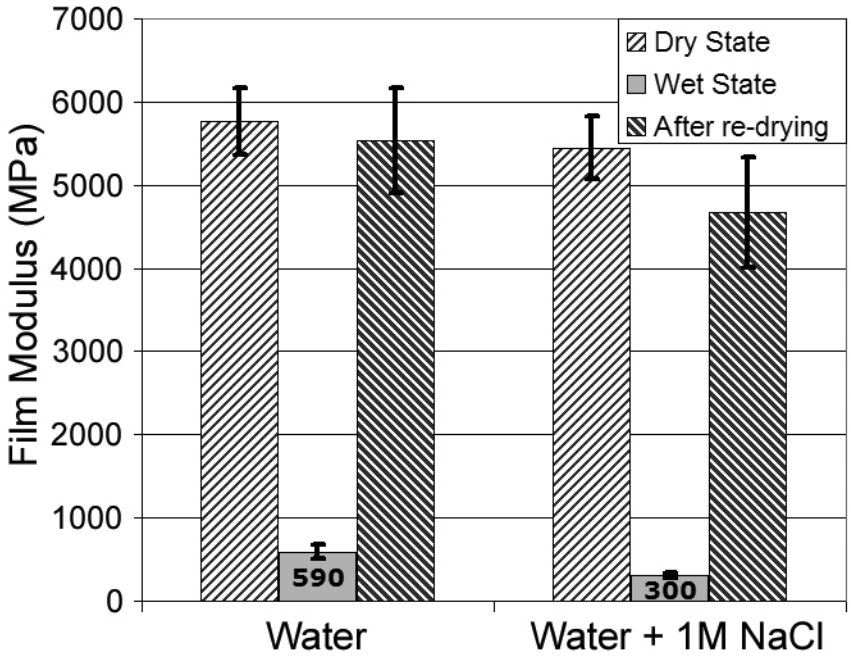

Figure 3.7. Dry- and wet-state modulus values of (PAH/PSS) films. Samples with 75 bilayers were tested in both DI water and 1 M NaCl solution. Modulus values of the films following drying of the swollen samples are also shown.

The sample immersed in DI water exhibited a decrease in modulus from 5.8 ± 0.4 GPa to 590 ± 90 MPa. The sample immersed in 1 M NaCl showed an even greater reduction in modulus, from 5.4 ± 0.4 GPa when dry to 300 ± 30 MPa in solution. The films showed corresponding thickness increases when wet, swelling 28% in water and 48% in the NaCl solution. These swollen film thicknesses are comparable with the results of previous work on this system.[186, 203, 204] Water is an excellent solvent for PEM films, inducing large reductions in modulus due to higher chain mobility in the swollen film and the possibility of breaking and reforming electrostatic crosslinks. The high salt concentration increases this effect by allowing charge screening of the electrostatic crosslinking groups. In addition, salt solutions can cause reorganization of the film structure to take place.[186] This latter effect is

evidenced by the fact that upon drying, the film swollen in water returned to a thickness of 136 nm, close to its original thickness of 130 nm, while the film swollen in salt returned to a thickness of 166 nm, a value still considerably higher than its original 130 nm thickness. Upon drying, the film that had been immersed in water returned to a modulus that was 96% of its original value, while the film swollen in NaCl solution only regained 86% of its original stiffness.

3.4.3 Comparison to Previous Studies*

The values of 590 ± 90 MPa (water) and 300 ± 30 MPa (1 M NaCl) measured for (PAH/PSS) multilayers in the wet-state fall within the range of values given so far in the literature. Vinogradova et. al., using AFM deformation[153-158] and osmotic swelling[152, 166] of (PAH/PSS) capsules have reported an estimated modulus of 100 to 200 MPa. On the other hand, Gau et. al., utilizing the osmotic-driven collapse of (PAH/PSS) capsules[146] (using different assumptions) report a higher value on the order of 1.5 - 2.0 GPa. Similarly high numbers (1.3-1.9 GPa) were obtained from (PAH/PSS) capsules by Dubreuil et. al. using AFM and reflection interference contrast microscopy.[141, 142] Most recently, Heuvingh, et. al. have reported a modulus of ≈ 400 ± 200 MPa for (PAH/PSS) capsules in 1 M NaCl solution.[167] This latter number is notably close to our reported value of 300 ± 30 MPa. To our knowledge, only one other group has previously reported a dry-state modulus for (PAH/PSS) multilayers. Hsieh et. al., using PEM-coated Lycra yarns, estimated the modulus of (PAH/PSS) multilayers to be between 1 and 9 GPa;[148, 149] the value of 4.4 GPa reported here falls within that range. Table 3.2 summarizes the results obtained in this work, as well as the recent literature results outlined above for Young's Modulus measurements of the (PAH/PSS) system.

* This comparison to other literature is not meant to be exhaustive of all modulus studies conducted on PEM films, but rather only to present results that have been reported for similar systems of (PAH/PSS).

Study	Film Topology	Method	Wet/Dry?	Reported E (GPa)
Gau, et al.	Microcapsule	Osmotic Collapse	Wet	1.5 – 2.25
Vinogradova, Sukhorukov, et al.	Microcapsule	AFM/Osmotic Swelling	Wet	0.001 – 0.24
Fery, et al.	Microcapsule	AFM	Wet	1.6, 0.4
Hsieh et al.	Cylinder	Tensile Testing of Coated Fibers	Dry	1.0 – 9.0
Nolte (this work)	Planar Film	Elastic Buckling	Wet/Dry	4.4 / 0.3 – 0.6

Table 3.2. Recently reported Young's modulus values for the (PAH/PSS) system from various literature sources. For references, see Section 3.4.3.

3.5 Conclusions

In conclusion, the Young's modulus of (PAH/PSS) films was determined successfully by the SIEBIMM method in both the dry- and the wet-states. To reduce the amount of uncertainty in the modulus, it is suggested that PEMs be grown to an adequate thickness to minimize film thickness measuring errors. In addition, measuring the modulus as a function of the number of bilayers deposited can provide information about how the stiffness changes with film thickness, which can help guard against measuring a modulus influenced by substrate-induced effects in very thin films.

The next chapter will focus on using SIEBIMM to test the mechanical properties of weak polyelectrolyte assemblies, which offer the possibility of tuning the mechanical properties of PEM films through pH control of the polycation and polyanion deposition solutions.[159, 160] An exciting avenue for future work is the possibility of creating complex physical property gradients throughout the depth of the multilayer film using the methods presented in Chapter 2. Such structures offer the chance of creating PEM-based thin films with enhanced

mechanical properties, such as increased resistance to indentation and sliding contact damage.[4] Some preliminary results aimed at examining the effect of incorporating silver nanoparticles into PEM assemblies are presented in Appendix B. The appendix also discusses the concept of buckle patterning and examines this effect for PEMs grown on the face of PDMS microcontact printing (μCP) stamps.

Numerous applications suggested in the literature clearly point to the need for a fast, accurate, and flexible way to measure the mechanical properties of very thin films in both the dry and wet states. The technique outlined in this chapter meets these demands, and suggests that anyone conducting layer-by-layer assembly by conventional methods may wish simply to include a PDMS substrate and use it to determine the stiffness of the multilayer films in that batch of samples, making it a routine characterization technique similar to film thickness or surface roughness measurements.

This chapter has demonstrated that the SIEBIMM method is positioned to become an extremely useful tool in the field of polyelectrolyte multilayer mechanical property characterization, but thus far results have only been presented from a system which assembles well on the PDMS surface. The next chapter will address the difficulties that sometimes arise when trying assemble certain systems on PDMS, and discuss a technique that can be used to broaden the applicability of SIEBIMM to the widest possible range of systems.

Chapter 4
A Two-Plate Buckling Approach for Young's Modulus Measurements on Polyelectrolyte Multilayer Films*

4.1 Introduction

Current interest in thin film materials is motivated by a number of factors such as the desire to advance microelectronics by moving to smaller device sizes, the need for protective or functional coatings, and the high degree of promise for thin films as actuator and sensor devices.[1] Knowledge of the mechanical properties of the film is often of fundamental interest for many of these applications. Traditional mechanical testing methods have generally relied upon macroscale manipulation of samples; however, thin films can often exhibit properties very different from their bulk values, and some very promising thin film materials exist for which there is no easily obtainable bulk counterpart. Such considerations have led to the development of a number of novel methods for thin film mechanical property measurements, including the "strain-induced elastic buckling instability for mechanical measurements" (SIEBIMM) technique,[168] which was introduced in Chapter 3. Not all systems are amenable to use with the SIEBIMM technique as it was originally developed, however. The current chapter addresses difficulties that sometimes arise when implementing this measurement technique with PEMs, and introduces an approach known as two-plate buckling that can be used to solve these problems.

4.2 Background and Motivation

4.2.1 The SIEBIMM Technique: Challenges from Hydrophilic Polymer Systems

SIEBIMM presents many advantages among the various thin film characterization techniques, including its straightforward and fast implementation, as well as its ability to do rapid combinatorial material screening without requiring expensive or specialized equipment.

* This chapter is reproduced in part with permission from Reference 205: Nolte, A. J.; Cohen, R. E.; Rubner, M. F., A two-plate buckling technique for thin film modulus measurements: Applications to polyelectrolyte multilayers. *Macromolecules* **2006,** 39, (14), 4841-4847. Copyright 2006 American Chemical Society.

The basic principle behind SIEBIMM is that a thin, stiff film deposited on an elastomeric substrate will undergo a buckling instability when subjected to planar compressive forces. Measurement of the wavelength of buckling (λ), combined with knowledge of the film thickness (d_f) and the substrate Young's modulus (E_s), allows one to calculate the unknown Young's modulus (E_{PEM}) of the thin film using Equation 3.10, which is reproduced here for convenience as Equation 4.1. Further details surrounding the derivation of Equation 4.1 can be found in Section 3.2.3.

Equation 4.1

$$\frac{E_{PEM}}{1-\nu_{PEM}^2} = 3 \cdot \frac{E_{PDMS}}{1-\nu_{PDMS}^2}\left(\frac{\lambda}{2\pi d_{PEM}}\right)^3$$

where ν_f and ν_s are the Poisson's ratios of the film and substrate and are typically assumed to be 0.33, in the case of glassy polymeric films, and 0.5 for the rubbery substrate.[168]

In its current form, however, SIEBIMM is limited to testing thin film materials that can be transferred or assembled onto a hydrophobic poly(dimethylsiloxane) (PDMS) substrate. In Chapter 3 the use of SIEBIMM was demonstrated to measure the Young's modulus of polyelectrolyte multilayer (PEM) thin films comprised of poly(allylamine hydrochloride) (PAH) and poly(styrenesulfonate) (PSS). In that case, PEM assembly onto the neutral, hydrophobic PDMS substrate was successful; however, it was found that later attempts to assemble specific multilayer systems comprised of PAH and poly(acrylic acid) (PAA) resulted in cloudy films that exhibited a very high surface roughness when deposited at certain values of pH. An example of this phenomenon is displayed in Figure 4.1.

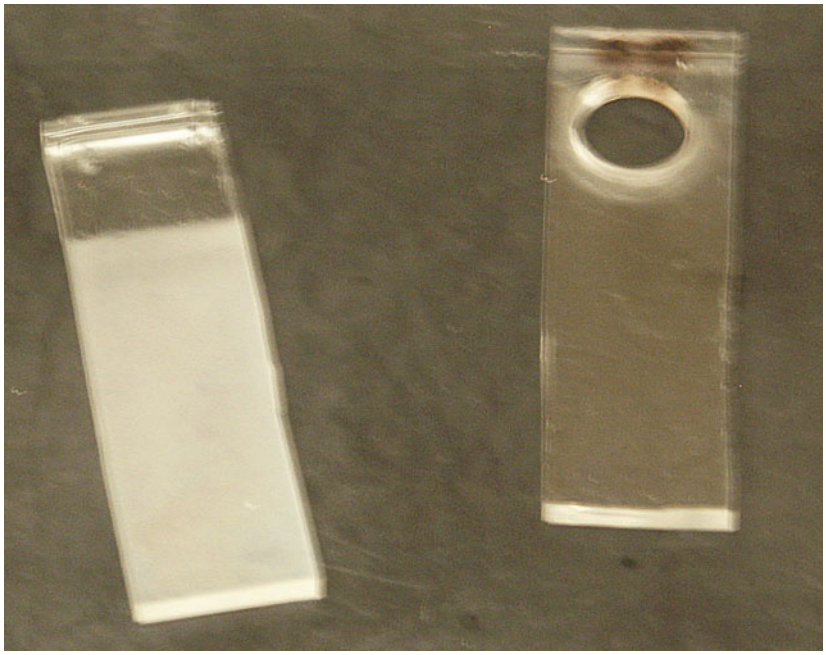

Figure 4.1. Effect of pH assembly conditions on (PAH/PAA) multilayer film roughness. The PDMS substrate on the left is coated with $(PAH6.5/PAA6.5)_{60}$, and the one on the right is coated with $(PAH7.5/PAA3.5)_{11.5}$. The (PAH7.5/PAA3.5) film was optically clear and supported buckling upon compression, while the (PAH6.5/PAA6.5) film was opaque and did not support a buckling transition. The circular hole in the substrate on the right is unrelated to these phenomena—it was created in removing material for compression testing.

Figure 4.1 is a photograph of two films composed of (PAH/PAA) deposited onto PDMS substrates. The rightmost film was assembled using the (PAH7.5/PAA3.5) (topped with PAH) system, and the leftmost film using the (PAH6.5/PAA6.5) system. Despite the use of the same polyelectrolytes in each case, the difference in pH during film assembly led to optically clear, low roughness (< 10 nm RMS) films in the case of (PAH7.5/PAA3.5) multilayers, while the (PAH6.5/PAA6.5) multilayers yielded a film with such high roughness that it was optically opaque. In addition to their roughness characteristics, it was found that the (PAH7.5/PAA3.5) multilayers supported clear, uniform buckling over the entire film surface upon compression, while the rough (PAH6.5/PAA6.5) film did not yield buckling upon compression. It has been proposed that hydrophilic polyelectrolyte systems may "dewet" from a hydrophobic substrate to yield light-scattering islands of polymer on the substrate surface.[206] Given that (PAH6.5/PAA6.5) films have been shown previously to deposit in very smooth, regular layers on glass substrates,[38] incompatibility between the

hydrophobic substrate and the highly charged PAH and PAA chains at pH 6.5 was suspected. Thus, a way of modifying the substrate was necessary in order to generalize the SIEBIMM method and allow for testing of a wider variety of PEM systems.

4.2.2 PDMS Surface Modification

Any suitably compliant elastomeric material could be used as the substrate, but PDMS is considered an ideal choice for such an application due to its optical transparency, ease of processing, easily tunable mechanical properties, and elasticity over large temperature ranges. SIEBIMM requires compatibility between the testing material and the substrate both for successful film transfer or deposition, as well as to insure good adhesion between the film and substrate to prevent the buckled film from delaminating and relaxing. This suggests that a suitable method of modifying the PDMS surface is needed. Many studies have explored this topic, with plasma, corona discharge, and UV/ozone treatments being the most popular techniques used to create a hydrophilic surface on normally hydrophobic PDMS.[207, 208] Because of the chemical nature of the siloxane backbone, however, such surface modification methods result in the growth of a brittle, silica-like layer on the surface of the PDMS.[209] This layer leads to an increase in the local surface modulus,[207] and can actually lead to buckling on the treated PDMS surface as the thin, brittle silica layer becomes compressed under thermally induced strains.[210] Furthermore, it has been suggested that the low glass transition temperature of PDMS (-123°C) allows it to quickly bury high-energy surface functionalities into the bulk,[209] a fact that might be problematic even if one could find a suitable carbon-based elastomer substitute. One possible solution to the preceding difficulties would be the deposition of a thin, glassy polymeric layer on the surface of the PDMS. If correctly chosen, such a layer would exhibit good adhesion to the PDMS, while presenting a deposition surface that could be easily modified by plasma techniques, and not prone to the above-mentioned difficulties facing direct modification of the PDMS surface.

In the results that follow, a modified buckling technique is presented that involves the deposition of PEMs onto a thin layer of polystyrene (PS) that has been previously transferred to the PDMS substrate.[168] Plasma modification permits tuning of the wetting properties of

the PS surface, enabling the assembly of polyelectrolyte systems not amenable to deposition on hydrophobic substrates. The resulting system consists of a two-plate composite of PS and PEM instead of a single, homogeneous PEM film. These PDMS-PS-PEM systems give rise to buckling exactly like their homogeneous counterparts, a fact that has been reported in other composite film systems as well.[211] By modifying the SIEBIMM equation to account for the presence of a two-plate composite film, and by measuring the thickness and buckling wavelength of the PS layer prior to PEM deposition, one can de-convolute its effects from the buckling behavior of the composite film to yield the Young's modulus of the PEM. In the following, the reliability of this technique is demonstrated by measuring the Young's modulus of two separate PEM systems with both the standard SIEBIMM technique and the two-plate method. Two polyelectrolyte multilayer systems that could not be evaluated by the conventional SIEBIMM approach due to PDMS incompatibility were also tested using the two-plate methodology.

4.3 Experimental Details

4.3.1 Polystyrene Thin Film and Substrate Preparation

PS pellets (Styron 663 W, Dow Chemical Company) were dissolved in toluene (Mallinckrodt Chemicals) to create solutions for spin-coating. Polished, single-crystal silicon wafers (p-type, WaferNet) were used as substrates. Wafers were cut into ≈ 2 cm × 3 cm pieces and treated for 5 min at high power (100W) in an air-plasma (Harrick Scientific PDC-32G plasma cleaner/sterilizer) operated at a pressure of 400 mTorr. Spin-coating (PWM32, Headway Research) was carried out for 20 sec at 2000 rpm with a ramp of 300 rpm/sec. A series of concentrations was initially spin-coated to find the dependence of PS thickness on solution concentration; the results from this experiment are displayed in Figure 4.2.

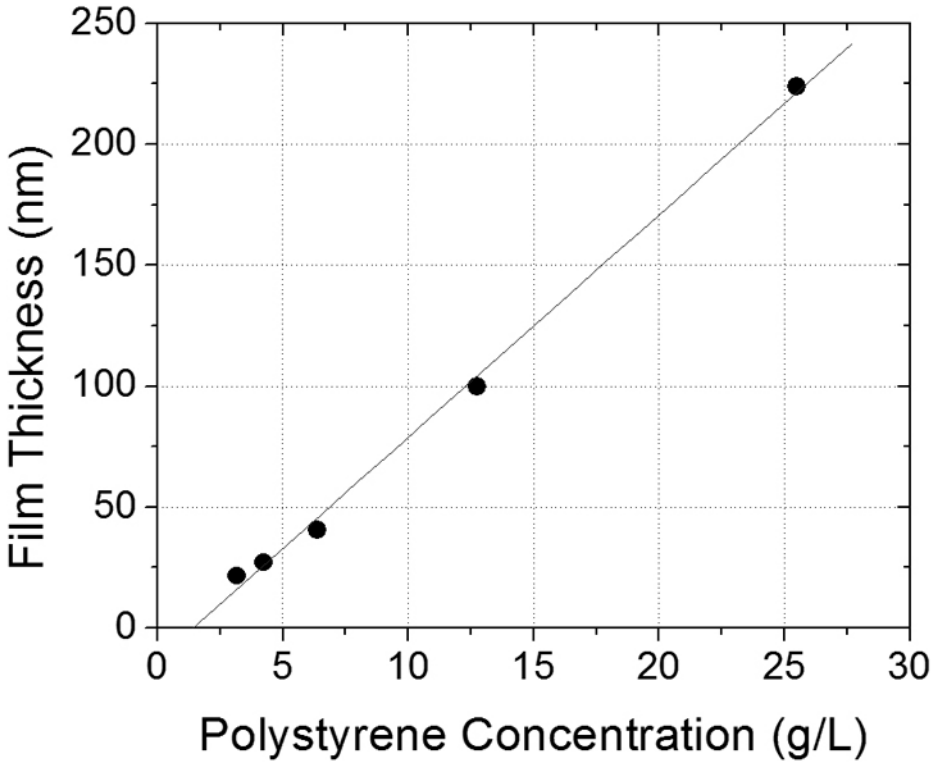

Figure 4.2. Film thickness of spin-coated polystyrene as a function of the solution concentration in toluene. The regression line for the data is shown, and was found to have a slope of 9.20 ± 0.27 with an intercept of –13.1 ± 3.6. The *R*-squared value is 0.999.

Based on the results presented in Figure 4.2, solutions with concentrations of 3.6 g/L and 9.0 g/L were prepared in order to create films with thicknesses of ≈ 20 nm and 70 nm, respectively. Pure toluene was spun onto each wafer surface immediately prior to spinning the PS solutions. PS-coated silicon samples were annealed under vacuum for ≈ 1 hr at 75°C and then removed from the oven and allowed to cool to room temperature before further processing.

PDMS was prepared as described in Section 3.3, and transfer of PS films from the wafer to the PDMS was carried out according to the method described by Stafford, et al.[168, 211] Briefly, the PS-coated side of the spin-coated sample was placed onto a piece of PDMS. Good contact between the PDMS and the PS was confirmed by observing the elimination of

the PDMS-PS air gap. The samples were then immersed under DI water and the wafer was slowly pulled from the PDMS, leaving the PS film adhered to the PDMS.

In cases where the experiment called for hydrophilic modification of the PS, the samples were treated for 30 sec in air plasma under the same conditions given above for wafer cleaning. In the case of the (PAH4.0/PAA4.0) system, an additional 10 sec treatment was used immediately prior to deposition due to some hydrophobic recovery of the PS surface.

4.3.2 Polyelectrolyte Film Assembly

PAH (M_w = 70 000, Sigma-Aldrich), PSS (sodium form, M_w = 70 000, Sigma-Aldrich), and PAA (25% aqueous solution, M_w = 90 000, Polysciences) were used without further purification to create polymer solutions of 0.01 M concentration by repeat unit. When PAH and PSS solutions were used together to construct multilayers, 0.1 M NaCl (Mallinckrodt Chemicals) was added to each polyelectrolyte solution. Milli-Q deionized water (Millipore) with a resistivity of 18.2 MΩ·cm was used for all procedures and preparations. Solutions were adjusted to the appropriate pH with 1.0 M HCl or NaOH immediately prior to PEM assembly.

Assembly of PEMs onto PDMS, PDMS-PS, and plasma-treated PDMS-PS substrates follows the method described in Section 3.3.

4.3.3 Sample Characterization

The methods for inducing buckling, conducting PDMS modulus measurements, calculating the average buckling wavelength, and obtaining the thicknesses of the PS (d_{PS}) and PEM (d_{PEM}) regions of the film are the same as described in Section 3.3. Except where otherwise indicated, the relative humidity was 50 ± 4% during testing of the (PAH3.0/PSS3.0) and (PAH7.5/PAA3.5) samples, and 20 ± 4% during testing of the (PAH3.5/PAA3.5) and (PAH4.0/PAA4.0) samples.

Young's modulus values were calculated using either Equation 4.1 (conventional SIEBIMM) or Equation 4.8 (two-plate method) as reported in the text. All error bars in this chapter represent standard deviations in the averaged modulus values.

Atomic Force Microscopy (AFM) (Dimension 3000 Scanning Probe Microscope, Digital Instruments) was conducted on PDMS and PS-PDMS substrates in tapping mode with silicon cantilevers.

Except where otherwise noted, samples appeared transparent and displayed uniform buckling across the film surface upon compression. Optical micrographs of buckled films appeared very similar to those shown in the inset in Figure 3.5.

4.4 Results and Discussion

4.4.1 Derivation of the Two-Plate Buckling Equation

For the case of a uniform PEM deposited directly on PDMS (Figure 4.3a), the mechanical stiffness and thickness of the film dictate the wavelength at which the buckling instability will occur. The relationship between these quantities can be written as:[196]

Equation 4.2

$$\overline{E}_{PEM} \cdot I_{PEM} = \frac{\overline{E}_s \cdot w}{4}\left(\frac{\lambda}{2\pi}\right)^3 .$$

where the variables are the same as described in Section 3.2.3. The quantity on the left in Equation 4.2 is known as the *flexural rigidity*,[212] and it provides a measure of the resistance of a material to bending based not only on the material's stiffness, but also on its distribution in space. Because the neutral axis is located directly in the middle of a single film, in the case where the PDMS is coated with a homogeneous PEM (Figure 4.3a), $I_{\mathrm{PEM}} = w \cdot d_{PEM}^3 / 12$ (as given in Section 3.2.3, Equation 3.3) and Equation 4.2 reduces to Equation 4.1.

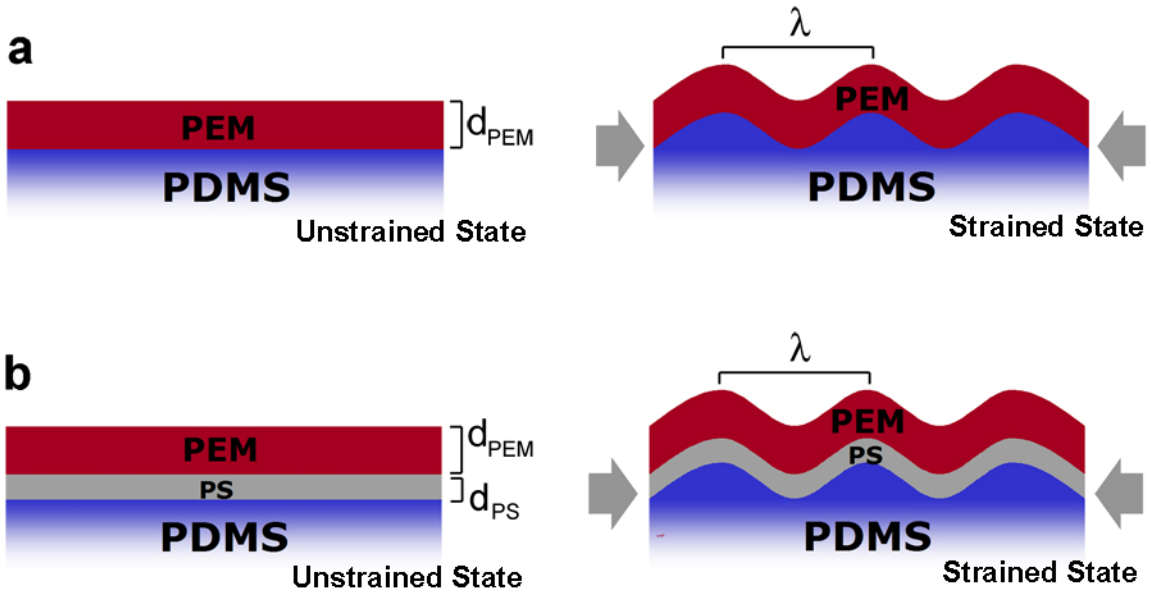

Figure 4.3. Cross-sectional illustrations showing both the unstrained and strained (undergoing buckling) states for (a) the conventional SIEBIMM technique with a PEM film, and (b) the two-plate method with a PS-PEM composite film.

When two plates of equal width appear in a laminated composite structure, as with a PS-PEM two-plate film (Figure 4.3b), both the PS and PEM undergo buckling together, and total resistance to this buckling is given by the sum of their individual flexural rigidities:[213]

Equation 4.3

$$\overline{E}_{PEM} \cdot I_{PEM} + \overline{E}_{PS} \cdot I_{PS} = \frac{\overline{E}_s \cdot w}{4}\left(\frac{\lambda}{2\pi}\right)^3 .$$

Thus, it is left to find I, the second moment of the area, for both the PS and the PEM regions. These are given by the following two expressions:[212]

Equation 4.4

$$I_{PS} = w \cdot \int_0^{d_{PS}} (y - Y)^2 \, dy$$

Equation 4.5

$$I_{PEM} = w \cdot \int_{d_{PS}}^{(d_{PS}+d_{PEM})} (y - Y)^2 \, dy \, .$$

where d_{PS} is the height of the PS layer, as depicted in Figure 4.3. The y axis is taken to be normal to the plane of the films, with its origin at the PDMS-PS interface, and Y is the neutral bending axis:[212]

Equation 4.6

$$Y = \frac{d_{PEM}^2 + 2 \cdot d_{PEM} d_{PS} + \frac{\overline{E}_{PS}}{\overline{E}_{PEM}} \cdot d_{PS}^2}{2 \cdot \left(d_{PEM} + \frac{\overline{E}_{PS}}{\overline{E}_{PEM}} \cdot d_{PS} \right)} \, .$$

Taking $d_t = d_{PS} + d_{PEM}$ and $\phi_{PS} = d_{PS} / d_t$, Equation 4.6 can be rewritten after some algebraic manipulation as:

Equation 4.7

$$Y = \frac{d_t}{2} \cdot \frac{1 + \phi_{PS}^2 \left(\frac{\overline{E}_{PS}}{\overline{E}_{PEM}} - 1 \right)}{1 + \phi_{PS} \left(\frac{\overline{E}_{PS}}{\overline{E}_{PEM}} - 1 \right)} = \frac{d_t}{2} \cdot \kappa$$

With the equation for Y written in the form presented in Equation 4.7, κ represents a type of deviation factor for the neutral axis of bending. In the simplest case, where the plane strain moduli of the PEM and PS are equal, $\kappa = 1$ and the neutral axis, as expected, is located in the middle of the film. Equation 4.7 can be used with Equation 4.4 and Equation 4.5 to find values for I_{PEM} and I_{PS}. Plugging those values into Equation 4.3 allows one to solve *implicitly* for the Young's modulus of the PEM to yield the following relationships:

Equation 4.8

$$\overline{E}_{PEM} = \frac{\frac{\overline{E}_{eff}}{4} - \overline{E}_{PS}\left[\left(\phi_{PS} - \frac{\kappa}{2}\right)^3 + \left(\frac{\kappa}{2}\right)^3\right]}{\left(1 - \frac{\kappa}{2}\right)^3 - \left(\phi_{PS} - \frac{\kappa}{2}\right)^3}$$

Equation 4.9

$$\overline{E}_{eff} = 3\overline{E}_s\left(\frac{\lambda}{2\pi d_t}\right)^3$$

Equation 4.10

$$\kappa = \frac{1 + \phi_{PS}^2\left(\frac{\overline{E}_{PS}}{\overline{E}_{PEM}} - 1\right)}{1 + \phi_{PS}\left(\frac{\overline{E}_{PS}}{\overline{E}_{PEM}} - 1\right)}$$

It should be noted that Equation 4.8 assumes elastic deformation in the materials and is only valid if both the PEM and PS layers are rigid enough to support the buckled state. When one or both of the materials undergoes plastic deformation or failure, the formalism presented above fails.

Equation 4.8 is solved implicitly for the unknown PEM modulus. Stafford et al. have discussed a related problem and have provided an equation giving $\overline{E}_{eff}$ when the modulus of both materials is known.[211] The two equations appear quite different on first inspection, but it has been confirmed that they are algebraically identical. Thus, two different approaches to solving this problem give identical results. The quantity $\overline{E}_{eff}$ in Equation 4.9 is referred to as the *effective modulus*, and it represents the calculated modulus of the two-plate composite as if it were a homogeneous film with thickness d_t.

Because Equation 4.8 is solved for $\overline{E}_{PEM}$ only implicitly, an initial value of $\overline{E}_{PEM} = \overline{E}_{PS}$ was assumed, which set $\kappa = 1$ (see Equation 4.10). Equation 4.8 then yielded a refined value of $\overline{E}_{PEM}$, which was used to calculate a new κ, and the process was iterated until $\overline{E}_{PEM}$ no longer changed. Equation 4.8 converged rapidly—all the results that follow required no more than 4 iterations, at which point $\overline{E}_{PEM}$ was unchanging to at least the 3rd decimal point. Actual (not plane strain) Young's modulus values are reported below according to the assumed Poisson's ratios given in Section 4.2 (0.33 for the PEM and 0.5 for the PDMS).

4.4.2 Validity Tests for the Two-Plate Method

The validity of Equation 4.8 was initially tested using two polyelectrolyte systems that were amenable to deposition on both untreated PDMS and PS. The (PAH3.0/PSS3.0) system was first assembled in the presence of 0.1 M NaCl. In total, 8 samples were used for dipping: 4 PDMS substrates as prepared, and 4 with $\approx$ 20 nm PS layers transferred to their surface (the precise thickness of each sample's PS layer was determined before PEM deposition). After measuring the buckling wavelength of the 4 PS-coated PDMS samples, all 8 substrates were coated with multilayers of (PAH3.0/PSS3.0). Two samples were removed during assembly (one PS-coated substrate, one uncoated) following the deposition of 43, 58, 71, and 100 bilayers. For all samples, the PEM thickness, buckling wavelength, and the PDMS stiffness were measured and the PEM Young's modulus was calculated using Equation 4.1 (for PDMS-PEM samples) and Equation 4.8 (for PDMS-PS-PEM samples). PEM thickness and modulus data found from both the conventional and the two-plate technique are graphed vs number of bilayers in Figure 4.4.

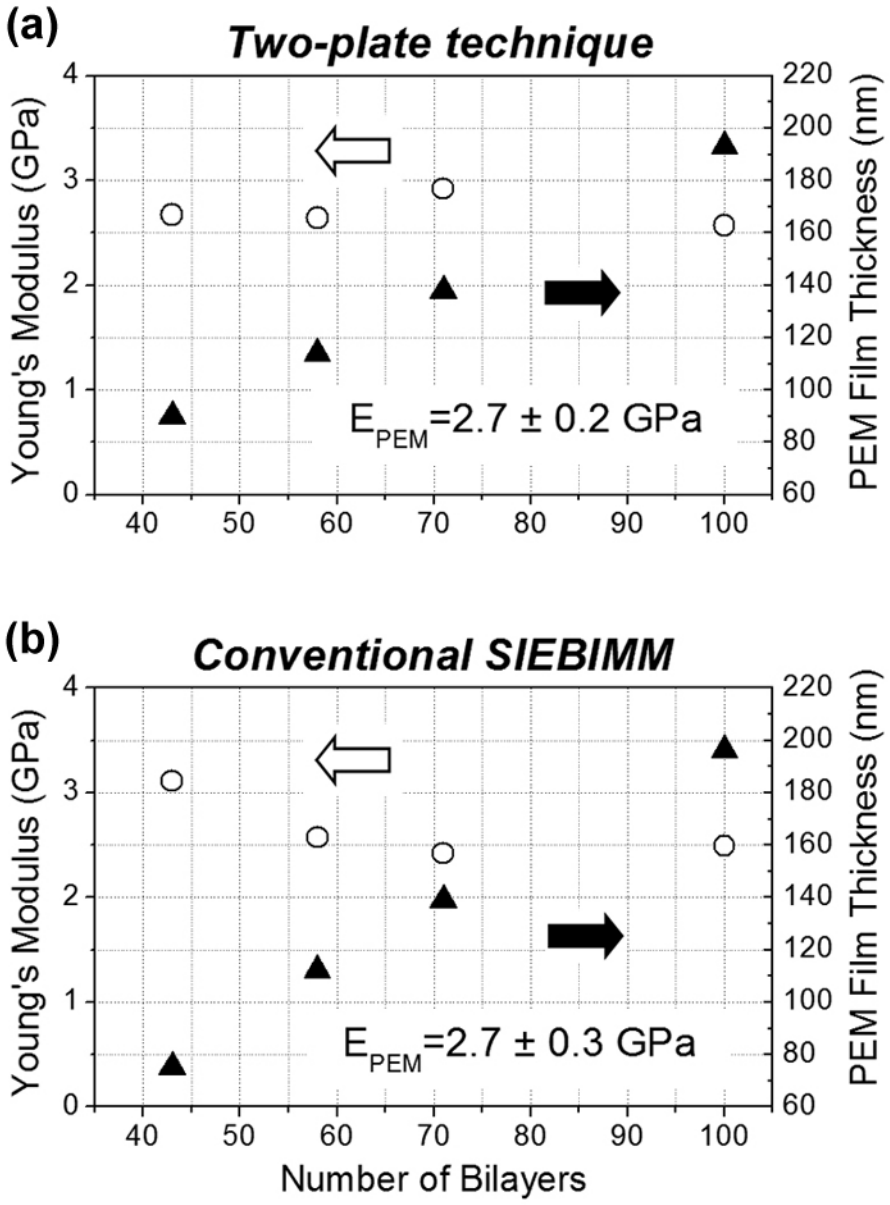

Figure 4.4. (PAH3.0/PSS3.0) film thickness (filled triangles) and Young's modulus (open circles) vs number of bilayers using the (a) two-plate and (b) conventional SIEBIMM techniques. The average modulus for each technique is displayed in each graph pane. The relative humidity was 50 ± 4%.

(PAH3.0/PSS3.0) multilayers grown on the PDMS-PS platform (Figure 4.4a) and directly on PDMS (Figure 4.4b) displayed linear growth, with thickness increments of 1.8 and 2.1 nm/bilayer, respectively. *R*-squared values were > 0.997 in both cases. Figure 4.4 illustrates that the PEM modulus as measured by both techniques remains basically constant as the film thickness increases, in agreement with previous results (see Figure 3.5). In addition, there is excellent agreement between the two methods, both giving an average Young's modulus of 2.7 ± 0.3 GPa for the (PAH3.0/PSS3.0) system.

Figure 4.5 provides a closer examination of the (PAH3.0/PSS3.0) two-plate modulus data that appear in Figure 4.4a, but now plotted alongside the effective modulus (see Equation 4.9) of the entire PS-PEM assembly. The similarity between the effective modulus and the PEM modulus values, as well as the lack of a rising or decreasing trend in the effective modulus with the decreasing fraction of PS in the film (also displayed in Figure 4.5) indicates a very close match in modulus between the (PAH3.0/PSS3.0) layers and the PS. Indeed, SIEBIMM testing on the uncoated PS films prior to deposition established an average Young's modulus of 2.3 ± 0.2 GPa, very close to the 2.7 ± 0.3 GPa value measured for the PEM.

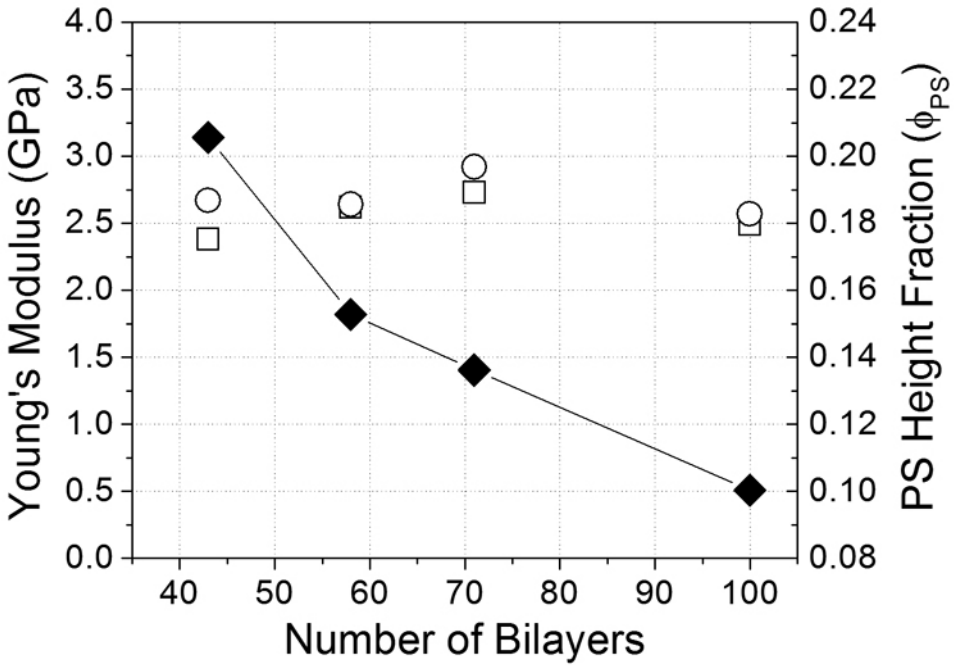

Figure 4.5. The Young's modulus of (PAH3.0/PSS3.0) PEM multilayers (open circles) and the effective Young's modulus of the entire PS-PEM assembly (open squares) graphed vs the number of bilayers. The fraction of the total film thickness taken up by the PS is also displayed (filled diamonds). The relative humidity was 50 ± 4%.

It is noted that 2.7 ± 0.3 GPa (measured at 50% relative humidity) is lower than the value of 4.4 ± 0.2 GPa that was reported for this system in Chapter 3. In that case, modulus results were obtained under humidity conditions that varied from ≈ 20 to 30% (see Section 3.3). It was suspected that the higher relative humidity was the cause of the lower modulus values in the present chapter, so the exact same films were tested at a later date when the ambient humidity had decreased to less than 20%. The average modulus during this second test was 5.6 ± 0.3 GPa, consistent with the notion that lower relative humidity values lead to stiffer PEM films.[29] This is not surprising, given that films measured in water, a good solvent for the (PAH3.0/PSS3.0) multilayers, can display modulus values an order of magnitude lower than the dry-state films (see Figure 3.7). Previous studies of (PAH/PSS)-coated fibers and free standing spin-assisted (PAH/PSS) multilayer films embedded with gold nanoparticles have yielded dry-state modulus values comparable to the numbers reported here.[148, 149, 214]

These results, however, also show that the stiffness of dry-state films can be significantly affected by the humidity conditions, emphasizing the importance of including humidity measurements with any report of Young's modulus for PEMs. This consideration will be examined in much more detail in Chapter 5.

A second system that was amenable to deposition both on the untreated PDMS and on the PS-coated PDMS substrates was the (PAH7.5/PAA3.5) system. For this system, 9 substrates were dipped—4 PDMS, and 5 PS-coated PDMS. One substrate of each type was removed during the dipping process, similar to the case with (PAH3.0/PSS3.0), after the completion of 9.5, 11.5, 13.5, and 16.5 bilayers (the extra PDMS-PS sample was also removed at 16.5). The results from two-plate and conventional SIEBIMM analysis are displayed in Figure 4.6.

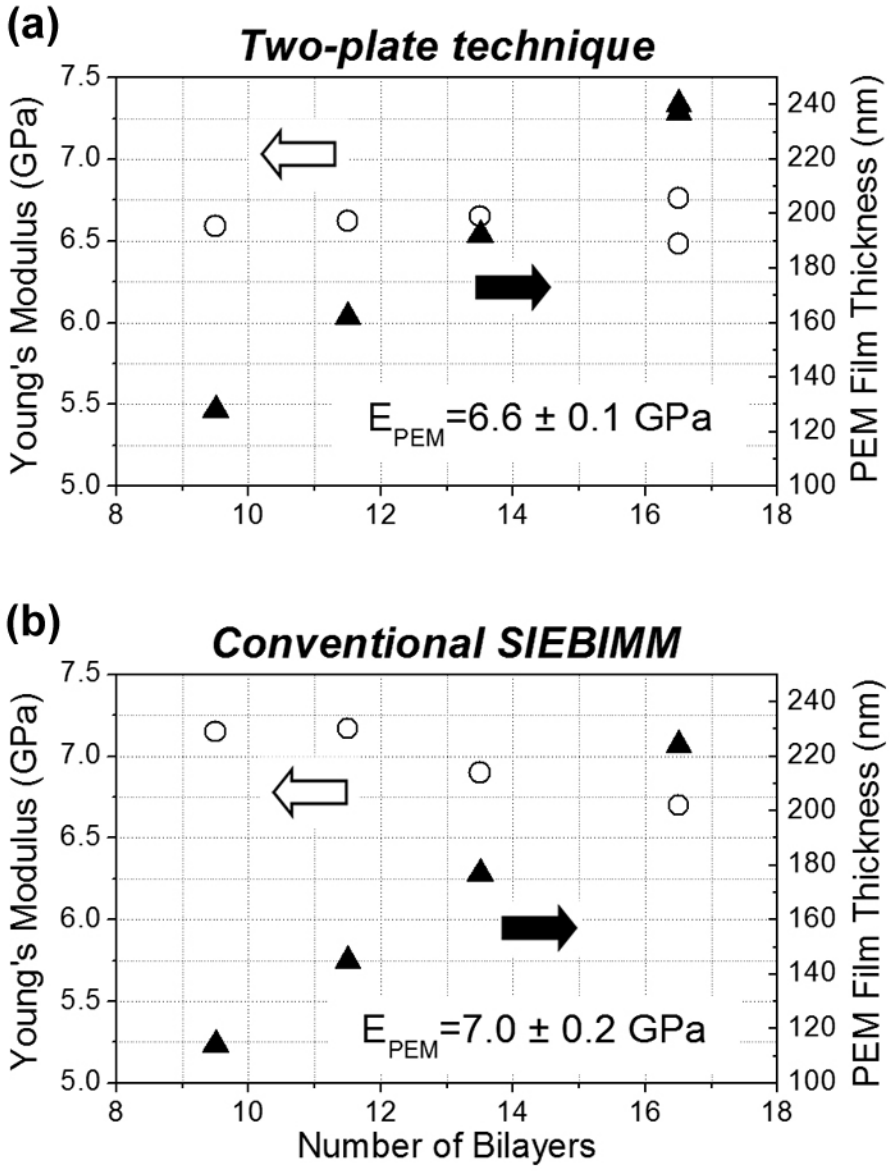

Figure 4.6. (PAH7.5/PAA3.5) film thickness (filled triangles) and Young's modulus (open circles) vs number of bilayers using the (a) two-plate and (b) conventional SIEBIMM techniques. The average modulus for each technique is displayed in each graph pane. The relative humidity was 50 ± 4%.

Linear growth was again observed for both sample types, with PEM thickness increments of 15.7 nm/bilayer (*R*-squared > 0.999) measured for both PDMS and PDMS-PS substrates. A Young's modulus of 6.6 ± 0.1 GPa was found for (PAH7.5/PAA3.5) multilayers using the two-plate technique. Conventional SIEBIMM yielded a value of 7.0 ± 0.2 GPa, again confirming good agreement between the results from the two techniques, both of which were carried out at 50% relative humidity. In addition, Pavoor, et al. have previously measured a value of 7.1 ± 1.0 GPa for the Young's modulus of the (PAH7.5/PAA3.5) system via nanoindentation at approximately the same humidity,[160] in very close agreement with the results given here. A subsequent test of the same (PAH7.5/PAA3.5) samples at 20% humidity revealed an increase in the average Young's modulus to a value of 10.5 ± 0.5 GPa, again demonstrating that the ambient humidity has a significant influence on the stiffness of these systems.

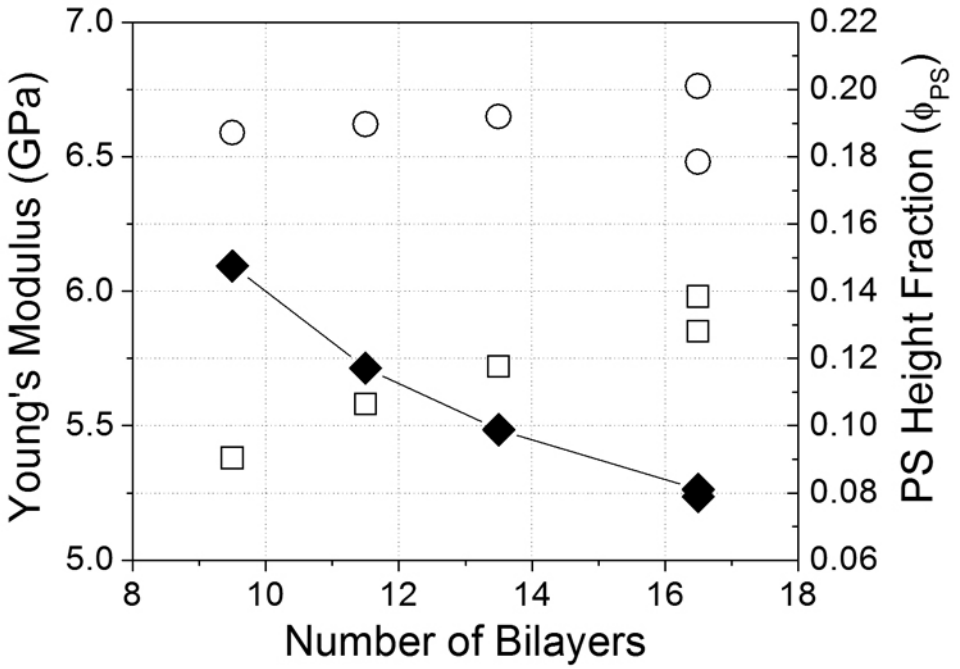

Figure 4.7. The Young's modulus of (PAH7.5/PAA3.5) PEM multilayers (open circles) and the effective Young's modulus of the entire PS-PEM assembly (open squares) graphed vs the number of bilayers. The fraction of the total film thickness taken up by the PS is also displayed (filled diamonds). The relative humidity was 50 ± 4%.

In Figure 4.7 the PEM modulus data measured using the two-plate technique are plotted along with the effective modulus of the entire PS-PEM assembly and the height fraction of PS in the film. In contrast to the situation previously described where (PAH3.0/PSS3.0) multilayers displayed a modulus very closely matched to that of the PS, the (PAH7.5/PAA3.5) system is more than twice as stiff as the PS on which it is deposited. As a result, the effective modulus of the PS-PEM assembly rises as the number of bilayers of PEM increases, as is evident from Figure 4.7. The modulus of the PEM, however, remains essentially constant, providing evidence that Equation 4.8 is able to successfully extract the Young's modulus of the PEM from the buckling behavior of the PS-PEM composite film.

4.4.3 The Effects of Plasma Treatment

Modulus measurements on the (PAH3.0/PSS3.0) and (PAH7.5/PAA3.5) systems confirmed the validity of Equation 4.8. After obtaining these results, two more systems that required a hydrophilic surface for uniform PEM film growth were measured. Plasma treatment of the PS-coated PDMS substrates was used to make the substrates amenable to PEM deposition. In addition to introducing charge and polar surface groups that render the surface hydrophilic, plasma treatment can lead to modulus enhancements in polymeric materials by introducing crosslinking.[215, 216] Consequently, the effects of plasma treatment on the PS films were monitored via spectroscopic ellipsometry, contact angle measurements, SIEBIMM analysis, and AFM.

The effects of plasma treatment are presented below for a set of 6 PS films on PDMS. All samples were spin-coated to a thickness of ≈ 70 nm—the exact thicknesses were measured by spectroscopic ellipsometry prior to all SIEBIMM measurements. Figure 4.8 shows images taken during contact angle analysis of samples during 4 stages of treatment.

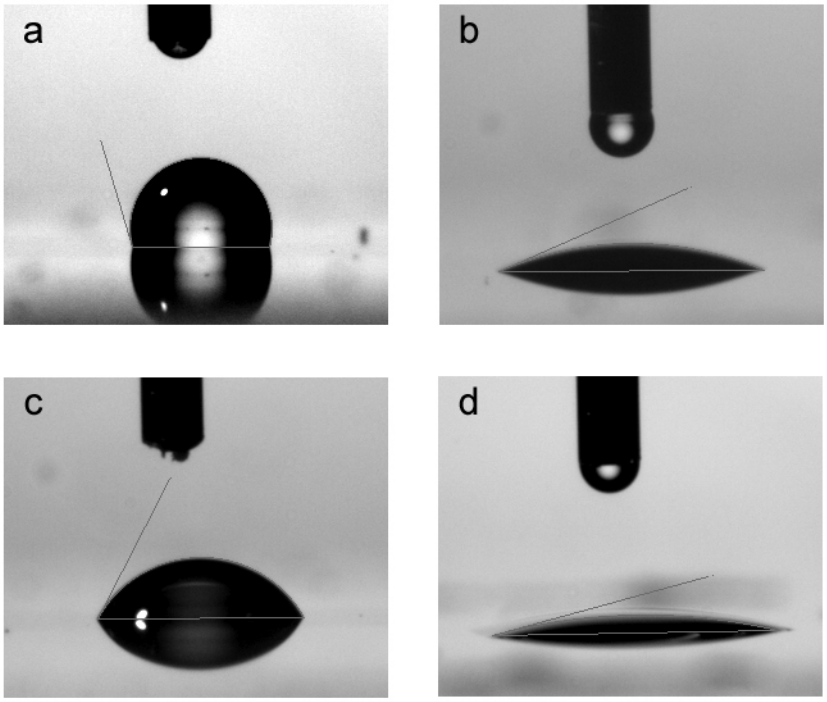

Figure 4.8. Typical side-view images of water droplets on the surface of PS films that have been transferred to PDMS substrates. The images represent (a) the untreated PS surface shortly after film transfer, (b) the PS surface following 30 sec of plasma treatment, (c) recovery of some hydrophobicity after aging for a day at ambient conditions, and (d) a return to a very low contact angle after an additional 10 sec plasma treatment.

An average contact angle of 105° (Figure 4.8a) was recorded for PS surfaces immediately following the transfer of the films from the silicon wafer spin-coating platform to the PDMS substrates. The contact angle decreased to an average value of 26° following 30 sec of plasma treatment as described in Section 4.3.1 (Figure 4.8b). To investigate the stability of the hydrophilicity of the treated surfaces, this batch of samples was stored at ambient conditions (25° C, 20% RH) for 1 day (≈ 24 hrs) and then the contact angles were re-measured. The samples recovered some of their original hydrophobicity, displaying an average contact angle of 69° (Figure 4.8c). Finally, samples were plasma treated once more for 10 sec. The average contact angle following this procedure was 14° (Figure 4.8d).

SIEBIMM was performed to monitor the effect of the plasma treatment on the PS modulus. The average modulus of the samples is graphed with the contact angle measurements in Figure 4.9.

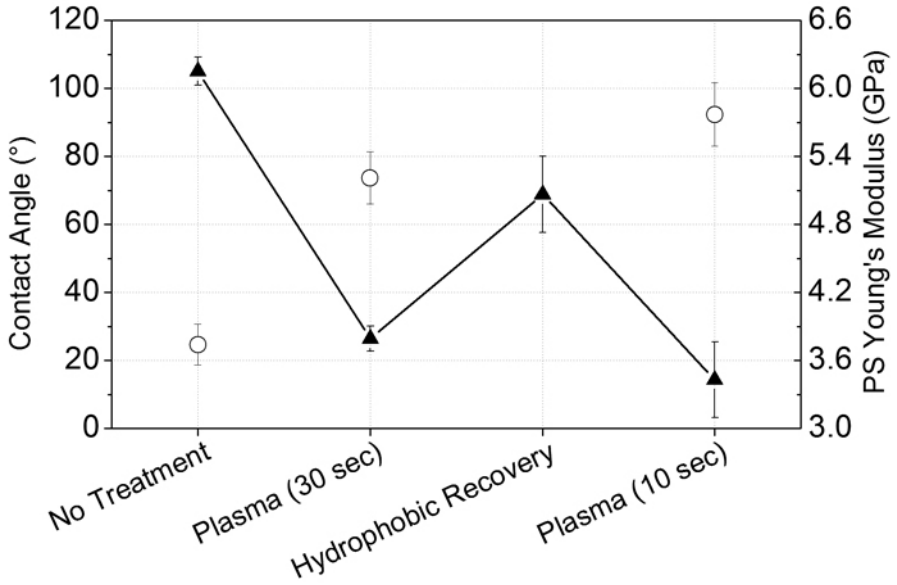

Figure 4.9. Average contact angle (filled triangles) and Young's modulus (open circles) as measured via SIEBIMM for 70 nm PS films on PDMS as a function of treatment.

The Young's modulus rises from 3.7 ± 0.2 GPa to 5.2 ± 0.2 GPa following the first 30 sec plasma treatment. The modulus was not measured following the 1 day aging period, but measurements following the additional 10 sec treatment showed an even higher modulus of 5.8 ± 0.3 GPa. As mentioned previously, the thickness of the PS films was also measured so that accurate modulus measurements could be made. The film thickness decreased on average only 2.7 ± 1.0% following the initial 30 sec treatment. The subsequent 10 sec treatment produced no statistically significant change in the film thickness.

There is a motivation to measuring the value of the contact angle and Young's modulus not just after the initial 30 sec treatment, but also following an addition 10 sec treatment subsequent to a hydrophobic recovery period. In general, the PDMS-PS platform is not

ready for film deposition immediately following the initial treatment step, as thickness and buckling measurements are needed to obtain accurate data for the PS film for subsequent two-plate calculations. If these measurements cannot be accomplished relatively quickly, the hydrophobicity of the PS may recover to an unacceptable degree for a particular application.[207] Here it is demonstrated that an additional, shorter treatment can then be employed to regenerate the PS surface hydrophilicity. In addition, this treatment produces a negligible effect on film thickness (eliminating the need to re-measure the thickness), and a small increase in the PS modulus that could be determined via a quick buckling experiment. In the results that follow in Section 4.4.4, measurements of the PS thickness and buckling wavelength were made following plasma treatment and immediately preceding PEM deposition.

The effects of plasma treatment on the surface topology of both PS films and bare PDMS substrates was studied using AFM. Two 20 nm PS film were transferred to PDMS substrates using the procedure outlined in Section 4.3, and one PS-coated PDMS substrate was treated in a 400 mTorr air plasma (high power) for 1 min. AFM images were taken on both the PS and PDMS surface on the plasma-treated and untreated samples. The results from scanning the PS surface on both the treated and untreated samples are shown in Figure 4.10.

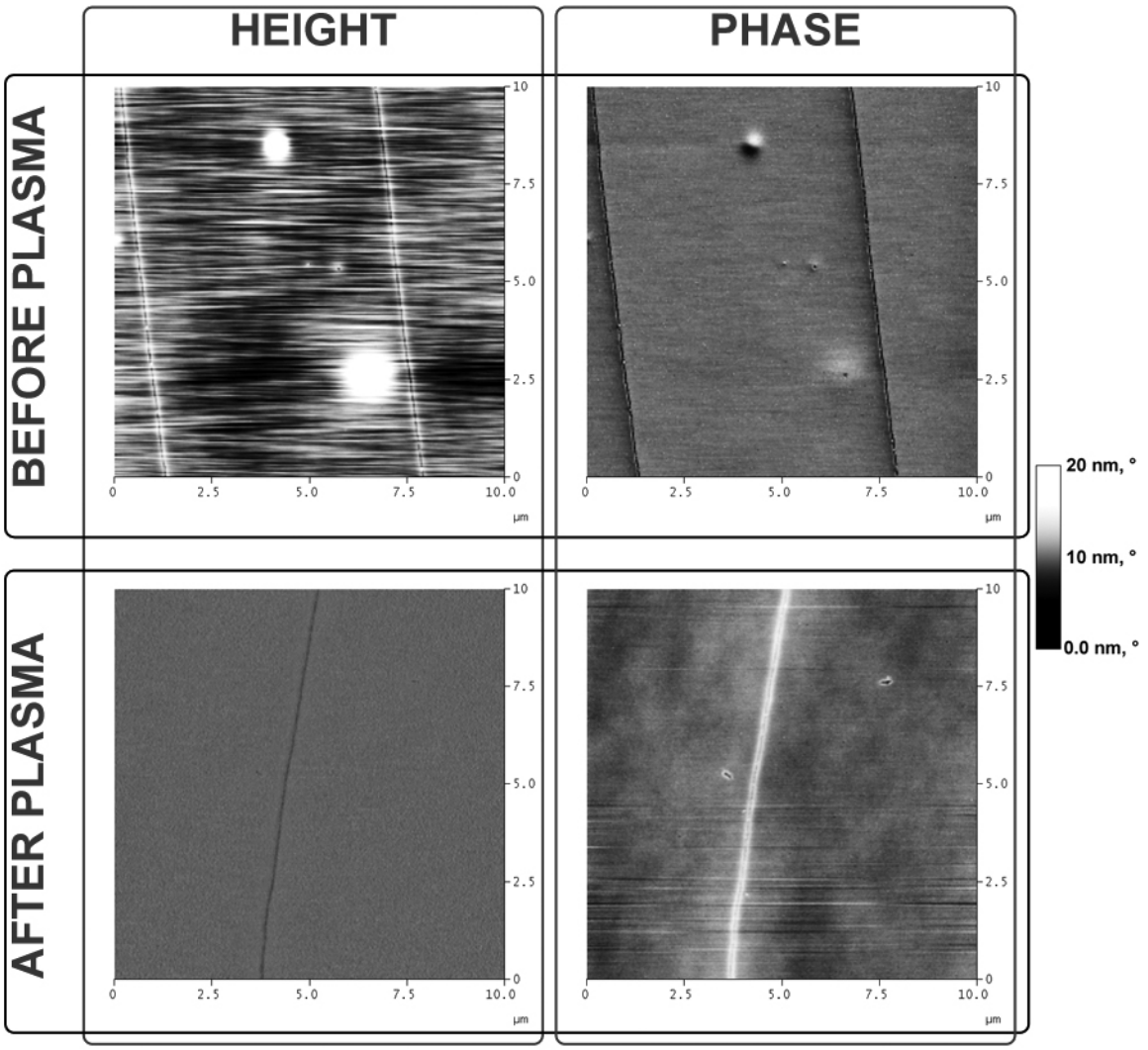

Figure 4.10. Atomic force microscopy images of a 20 nm polystyrene film before and after air plasma treatment. The film was examined in tapping mode before (top row) and after (bottom row) treatment. The left and right columns show height and phase images, respectively. The z-scale ranges from 0 to 20 in units of both nm and degrees. Images are 10 µm square.

The untreated PS surface was found to have a somewhat rippled topology, with the amplitude of undulations being on the order of 10 nm. The origin of this topology may lie in the peeling of the PS from the silicon wafer during film transfer—similar ripples have been observed on the fracture surface of certain polymer samples.[217] The ripples do not appear in the corresponding phase image. Plasma treatment smoothes the PS surface, with a change in RMS surface roughness from 2.40 nm to 0.756 nm. The phase images both appear very smooth both before and after plasma treatment, with RMS roughness values of 0.499° and

0.214°, respectively. Thus, plasma treatment of the PS surfaces seems to smooth height irregularities in the transferred film without introducing surface modulus heterogeneities, which would presumably be reflected by a higher roughness in the phase scans.

The effects of plasma treatment on surface of PDMS can be seen in Figure 4.11.

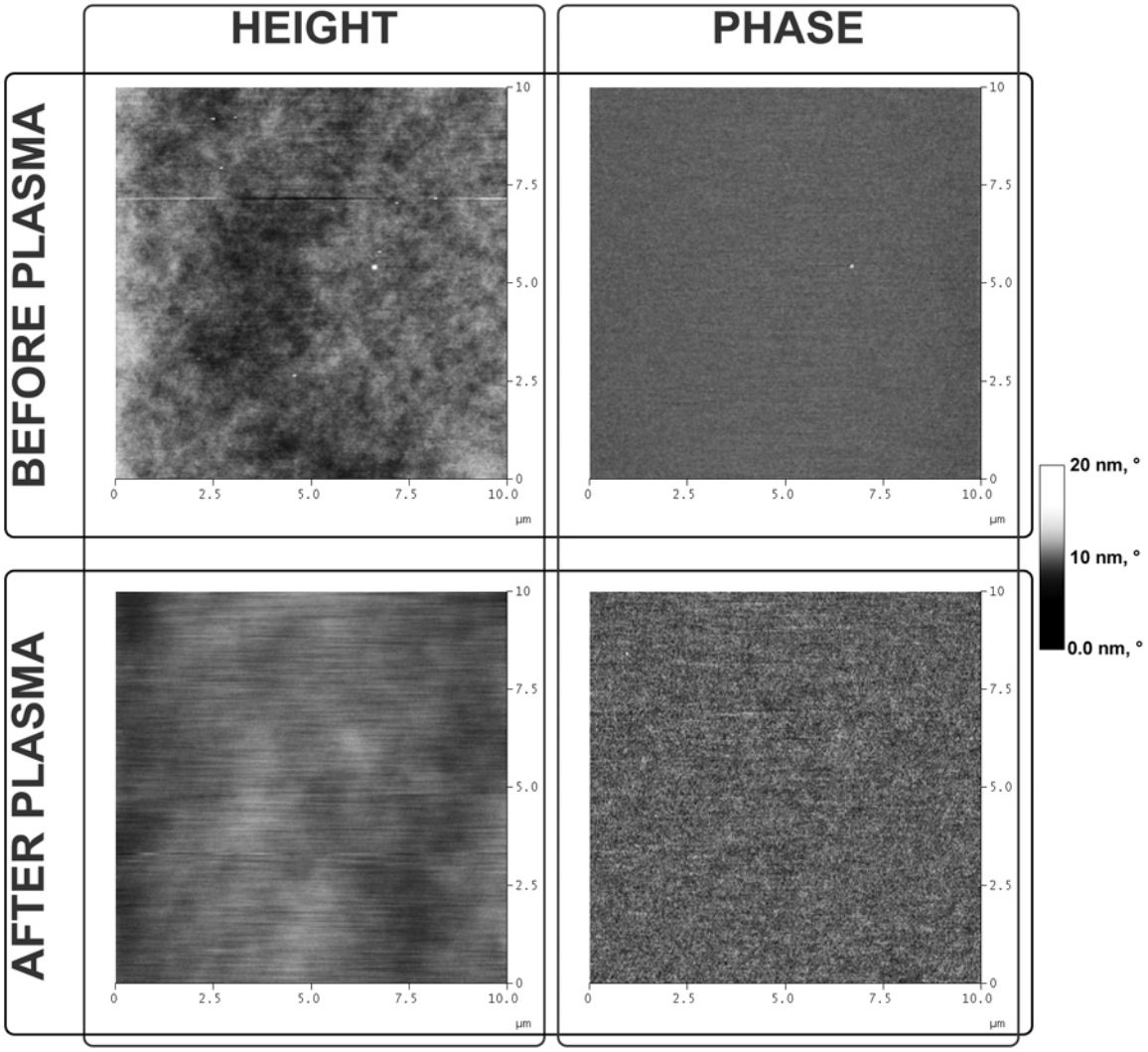

Figure 4.11. Atomic force microscopy images of a PDMS surface before and after air plasma treatment. The PDMS surface was examined in tapping mode before (top row) and after (bottom row) treatment. The left and right columns show height and phase images, respectively. The z-scale ranges from 0 to 20 in units of both nm and degrees. Images are 10 µm square.

In the case of PDMS, a smooth surface is observed both before and after plasma treatment, with RMS roughness values of 0.761 nm and 0.524 nm, respectively. The corresponding phase images, however, show a visible increase in roughness with RMS values rising from 0.223° to 0.766° following treatment. Because the lengthscale of induced roughness in the phase image (lower right panel in Figure 4.11) appeared quite small over the 100 μm^2 scan area, a more detailed scan was conducted over a 0.04 μm^2 area. The results of this scan are shown in Figure 4.12.

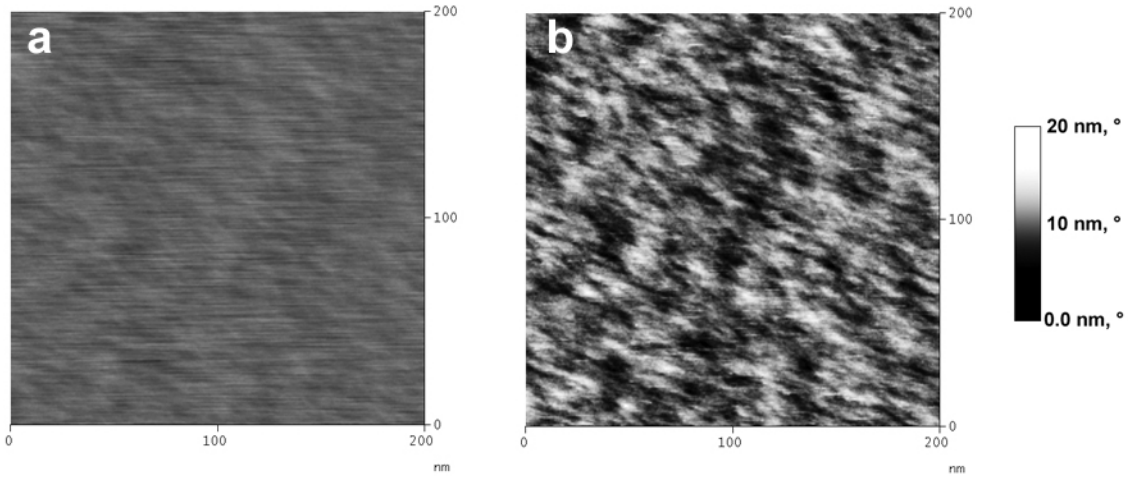

Figure 4.12. Detailed atomic force microscopy images of the PDMS surface after air plasma treatment. Height (a) and phase (b) images were taken over a smaller area than in Figure 4.11. The z-scale ranges from 0 to 20 in units of both nm and degrees. Images are 200 nm square.

While the height image shown in Figure 4.12a remains quite smooth over the smaller scan area (RMS roughness of 0.284 nm), the inhomogeneities in the phase image shown in Figure 4.12b are now quite prominent. The RMS roughness of the phase image is 1.47°.

The results of this study indicate that plasma treatment introduces inhomogeneities in the surface modulus of PDMS that are detectable through AFM phase imaging. While plasma treatment smoothes and does not seem to affect the surface modulus uniformity of the PS film (even though the overall surface modulus is enhanced as seen in Figure 4.9), the non-uniformity of the PDMS surface post-treatment suggests the formation of localized areas of enhanced stiffness due to oxide formation, as has been previously discussed in Section 4.2.

The AFM findings further underscore the importance of treating a PS-coated PDMS substrate to obtain the most uniform surface for PEM assembly and subsequent mechanical testing. The following section will present results from PEM systems grown on the plasma-treated PS-PDMS platform.

4.4.4 Results for Systems Not Amenable to Direct Assembly onto PDMS

The first system assembled on the plasma treated PDMS-PS substrates was (PAH3.5/PAA3.5). This system was chosen because of the difficulty of assembling PAH and PAA at this pH onto untreated PDMS, and, as with the case of the (PAH7.5/PAA3.5) system, results from previous nanoindentation studies were available for comparison.[160] Similar to previous experiments, substrates were removed during dipping to obtain samples with differing PEM film thicknesses. In the case of (PAH3.5/PAA3.5), samples were collected following the deposition of 17.5, 25.5, 45.5, 59.5, 98.5, 144.5, and 150.5 bilayers. The PEM thickness and Young's modulus, as determined via the two-plate analysis (Equation 4.8), are graphed in Figure 4.13.

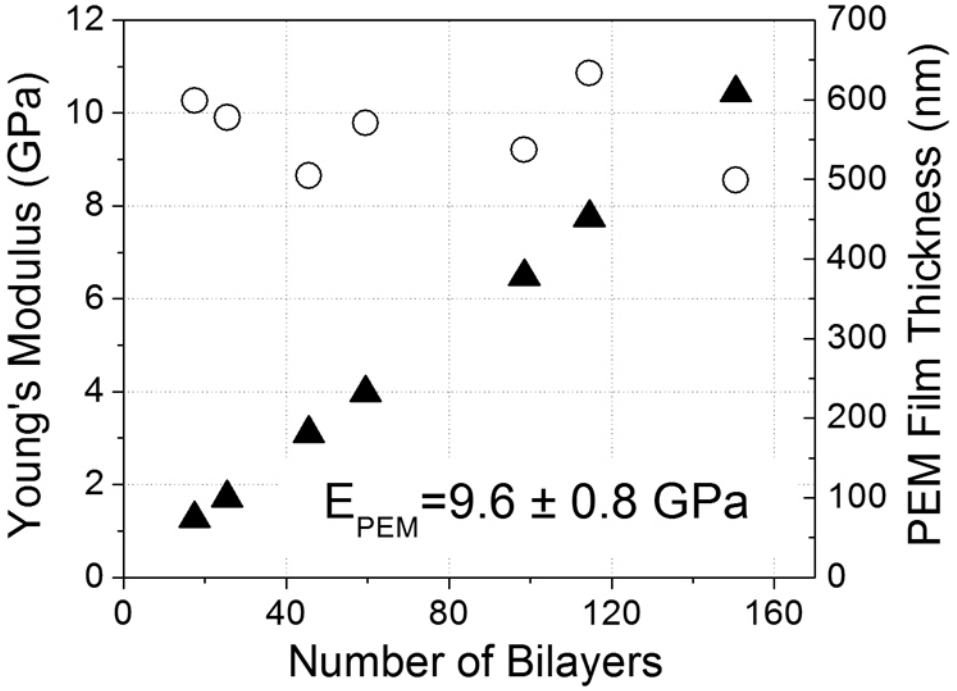

Figure 4.13. (PAH3.5/PAA3.5) film thickness (filled triangles) and Young's modulus (open circles) vs number of bilayers as measured via the two-plate SIEBIMM technique. The average Young's modulus is 9.6 ± 0.8 GPa. The relative humidity was 20 ± 4%.

As for the previous systems, the film thickness of (PAH3.5/PAA3.5) multilayers showed very precise linear growth, with a calculated thickness increment of 4.0 nm/bilayer (*R*-squared = 0.999). The PEM Young's modulus, which again remained constant with increasing film thickness, was 9.6 ± 0.8 GPa. The value of 9.6 ± 0.8 GPa was obtained at a relative humidity of 20%; previous nanoindentation studies of this multilayer system conducted at a relative humidity of ≈ 50% provided a value of 16.1 ± 2.8 GPa, higher than the value given here.[160] Thus, under more humid conditions, nanoindentation suggests an even higher modulus value. Given the considerable differences between the buckling technique and nanoindentation, especially in the nature of the sample deformations, agreement in the absolute value of the modulus for any given system is not necessarily expected; however, the two techniques also reveal different trends in the modulus values when comparing films at the same humidity.

Our next choice of system for testing was the (PAH4.0/PAA4.0) system, which also required a hydrophilic substrate for good multilayer growth. Although the deposition pH of the (PAH4.0/PAA4.0) system is very close to that of the (PAH3.5/PAA3.5) system, it is well known that weak polyelectrolyte film thickness, chain organization, and network structure can change dramatically over very small changes in deposition conditions.[38] In addition, there has been recent interest in (PAH4.0/PAA4.0) PEMs as candidate platforms for controlling cell growth, leading to nanoindentation studies of the wet-state mechanical properties of this system;[7] there is no information, however, on the dry-state mechanical properties.

During the deposition of (PAH4.0/PAA4.0), samples were removed after completion of 10.5, 22.5, 25.5, 30.5, and 50.5 bilayers. The PEM thickness and Young's modulus for this system, as determined via the two-plate analysis, are graphed in Figure 4.14.

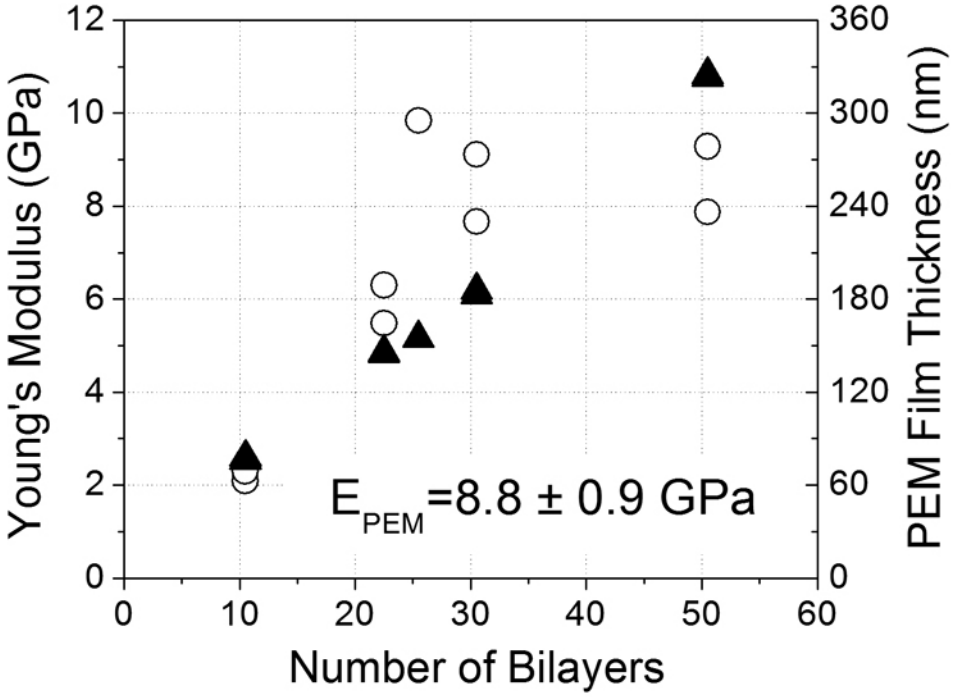

Figure 4.14. (PAH4.0/PAA4.0) film thickness (filled triangles) and Young's modulus (open circles) vs number of bilayers as measured via the two-plate SIEBIMM technique. The average modulus of films with 25.5 or more bilayers is 8.8 ± 0.9 GPa. The relative humidity was 20 ± 4%.

It is evident from Figure 4.14 that the Young's modulus of the (PAH4.0/PAA4.0) samples displays a very different trend from that measured for the (PAH3.5/PAA3.5) system. Linear regression of the data revealed a thickness increment of 6.2 nm/bilayer, a value ≈ 50% higher than the value of 4.0 nm/bilayer obtained for the (PAH3.5/PAA3.5) system. In addition, though the thickness data are still linear with the number of bilayers deposited, the *R*-squared value was 0.994, which was lower than those of the previous systems, implying less uniformity in the growth rate. The modulus rises from a value of ≈ 2 GPa for 10.5 bilayer samples and levels off at an average value of 8.8 ± 0.9 GPa for samples with 25.5 or more bilayers.

The trend in modulus data for the (PAH4.0/PAA4.0) system is very similar to that observed for (PAH3.0/PSS3.0) multilayers deposited on PDMS substrates that had been

pretreated by soaking in water prior to film deposition (see Figure 3.6). In that case it was concluded that the layers near the PDMS surface assumed a different chain conformation due to interactions with the water treated surface. In the results reported in Chapter 3, the value at which the (PAH3.0/PSS3.0) Young's modulus leveled off was very close to the average value measured on non-treated substrates (see Figure 3.5 and Figure 3.6). In the case of the (PAH4.0/PAA4.0) multilayers, the asymptotic value of Young's modulus of 8.8 ± 0.9 GPa obtained from averaging samples with 25.5 or more bilayers is close to the value of 9.6 ± 0.8 GPa obtained for the (PAH3.5/PAA3.5) system. The proximity of these two values leads to the conclusion that for films of sufficient number of bilayers the stiffness of PAH and PAA multilayers does not change dramatically when the deposition pH is changed from 3.5 to 4.0. The decrease in mechanical stiffness at low bilayer numbers, however, again confirms our earlier suggestion given in Chapter 3 that it is advisable to monitor the Young's modulus as a function of thickness if one wishes to obtain a reliable measurement for a thin PEM film.

The Young's modulus values of the (PAH7.5/PAA3.5), (PAH3.5/PAA3.5), and (PAH4.0/PAA4.0) films at 20% humidity were found to be 10.5 ± 0.5 GPa, 9.6 ± 0.8 GPa, and 8.8 ± 0.9 GPa, respectively. These values do not reveal a significant dependence of stiffness on the pH assembly conditions of PAH and PAA, even though different chain organizations are expected for each system.[38] In comparison, these values are all significantly higher than the modulus of 5.6 ± 0.3 GPa measured for (PAH3.0/PSS3.0) at the same humidity. Thus, these results suggest that polyelectrolyte type and the ambient humidity are the most significant factors in determining the dry-state modulus of a PEM film. The pH of deposition, at least for the weak polyelectrolyte systems that have been tested here, appears to be a less important factor. These same considerations do not apply to films in the wet state, however. Given that deposition pH controls both the internal structure and the crosslink density of films assembled using weak polyelectrolytes such as PAH and PAA, films swollen underwater have been shown to display significant differences in stiffness that correspond to the amount of electrostatic bonding present in the multilayer.[7]

A Young's modulus on the order of 10 GPa for (PAH/PAA) films at low ambient humidity is ≈ 2 to 3 times larger than is typically reported for crosslinked polymer resins.[218]

Previous work (using nanoindentation and assuming a Poisson's ratio of 0.33) found values of 8.47 ± 0.25 GPa and 1.20 ± 0.52 GPa for the PAA and PAH homopolymers, respectively, and suggested that the interchain ionic crosslinking present in multilayer films of (PAH/PAA) contributed to enhancing PEM stiffnesses to values greater than either homopolymer.[160] The present work has shown, however, that absolute modulus values from buckling and nanoindentation are not always directly comparable. Thus, more investigation is needed to formulate a full explanation of the high modulus values exhibited by certain PEM films.

4.5 Conclusions

In conclusion, a two-plate buckling instability technique has been introduced to make the SIEBIMM technique applicable to a wider variety of thin film systems. Because of the difficultly in obtaining a stable, hydrophilic surface through direct modification of PDMS without interfering with the mechanical properties of its surface, a thin PS layer was transferred to the PDMS surface. After transfer, the PS was modified by plasma to change the wettability. Using PEMs, it has been demonstrated that thin film systems not otherwise amenable to deposition on untreated PDMS can be successfully assembled and tested on this new platform over a wide range of thicknesses, creating PS-PEM two-plate composite films that undergo buckling instabilities like their homogeneous counterparts. By using the proper mechanical analysis, the unknown Young's modulus of the PEM layer can be extracted from the overall mechanical properties of the two-plate composite film.

The technique introduced in this work should prove especially useful for the polyelectrolyte multilayer community, where properties such as the surface wettability and film thickness growth increment can vary widely from system to system. The two-plate method, like conventional SIEBIMM, allows measurements to be performed in both the dry and wet states. Although the two-plate technique has been used here for testing multilayer films of polyelectrolytes, the method should be applicable to other types of materials systems as well. This could be an important consideration as thin film mechanical properties measurements become increasingly important in a wide variety of fields.

One important conclusion from the results in this chapter is that changes in humidity can have significant effects on the stiffness of PEM systems. The next chapter will focus on elucidating these effects in more detail, providing results from SIEBIMM testing of three PEM systems under controlled humidity conditions.

Chapter 5
The Effect of Relative Humidity on the Young's Modulus of Polyelectrolyte Multilayer Films*

5.1 Introduction

As has been noted in previous chapters, the layer-by-layer assembly of PEMs represents an area of rapidly growing interest in surface science, due mainly to the unusually broad spectrum of applications for these materials, which includes potential uses in biology,[7-9, 47, 135, 138, 140, 162, 170-174, 177-184, 191] medicine,[219, 220] sensing, [221, 222] tribology,[5] and optics.[58, 59, 62] Despite the relative ease with which PEMs can be assembled onto a variety of substrate types and topologies, characterization of certain fundamental properties of these materials has remained difficult due to the inherent challenges of probing materials that exist only as ultrathin films. In Chapter 3, it was demonstrated that that the SIEBIMM buckling instability method[168] can be applied to PEMs to obtain fast and accurate measurements of the Young's modulus. In Chapter 4, a two-plate buckling method was introduced to allow SIEBIMM to be expanded to a broader array of thin film systems. Consequently, this allowed the exploration of the effect of polyelectrolyte type, assembly conditions, and humidity on the modulus of PEM assemblies. Previous studies, including the work that was presented in Chapter 4, have reported that increases in relative humidity can lead to decreases in the stiffness of PEMs,[29] but no systematic study of this phenomenon has yet been reported. This chapter, therefore, will present the results of a more detailed study of the effect of humidity on the Young's modulus of polyelectrolyte multilayer films.

5.2 Background and Motivation

Among the factors that influence the mechanical properties of PEMs, humidity would seem to occupy a position of unique importance. Unlike polyelectrolyte type or assembly conditions, the ambient humidity is a dynamic environmental variable that continues to affect the mechanical properties of the film following the assembly process.

* The author acknowledges the collaboration of Neil Treat in performing the research described in this chapter.

PEMs have been proposed for a number of different uses; among these are applications such as antireflection coatings[58] and anti-fog coatings,[58, 78] where exposure to widely varying climatic conditions could reasonably be expected. The performance and suitability of PEMs in these circumstances will depend in some measure on their mechanical properties under different environmental conditions, such as different relative humidity.

Another motivation for investigation of PEMs as a function of relative humidity is the possibility of obtaining insights into the internal structure and interactions within the film. Although assembled films are crosslinked through electrostatic interactions between polyelectrolytes, water is able to swell and plasticize PEMs, as is evidenced by the SIEBIMM study of "wet-state" (PAH/PSS) films immersed in water that was presented in Chapter 3 (see Figure 3.7). Even dry films, however, are expected to contain a certain amount of water. The amount of swelling due to water uptake by a specific PEM system is expected to be governed by both the chemical identity of the film, as well as the activity of water in the ambient environment, of which relative humidity is a measure. The chemical identity of the film will be determined in part by the types of polyelectrolytes comprising the multilayer. Even in systems assembled from the same types of polyelectrolytes, however, changing the assembly conditions can change the chemical identity of the multilayer. As an example of this, consider the discussion in Chapter 1 of the effect of pH of assembly conditions on multilayers of (PAH/PAA) (see Figure 1.2). When assembling polyelectrolytes from solutions where the both chains are fully charged, very flat, highly crosslinked films are obtained.[38] Assembly at a low pH, however, leads to multilayers with a large number of unpaired, protonated carboxylic acid groups within the film, which were shown in Chapter 2 to be useful for subsequent nanoreactor chemistry. Depending upon the relative affinity of water molecules for ionic crosslinks versus, say, protonated carboxylic acid groups, these films should display different degrees of swelling at a given relative humidity.

Besides the amount of electrostatic crosslinking and the chemical nature of the uncrosslinked moieties within the film, secondary-bonding interactions can also play an important role in determining the amount of water uptake in a PEM system. (PAH/PSS)

multilayers deposited at high pH, for example, have been shown to undergo hysteretic swelling transitions due to hydrophobic association of partially charged PAH repeat units within the bulk of the film.[203] Similar types of transitions have also been observed in polymer gels containing both electrostatic and hydrogen bonding interactions.[223] In the two aforementioned cases, the systems were being studied in a fully hydrated state. Nevertheless, similar phenomena are expected to occur in films exposed to sufficiently high humidity.

In this chapter, the degree of swelling and the Young's modulus of three PEM systems are investigated as a function of the relative humidity. The systems chosen for investigation were multilayers of (PAH7.5/PAA3.5) and (PAH3.0/PSS3.0), both of which were examined in the previous chapter, and (PAH2.5/PAA2.5) films, which had been previously untested. The choice of (PAH7.5/PAA3.5) and (PAH3.0/PSS3.0) multilayers was motivated by the fact that both of these systems had been examined previously (see Chapter 3 and Chapter 4); thus, they provided a measure of comparison for the humidity-dependent results. The study of (PAH2.5/PAA2.5) films allowed for examination of the effects of changing the deposition pH on the modulus of (PAH/PAA) assemblies. This particular system, which is assembled at low pH where PAA is only partially ionized, is also technologically interesting because of the ability of free carboxylic acid groups within the film to template post-assembly nanoreactor chemistry.[51] It was also expected that films of (PAH2.5/PAA2.5) multilayers may display a greater sensitivity to humidity effects due to the fact that (PAH2.5/PAA2.5) films assembled with PAA on top have been known to be quite hydrophilic, presumably also due to the abundance of polar, protonated carboxylic acid groups at the film surface.[37] Details of the experiments and results from testing these three PEM systems are provided in the following sections.

5.3 Experimental Details

PAH (M_w = 70 000, Sigma-Aldrich), PSS (sodium form, M_w = 70 000, Sigma-Aldrich), and PAA (25% aqueous solution, M_w = 90 000, Polysciences) were used without further purification to create polymer solutions of 0.01 M concentration by repeat unit. In addition, 0.1 M NaCl (Mallinckrodt Chemicals) was added to each polyelectrolyte solution when

multilayers of PAH and PSS were being assembled. Milli-Q deionized water (Millipore) with a resistivity of 18.2 MΩ·cm was used for all procedures and preparations. Solutions were adjusted to the appropriate pH with 1.0 M HCl or NaOH immediately prior to PEM assembly.

Assembly of PEMs onto PDMS was performed by an automated programmable slide stainer (HMS slide stainer, Zeiss). Substrates were first immersed in the polycation (PAH) for 15 min, followed by three 1 min rinse steps. The samples were then immersed in the polyanion (PSS) for 15 min, followed again by three 1 min rinses. This process was cycled until the desired number of bilayers were deposited. If more than 10 bilayers were deposited, the immersion time in the polyelectrolyte baths was decreased to 5 min for the 11^{th} and all subsequent bilayers. Following the completion of PEM assembly, samples were allowed to air dry. Samples were stored in air at ambient conditions.

Probing the Young's modulus of PEMs at controlled relative humidity levels necessitated modifications to the typical experimental procedure for PEM SIEBIMM analysis (see Section 3.3). Measurements of the buckling wavelength were conducted by performing He-Ne (632.8 nm wavelength) laser diffraction measurements on a strained sample in a controlled-humidity glove box (Electro-Tech Systems) (see Figure 5.1). Samples were first equilibrated for ≈ 1 week in a desiccator containing LiCl before being moved to the humidity chamber, which was equilibrated at 12% humidity. After a few hours, the first buckling and ellipsometer measurements were taken, after which the humidity was increased to the next value and the film was allowed to equilibrate for ≈ 1 day. A photograph of the experimental setup and an image of a film being subjected to laser diffraction are shown in Figure 5.1.

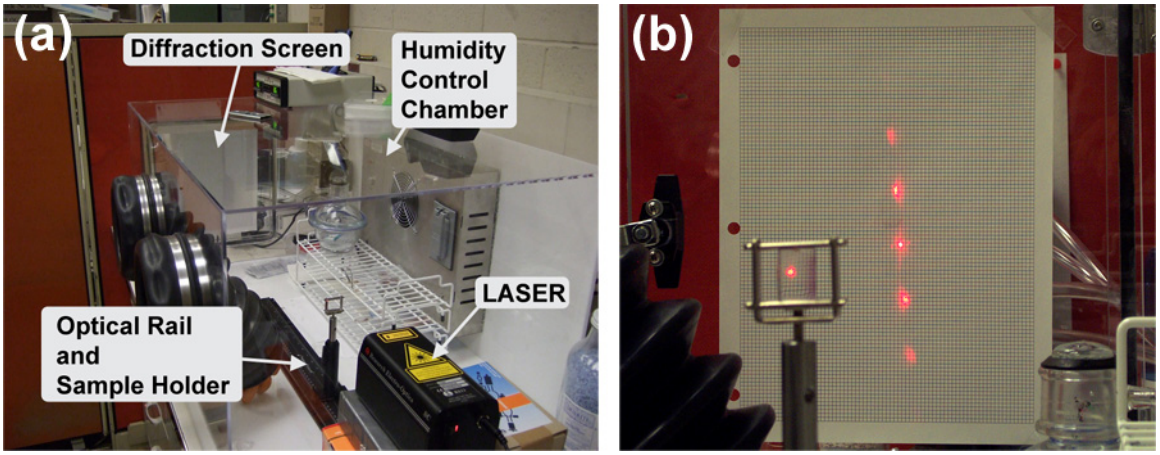

Figure 5.1. Experimental setup for laser diffraction measurements of the buckling wavelength. (a) A photograph of the humidity control chamber and laser diffraction experimental setup. (b) Photograph of the diffracted laser beam from a sample ((PAH3.0/PSS3.0), 12% RH) undergoing buckling. Two diffracted orders of the beam can be seen.

Ellipsometry measurements were performed as follows: while still in the controlled humidity chamber, samples were hermetically sealed in a quartz cell using Parafilm and transferred to a spectroscopic ellipsometer for thickness characterization; these measurements were performed using previously described methods (see Section 3.4.1). The error in the thickness measurement was taken to be the larger of the ellipsometer-determined surface roughness or 0.5 nm.

The humidity chamber was equipped with an optical rail so that the strained sample could be translated regular distances parallel to the laser beam while taking digital pictures of the diffraction pattern. A graph of the center spot to 1st-order peak distance vs distance along the optical rail yielded a straight line. Linear regression yielded the slope of the line, m, from which the buckling wavelength (λ) could be calculated as:[168]

Equation 5.1

$$\lambda = \frac{632.8\,nm}{m}.$$

The uncertainty in m (δ_m) was calculated using the R-squared (R^2) value of the regression line as:[224]

Equation 5.2

$$\delta_m = |m| \cdot \sqrt{\frac{1-R^2}{(N-2)\cdot R^2}}\,.$$

where N was the number of separate diffraction measurements. The uncertainty in the buckling wavelength (δ_λ) was then calculated by propagation of error to be:[199, 200]

Equation 5.3

$$\delta_\lambda = \lambda \cdot \frac{\delta_m}{|m|}\,.$$

For the results obtained in this chapter, the PDMS Young's modulus and Poisson's ratio were assumed to be 1.8 ± 0.1 MPa and 0.50, respectively.

The plane strain Young's modulus was calculated using Equation 3.10 (with Equation 3.4). Plane strain PEM modulus values (see Equation 3.4) are reported in this chapter due to the uncertainty in the Poisson's ratio of the PEMs at various relative humidity values. A value of 0.33 for dry-state films and 0.5 for films immersed in water has previously been assumed; depending upon the level of humidity, the Poisson's ratios for the films in this chapter should lie between those two limiting values. Errors bars in all reported data represent propagated uncertainties from the estimated error in each measurement step.[199, 200] The temperature in the humidity chamber was maintained in the range of ≈ 25-28°C during all experiments.

5.4 Results and Discussion

Although there have been no detailed systematic studies of PEM mechanical properties as a function of relative humidity, a handful of researchers have examined the humidity-dependent swelling behavior of PEMs. Among these, reported equilibration times for PEM film swelling in controlled humidity environments range widely, from anywhere as short as 15 min[225] to several hrs.[226, 227] In the experiments presented in this chapter, samples were allowed to equilibrate for ≈ 1 day at each humidity value. Three systems were examined in

this study: $(PAH3.0/PSS3.0)_{75}$, $(PAH7.5/PAA3.5)_{10.5}$, and $(PAH2.5/PAA2.5)_{20}$. Presentation of the results will begin with a comparative overview of the humidity dependence of the Young's modulus for all three films. The swelling and Young's modulus data of each particular system will then be examined in more detail.

5.4.1 Overview of the Humidity-Dependent Young's Modulus Results*

Figure 5.2 displays a graph of the Young's modulus vs relative humidity for the three PEM systems studied in this chapter. The (PAH7.5/PAA3.5) system generally exhibited the highest modulus values under dry, i.e., < 50% relative humidity (RH) conditions. This finding agrees with the results presented in Chapter 4, where (PAH7.5/PAA3.5) multilayers were found to have comparatively higher moduli than any of the other ((PAH3.5/PAA3.5), (PAH4.0/PAA4.0), and (PAH3.0/PSS3.0)) systems tested. The values of the Young's modulus reported in that case for the (PAH7.5/PAA3.5) system at 20% and 50% RH were 10.5 ± 0.5 GPa and 7.0 ± 0.2 GPa, respectively. In the study conducted in this chapter, the values at similar humidity values (24% and 48%) yielded Young's moduli (converted from the plane strain values by using a Poisson's ratio of 0.33) of 8.3 ± 0.9 GPa and 5.1 ± 0.7 GPa, respectively. The agreement between studies is good, especially considering the significant differences between measurement techniques, most notably in the switch from optical microscopy to laser diffraction as the method for determining the buckling wavelength. The Young's modulus values obtained for the (PAH3.0/PSS3.0) system, also tested both in Chapter 4 and in the current chapter, showed similarly good agreement between studies. In the former study, values of 5.6 ± 0.3 GPa and 2.7 ± 0.3 GPa were measured at 20% and 50% RH, respectively; here, values of 5.4 ± 0.5 GPa and 3.7 ± 0.3 GPa for the same system at 24% and 48% RH were obtained.

* In addition to PEM systems discussed in this chapter, the thickness and Young's modulus of two thin polystyrene samples were measured as a function of humidity. These data can be found in Appendix B.

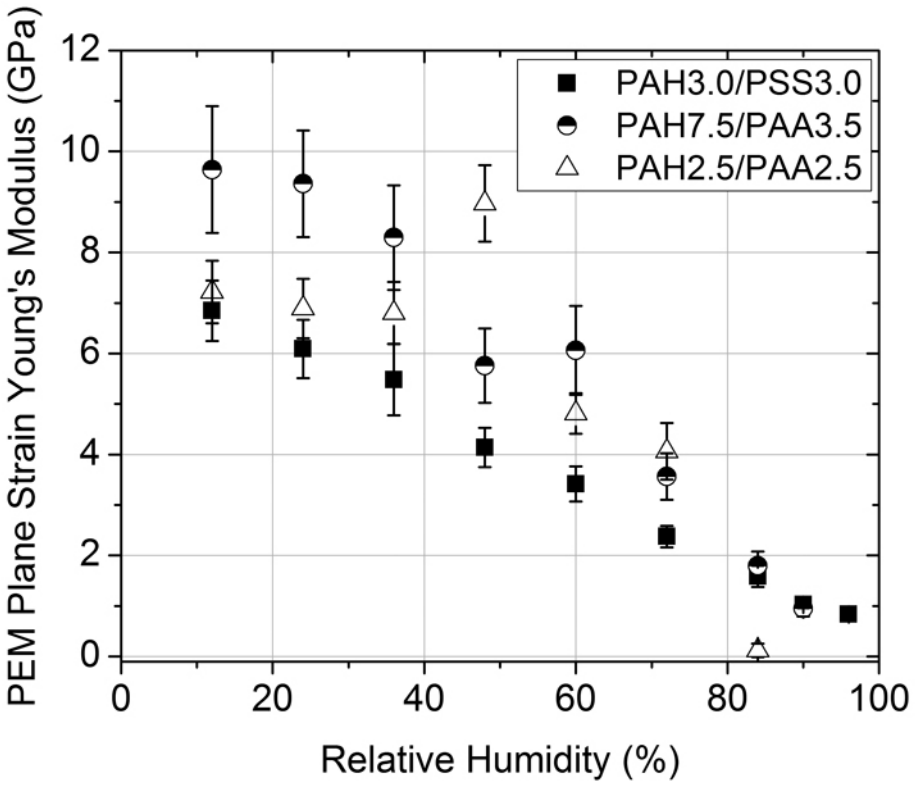

Figure 5.2. Plane strain Young's modulus vs relative humidity for three PEM systems (see legend). Samples were allowed to equilibrate ≈ 24 hrs at each relative humidity value before measurements were taken.

Figure 5.2 highlights many interesting trends among the humidity dependent Young's modulus data for the three systems examined in this study. For example, while the (PAH7.5/PAA3.5) system is notably stiffer than the (PAH3.0/PSS3.0) system at low humidity, the systems exhibit near identical modulus values at higher humidity (84-90% RH). At 96% RH, the plane strain modulus of the (PAH7.5/PAA3.5) system dips below that of the (PAH3.0/PSS3.0) system, for which a plane strain modulus of 0.84 ± 0.06 GPa was measured. The (PAH7.5/PAA3.5) system did not even exhibit detectable buckling at this humidity, suggesting a Young's modulus very close to or smaller than that of the PDMS substrate (1-2 MPa). Thus, while the (PAH7.5/PAA3.5) system possesses a higher Young's modulus than the (PAH3.0/PSS3.0) system at low humidity, it is also more sensitive to humidity changes, becoming more compliant than the (PAH3.0/PSS3.0) system at ≈ 85% RH.

Figure 5.2 also demonstrates the significant effect that deposition pH can have on the properties of films assembled from the same polyelectrolyte pair. (PAH7.5/PAA3.5) multilayers exhibit higher modulus values than (PAH2.5/PAA2.5) films at relatively low humidity (12-36%). At intermediate humidity values (48-72%) the two systems exhibit moduli that are equal within error (the unusually high modulus value for the (PAH2.5/PAA2.5) system at 48% RH is possibly an outlier). Between the relative humidity values of 72% and 84%, however, the (PAH2.5/PAA2.5) system undergoes a dramatic drop in modulus that is not correspondingly observed in the (PAH7.5/PAA3.5) system, decreasing over an order of magnitude from 4.1 ± 0.6 GPa to 0.12 ± 0.13 GPa. Over the same humidity range, the (PAH7.5/PAA3.5) system exhibits a more modest decrease, going from 3.6 ± 0.5 GPa to 1.8 ± 0.3 GPa.

Figure 5.2 demonstrates that for all systems tested in this study, water is an effective plasticizer, swelling the films and facilitating chain motions with a consequent decrease in the Young's modulus. As has been demonstrated previously with other types of hydrophilic polymer gels, the relative humidity determines the concentration of water in the film, which in turn determines the magnitude of the plasticizing effect.[228] While knowledge of the Young's modulus provides many important details about how PEM films respond to the presence of water in the ambient environment, even more information can be obtained by studying the modulus results in tandem with humidity-dependent measurements of the film thickness. In the following section, each of the three systems shown in Figure 5.2 will be examined in closer detail.

5.4.2 Equilibrium Swelling and Young's Modulus Data

In Figure 5.3, the plane strain Young's modulus data from for the $(PAH7.5/PAA3.5)_{10.5}$ film are graphed along with the PEM film thickness as a function of relative humidity. As was noted above, at low humidity the (PAH7.5/PAA3.5) system displayed the highest Young's modulus among the three systems tested in this study. The affinity of the PEM for water leads to a substantial decrease in modulus with increasing humidity, with a decrease in plane strain modulus of an order of magnitude (9.6 ± 1.3 GPa to 0.94 ± 0.16 GPa) over the

humidity range of 12-90%. The system also was tested at 96% RH, but no buckling was observed, suggesting that the film Young's modulus had assumed a value comparable to or smaller than that of the PDMS substrate (1-2 MPa). The thickness data in Figure 5.3 display a somewhat less steep rise with humidity in the range of 12-48% RH as opposed to the data collected in the range of 60-90% RH. Though the effect is slight, the modulus data, especially at 12 and 24% RH, appears to mirror this effect, plateauing off at ≈ 9 GPa. This same effect is noticed again, but much more distinctively, in the (PAH3.0/PSS3.0) system.

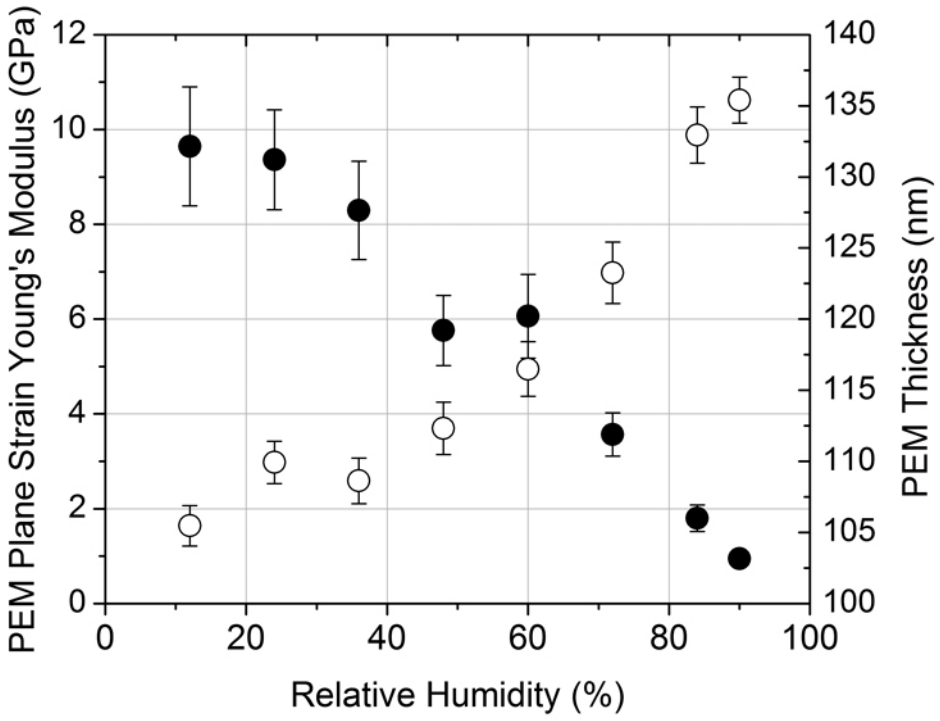

Figure 5.3. Plane strain Young's modulus (solid circles) and PEM thickness (hollow circles) for $(PAH7.5/PAA3.5)_{10.5}$ multilayer films. Samples were allowed to equilibrate ≈ 24 hrs at each relative humidity value before measurements were taken.

Figure 5.4 displays the plane strain Young's modulus data for the $(PAH3.0/PSS3.0)_{75}$ film along with the PEM film thickness as a function of relative humidity. In this system, the above-mentioned increased swelling effect at high humidity values is clearly evident. A cursory look at the data suggests that the PEM thickness response can be divided into two regimes, with a transition at ≈ 60% RH. The thickness increases linearly with humidity in

each regime, but with a steeper slope at higher humidity values. To quantify this effect, separate regression lines were calculated for the thickness values measured at the four lowest (12, 24, 36, and 48% RH) and the four highest (72, 84, 90, and 96% RH) humidity values. These calculations revealed an incremental film thickness change of 0.29 ± 0.02 nm/(%RH) in the low humidity regime, and a value of 0.75 ± 0.04 nm/(%RH) in the high humidity regime.

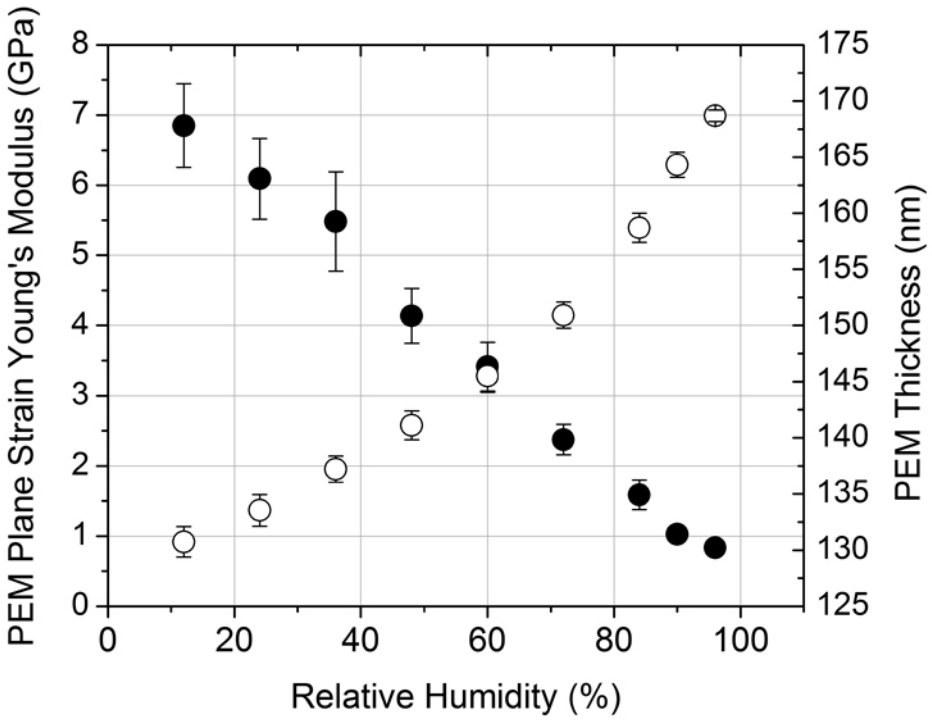

Figure 5.4. Plane strain Young's modulus (solid circles) and PEM thickness (hollow circles) for $(PAH3.0/PSS3.0)_{75}$ multilayer films. Samples were allowed to equilibrate ≈ 24 hrs at each relative humidity value before measurements were taken.

This observation of two distinct swelling regimes for the (PAH/PSS) multilayer system is not unique. Very similar behavior of the film thickness is evident in the graphs provided by Wong, et al. in their study of the swelling behavior of (PAH/PSS) films, though they offer no comments concerning the appearance of the data in this regard.[225] The data of these researchers also provides evidence that this effect is more pronounced when the thin multilayers that they are working with are capped with PAH as opposed to PSS. Evidently,

the presence of PAH as the outermost layer leads to a more hydrophobic film with a greater propensity to drive out water from the PEM matrix, at least for low bilayer numbers.[225, 229] The fact that the "two-regime" mode of swelling is more pronounced in PEM systems with a higher degree of hydrophobicity points to a possible physical explanation of the effect.

At low humidity, water entering the dry film associates at first with the ionic crosslinks between polyelectrolyte chains, being excluded from the more hydrophobic regions of the film that are absent of ionic crosslinks. Eventually, at higher humidity, the activity of the water is high enough so that the water, which had a tendency to cluster around the ionic crosslinks at lower humidity values, begins to coalesce and form a continuous water phase throughout the film, leading to enhanced swelling. The above hypothesis has been suggested to explain the swelling behavior of Nafion membranes in controlled humidity environments.[230-232] Nafion, which consists of a perfluoronated polymer backbone with sulfonic acid side chains, provides a decent comparison for the (PAH/PSS) system, where humidity-responsive ionic groups are present within a matrix that tends to exclude water due to strong hydrophobic interactions. In the low humidity regime, the hydrophobic associations within the (PAH/PSS) network resist swelling; in the higher humidity regime, these interactions are overwhelmed by the high chemical potential of the water molecules, and the film swells more dramatically. A somewhat similar argument has been invoked to explain hysteretic swelling transitions in (PAH/PSS) films deposited under high pH conditions.[203]

The swelling behavior presented in Figure 5.3 for the (PAH7.5/PAA3.5) system also possesses a transition in swelling behavior, albeit one that is considerably less defined. In addition, this transition occurs at a lower relative humidity value ($\approx$ 40%). The lack of clear definition in this transition, as well as its presence at a lower value of relative humidity (and hence lower water activity), both suggest that the (PAH7.5/PAA3.5) matrix is more hydrophilic and less resistant to swelling by water. This conclusion is consistent with the results of contact angle measurements performed on each system.[45, 225]

The plane strain Young's modulus change with humidity for (PAH3.0/PSS3.0) multilayers remains fairly linear over the range shown in Figure 5.4. Perhaps somewhat remarkably, the modulus does not reflect the corresponding transition between swelling regimes, and even counterintuitively plateaus off between the values of 90 and 96% RH. The reason for this behavior is not fully clear, but could be related to the fact that upon percolation of the water throughout the film it assumes a modulus value very close to its "wet-state" value, which is the modulus of a film completely immersed in liquid water. Indeed, when a Poisson's ratio of 0.50 is assumed, the Young's modulus of the film measured at 96% RH in Figure 5.4 is 0.63 ± 0.05 GPa, which is in remarkable agreement with the value of 0.59 ± 0.09 GPa given in Chapter 3 for (PAH3.0/PSS3.0) films swollen in water (see Figure 3.7).

Figure 5.5 presents the plane strain Young's modulus and PEM film thickness data for $(PAH2.5/PAA2.5)_{20}$ films as a function of relative humidity. The behavior of this system is qualitatively different from that observed for (PAH7.5/PAA3.5) and (PAH3.0/PSS3.0) multilayers in Figure 5.3 and Figure 5.4. The (PAH2.5/PAA2.5) film displays remarkable resistance to swelling and plasticization at low humidity (12-36% RH). It then enters an intermediate regime where the film thickness begins to increase and the modulus begins to decrease (48-72% RH), before finally swelling very abruptly to a high value, with a corresponding drop in plane strain modulus to 0.12 ± 0.13 GPa at 84% RH, which represented the lowest value recorded at any humidity value among the systems tested in this study. Apparently, the modulus continued to decrease substantially with increasing humidity, as no buckling was observed at either 90 or 96% RH for this system.

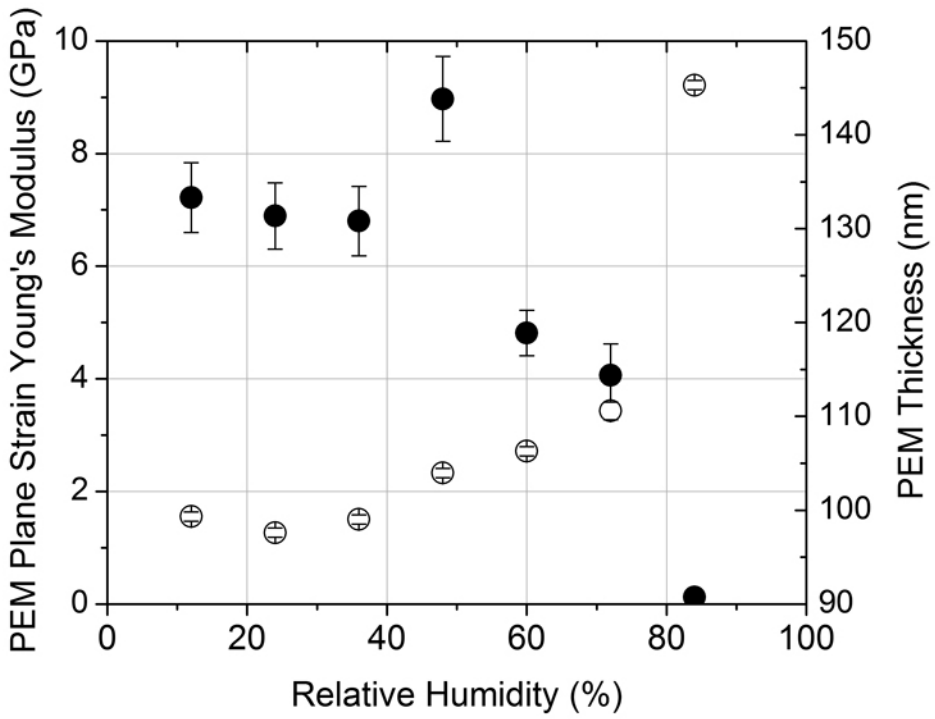

Figure 5.5. Plane strain Young's modulus (solid circles) and PEM thickness (hollow circles) for $(PAH2.5/PAA2.5)_{20}$ multilayer films. Samples were allowed to equilibrate ≈ 24 hrs at each relative humidity value before measurements were taken.

The (PAH2.5/PAA2.5) system's behavior is puzzling at first: resistance to swelling and plasticization at low humidity, and then a sharp transition to a very compliant system at ≈ 80% RH. Clues to the mechanism underlying this behavior can be found by considering the chemical nature of films assembled from PAH and PAA at low pH. At low pH values, multilayers of PAH and PAA are expected to contain a large amount of free, protonated carboxylic acid groups,[38, 51] the presence of which at the surface of the PEM has been shown to lead to very low contact angles.[37] Thus, it would seem as if the (PAH2.5/PAA2.5) system should be readily swollen by water. Carboxylic acid groups, however, can also engage in hydrogen bonding—it is conceivable that in large numbers, hydrogen bonding interactions could stitch the film tightly together and resist swelling. As the humidity increases, the increase in chemical potential drives enough water into the film to allow the carboxylic acid functionalities to begin to dissociate. Dissociation of the acid groups will lead to abrupt swelling of the film due to both the loss of cohesive hydrogen bonding as the

carboxylate groups de-protonate, as well as the increase in osmotic driving force for water into the film due to the presence of the ionized acid functionalities.

Although the sharp swelling transition reported here for the (PAH2.5/PAA2.5) system has not been previously reported, the proposed mechanism is supported in part by previous research. Izumrudov et al. have demonstrated that for multilayer systems in solution, hydrogen bonding can act to hold the film together at ionic strengths where it would otherwise be favored to dissolve.[233] Annaka et al. have also demonstrated that competitive binding between hydrogen and electrostatic bonds in polymer gels can lead to multiple stable swollen phases.[223] These studies demonstrate the importance that secondary interactions can have in determining the cohesive binding and swelling in hydrophilic polymer gels such as PEMs, and lend confidence to the hypothesis advanced to explain the swelling transition in the (PAH2.5/PAA2.5) system.

5.5 Conclusions

The results in this chapter have demonstrated that the SIEBIMM technique can be successfully implemented under controlled humidity conditions with in situ ellipsometry to study the humidity dependence of the Young's modulus and thickness of PEM films. An experimental apparatus (see Figure 5.1) was assembled to allow both the buckling wavelength and the thickness of the films to be determined in situ. Good agreement was found between measurements of the moduli of the (PAH7.5/PAA3.5) and (PAH3.0/PSS3.0) systems using both the new technique in this chapter, as well as the conventional technique as presented in Chapter 3 and Chapter 4.

The differences in humidity responsiveness among the three systems examined here suggest that changes in polyelectrolyte type and adsorption pH during film assembly can lead to considerable differences in the internal bonding interactions within the film. Although each of the systems examined in this chapter showed the same general response to humidity—i.e., increased plasticization and swelling with increased relative humidity—the types of polyelectrolytes and even the assembly pH for the (PAH/PAA) system led to very

different swelling and mechanical property behavior in response to changes in the relative humidity.

Careful examination of the humidity responses for the different systems reflect details about the internal film structure and its ability to accommodate the uptake of water. For example, the hydrophobic nature of the (PAH3.0/PSS3.0) matrix leads to two different swelling regimes: at low humidity, water molecules cluster mainly around ionic crosslinks, while at higher humidity the increased chemical potential drives water throughout the entire PEM network, leading to increased swelling. The more hydrophilic (PAH7.5/PAA3.5) network is solvated by water at lower humidity, leading to a relatively linear swelling response over the range of humidity values that were tested. The (PAH2.5/PAA2.5) demonstrated a resistance to swelling at low humidity, followed by a sharp swelling transition between 72 and 84% RH with a concomitant drop in Young's modulus. Hydrogen bonding between protonated carboxylic acid groups is likely responsible for the suppressed swelling effect at low humidity; at high humidity, solvation of the acid groups leads to disassociation and the loss of cohesive hydrogen bonding, swelling the network.

A topic for further study is the effect of drying treatment on Young's modulus of PEM films. Although it was not addressed in this chapter, it was generally observed that the method of drying the PEM (blow dry, drip dry, etc.) can effect the thickness and stiffness of the PEM, even for films assembled and tested at the same humidity. Films that were blown dry with compressed air seemed to exhibit the smallest thicknesses and highest Young's modulus values—films allowed to "drip dry" in a moderately humid environment exhibited comparatively higher thicknesses and lower Young's modulus values. The cause of this effect is not entirely certain, though it may be due to the fact that compressed air is assumed to drive bound water out of the film more aggressively, resulting in a more extensive collapse of the chain structure than is experienced by films simply allowed to dry undisturbed in the ambient atmosphere. The films with the more compressed chain structure then in turn exhibit enhanced Young's moduli due to the increased density of the PEM.

This chapter has demonstrated that humidity-dependent SIEBIMM analysis can reveal much about internal interaction within PEM films and their responses to different environmental humidity values. Besides providing scientific value in this regard, this technique could also be of interest to those who are interested in PEM sensors or applications where the humidity dependence of the mechanical properties may be an important figure of merit.

Chapter 6
Controlled Lithographic Patterning of Polyelectrolyte Multilayer Films by Salt Etching*

6.1 Introduction

The ability to create finely-controlled patterns in thin polymer films has been instrumental in the development of many important modern technologies, having significant impact in fields such as semiconductor fabrication[1] and biotechnology.[6] Although PEMs have emerged as a facile route to build up thin polymer films with precise film thicknesses and chemical functionalities on a variety of surface types and geometries,[17-19] the demonstrated importance of lithographic polymer patterning[1] suggests that the ability to controllably remove PEMs from a surface could conceivably be just as technologically important. This chapter will discuss the patterning of PEMs via etching in salt-containing solutions. A general model for understanding the controlled dissolution of PEM films in solutions of salt is presented and discussed in terms of its ability to explain our observations, as well as those of previous researchers. Simple lithographic applications are demonstrated through surface screening, and precise control of the z-direction etching depth is demonstrated to be possible through control of the salt concentration and etch time.

6.2 Background and Motivation

Several previous researchers have reported the partial of complete loss of PEM films upon exposure to salt-containing solutions, and the work in particular of Cohen Stuart et al.,[188, 234] Sukhishvili et al.,[35, 233, 235, 236] and Schlenoff et al.[237-239] has sought to quantify and describe these phenomena in more detail. As an ionically crosslinked film of positively and negatively charged polyelectrolytes, a PEM can be understood as constituting a large, surface-bound insoluble polyelectrolyte complex (PEC). It is little surprise, then, that knowledge of the solution-phase behavior of PECs can elucidate analogous processes encountered in the study of PEMs. For example, it is well established that both the molar

* The author acknowledges the collaboration of Nobuaki Takane, Whitney Gaynor, and Evan Hindman in performing the research described in this chapter.

ratio of positively to negatively charged polyelectrolyte repeat units and the ionic strength of the solution help determine whether a PEC will be soluble or precipitate.[240-243] In a similar manner, PEM films have been shown to undergo dissolution when an excess of one polyelectrolyte is added to the system, or the ionic strength of the solution is altered.[188]

Although many researchers have reported the destruction of multilayers under various solution conditions, few studies have focused on controlling the PEM dissolution process. As discussed above, the ability to controllably remove PEMs from a surface not only at different locations, but also in different amounts (PEM "etching") could have important technological implications. With a few notable exceptions that will be discussed below in more detail, most literature reports have approached PEM etching as an "all or nothing" phenomenon, whereby a given film is expected to either remain more or less intact or dissolve completely. The present chapter examines the etching behavior of films comprised of poly(allylamine hydrochloride) (PAH) and poly(acrylic acid) (PAA), and films comprised of PAH and poly(styrene sulfonate) (PSS). When immersed in solutions of NaCl, these films undergo a controlled loss of material and re-equilibrate to a new film thickness that depends upon the concentration of the NaCl solution.

The experimental evidence presented in this chapter suggests that salt etching of PEMs involves structural rearrangements of the entire film leading to ejection of near-stoichiometric amounts of polycation and polyanion repeat units into solution. The strength and extent of polyelectrolyte interactions, as well as the molecular weight distribution of the polyelectrolytes comprising the film, are shown to be important factors in determining the etching behavior of a given system. Finally, a mechanism is proposed to describe the kinetics and equilibrium behavior of salt-induced etching of PEM films. Two basic examples of how this technique can be employed to generate both discrete and continuously graded thickness patterns over large spatial areas are then demonstrated.

6.3 Experimental Details

PAH (M_w = 70 000, Sigma-Aldrich), PSS (sodium form, M_w = 70 000, Sigma-Aldrich), and two types of PAA: "high-PDI" (25% aqueous solution, M_w = 90 000, Polysciences, PDI

= 6.2) and "low-PDI" (solid, M_n = 86 100, Polymer Source, PDI = 1.12) were used without further purification to create polymer solutions of 0.01 M concentration by repeat unit. PAH and PSS solutions additionally contained 0.1 M NaCl (Mallinckrodt Chemicals). Milli-Q deionized water (Millipore) with a resistivity of 18.2 MΩ·cm was used for preparation of all solutions and rinse baths. Polymer solutions were pH-adjusted using either 1.0 M HCl or NaOH immediately prior to PEM assembly.

Single-crystal polished silicon wafers (p-type, WaferNet) were used as substrates, except where the use of poly(dimethylsiloxane) (PDMS) was necessitated as indicated in the text. Silicon substrates were sonicated for 15 min in a dilute detergent solution, followed by 10 min in pure water. They were then treated for 8 min in an air plasma (Harrick Scientific PDC-32G plasma cleaner/sterilizer, 100 W, 400 mTorr) directly prior to PEM assembly. PDMS substrates (Sylgard 184, Dow Corning) were prepared as described in Section 3.3.

Etching baths consisted of NaCl solutions prepared at the appropriate concentration. Samples were immersed in the salt solution with mild agitation, and upon removal were immediately rinsed with agitation in pure water for 1 min, after which they were blown dry with air. Etching times are indicated for samples in the kinetic tests; all other samples were etched for 1 hr, except for those shown in Figure 6.3 (10 min etch times) and Figure 6.4 and Figure 6.5 (3 min etch times).

Thickness characterization was performed using spectroscopic ellipsometry (M-2000D, J.A. Woollam Co.) according to the method described in Section 3.4.1. Ellipsometer fits for the roughness of the samples were used as indicated in the text to estimate errors in the thickness measurements when multiple samples could not be measured to obtain an average and standard deviation. Unless otherwise indicated, the assumed thickness error was taken to be the larger of the modeled sample roughness or 1 nm.

6.4 Results and Discussion

6.4.1 Salt Etching Experiments

The first etching experiments were conducted on (PAH7.5/PAA3.5) films exposed to different concentrations of NaCl solution for 1 hr, followed by a 1 min rinse in water. Three films of increasing number of bilayers (film thickness) were tested, and the ellipsometry results are displayed in Figure 6.1.

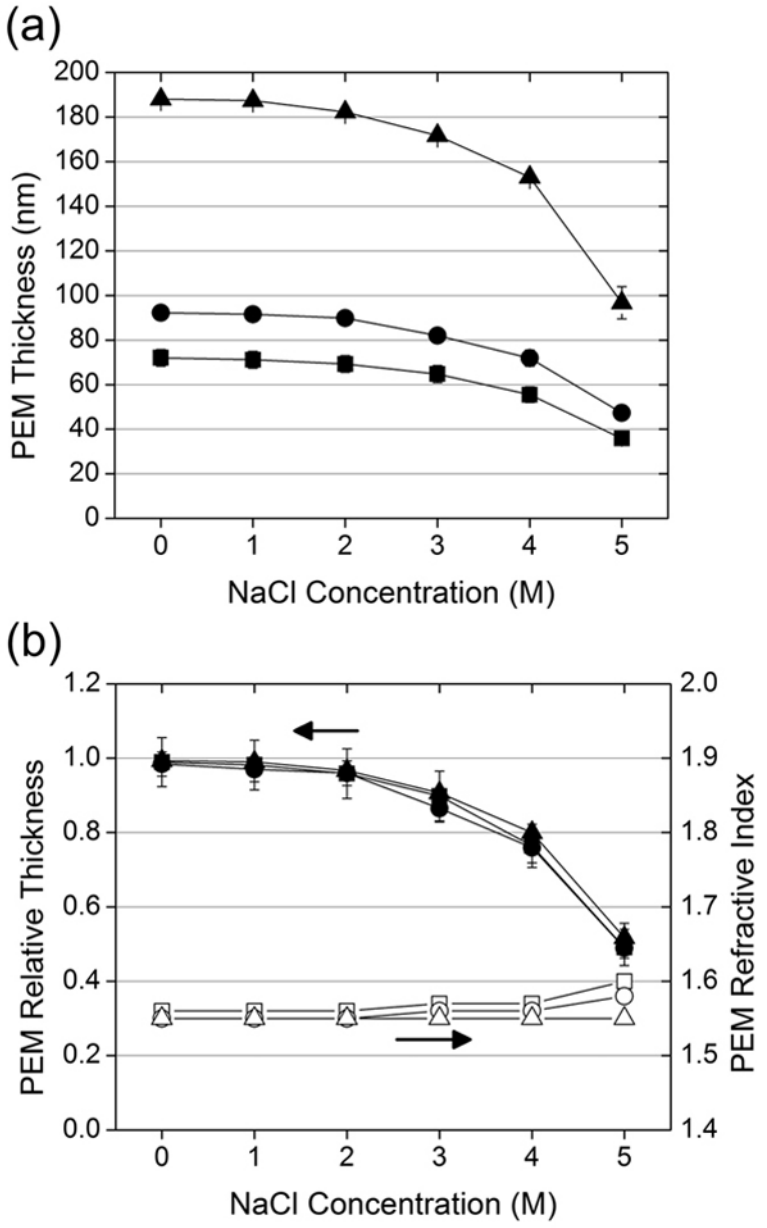

Figure 6.1. Salt etching of $(PAH7.5/PAA3.5)_x$ films of various thicknesses. Films prior to etching had thicknesses of 70 nm (x = 7.5, squares), 90 nm (x = 9.5, circles), and 190 nm (x = 16.5, triangles). Films were etched at a given salt concentration for 1 hr, after which they were rinsed and blown dry. (a) Absolute film thicknesses are shown as a function of salt concentration. (b) Normalizing film loss by the original film thickness demonstrates that films exhibit identical relative etching amounts. The refractive indices of the dried films are given as open symbols.

Figure 6.1 highlights some important characteristics of PEM salt etching. Figure 6.1a shows the absolute film thickness of three samples as a function of the NaCl concentration during etching. For all films, higher salt concentrations led to increased thickness losses. Normalizing the thickness of all samples to their original values revealed essentially identical changes in the relative thicknesses of all samples (Figure 6.1b). These results indicate that salt etching does not consist of polyelectrolyte material simply being removed from the surface of the PEM without interaction with the rest of the film material—the entire bulk of the film must be sampled, as the film thickness decreases in proportion to the total thickness of PEM. Furthermore, the nearly constant refractive indices of the etched films (Figure 6.1b) indicate that the decrease in film thickness in these samples is due to actual loss of material, and not shrinking or densification of the films, for which increased refractive indices would be expected. Figure 6.1b actually shows that a small increase in the refractive index was recorded for the two thinnest samples tested. This effect may in fact be an artifact, as less accurate model fits were obtained from the ellipsometer software for these thinner (< 50 nm) samples; a corresponding increase in refractive index was not observed with the thickest sample, for which a more confident data fit was be obtained.

In order to determine whether the films equilibrated at the thicknesses indicated in Figure 6.1 rather than being simply interrupted during a kinetically slow dissolution process, time studies were conducted on two (PAH7.5/PAA3.5) films with initial thicknesses of 120 nm and 270 nm. A solution with an NaCl concentration of 4 M was used for the kinetic tests; the films were divided into multiple smaller samples and each piece was immersed in the NaCl solution for the indicated time; all samples were washed for 1 min in water following the salt immersion. The absolute and relative PEM thickness vs time plots for these samples are shown in Figure 6.2a and Figure 6.2b, respectively.

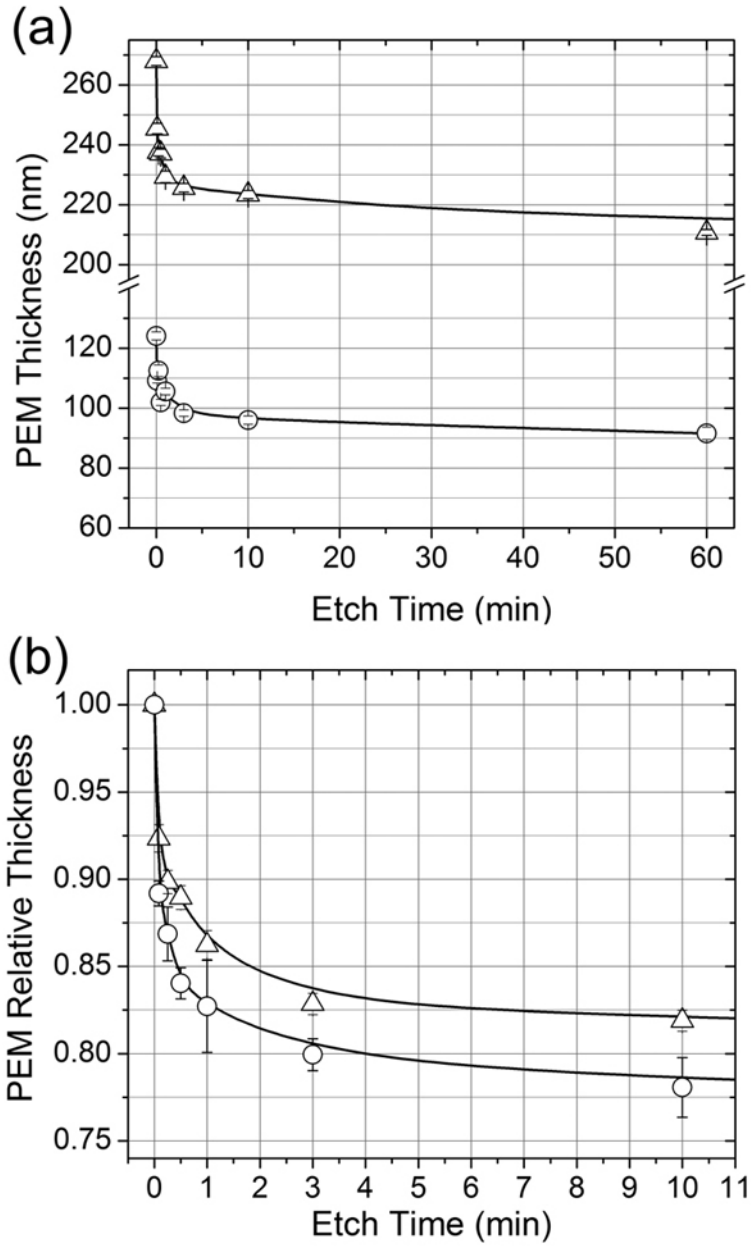

Figure 6.2. Absolute (a) and relative (b) PEM thickness vs time plots for two $(PAH7.5/PAA3.5)_x$ films. Films had initial thicknesses of 120 nm (x = 10.5, circles) and 270 nm (x = 21.5, triangles). The films were etched in a 4 M NaCl solution. The solid lines are guides to the eye.

Figure 6.2 suggests that the data follow a relationship at least qualitatively similar to an exponential function. The exact functional form followed by these data provides information

concerning the mechanism of the etching process, and will be examined at greater depth in Section 6.4.3. With only a cursory glance at the data, however, one can gather that etching happens quickly at relatively small times, with the film thickness eventually leveling off at an equilibrium value. These data also confirm the results presented in Figure 6.1b; namely, that films equilibrate to a thickness relative to the initial thickness of the PEM. The relative thicknesses of 0.75 (measured after 1 hr) and 0.77 (measured after ≈ 19 hr, not displayed in Figure 6.2a) reached at long times by the 120 nm and 270 nm thick films were essentially equal. The data suggest slower kinetics in the case of the thicker film, however, which provides another argument against the notion that etching could be due to a top-down loss of polyelectrolyte chains from the surface, as the kinetics of such a process would presumably be unaffected by the film thickness.

One explanation for why a film might only dissolve partially and equilibrate at a film thickness greater than zero is that the PEM is favored to dissolve completely, but that the salt solution into which the film dissolves becomes saturated with polyelectrolyte material and an exchange equilibrium is established, forbidding further thickness changes. This hypothesis was tested by subjecting a single $(PAH7.5/PAA3.5)_{16.5}$ film (190 nm thickness) to multiple etch steps at the same concentration, exchanging the etching bath with fresh solution after every step. The film was taken through 3 etch steps at 0 M NaCl (water with no added salt), followed by 3 successive steps in each of 1 M, 2 M, 3 M, 4 M, and 5 M NaCl baths. All etch steps lasted for 10 min. The results from this experiment are displayed in Figure 6.3.

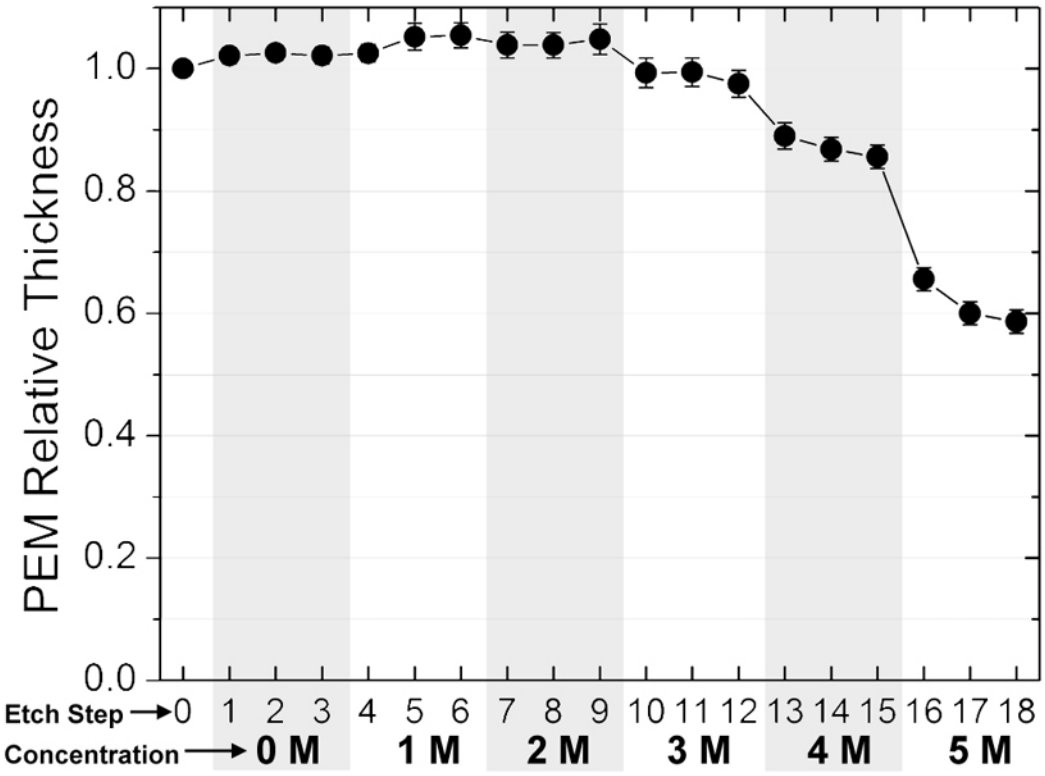

Figure 6.3. Relative thickness change of a $(PAH7.5/PAA3.5)_{16.5}$ film subjected to multiple etching steps at increasing concentrations. Each etch step consisted of a 10 min immersion in a fresh NaCl solution of the indicated concentration, followed by a 1 min rinse in water. The concentration of the etch solution, given below the etch step numbers along the abscissa, was incremented 1 M following 3 successive steps at a given concentration.

The minimal change in PEM film thickness displayed previously in Figure 6.1 for etch concentrations below 3 M may explain why the film in Figure 6.3 did not begin to decrease in thickness until the 10th etch step. The two following steps at 3 M produced very little further change in film thickness, but a jump to a smaller thickness was again observed at the 13th etch step, when the salt concentration was increased to 4 M. The film did not exhibit another abrupt decrease in thickness until the 16th step, which was the first immersion into the 5 M NaCl solution. The thickness only decreased slightly for the last two steps, which were subsequent immersions into 5 M NaCl solutions.

The results in Figure 6.3 disprove the hypothesis that polyelectrolyte chains in the film are establishing an exchange equilibrium with dissolved polyelectrolyte material in solution, and thus prohibiting further dissolution. If this were the case, then the film would have been

expected to re-equilibrate with a sudden decrease in film thickness for each successive etch step in fresh salt solutions. These decreases for subsequent steps should have been most apparent at high salt concentrations (steps 14-15 and 17-18), but instead only minimal further film dissolution (due to the fact that films had not completely equilibrated, as only 10 min etch times were used) followed for these steps, despite immersion in fresh solutions.

Thus, successive immersion steps into fresh salt solutions will not result in total film dissolution; a given film will dissolve only partially even when immersed into an essentially infinite reservoir of solution. Similar results for PEMs containing a weak polycarboxylic acid group have been reported by Izumrudov, who showed that hydrogen bonding between protonated carboxylate groups could result in the increased stabilization of multilayers exposed to solutions of NaCl at lower values of pH.[233] The results presented in this work, however, were obtained in pH-neutral NaCl solutions with measured pH in the range of 6.2-6.8. Furthermore, it has been established that strong preferential binding between PAA and PAH groups leads to a shift of the PAA pK_a from its solution value of 6.5 to a value of $\approx$ 3.5 when PAA is assembled with PAH.[39] These considerations suggest that under the conditions considered in this chapter, PAA groups in the film remain nearly fully ionized.

Stabilization of multilayer films at intermediate thicknesses has also been reported by Kovačević and co-workers, who observed a similar phenomenon for PEMs subjected to an essentially infinite reservoir of salt and polyelectrolyte.[188] They explained the lack of total film dissolution in terms of the "three zone" model of Ladam et al.,[202] suggesting that the majority of the PEM will be lost when dissolution is favored, but a small fraction of PEM chains near the substrate will remain because they are "vitrified" by their proximity to the solid substrate. This explanation does not satisfactorily account for the observations reported here, however, as the films exhibited only small fractional losses of material over the majority of salt concentrations tested. Furthermore, the three zone model proposes that the size of the region of less mobile polymer chains is not dependent upon the total film thickness, whereas the changes in film thickness reported here have been shown to be relative to the initial thickness of the PEM.

Figure 6.3 shows a slight increase in film thickness for immersions in the 0 M, 1 M, and 2 M concentration solutions. The cause of this increase is believed to be due to the fact that at low salt concentrations the polyelectrolyte chains in the hydrated PEM still have enough freedom to reorganize at low salt concentrations where the ionic strength is not yet high enough to induce film dissolution. A similar observation was reported in Chapter 3 with a (PAH/PSS) multilayer exposed to 1.0 M NaCl solution (see Figure 3.7).

To elucidate any changes in the structure of the film with increasing concentration of the etching solution, the dry- and wet-state thicknesses of four (PAH7.5/PAA3.5) films following etching at increasing concentrations were examined. The results of this study are shown in Figure 6.4.

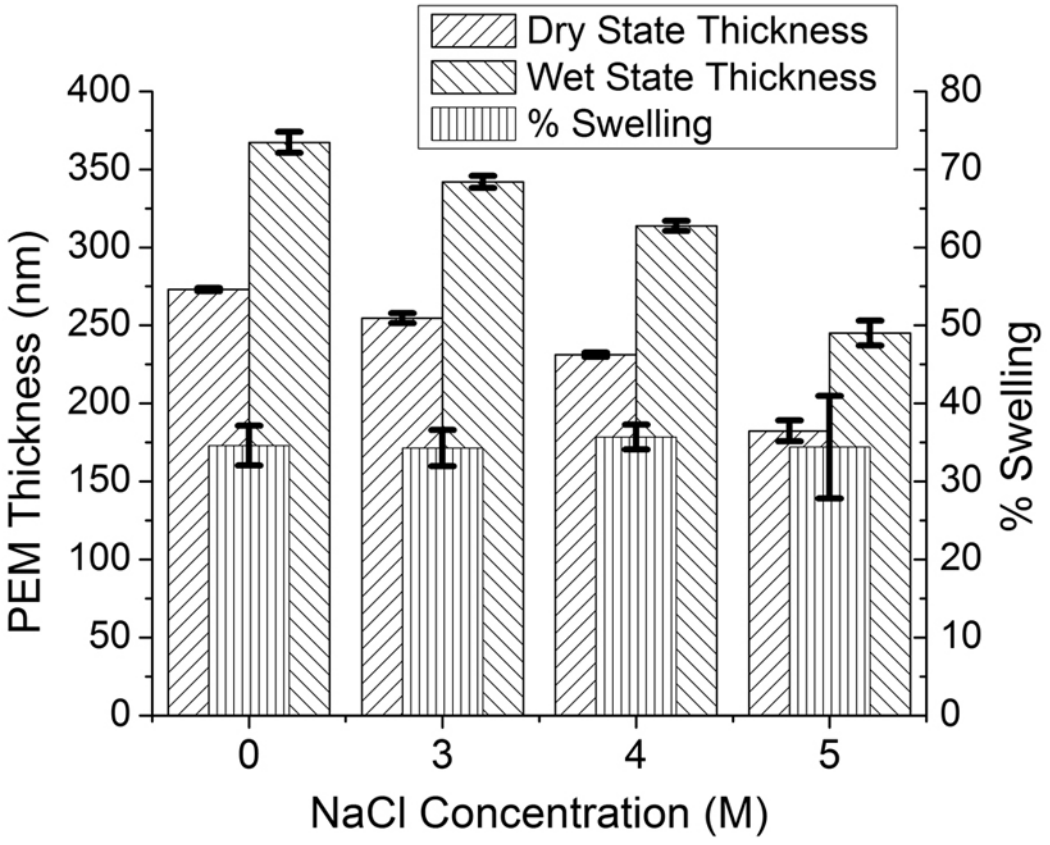

Figure 6.4. Dry- and wet-state thicknesses of (PAH7.5/PAA3.5)20.5 films following etching in NaCl baths of concentration 0 M, 3 M, 4 M, and 5 M. The films were swollen in water with no added salt. The swelling percentage of each film is also given. Error bars represent the standard deviation of measurements on three similar samples at each concentration value.

The dry-state thicknesses of the etched films shown in Figure 6.4 exhibit the same decreasing trend that was observed in Figure 6.1. The same films were then allowed to swell in pure water (no added salt) for ≈ 4 hrs, after which time their thicknesses were measured using in-situ ellipsometry (see Section 3.4.1). These wet-state measurements are shown along with the calculated swelling percentage, which is taken as the difference between the wet- and dry-state thicknesses, divided by the dry-state value. The lack of discernable change in the swelling percentage implies that there is little change in the ionic crosslink density with increased etching. These results are not immediately surprising, as previous researchers have shown that PEMs, even when assembled from or annealed in solutions with salt, tend to exhibit a strong preference for paring with one another,[192, 244] leaving very few bound salt ions within the PEM.

The lack of change in crosslink density suggests that etching leads to the loss of charged polycation and polyanion repeat units in approximately equimolar amounts. According to the stoichiometric principles suggested by Schlenoff and co-workers,[186, 187] the alternative option, that one polyelectrolyte is ejected preferentially to the other, would require inclusion of salt ions into the multilayer to balance the resulting unpaired groups. The inclusion of these ions would lead to broken crosslinks between polyelectrolytes, and presumably more swellable films following the etching treatment.

The conclusion that neither the polyelectrolyte composition nor the crosslink density of the films is altered upon etching is further supported by buckling instability measurements using the SIEBIMM method (see Chapter 3) which established that there was no discernable change in Young's modulus for $(PAH7.5/PAA3.5)_{20.5}$ films etched at increasing concentrations of NaCl over the range of 0 to 5 M. All films (including the one soaked in pure water, 0 M NaCl) displayed a slight decrease in modulus, but no discernable trend in the modulus is observed with increased concentration of the etching bath; these results are displayed in Figure 6.5.

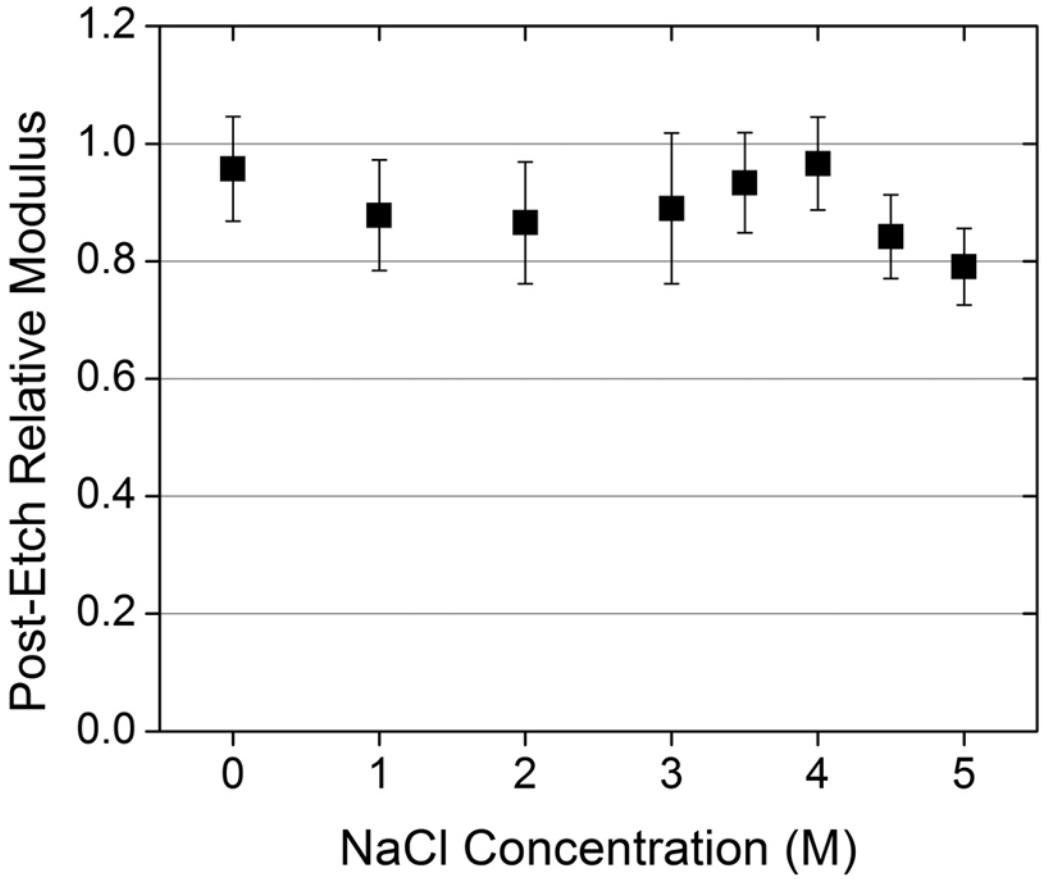

Figure 6.5. Relative post-etch Young's modulus values for $(PAH7.5/PAA3.5)_{20.5}$ multilayer films. The average pre-etch modulus of the films was 6.2 ± 0.2 GPa. The average post-etch modulus was 5.5 ± 0.4 GPa. Error bars were calculated by propagation of the uncertainties of each measurement step.

Additional etching tests were conducted on $(PAH6.5/PAA6.5)_{100.5}$ and $(PAH3.0/PSS3.0)_{100.5}$ multilayers to see how other PEM systems would respond to the etching treatment. These results are shown in Figure 6.6.

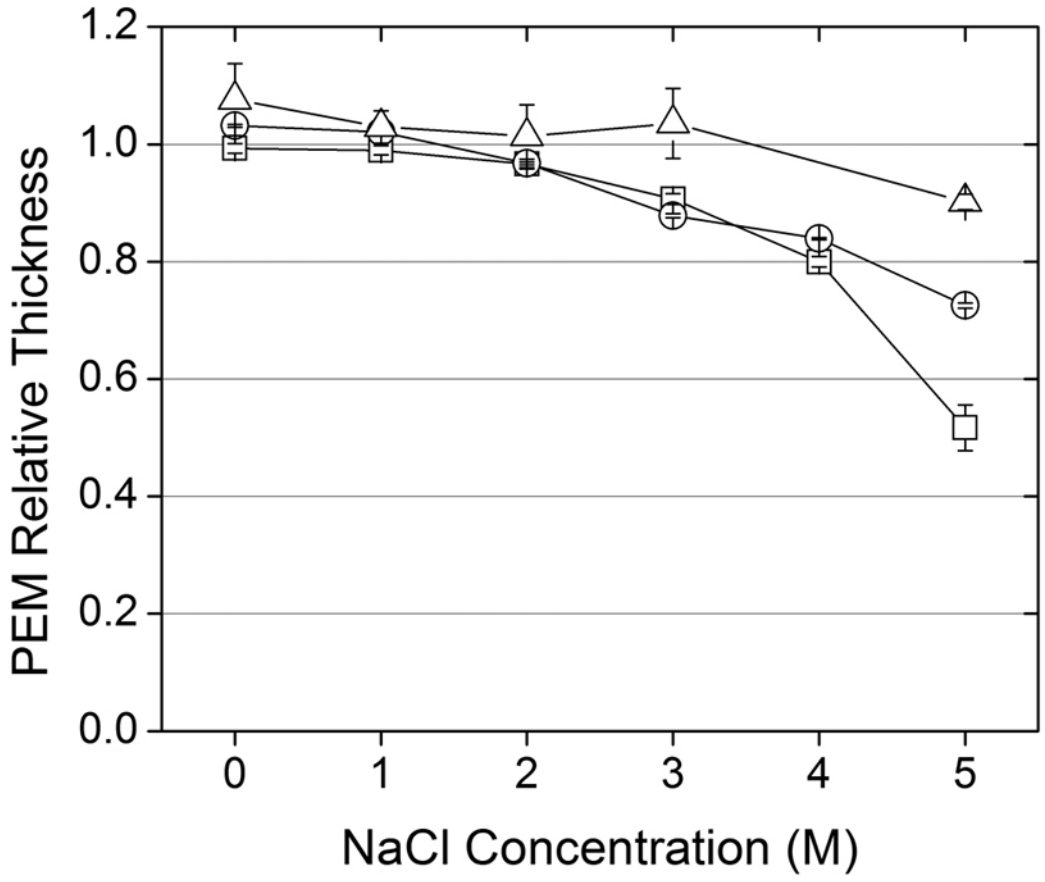

Figure 6.6. Relative thickness change for (PAH7.5/PAA3.5) (squares), (PAH6.5/PAA6.5) (circles), and (PAH3.0/PSS3.0) (triangles) multilayer films exposed to NaCl etching solutions. The 5 M data point for the (PAH3.0/PSS3.0) system was obtained from a different batch of films assembled on PDMS substrates (see text for further explanation).

Figure 6.6 demonstrates that the thickness change due to etching is affected not only by the choice of polyelectrolytes, but also by the internal bonding strength of the PEM assembly. Unlike the (PAH7.5/PAA3.5) system, which contains some unpaired (extrinsically compensated) groups, (PAH6.5/PAA6.5) multilayers are expected to possess a fully crosslinked internal structure.[38] Thus, this system permitted examination of the effect of increasing the degree of electrostatic crosslinking without changing the chemical nature of the crosslinks themselves. Alternatively, the (PAH/PSS) system allowed for testing the effect of changing the chemical nature of the ionic crosslinks while retaining nearly complete internal crosslinking within the film, as both PAH and PSS are fully charged at pH 3.0.[50]

The (PAH6.5/PAA6.5) system displayed very similar behavior to the (PAH7.5/PAA3.5) system for all salt concentrations less than 3 M. At 4 M and 5 M concentrations, the (PAH6.5/PAA6.5) films showed an increased resistance to film loss, at least for the 1 hr etching times used in this experiment. The (PAH3.0/PSS3.0) system, however, showed no measurable loss of material for NaCl concentrations up to 3 M. At etching concentrations of 4 M and 5 M, the film was removed completely from the silicon substrate. To determine whether the film had delaminated or dissolved, an etch of the (PAH3.0/PSS3.0) system in 5 M NaCl was repeated for a film that had been assembled on a PDMS substrate, for which good adhesion of (PAH/PSS) multilayers had been previously observed (see Chapter 3). The 5 M etch of (PAH3.0/PSS3.0) multilayers on PDMS resulted in the loss of only 10% the original film thickness, indicating that substrate adhesion was the cause of the total loss of the film for the 4 M and 5 M experiments conducted on silicon substrates.

Figure 6.6 demonstrates that (PAH/PAA) multilayers displayed a substantially greater propensity towards controlled etching over a larger range of film thickness than the (PAH/PSS) system. To examine the interactions within the (PAH/PAA) films in more detail, two $(PAH7.5/PAA3.5)_{10.5}$ films were tested in which the PAA had very different molar mass distributions. In one batch, PAA with a wide molar mass distribution (Polysciences, M_n = 90 000, PDI = 6.2) was used, and in the other system PAA with a similar average molecular weight but much narrower molecular weight range was employed (Polymer Source, M_n = 86 100, PDI = 1.12). Only the type of polyanion differed between films; the same type of PAH was used in each case. Both sets of films were subjected to identical etching treatments, the results of which are displayed in Figure 6.7.

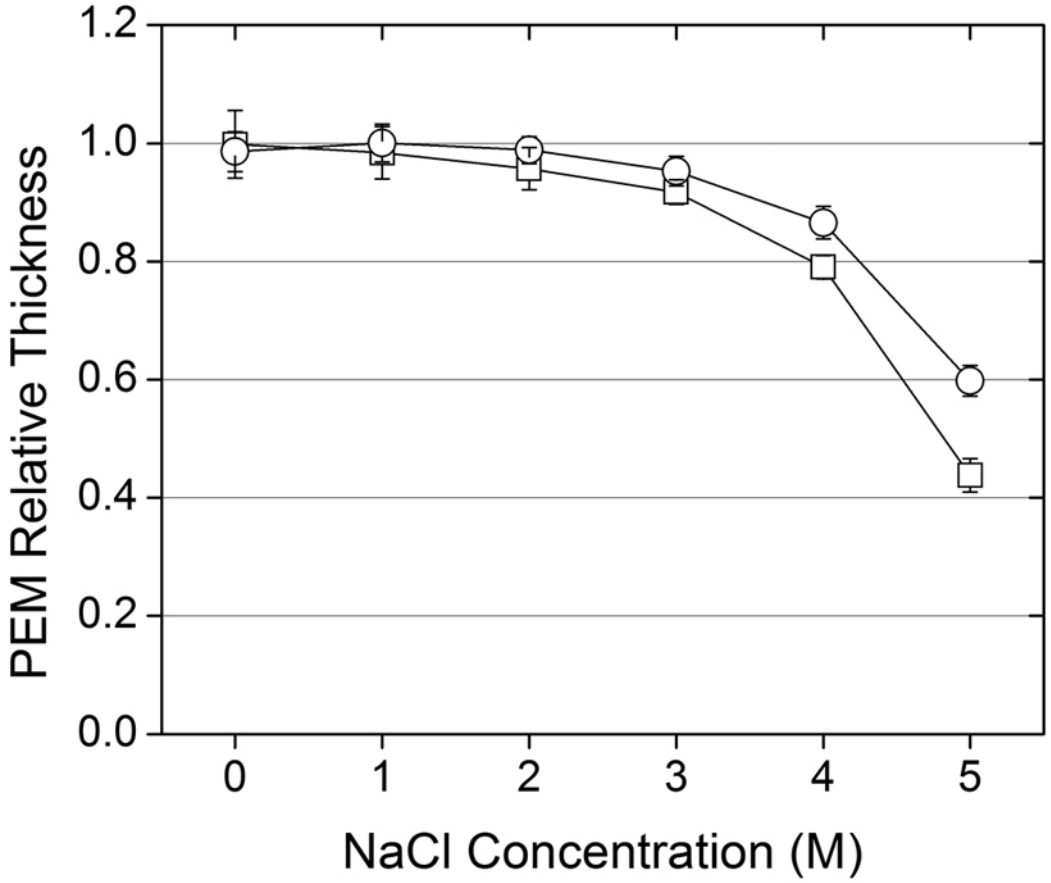

Figure 6.7. Relative thickness change for $(PAH7.5/PAA3.5)_{10.5}$ multilayer films exposed to NaCl etching solutions. Films were assembled using PAA with either a narrow (circles, PDI = 1.12) or wide (squares, PDI = 6.2) molar mass distribution. The same type of PAH was used in both cases.

The as-assembled average film thicknesses for $(PAH7.5/PAA3.5)_{10.5}$ multilayers assembled using the low and high PDI PAA were 158.1 ± 7.0 nm and 125.1 ± 1.9 nm, respectively. This difference in thickness for films assembled with the same number of bilayers at the same assembly conditions reveal that the molar mass distribution of the PAA is instrumental in determining the average bilayer thickness increment. In addition, Figure 6.7 indicates that changing only the molar mass distribution of one of the polyelectrolytes can alter the etching characteristics of (PAH/PAA) films. The PAA with a low PDI resulted in films that possessed a greater resistance to etching than films assembled under the same conditions with PAA possessing a large PDI. A comprehensive mechanism for salt etching must possess a means by which this and all of the above data can be understood.

6.4.2 A Mechanism for PEM Salt Etching

Thus far, it has been established that a (PAH/PAA) film immersed in a given concentration of salt equilibrates to a new thickness that is dependent upon the concentration of NaCl used. Films actually equilibrate, and are not simply interrupted during a complete dissolution process. Furthermore, the equilibrium thickness is relative to the initial thickness value; i.e., films of different thicknesses lose the same fraction of material, precluding an etching mechanism that only involves material at the surface of the film. In addition, films maintain this thickness in an effectively infinite reservoir of NaCl, indicating that some intrinsic property of the film has changed, and that it has not simply established an exchange equilibrium with dissolved species in the etching solution. This change of film property does not seem to be linked to the degree of electrostatic crosslinking, as in-situ ellipsometry studies have indicated no major change in the swelling percentage of post-etched films immersed in pure water, indicating that PAH and PAA repeat units must leave the film in an $\approx$ 1:1 ratio. The amount of etching in the (PAH/PAA) system can be controlled by varying the crosslink density of the film, as well as the molar mass distribution of one of its components, indicating the apparent relevance of both of these parameters to the etching mechanism. Finally, studies of the (PAH/PSS) system indicate that it too displays etching behavior, although substantially less so than (PAH/PAA) films.

Previous researchers have been successful in correlating observed properties of PEMs with the phase behavior of free polyelectrolyte complexes in solution.[188, 245] A schematic phase diagram for PECs, reproduced based on the schematic given by Kovačević, et al.,[188] is shown in Figure 6.8.

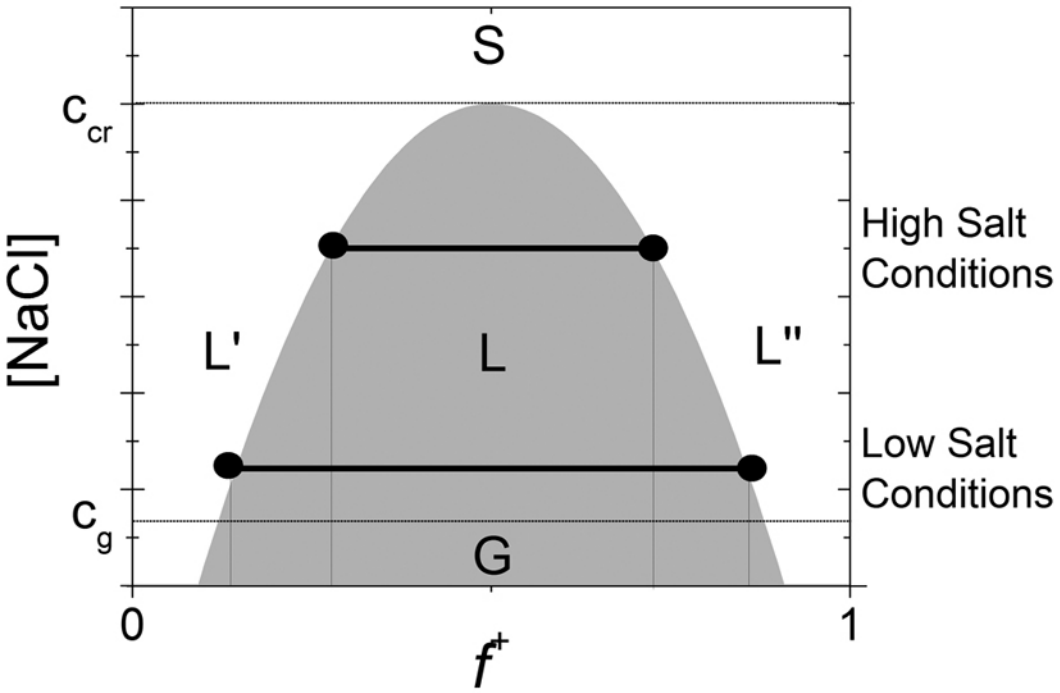

Figure 6.8. Illustration of the phase diagram for polyelectrolyte complexes (PECs) in solution. NaCl concentration is shown along the vertical axis, while f^+, the mole fraction of positively charged polymer repeat units within the PEC, is given along the horizontal axis. The darkened area indicates the region of insolubility. The lightened lines marked c_g and c_{cr} denote the glass transition and critical salt concentrations, respectively.[188] The regions on the diagram are described by the following: *G*: PECs are insoluble and chains are practically immobile, *L*: PECs are insoluble but chains are mobile, *L'*: PECs are soluble and negatively charged (majority polyanion), *L''*: PECs are soluble and positively charged (majority polycation), and *S*: PECs are soluble for all ratios of polycation to polyanion repeat units. Tie lines are shown to illustrate the required fractional composition of PECs that can be removed from the PEM film; soluble PECs are favored for f^+ values less than or greater than the values indicated by the bold points on the left and right sides of the darkened insolubility region, respectively.

In Figure 6.8, increasing NaCl concentration is shown along the vertical axis, while f^+, the mole fraction of positively charged polymer repeat units within the PEC, is given along the horizontal. Kovačević suggests that the different regions on the phase diagram, labeled with capital letters, can be interpreted as follows:[188] *G* indicates a glassy phase for which the salt concentration is not high enough to allow for polyelectrolyte chain mobility ([NaCl] < c_g), and *S* designates the region for which the salt concentration is greater than some critical value ([NaCl] > c_{cr}) and PECs are soluble for all molar ratios of cationic to anionic groups. In between these two concentrations lies a region where for $f^+ \approx 0.5$ PECs are insoluble

(region *L*), but for low and high values of f^+ where the ratio of charged units in the PEC is composed predominately of either the polyanion (*L'*) or polycation (*L''*), respectively, then soluble PECs are favored.

Figure 6.8 can help to explain the dissolution behavior of films of (PAH/PAA) immersed in solutions of increasing salt concentration if film loss is understood as the formation of water-soluble PECs (WPECs) from chains comprising the multilayer film. Formation of WPECs presumably requires mobility of polyelectrolytes within the film to permit for association of chains and detachment of the WPEC from the PEM surface. In films immersed in solutions with very little or no added salt, the polyelectrolyte chains are essentially immobile and this process cannot take place, explaining why there is no loss of material for NaCl concentrations less than ≈ 1 M (see Figure 6.1). As the solution concentration of salt is increased, increased "doping" of the PEM by salt ions leads to increased chain mobility within the film[186] and WPECs can be formed from polyelectrolytes comprising the PEM. These WPECs are expected to be rich in repeat units of either PAA or PAH, with concentrations of f^+ given by the bold points on the tie line marked "low salt conditions" in Figure 6.8. As the solution concentration of salt is increased, the formation of WPECs is favored over a broader range of f^+ values, and more of the PEM can dissolve.

The above mechanism explains the observations reported in this chapter, including why film dissolution seems to only begin at a certain salt concentration (c_g) where the film presumably loses its "glassy" nature and the polyelectrolytes become sufficiently mobile. This concentration will necessarily be larger for stronger interpolyelectrolyte interaction energies, explaining why no dissolution of the PEM takes place in the (PAH/PAA) system for concentrations less than 1 M NaCl, while for other systems complete film dissolution has been reported at even lower concentrations.[233, 237] These results are consistent with the reportedly strong favorability of PAH-PAA interactions.[39] Previous work would seem to indicate that even stronger interactions should exist between repeat units in the (PAH/PSS) system.[186] These findings are also consistent with the data presented in Figure 6.6, which illustrate that the (PAH/PSS) system resists loss of material in NaCl solutions with concentrations up to 3 M NaCl.

The PEC phase diagram also helps to answer the question of why films maintain an equilibrium thickness when exposed to an infinite reservoir of solvent. Figure 6.8 indicates that at a given salt concentration WPECs can only be formed for a limited range of ratios of polycation to polyanion repeat units. Given that WPECs are expected to contain only one chain of the longer polyelectrolyte,[245] a sufficiently wide distribution of polyelectrolyte chain lengths is needed to allow formation of WPECs over a broad range of f^+ values. In addition, Figure 6.8 implies that formation of both negatively ($f^+ \approx 0$, region *L'*) and positively ($f^+ \approx 1$, region *L''*) charged WPECs should happen simultaneously, explaining how the overall ratio of polycation to polyanion repeat units in the PEM could remain constant, as is implied by the results presented in Figure 6.4.

It is proposed that the combination of broad polyelectrolyte molar mass distributions and the relatively high strength of PAH-PAA crosslinks leads to dissolution of (PAH/PAA) films over a broad range of relatively high NaCl concentrations. Alternatively, cases in which abrupt dissolution of other systems have been reported at low salt concentrations[237] could be due to the converse scenario; i.e., narrow polyelectrolyte molecular weight ranges and relatively weaker ionic crosslinks. When films were assembled with PAA possessing the same average molecular weight but a much smaller PDI, increased resistance to etching was observed. Etching of the film containing the low-PDI PAA proceeded in a qualitatively similar manner to the high-PDI PAA film, but with less film removal for all salt concentrations, possibly pointing to the inability of the system to form WPECs as readily due to the lack of availability of PAA chains much longer or shorter than the average length.

6.4.3 Kinetic Analysis of PEM Salt Etching

In order to further elucidate the process of salt etching, a model was developed to analyze in more detail the kinetic data presented in Figure 6.2. The basic line of argument follows treatments from previous researchers who studied the absorption and desorption of uncharged polymer species from solution.[246] A PEM is considered with time dependent thickness *h(t)* immersed in a salt solution containing sufficient ionic strength to mobilize the chains within the film. Let *c(t)* represent the average concentration of diffusing polymeric

material in a film with a surface of area A exposed to a solution of salt where the concentration of polymer is effectively zero. The thickness of the film, *h(t)*, decreases with time due to the diffusion of polyelectrolytes to the surface of the film, and their detachment as PECs. This loss of material from the film, expressed in terms of the flux of mols of polyelectrolyte repeat units away from the surface, can be represented by:

Equation 6.1

$$\frac{dc(t)}{dt} \cdot \frac{V(t)}{A} = \frac{dc(t)}{dt} \cdot h(t)$$

where $V(t) = A \cdot h(t)$ is the film volume. Because the surface of the PEM is expected to be rich in extrinsic charge (polyelectrolyte chains highly compensated by solution ions),[187] it is assumed that the loss of PECs from the film is diffusion-limited, i.e. the diffusion of polyelectrolytes to the film surface is the rate-limiting step of material loss. If this is true, then the flux from the surface can be expressed as:[246]

Equation 6.2

$$\frac{dc(t)}{dt} \cdot h(t) = -c(t) \cdot \sqrt{\frac{D}{\pi \cdot t}}$$

where D is the diffusion constant of the diffusing polyelectrolyte chain within the film. The concentration of the diffusing polyelectrolyte can be expressed in terms of the thickness of the film as:

Equation 6.3

$$c(t) = \frac{\rho \cdot A}{V(t)} \cdot \left(h(t) - h_\infty\right) = \rho \cdot \left(1 - \frac{h_\infty}{h(t)}\right)$$

where ρ is the molar density (assumed for simplicity to be constant throughout the film) and h_∞ is the equilibrium film thickness ($h(t) \rightarrow h_\infty$ as $t \rightarrow \infty$). Equation 6.2 can be rewritten using Equation 6.3 to yield:

Equation 6.4

$$\frac{dh(t)}{dt} = -\sqrt{\frac{D}{h_\infty^2 \pi \cdot t}} \cdot \left(h(t) - h_\infty\right).$$

Equation 6.4 can be solved by separation of variables to yield:

Equation 6.5

$$\frac{h(t) - h_\infty}{h_0 - h_\infty} = \frac{f(t) - f_\infty}{1 - f_\infty} = \exp\left[-\left(\frac{t}{\tau}\right)^\beta\right]; \quad \beta = \frac{1}{2} \qquad \tau = \frac{\pi \cdot h_\infty^2}{4 \cdot D}$$

where h_0 is the initial PEM film thickness, and $f(t) = h(t)/h_0$ is the fractional thickness change.

A major limitation of the theoretical treatment so far has been the assumption that D is a constant. According to the mechanism for PEM etching presented above, WPEC formation at the surface of the film would require polyelectrolytes of very different molecular weights, and thus a wide spectrum of time constants (τ) would presumably enter into the kinetic response of the film. Such problems have been previously considered for the so-called "stretched exponential function" in Equation 6.5, with the result that β in Equation 6.5 takes on a value less than ½.[246]

The precise values of β and τ can be found through linear regression of the data shown in Figure 6.2. If the data are assumed to follow the stretched exponential relationship of Equation 6.5, then by applying the natural logarithm twice to both sides of the equation one obtains:

Equation 6.6

$$\ln\left[-\ln\left(\frac{f(t) - f_\infty}{1 - f_\infty}\right)\right] = \beta \cdot \ln(t) - \beta \cdot \ln(\tau) \qquad \tau = \frac{\pi \cdot h_\infty^2}{4 \cdot D}$$

so that the data can be linearized by making the following change of variables:

Equation 6.7

$$X = \ln(t)$$
$$Y = \ln\left[-\ln\left(\frac{f(t) - f_\infty}{1 - f_\infty}\right)\right].$$

The plot of Y vs X for the data given in Figure 2.1 is shows a linear relationship for both films. These data are presented in Figure 6.9.

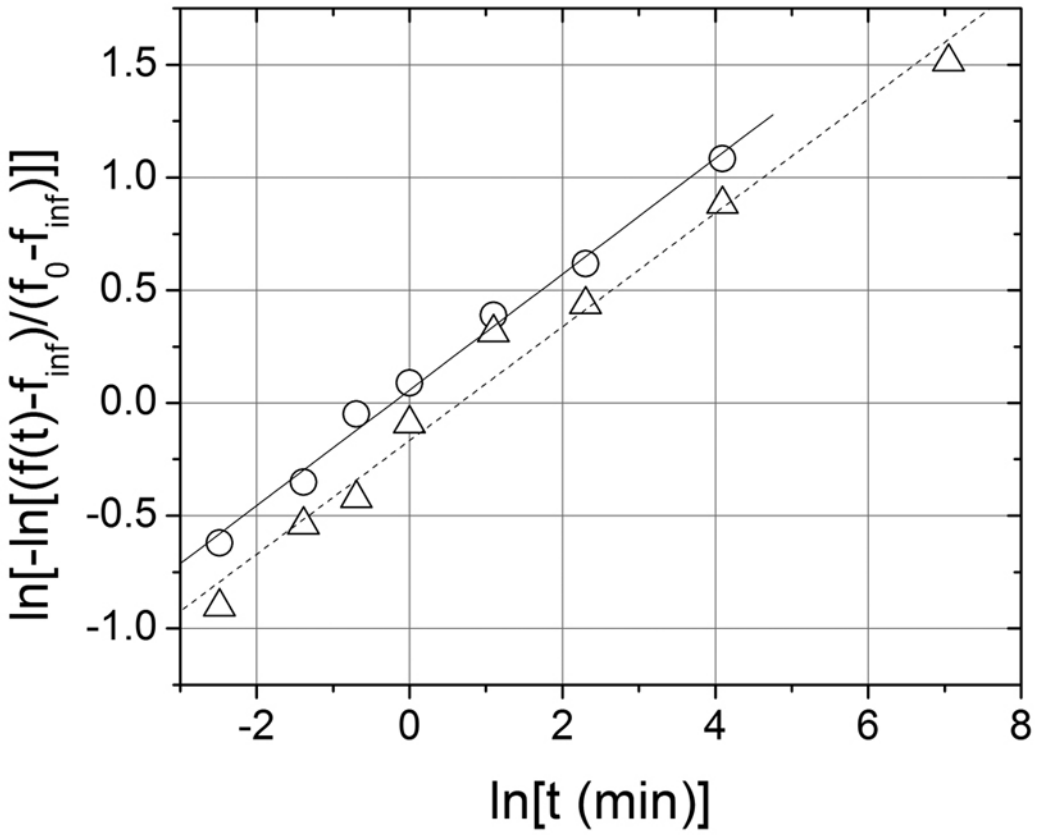

Figure 6.9. Kinetic data from Figure 6.2 replotted according the change of variables given in Equation 6.7. Data are shown for the films with 10.5 (circles, solid regression line) and 21.5 (triangles, dashed regression line) bilayers. *R*-squared values for the regression lines for the 10.5 and 21.5 bilayer films were 0.993 and 0.983, respectively.

The regression lines shown in Figure 6.9 allow calculation of β and τ from the relationships given in Equation 6.6. These values are displayed in Table 6.1.

Initial PEM Thickness (nm)	β	τ (min)	D (m^2/sec)
120	0.26	0.80	$1.4 \cdot 10^{-16}$
270	0.25	1.9	$2.9 \cdot 10^{-16}$

Table 6.1. Linear regression results from the data in Figure 6.9.

The values of β for both films were found to be $\approx$ 0.25. As mentioned previously, this deviation from the expected value of ½ points to a process taking place over a wide spectrum of time scales, which is expected since polyelectrolytes of different lengths are expected to possess different diffusion coefficients within the film.[187] Thus, the diffusion constants calculated using Equation 6.6 and given in Table 6.1 are not true diffusion constants, but rather a type of average over all the mobile chains in the PEM contributing to the dissolution phenomena. Still, these calculations are expected to give a reasonable estimate for the diffusivity of the average polyelectrolyte chain throughout a (PAH7.5/PAA3.5) film at 4 M NaCl. A value on the order of 10^{-16} m^2/sec seems reasonable based on previously reported literature values. Jomaa et al., for example, estimated a diffusion coefficient on the order of 10^{-17} m^2/sec for multilayers assembled from poly(diallyldimethylammonium chloride) (PDAC) and PSS when annealed in 0.8 M NaCl solution.[187] The time constant, τ, is expected to increase with film thickness (see Equation 6.6), with the result that thicker films take longer to equilibrate. This is indeed reflected in the data, with values of τ calculated by regression to be 0.80 and 1.9 min for the 120 nm and 270 nm thick films, respectively.

6.4.4 Applications for PEM Salt Etching*

Preliminary work was been conducted to demonstrate how the etching technique described in this chapter can employed in a lithographic methodology to create, from an initial PEM of uniform thickness, a patterned film with spatially distributed areas of different height. A multiple color reflector was fabricated by masking the areas of a (PAH7.5/PAA3.5) film deposited on a silicon substrate with adhesive numerals. The "1", "2", and "3" were applied before subjecting the film to a short (3 min) immersion in a solution of 5.5 M NaCl, followed by rinsing with water and drying. The "1" mask was removed, and the substrate was treated

* Nobuaki Takane is credited for his work on obtaining the results and photographs presented in this section.

in 5 M NaCl solution, after which the "2" mask was removed. The substrate was then treated in 4 M NaCl solution, before removing the "3" mask to uncover a region of untreated film. The completed reflector is shown in Figure 6.10.

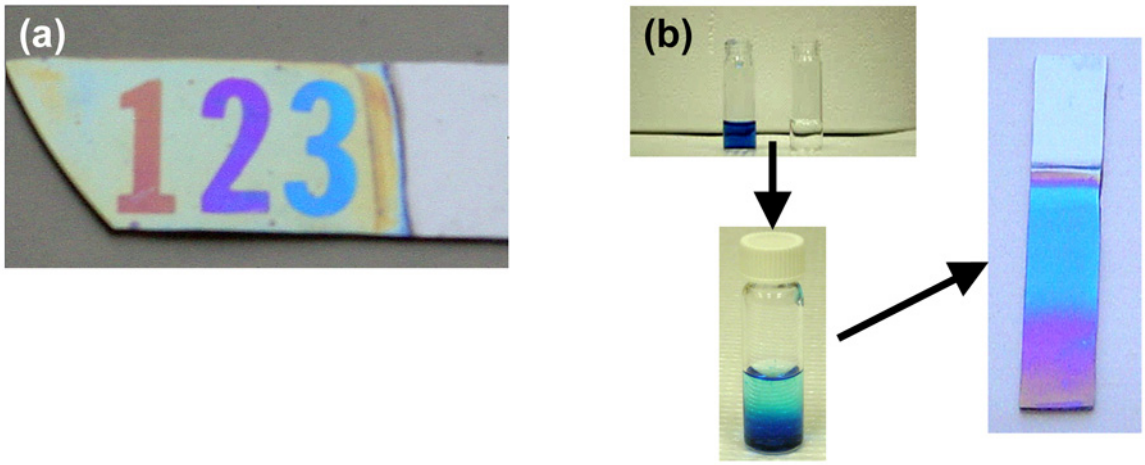

Figure 6.10. Application of salt etching to create patterned areas in a (PAH7.5/PAA3.5) film that has been deposited on silicon. (a) Masking combined with immersion into etching baths of decreasing concentration can create regions with discrete thickness increments. (b) Films with gradients in surface thickness can be created by employing a gradient density salt column.

Because of the different film heights in the four regions in Figure 6.10a, different interference colors are observed. PEM films can also be created with spatial gradients in the film thickness. By carefully combining a denser, concentrated NaCl solution (shown in Figure 6.10b on the left, colored with methylene blue for clarity) with a solution of pure water (shown on the right) a gradient density salt column can be created, which has an increasing NaCl concentration from the liquid surface to the bottom of the vessel. Etching a film in such a column will produce a film possessing a spatial gradient in film thickness as shown in the rightmost image in Figure 6.10b.

6.5 Conclusions

In conclusion, this chapter has discussed the etching of PEMs containing PAH and PAA in solutions of NaCl. Because it equilibrates at fractional changes in thickness over a broad range of salt concentrations, this system is ideal for studying the mechanism of PEM decomposition in salt solutions. Relative changes in film thickness were observed that

stabilized to a particular value that was dependent upon the NaCl concentration. Previous explanations for such a phenomenon that have invoked arguments about chain mobility[188] or secondary bonding restrictions[233] cannot be applied to these systems. Instead, a mechanism is suggested whereby film reorganization leads to the release of water-soluble polyelectrolyte complexes (WPECs), causing a reduction in film thickness. The equilibrium thickness loss at a particular salt concentration is controlled by the PEC phase diagram (see Figure 6.8), which only allows for the formation of WPECs within a specified range of chain length ratios; increasing the salt concentration in turn widens the composition range for WPEC formation, and thus results in further film dissolution. Kinetic data support the argument that etching involves the diffusion of polyelectrolyte species throughout the film (film rearrangement). In addition, the data presented in Figure 6.7 support the notion that the molar mass distributions of the polyelectrolyte species are instrumental in controlling the equilibrium thickness reached by the film.

Although various innovative techniques have been advanced for creating well-defined planar patterns of PEMs on surfaces, thus far no satisfying solutions for reliably and controllably reducing the thickness of PEM films has been proposed. Two very simple possibilities for spatially patterning the film thickness of PEMs using the salt etching technique have been demonstrated in Section 6.4.4. In addition to advancing the understanding of the internal dynamics and stability of PEM films, the results presented in this chapter may provide useful ideas for ways in which polyelectrolyte multilayers can be used in more advanced lithographic schemes, and thus expand the technological importance of PEMs into an important and rapidly growing area of materials research.

Chapter 7
Conclusions and Directions for Future Research

7.1 Thesis Summary

This thesis has presented the results of fundamental studies concerning the optical, mechanical, and lithographic etching behavior of polyelectrolyte multilayer films. The following is a brief summary of the research that has been presented in this thesis, along with suggestions for future work on these topics.

Chapter 1 presented information about the PEM assembly technique and provided background information necessary for understanding the broader scientific concepts that were addressed as part of this thesis research.

Chapter 2 introduced the basic operational principles of optical interference filters before describing the creation of rugate interference filters using the PEM-templated growth of silver nanoparticles. Rugate filters possess a periodic, continuous change in refractive index. This research demonstrated that PEMs could be formed from multilayers of (PAH/PAA) and (PAH/PSS) so that the silver-binding (PAH/PAA) regions can template subsequent silver nanoparticle growth in well-defined regions of precisely controlled thickness. Because these regions are much smaller than the wavelength of light, light "sees" an effectively continuous variation in refractive index, and characteristic rugate features, such as the suppression of reflection sidebands, are observed.

Chapter 3 introduced mechanical property measurements of PEM films. A strain-induced elastic buckling instability method was employed to measure the Young's modulus of the (PAH3.0/PSS3.0) system, and its modulus was shown to be constant with film thickness for films assembled past a certain film thickness. Measurements were also performed in aqueous solutions, demonstrating that water acts as a plasticizing agent for (PAH3.0/PSS3.0) multilayers, and that adding NaCl can increase the effectiveness of the water in this regard.

Chapter 4 extended the work of Chapter 3, introducing a two-plate buckling methodology developed to allow for mechanical measurements on a wide variety of PEM systems. By depositing a PS film on the substrate prior to PEM assembly, two-plate composite films were created. The mechanical properties of the PEM were then de-convoluted from the buckling wavelength of the two-plate composite film using a mechanics-based mathematical analysis.

Chapter 5 introduced a technique for obtaining mechanical property and thickness measurements of PEMs under controlled relative humidity conditions. The Young's modulus and film thickness of three PEM systems were measured as a function of humidity, and the data revealed important information about internal structure and bonding interactions within each multilayer system.

Chapter 6 examined the ability of certain (PAH/PAA) multilayer systems to undergo controlled dissolution (etching) over a range of solution salt concentrations. A mechanism to explain these data was proposed from consideration of the polyelectrolyte complex phase diagram. This mechanism provides a broad framework for understanding not only our results, but also the findings of other researchers investigating related phenomena. In addition, these results suggest ways in which PEM etching could be further controlled, leading to possible applications for lithographic removal of LbL films.

7.2 Suggestions for Future Research

7.2.1 Complex Property Gradients

Chapter 2 introduced the idea of constructing PEMs with complex refractive index gradients through the incorporation of silver nanoparticles. PEM nanoparticle composites, however, are expected to possess enhanced mechanical properties when compared with their unmodified forms.[27, 29, 31] In addition, because gradients in modulus are known to lead to advantageous effects such as reduced contact damage at interfaces,[4] it is possible that the rugate design methodology could be useful for designing Young's modulus gradients in PEM films. Such films may then provide, for example, increased resistance to fracture or scratch protection for underlying objects.

7.2.2 Young's Modulus Measurements of PEMs

The PEM buckling instabilities presented in Chapter 3, Chapter 4, and Chapter 5 present many possibilities for future work. Because of the large number of polyelectrolytes that exist, as well as the countless number of ways in which these can be assembled in pairs at various solution conditions to produce PEM films, years of research could be dedicated simply to cataloguing the mechanical properties of various PEM assemblies. Brute force studies such as this are seldom the most fruitful endeavors in science, however, unless there is order to the plan being considered. One possible approach would be to examine the properties of PEM films constructed from two polyelectrolytes, such as PAH and PAA, under various assembly conditions. In this way, one could create a "matrix" diagram of mechanical properties, much like those that have already been produced for thickness increments in this system.[38]

An additional area for study is the time dependence of Young's modulus and thickness changes in PEM films as a result of sudden changes in humidity. Although some researchers have examined the time dependence of PEM swelling for films immersed in water,[247, 248] no studies of this type are known for PEM swelling at different humidity values. As was demonstrated in Chapter 5, measuring the film Young's modulus concurrent with measurements of the film's thickness can provide additional information that can be used to elucidate swelling processes in PEMs. Time dependent measurements are difficult to obtain using the experimental setup that is pictured in Figure 5.1, as transferring the film outside of the box to an ellipsometer consumes too much time. Instead, it is suggested that a way of measuring the film thickness be incorporated directly into the humidity control chamber itself.

Immediate future work will focus on testing the hypotheses presented in Section 5.4.2 concerning the origin of the unique swelling characteristics of the (PAH2.5/PAA2.5) system. In particular, IR spectroscopy will be performed on films exposed to different humidity levels in an effort to view ionization of the carboxylic acid groups and/or the dissociation of hydrogen bonding interactions in the film. Such measurements should provide direct proof

of the notion that secondary bonding interactions are responsible for the sharp transition in film thickness with increasing humidity.

In addition to study of the mechanism governing film swelling, the swelling transition in (PAH2.5/PAA2.5) multilayers could be considered for possible use as a humidity sensor.[249, 250] Such transitions could be particularly useful if, for example, they could be tuned through film treatment or assembly pH to occur at specific humidity values, providing a visual or other indication that a trigger humidity level has been reached.

7.2.3 A Method for Measuring Low Young's Modulus Values

Another possible avenue for study would be investigating implementation of the buckling technique for films with low Young's modulus values. As discussed in Chapter 5, certain PEM systems show no evidence of buckling upon compression in high humidity or solution environments, e.g. (PAH7.5/PAA3.5) and (PAH2.5/PAA2.5) multilayers. Other systems, such as (PAH3.0/PSS3.0) exhibit buckling values both in solution (see Figure 3.7) and also, predictably, at high humidity conditions (see Figure 5.4).

The absence of buckling in certain multilayer systems is due to the lack of modulus mismatch between the film and the PDMS. For low enough values of the PEM Young's modulus, the film essentially begins behaving as an extension of the substrate, and all buckling disappears. This phenomenon could be exploited to measure the Young's modulus of the compliant PEM by treating it as the substrate through construction of a much thinner, stiffer PEM region on its surface—multilayers of (PAH/PSS), for example. In this case, the PDMS would not be deformed out of the plane—it would simply act as a substrate for transferring a strain in the plane of the film to the compliant PEM. A schematic of this experimental design is displayed in Figure 7.1.

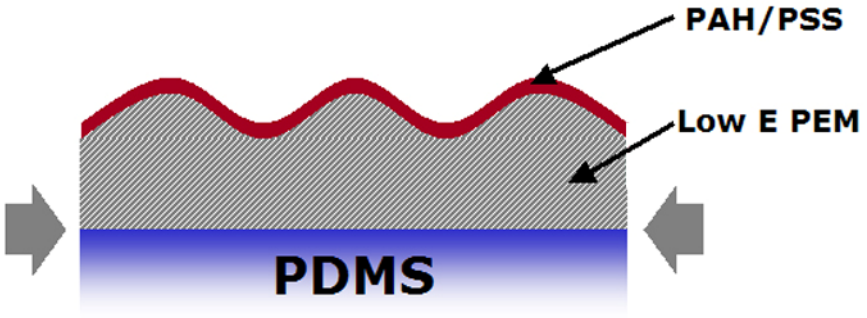

Figure 7.1. One possible approach to buckling-based Young's modulus measurements on low modulus PEM films. The more compliant PEM system is grown as the underlayer in a heterostructured film, and capped with a thin region of the stiffer (PAH/PSS) system. If the low modulus PEM region is thick enough, the buckling (PAH/PSS) will sample the "substrate" of low modulus PEM, and the buckling equation can be reversed (see Equation 7.1) to yield the Young's modulus for the low modulus PEM region.

In Figure 7.1, a thin region of (PAH/PSS) multilayers grown on top of a thicker, more compliant PEM system is shown buckling under applied strain. In this case, knowing the modulus of the (PAH/PSS) system, Equation 4.1 can be inverted to solve for the substrate modulus (here the compliant PEM) to yield:[251, 252]

Equation 7.1

$$E_{PEM} = \frac{E_{PAH/PSS}}{3} \cdot \left(\frac{2\pi d_{PAH/PSS}}{\lambda} \right)^3$$

where here the Poisson's ratios of both multilayer systems have been assumed to be equal and thus cancel from the equation. Equation 7.1 will hold true only if the stress field from the buckling (PAH/PSS) film is suitably confined to the low modulus film and not sampling the PDMS substrate. It has been shown before that the stress field due to a buckling film decays as:[251, 252]

Equation 7.2

$$\sigma(z) \sim \exp\left[-\frac{2\pi}{\lambda} z \right]$$

where z is the distance from the interface of the buckling film into the substrate. If it is deemed satisfactory for the stress field to have decayed to 10%, say, of its maximum value within the PEM, then Equation 7.2 can be combined with Equation 7.1 to yield the following necessary condition:

Equation 7.3

$$\frac{d_{PEM}}{d_{PAH/PSS}} \approx 1.60 \cdot \left(\frac{E_{PEM}}{E_{PAH/PSS}} \right)^{-1/3}.$$

A graph of Equation 7.3 is shown in Figure 7.2. Equation 7.3 stipulates that to meet the 10% requirement mentioned above for confinement of the stress distribution within the PEM region (and hence accurate sampling of the PEM Young's modulus) that the ratio of thicknesses of the compliant PEM and (PAH/PSS) regions must lie on or above the line shown in Figure 7.2.

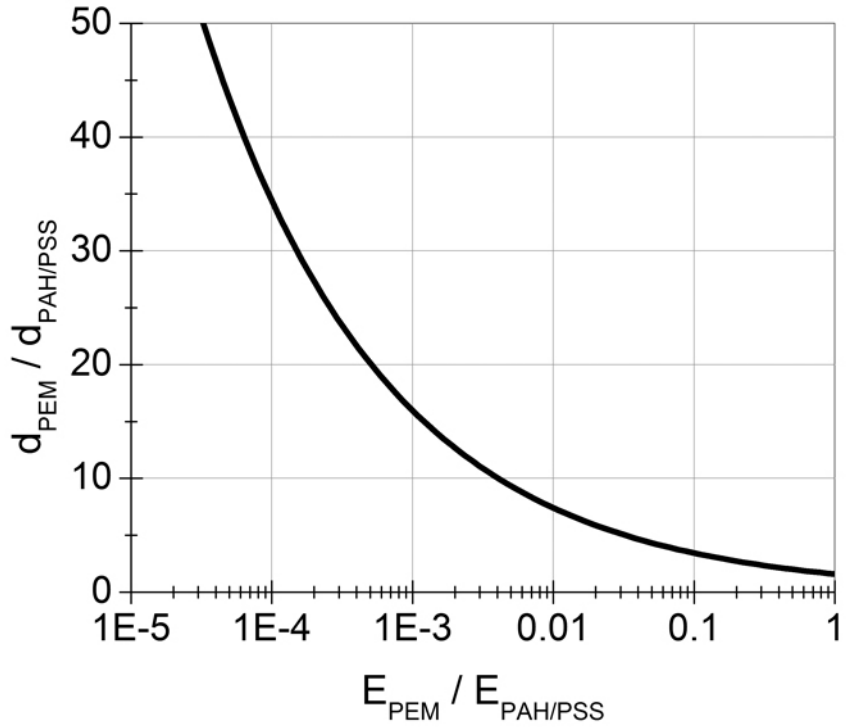

Figure 7.2. Graph of the ratio of thicknesses of the compliant PEM region to the (PAH/PSS) region vs the ratio of the Young's moduli (see Figure 7.1). The ratio of film thicknesses must lie on or above the graphed line for the stress distribution to decay of 10% of its original value within the compliant PEM region.

7.2.4 Buckling as an Erasable Template for Ordering Materials

The buckling instability method could be used for a number of applications outside of performing Young's modulus measurements on thin films. A unique feature of this technique is its ability to create ordered surface patterns that are "erasable" simply by releasing the strain on the substrate. A possible application could be the ordering of colloids on buckled surfaces. Previous research has shown that even very slight corrugations in substrate topology can lead to self-assembly of colloids in the surface depressions.[253] Self-assembly of colloidal particles in the "valleys" of buckles, followed by release of the strain on the substrate, would lead to patterned colloidal surfaces with no trace of the corrugation that templated the colloidal order.

7.2.5 PEM Salt Etching

Future work concerning the salt etching of PEMs is suggested to improve the technique and further demonstrate its practicality. In Chapter 6, evidence was presented that the molar mass distribution of polyelectrolyte chain lengths is at least partly responsible for the broad dissolution profile in (PAH7.5/PAA3.5) multilayer systems. Changing the PAH molar mass distribution may permit an even wider range of accessible etch thicknesses within the solubility limits of sodium chloride. In addition, it has been shown that divalent salts lead to increased film etching a lower solution concentration.[254] Further investigation of the effect of the salt ion type on film dissolution could also lead to greater control over the etching process.

In addition to pursuing better z-directional control of the etching process, future research should also focus on determining the lateral resolution of the technique. The numerals shown in Figure 6.10a are on the order of centimeters in dimension. Pushing the feature size smaller and examining the inherent limits of PEM salt etching in this regard will be important in evaluating the feasibility of this technique for actual applications.

Overall, the results of this thesis research have underscored the importance of being able to measure and control chemical and bonding interactions within PEM films. It is hoped that the detailed study of the particular topics presented herein will lead to a better understanding of how PEMs can be assembled, disassembled, and react to changes in their environment. Such knowledge will be central to advancing PEM-based technologies as real solutions to some of the many needs and challenges arising in the field of thin film and interface science.

Appendix A
Calculating the Optical Response of Thin Films

This appendix contains further information concerning the simulation of the optical properties of thin film interference filters. Section A.1 presents an overview of the matrix method. Section A.2 discusses methods for simulating the optical response of filters containing a continuous gradient in refractive index. This section includes a derivation of the Riccati equation that describes the behavior of the reflection coefficient for light traversing a continuous index profile. Finally, Section A.3 is a user's manual for the MATLAB®-based *Photonic Calculator* program. *Photonic Calculator* was developed as part of this thesis research to calculate the theoretical spectral properties of user-defined thin film interference filters.

A.1 The Matrix Method

The "matrix method" refers to a methodology for calculating the reflectance and transmittance of optical interference filters (OIF) using matrix algebra. OIFs are composed of stacks of thin regions of differing thickness and refractive index, surrounded by an incident medium on one side and a substrate medium on the other (in the case of free-standing films, the incident medium and the substrate medium have the same optical properties). The propagation of light, or, more generally, electromagnetic radiation (EM) in an OIF can be understood by examining the relevant physics over one layer in the system, as depicted in Figure A.1.

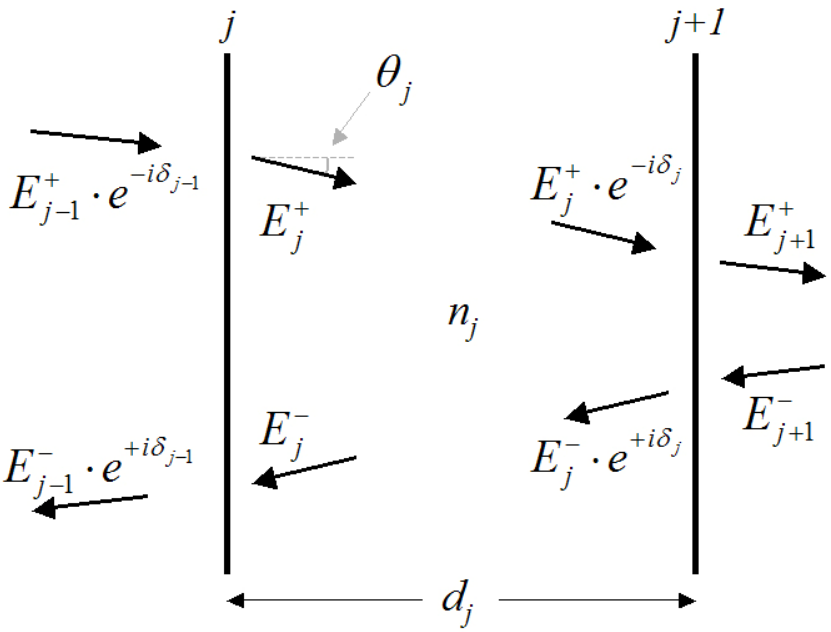

Figure A.1. Schematic diagram of electromagnetic radiation propagation in one region of an optical interference filter.

In Figure A.1, one region in an OIF, labeled "*j*", is shown. The refractive index and physical thickness of this region are denoted n_j and d_j, respectively. In an OIF containing *J* distinguishable regions, there are *J+1* interfaces in the structure. The incident medium is labeled with a subscript of "0", and the substrate medium with an index of "*J+1*". Inside region *j*, EM radiation undergoes a shift in phase of $i \cdot \delta_j$ in traversing the region:[10, 255]

Equation A.1

$$\delta_j = \frac{2\pi \cdot n_j \cdot d_j \cdot \cos\theta_j}{\lambda}$$

where λ is the wavelength of the incident radiation, and θ_j is the angle of propagation in layer *j*, which by Snell's Law is given by:[255]

Equation A.2

$$n_0 \cdot \sin\theta_0 = n_j \cdot \sin\theta_j$$

where, by the notation introduced above, n_0 and θ_0 are the refractive index and angle of incidence in the incident medium, which is usually air ($n_0 = 1$).

Two different matrix formalisms can be developed from the considerations above. The first considers the total electric (E) and magnetic (H) field magnitudes at each particular interface. E and H are given by:[255]

Equation A.3

$$\begin{aligned} E_{j,TE} &= E_j^+ + E_j^- \\ H_{j,TE} &= \eta_{j,TE} \cdot \left(E_j^+ - E_j^-\right) \\ E_{j,TM} &= \left(E_j^+ - E_j^-\right) \cdot \cos\left(\theta_j\right) \\ H_{j,TM} &= \eta_{j,TM} \cdot \left(E_j^+ + E_j^-\right) \cdot \cos\left(\theta_j\right) \end{aligned}$$

where the particular form of η_j, the optical admittance, depends upon the polarization:

Equation A.4

$$\begin{aligned} \eta_{j,TE} &= \sqrt{\frac{\varepsilon_0}{\mu_0}} \cdot n_j \cdot \cos\theta_j \quad \left(for\ TE\ (s)\ polarized\ radiation\right) \\ \eta_{j,TM} &= \sqrt{\frac{\varepsilon_0}{\mu_0}} \cdot n_j \Big/ \cos\theta_j \quad \left(for\ TM\ (p)\ polarized\ radiation\right) \end{aligned}$$

It should be clear from Equation A.4 that for normal incidence (where polarization is meaningless for filters with isotropic planar properties) $\eta_s = \eta_p$. The terms ε_0 and μ_0 are known as the permittivity and permeability of a vacuum, respectively, and are given by:

Equation A.5

$$\begin{aligned} \mu_0 &= 4\pi \cdot 10^{-7}\ \frac{H}{m} \\ \varepsilon_0 &= \frac{1}{c^2 \cdot \mu_0} \approx 8.85 \cdot 10^{-12}\ \frac{F}{m} \end{aligned}$$

where c is the speed of light in a vacuum ($\approx 3.00 \cdot 10^8$ m/sec).

The above equations yield the following matrix equation that relates the electric and magnetic fields at interfaces j and $j+1$ in terms of the properties of region j:[10, 255]

Equation A.6

$$\begin{bmatrix} E_j \\ H_j \end{bmatrix} = \begin{bmatrix} \cos\delta_j & \dfrac{i \cdot \sin\delta_j}{\eta_j} \\ i \cdot \eta_j \cdot \sin\delta_j & \cos\delta_j \end{bmatrix} \begin{bmatrix} E_{j+1} \\ H_{j+1} \end{bmatrix} = M_j \begin{bmatrix} E_{j+1} \\ H_{j+1} \end{bmatrix}$$

where M_j is known as the *characteristic matrix* of region j. A total transfer matrix (M_T), or characteristic matrix for the entire filter, can be obtained by multiplying the characteristic matrices for the individual regions:

Equation A.7

$$M_T = M_1 \cdot M_2 \cdots M_J = \prod_{j=1}^{J} M_j = \begin{bmatrix} m_{11} & m_{12} \\ m_{21} & m_{22} \end{bmatrix}.$$

$$\begin{bmatrix} E_0 \\ H_0 \end{bmatrix} = M_T \begin{bmatrix} E_{J+1} \\ H_{J+1} \end{bmatrix}$$

The amplitude reflection (r) and transmission (t) coefficients can be found from M_T as follows:[255]

Equation A.8

$$r_{TE} = \frac{E_0^-}{E_0^+} = \frac{\eta_{0,TE} m_{11} + \eta_{0,TE}\eta_{J+1,TE} m_{12} - m_{21} - \eta_{J+1,TE} m_{22}}{\eta_{0,TE} m_{11} + \eta_{0,TE}\eta_{J+1,TE} m_{12} + m_{21} + \eta_{J+1,TE} m_{22}}$$

$$t_{TE} = \frac{E_{J+1}^+}{E_0^+} = \frac{2\eta_{0,TE}}{\eta_{0,TE} m_{11} + \eta_{0,TE}\eta_{J+1,TE} m_{12} + m_{21} + \eta_{J+1,TE} m_{22}}$$

$$r_{TM} = -\frac{\eta_{0,TM} m_{11} + \eta_{0,TM}\eta_{J+1,TM} m_{12} - m_{21} - \eta_{J+1,TM} m_{22}}{\eta_{0,TM} m_{11} + \eta_{0,TM}\eta_{J+1,TM} m_{12} + m_{21} + \eta_{J+1,TM} m_{22}}$$

$$t_{TM} = \frac{2\eta_{0,TM}}{\eta_{0,TM} m_{11} + \eta_{0,TM}\eta_{J+1,TM} m_{12} + m_{21} + \eta_{J+1,TM} m_{22}} \cdot \frac{\cos(\theta_0)}{\cos(\theta_s)}$$

from which the reflectance (R) and transmittance (T), which are the actual fractions of reflected and transmitted radiation intensity, respectively, can be calculated:

Equation A.9

$$R = r \cdot r^*$$

$$T = t \cdot t^* \cdot \frac{\Re(n_s) \cdot \cos[\Re(\theta_s)]}{\Re(n_0) \cdot \cos[\Re(\theta_0)]}.$$

$$A = 1 - R - T$$

A is the absorptance—the fraction of the incident power that is absorbed by the structure and not reflected or transmitted. The equations in this section can be implemented, as in the *Photonic Calculator* program (see Section A.3), to solve for R, T, and A in any specified OIF.

A.2 Calculating the Optical Response of Continuous Index Profiles: Derivation of the Riccati Equation

Section A.1 described the method for calculating the optical response (reflectance, transmittance, and absorptance) of OIFs with piecewise constant refractive index profiles. As depicted in Figure A.1, the refractive index in such filters is constant over some finite distance before changing sharply at an interface to a different value. The refractive index of continuous-index optical filters, in comparison, varies smoothly and can be simulated by a couple of different methods. The more conceptually straightforward approach involves

approximating the continuous index profile with a piecewise-constant function, such as that given for the smoothly varying quintic function in Figure 2.4b. A more direct way of solving the problem exists, however, and it involves finding and solving an initial value differential equation for the continuous reflection coefficient function, *r(x)*. The derivation of this non-linear equation, which is denoted the *Riccati Equation*, is given in this section. The derivation of the Riccati Equation is difficult to find in the literature; the reader is directed to the treatment of waves in inhomogeneous media by Chew for more information.[256] For the purpose of simplifying the equations, the Ricatti equation will be derived here for the case of normal incidence. The equation could be generalized to all angles of incidence in an analogous fashion by using the appropriate forms of Equation A.3 and Equation A.4.

Consider the interference filter depicted in Figure A.1. By utilizing the fact that the total electric and magnetic fields remain constant in traversing an interface, the following relationship can be derived from considering the fields at interface *j+1*:

Equation A.10

$$E_{j+1}^{+} + E_{j+1}^{-} = E_j^{+} e^{-i\delta_j} + E_j^{-} e^{+i\delta_j}$$
$$\left(E_{j+1}^{+} - E_{j+1}^{-}\right) = \frac{n_j}{n_{j+1}} \left(E_j^{+} e^{-i\delta_j} - E_j^{-} e^{+i\delta_j}\right).$$

Equation A.10 can be solved to yield the following matrix equation:

Equation A.11

$$\begin{bmatrix} E_{j+1}^{+} \\ E_{j+1}^{-} \end{bmatrix} = \begin{bmatrix} \frac{1}{2}\left(1 + \frac{n_j}{n_{j+1}}\right) e^{-i\delta_j} & \frac{1}{2}\left(1 - \frac{n_j}{n_{j+1}}\right) e^{+i\delta_j} \\ \frac{1}{2}\left(1 - \frac{n_j}{n_{j+1}}\right) e^{-i\delta_j} & \frac{1}{2}\left(1 + \frac{n_j}{n_{j+1}}\right) e^{+i\delta_j} \end{bmatrix} \begin{bmatrix} E_j^{+} \\ E_j^{-} \end{bmatrix}.$$

Equation A.11 relates the forward and backwards propagating waves just to the right of interface *j+1* to those just to the right of interface *j*, and can be used as the starting point for solving the continuous index problem.

Consider a continuous index profile *n(x)*, where the positive direction of *x* denotes the direction from the incident interface into the film and towards the substrate. A good approximation to *n(x)* can be constructed by discretizing the index profile into many thin regions, each with a thickness of $d_j = \Delta x$. As each region shrinks in size, the following identities will hold (neglecting 2nd-order and higher differential terms):

Equation A.12

$$\lim_{\Delta x \to dx} \frac{1}{2}\left(1 + \frac{n}{n + \Delta n}\right) \to 1 - \frac{1}{2}\frac{dn(x)}{n(x)}$$
$$\lim_{\Delta x \to dx} \frac{1}{2}\left(1 - \frac{n}{n + \Delta n}\right) \to \frac{1}{2}\frac{dn(x)}{n(x)}$$
$$\lim_{\Delta x \to dx} e^{\pm i\delta} \to 1 \pm ik(x)dx; \quad k(x) = \frac{2\pi}{\lambda} n(x)$$

Using Equation A.12,the matrix equation in Equation A.11 can be rewritten as:

Equation A.13

$$\begin{bmatrix} E^+(x) + dE^+(x) \\ E^-(x) + dE^-(x) \end{bmatrix} = \begin{bmatrix} \left(1 - \frac{1}{2}\frac{dn}{n(x)}\right)\cdot(1 - ik(x)dx) & \left(\frac{1}{2}\frac{dn}{n(x)}\right)\cdot(1 + ik(x)dx) \\ \left(\frac{1}{2}\frac{dn}{n(x)}\right)\cdot(1 - ik(x)dx) & \left(1 - \frac{1}{2}\frac{dn}{n(x)}\right)\cdot(1 + ik(x)dx) \end{bmatrix} \begin{bmatrix} E^+(x) \\ E^-(x) \end{bmatrix}.$$

Writing out the above equations and discarding all 2nd-order differential terms yields:

Equation A.14

$$E^+(x) + dE^+(x) = E^+(x)\cdot\left(1 - \frac{1}{2}\frac{dn(x)}{n(x)} - ik(x)dx\right) + E^-(x)\cdot\frac{1}{2}\frac{dn(x)}{n(x)}$$
$$E^-(x) + dE^-(x) = E^+(x)\cdot\frac{1}{2}\frac{dn(x)}{n(x)} + E^-(x)\cdot\left(1 - \frac{1}{2}\frac{dn(x)}{n(x)} + ik(x)dx\right)$$

By dividing Equation A.14 by $E^+(x)$ and defining the reflection coefficient function as:

Equation A.15

$$r(x) = \frac{E^{-}(x)}{E^{+}(x)}; \quad \frac{dr(x)}{r(x)} = \frac{dE^{-}(x)}{E^{-}(x)} - \frac{dE^{+}(x)}{E^{+}(x)}$$

the following differential equation can be obtained:

Equation A.16

$$\frac{dr(x)}{dx} = \frac{1}{2}\frac{dn(x)}{n(x)}\left(1 - r(x)^2\right) + \frac{4\pi i}{\lambda} n(x) \cdot r(x).$$

Equation A.16 is known as the Riccati equation due to its particular functional form.[257] This non-linear differential equation can be solved using a computer with an initial-value differential equation solver given the initial condition that $r(x) = 0$ inside the (semi-infinite) substrate.

A.3 A User's Manual for the *Photonic Calculator* Program

This section serves as a users manual for the *Photonic Calculator* program, which is a MATLAB® function that was developed as part of this thesis work to solve for the reflectance (`R`), transmittance (`T`), and absorptance (`A`) of optical interference filters. The function is implemented from the MATLAB® command line by typing:

```
[R,T,A] = photonic_calc60(theta0,P,lambda,d,n,n0,ns,Rplot,Tplot,
Aplot,plot_choice,substrate_account,xlimits,ylimits);
```

The following subsections will describe the various input and output parameters involved with running the program to calculate the spectral response of an optical interference filter.

A.3.1 Incidence Angle: theta0

The angle of incidence, `theta0`, is the angle at which the incident light is impinging upon the interference filter, measured from the normal to the plane of the interference filter. It is entered in degrees (°) and can take any value between 0 and 90. For light at normal incidence use `theta0=0`.

A.3.2 Polarization: P

The polarization, `P`, denotes the degree of polarization of the incident light, expressed as a number between 0 and 1, where "0" represents completely TE-polarized light, and "1" represents completely TM-polarized light. A number in between these two values provides a weighted calculation. For natural, unpolarized light, use `P=0.5`. *Photonic Calculator* assumes that the optical properties of the interference filter are isotropic in the plane, so all values of `P` such that `0≤P≤1` generate the same results at normal incidence.

A.3.3 Wavelength Range: lambda

Photonic Calculator calculates `R`, `T`, and `A` at each wavelength value that is specified in `lambda`, which is a column vector (1-column matrix). Wavelengths should be given in nanometers (nm). Column vectors are specified by placing a tick (`'`) just following the brackets (`[]`) that denote a vector in MATLAB®. Including more wavelength values in `lambda` generates smoother graphs of the optical response, but requires more time. The following are two examples of how `lambda` can be created via the MATLAB® command line:

- `lambda=[300:700]';` This command generates a column vector containing the wavelength values 300, 301, 302 ... 700 nm). This works well for the visible range.
- `lambda=[300:10:2000]';` This command generates a column vector containing the wavelength values 300, 310, 320, ...2000 nm. Because of the larger range of wavelengths, the program runs faster by calculating `R`, `T`, and `A` only every 10 nm.

A.3.4 The Structure Matrix: d

The structure matrix, `d`, physically defines the structure of the interference filter (i.e. where and how thick the various regions of different refractive index are located). The structure matrix has two columns. The first column contains the thicknesses (measured in nm) of each separate refractive index region in the interference filter. The second column contains a positive integer that corresponds to the column of the refractive index matrix (`n`) that contains the wavelength-dependent refractive index data for that particular region (see below). The rows in `d` should appear in the same order in `d` that they appear in the interference filter. The

first row in `d` corresponds to the region next to the incident interface, and the last row to the region nearest the substrate.

A.3.5 The Refractive Index Matrix: n

The refractive index matrix, `n`, contains the wavelength-dependent refractive index information for all different material types that appear in the interference filter. Each column in `n` contains the refractive index data for a particular material type, so `n` must have at least as many columns as the highest value integer found in the second column of the structure matrix (see above). The individual rows of `n` correspond to the wavelength values provided in `lambda`, so the number of rows in `n` should be equal to the number of rows in `lambda`.

Oftentimes, it is assumed that the refractive index does not change significantly with wavelength. In the case where the user wishes to assume that all refractive index values in `n` remain constant with wavelength, `n` can be entered as a one-row vector of refractive index information.

Photonic Calculator supports complex refractive indices in its calculations. These should appear in the form $n - ik$.

A.3.6 The Incident and Substrate Mediums: n0, ns

The refractive indices of the incident and substrate mediums are given in `n0` and `ns`, respectively. Each of these input variables can appear either as a scalar (real or complex) or as a column-vector with the wavelength-dependent refractive index values of these terms. If column-vectors are used, they should have the same number of rows as `lambda`.

A.3.7 The Plot Switches: RPlot, TPlot, APlot

The plot switches `RPlot`, `TPlot`, and `APlot` control whether or not the program, upon completion, should plot in MATLAB® the % reflectance, % transmittance, and % absorptance, respectively. Each of these input variables can take the value of either "0" or "1", where "0" turns plotting off, and "1" turns plotting on.

A.3.8 The Plot Choice: plot_choice

Entering a value of "1" for `plot_choice` specifies that the reflectance, transmittance, and absorptance will be plotted vs wavelength. This is the typical choice. Entering a value of "0" plots vs angular frequency (given wavelength values are converted to angular frequencies). This is sometimes useful for seeing symmetry in the optical response of filters.

A.3.9 Accounting for Substrate Influences: substrate_account

The input variable `substrate_account` specifies how the program should treat the presence of the substrate during calculations. A value of "0" assumes a semi-infinite substrate; thus no back-reflections are accounted for. By entering a value of "1", the program takes into account reflections off of the uncoated back of a substrate. A value of "2" assumes that both sides of the substrate are coated with the same optical interference filter structure, and that there is a mirror symmetry plane running down the middle of the substrate, parallel to the interference filter plane. This setting is particularly useful for calculating the optical response of PEM-coated substrates.

When a complex refractive index is specified for the substrate (the substrate is absorbing), the substrate thickness becomes an important parameter. Because it is not commonly changed, its default value is set to 1.09 mm (the thickness of a standard glass slide). Changes to the substrate thickness must be done by editing the program code.

A.3.10 Graph Limits: xlimits, ylimits

The input variables `xlimits` and `ylimits` are each two-element row vectors that specify the lowest and highest values of the abscissa and ordinate, respectively. These limits allow the user to manually set the limits of the plot range on the x-axis (wavelength or angular frequency) and the y-axis (reflectance, transmittance, or absorptance). For example, if one had calculated the optical response of a particular filter from 300 to 2000 nm but was only interested in viewing the reflectance from 300 to 700 nm over the range of 10-30%, one would enter `xlimits=[300 700]`, `ylimits=[10 30]`.

Allowing MATLAB® to automatically set the axis limits is recommended in most cases. This is accomplished by simply entering `[0 0]`.

A.3.11 Program Output: R, T, A

Photonic Calculator returns the reflectance (`R`), transmittance (`T`), and absorptance (`A`) of the optical interference filter. Each of these outputs are column vectors whose entries correspond to the wavelengths given in lambda. NOTE: `R`, `T`, and `A` are given in fractional form, as opposed to their percentage forms that are graphed in MATLAB® when the plot switches are turned on.

Appendix B
Additional Buckling Instability Work

B.1 Young's Modulus of Polystyrene as a Function of Humidity

The Young's moduli of two PS films were tested as a function of relative humidity. These films were only allowed to equilibrate for ≈ 30 min at each humidity value. Thickness values were obtained via in situ ellipsometry for Sample 2; the thickness of Sample 1 was calculated based on the relative change in Sample 2. A Poisson's ratio of 0.33 was assumed for PS at all humidity values. Error values in the PS thickness were assumed to be 3%.

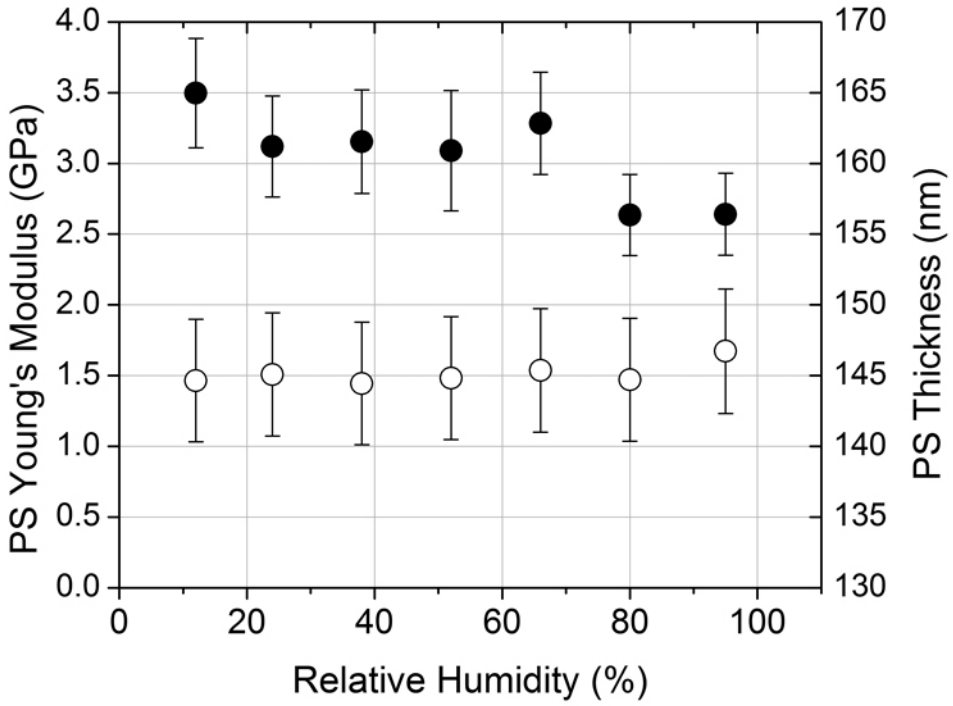

Figure B.1. Young's modulus (solid circles) and film thickness (hollow circles) for a PS film (Sample 1).

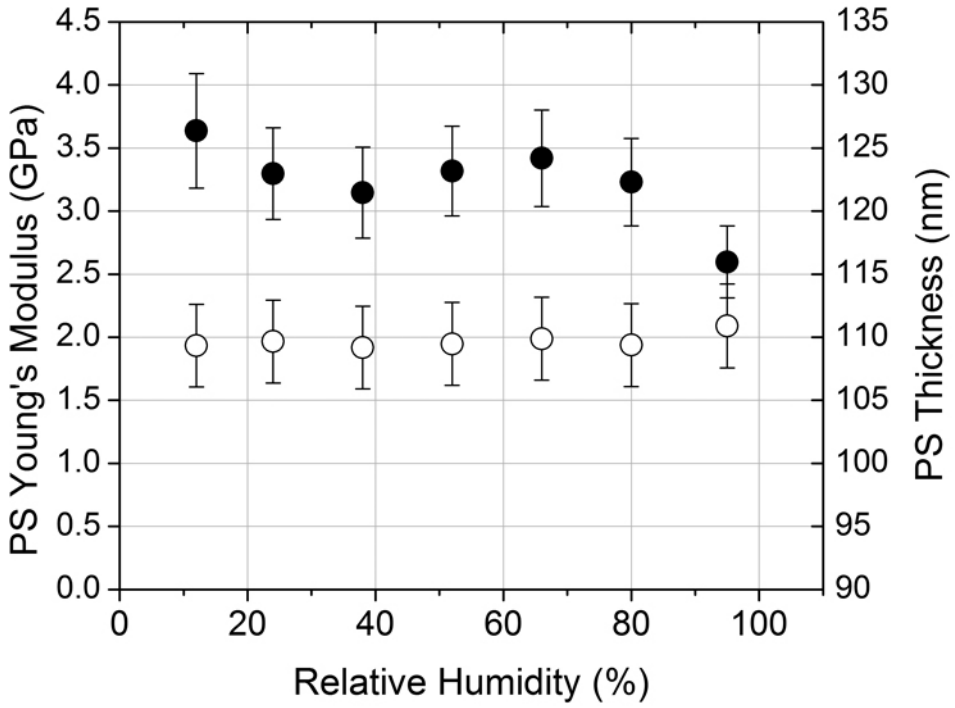

Figure B.2. Young's modulus (solid circles) and film thickness (hollow circles) for a PS film (Sample 2).

B.2 Effect of Silver Exchange and Reduction on the Young's Modulus of the (PAH2.5/PAA2.5) System

Multilayer systems comprised of $(PAH2.5/PAA2.5)_{20.5}$ were assembled on PDMS. The Young's modulus values of the films were measured via SIEBIMM, after which the PEM was subjected to 5 cycles of silver loading and reduction. Silver exchange was performed according to the usual procedure (see Section 2.3), and silver reduction was accomplished by subjecting the samples to 2 atm hydrogen gas at 80°C for ≈ 1 day. The Young's modulus was measured directly following each reduction step—the results of these tests are displayed in Figure B.3.

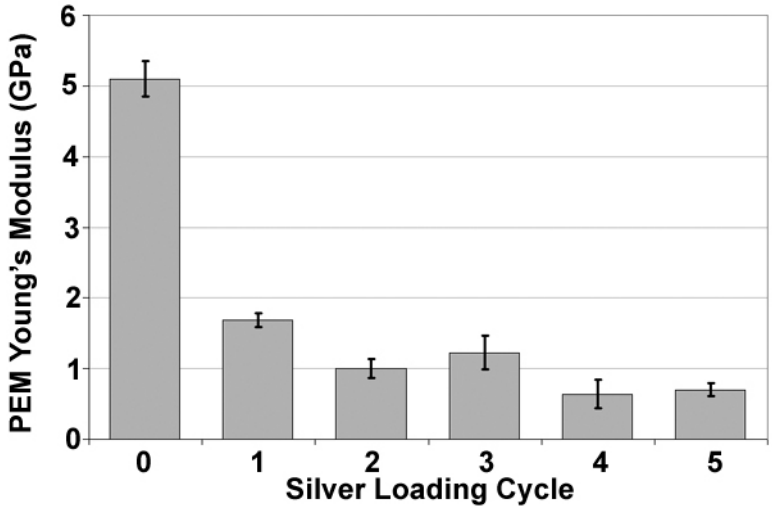

Figure B.3. The Young's Modulus of (PAH2.5/PAA2.5) films as a function of the number of cycles of silver loading and reduction.

Images of the films from Figure B.3 undergoing buckling are displayed in Figure B.4.

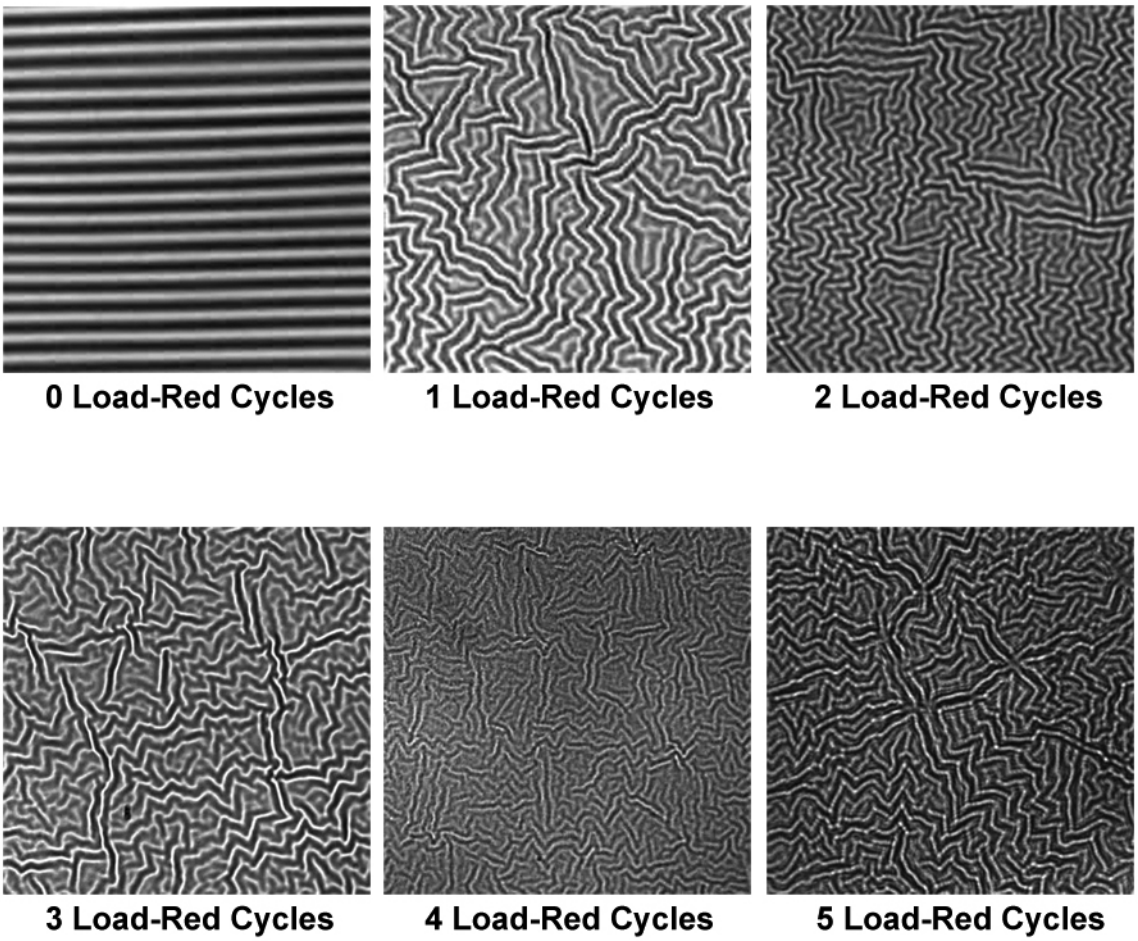

Figure B.4. Images of the $(PAH2.5/PAA2.5)_{20.5}$ films from Figure B.3 for different numbers of silver loading-reduction cycles. The untreated film required in-plane compression to induce buckling; the reduction treatment induced buckling in subsequent films. The side of each image measures 100 μm.

In order to understand the source of the decrease in Young's modulus with the loading and reduction of silver inside the PEM film, an untreated film was first subjected to a 1 hr soak in water to simulate the silver-loading process. Following this treatment, the Young's modulus was remeasured. The film was then baked in an oven to simulate the reduction process (no silver was present in this film). Although soaking the film in water for 1 hr led to essentially no change in stiffness, a decrease in Young's modulus was readily apparent following the oven treatment. These results are shown in Figure B.5.

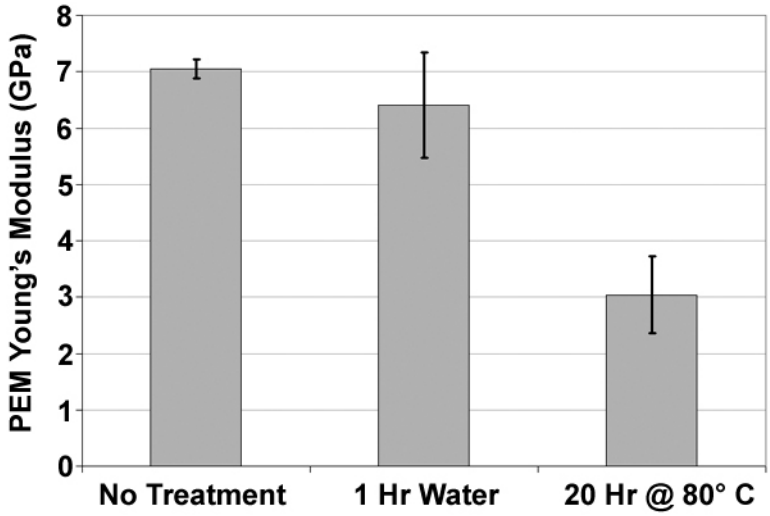

Figure B.5. Young's modulus of $(PAH2.5/PAA2.5)_{20.5}$ films as a function of treatment type.

These results suggest that heating PEM films on PDMS substrates may lead to a decrease in the Young's modulus. An alternative explanation for the results here is that a large, thermally-generated mismatch strain was compressing the films so far past the onset of buckling that artificially low Young's modulus values were calculated.[198]

B.3 Patterned Buckling Patterns with Polyelectrolyte Multilayer Films

This section demonstrates how the buckles exhibited by a PEM film on a PDMS surface can be ordered by controlling the substrate topology. $(PAH3.0/PSS3.0)_{70}$ films were assembled on PDMS microcontact printing (μCP) stamps, and the coated stamps were subsequently heated for ≈ 49 hr at 180°C before being cooled to room temperature. The film surface was found to be buckled without imposition of an external strain, presumably due to a strain mismatch caused during the heating and cooling process.

The figures below show ordered buckling patterns due to the raised areas on the μCP stamp, which introduce local orientation of the stress field. This type of phenomenon was described by Bowden et al., who reported the observation of ordered buckles on PDMS substrates coated with metal[258] and silica.[259]

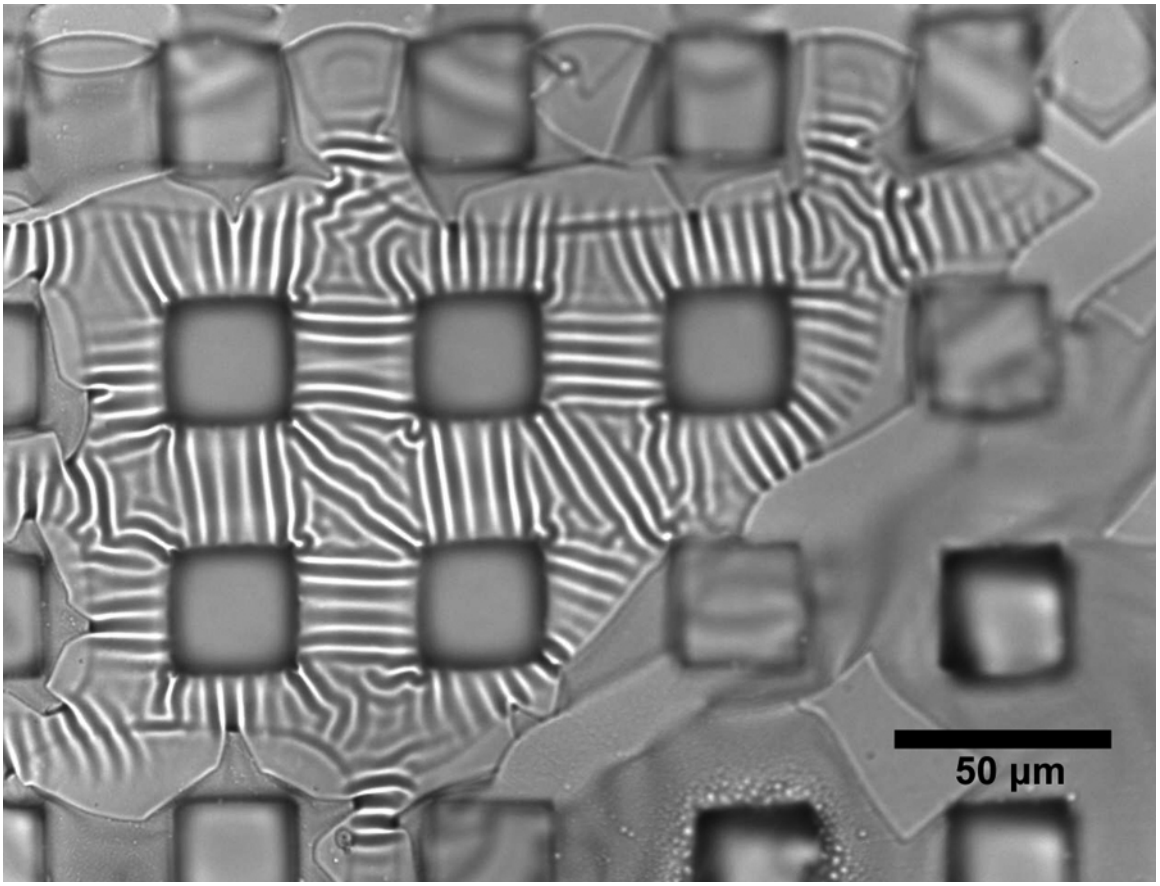

Figure B.6. $(PAH3.0/PSS3.0)_{70}$ system undergoing buckling on the surface of a microcontact printing stamp (Image 1). Biaxial strain was introduced through a heating-cooling treatment.

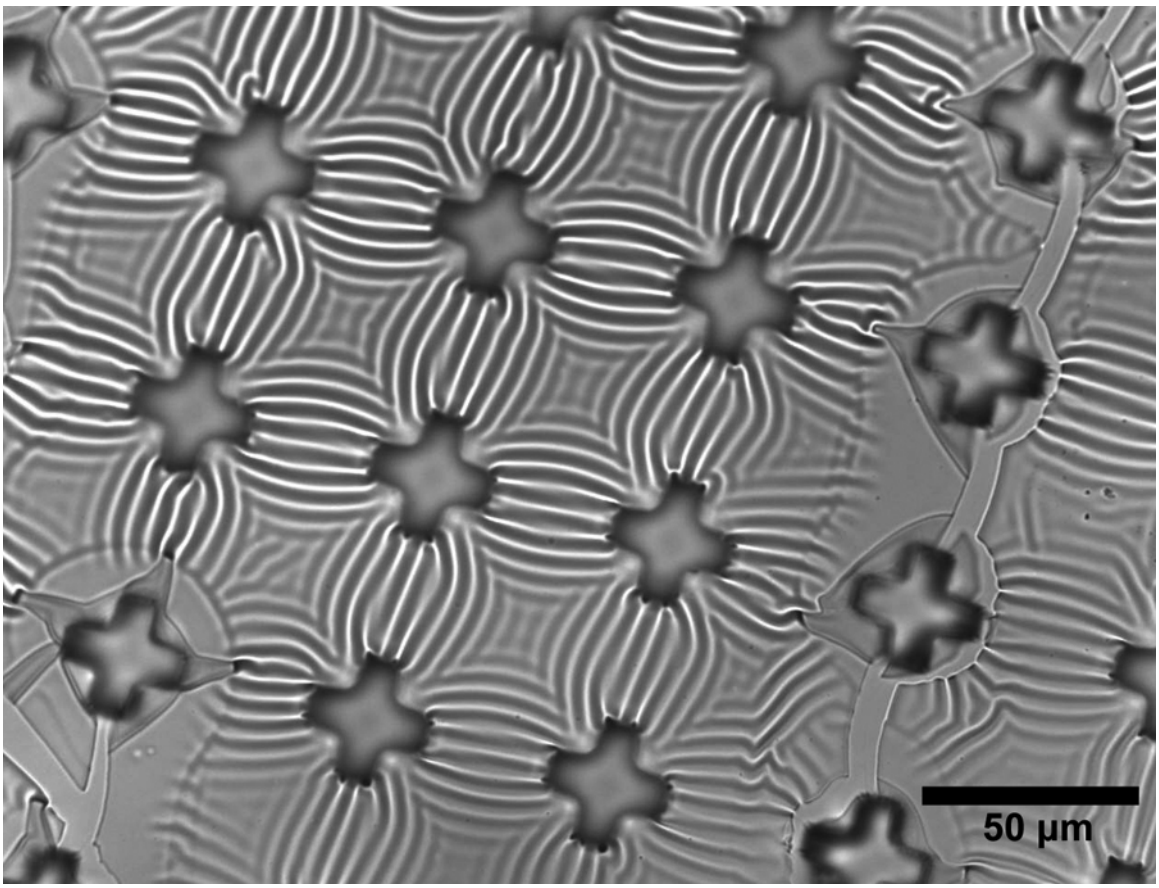

Figure B.7. $(PAH3.0/PSS3.0)_{70}$ system undergoing buckling on the surface of a microcontact printing stamp (Image 2). Biaxial strain was introduced through a heating-cooling treatment.

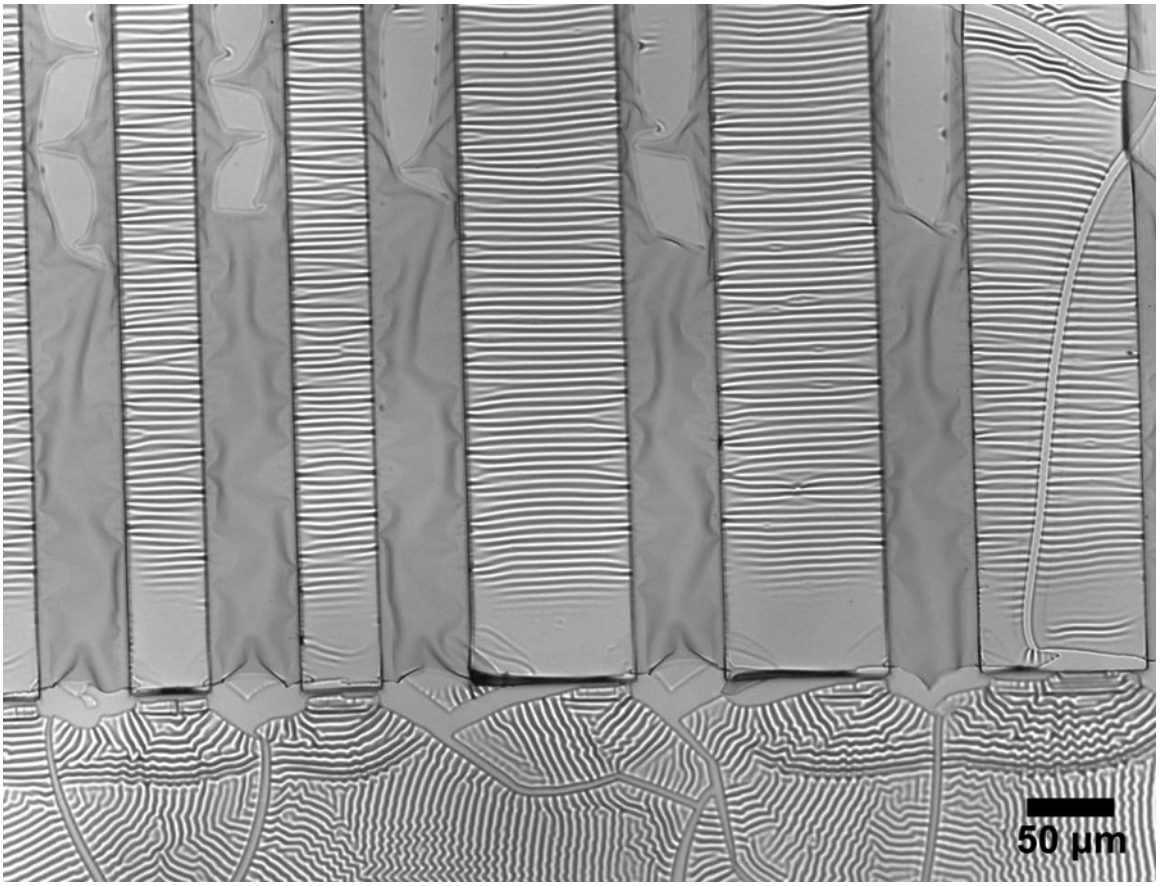

Figure B.8. $(PAH3.0/PSS3.0)_{70}$ system undergoing buckling on the surface of a microcontact printing stamp (Image 3). Biaxial strain was introduced through a heating-cooling treatment.

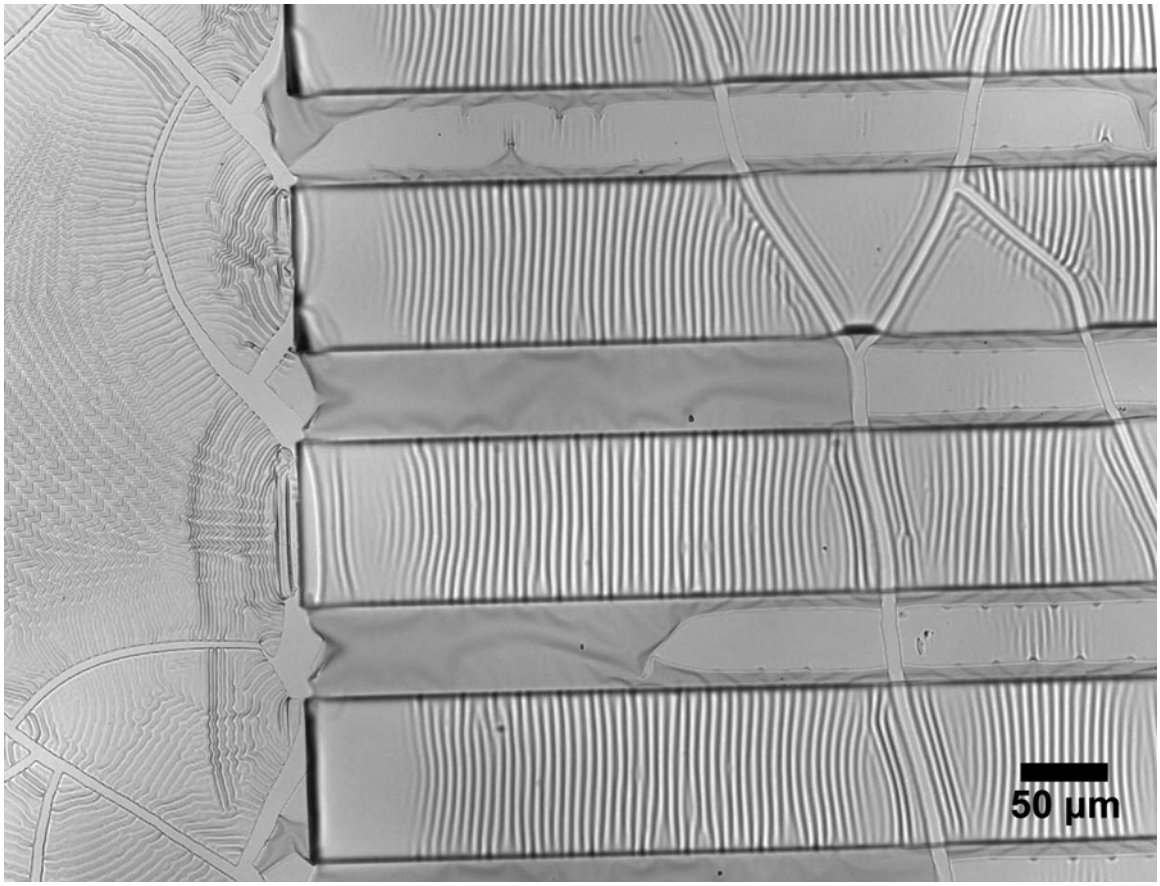

Figure B.9. $(PAH3.0/PSS3.0)_{70}$ system undergoing buckling on the surface of a microcontact printing stamp (Image 4). Biaxial strain was introduced through a heating-cooling treatment.

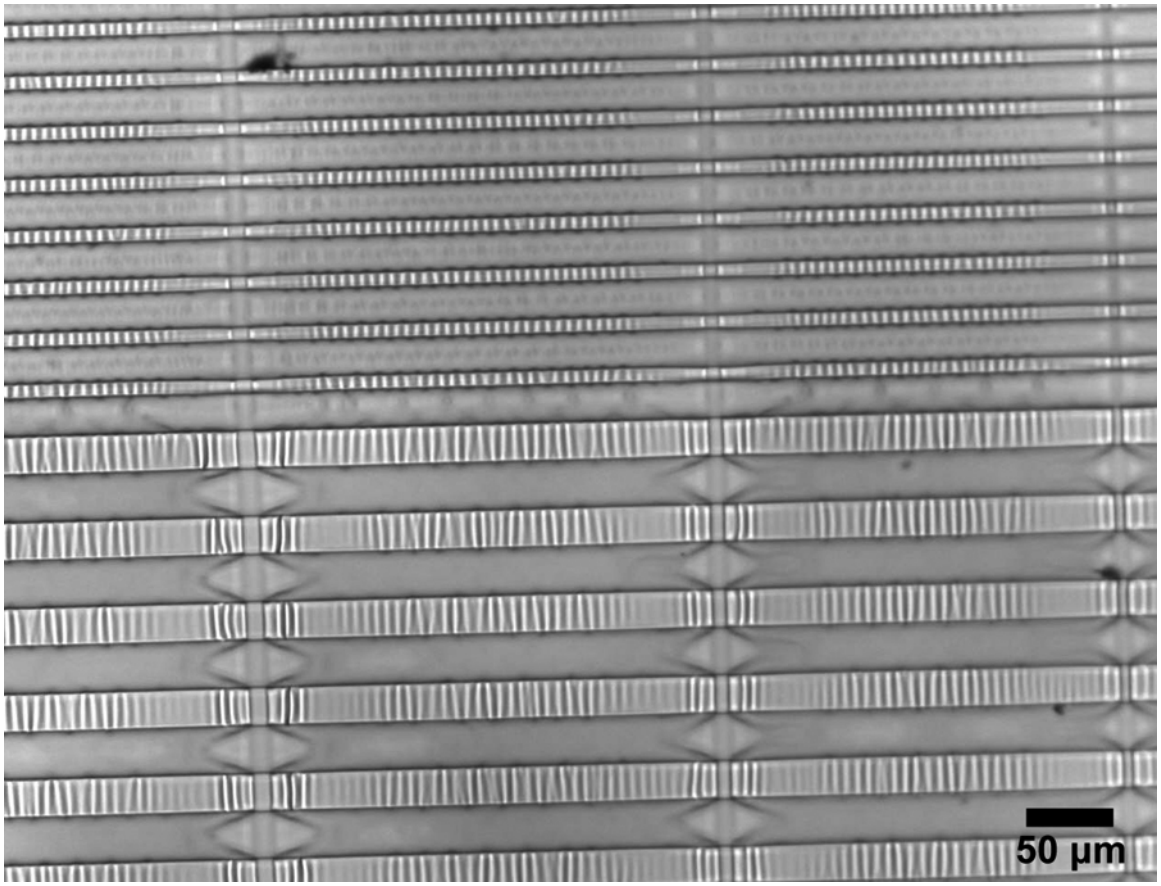

Figure B.10. $(PAH3.0/PSS3.0)_{70}$ system undergoing buckling on the surface of a microcontact printing stamp (Image 5). Biaxial strain was introduced through a heating-cooling treatment.

Appendix C
Fourier Transform Analysis: Optical Micrographs and Laser Diffraction Measurements

This appendix describes the method for computing and analyzing Fourier transforms on optical microscope images. This technique is closely related to the laser diffraction method (see Section 5.3) of measuring buckling wavelengths, which will also be described.

C.1 Fourier Transform Analysis of Optical Microscopy Images

Fourier transforms (FTs) convert images in the spatial domain to the frequency domain, where the length scale of periodic features in the spatial domain are identified by characteristic peaks in the frequency domain, allowing easy calculation of, for example, the average buckling wavelength of a sample. When conducted on discrete data sets such as digitally sampled data or pictures, Fourier transforms are sometimes known as discrete Fourier transforms (DFTs). So-called "fast" Fourier transforms (FFTs) use efficient algorithms, usually only applicable for certain data set sizes, to compute DFTs more quickly.

The `imageFFT()` program (Section E.2.1) uses MATLAB®'s FFT algorithms to compute the DFT of a 1024 × 1024 pixel (px) TIFF image. The output of the program is the power spectrum Fourier transform image, which is another TIFF image of the same dimensions as the input image that displays the magnitude of each pixel value (FTs generate complex number data sets from real number inputs). Images must first be cropped to a 1024 × 1024 px square in Photoshop or an equivalent program before implementing `imageFFT()`. Care must be taken to retain knowledge of the spatial scale (μm/px) of the image, especially if the image resolution is changed when creating the 1024 × 1024 px area. The procedure for conducting FT analysis on an OM is illustrated in Figure C.1.

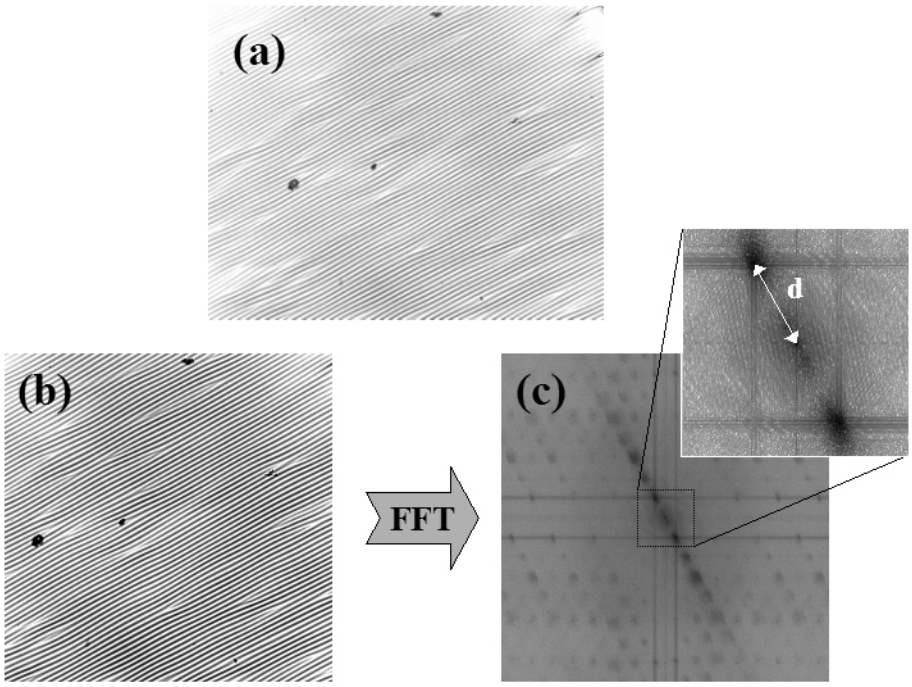

Figure C.1. Fourier transform analysis of optical microscopy images. (a) The unedited microscope image is obtained for which the spatial scale (μm/px) is known. (b) The image is cropped/resized to the dimensions of 1024 × 1024 px. (c) After implementing imageFFT() or an equivalent program to compute the power spectrum image, the center to 1st-order peak distance (*d*) can be found. In the inset detailed image in (c), a levels adjustment has been applied in Photoshop to facilitate measuring *d*.

After finding the center to 1st-order peak distance, *d* (measured in px), the average wavelength of buckling (λ) can be found using Equation C.1:

Equation C.1

$$\lambda = \frac{s}{d} \cdot (1024\, px)$$

where s is the image scale, in units of distance (usually μm) per px. The image scale, s, can be obtained roughly from knowledge of the microscope lens power, but usually more accurately from within the microscope software. For the Zeiss Axioplan 2 that was used for this thesis research,* the scales at the different magnification powers are given in Table C.1.

Lens Power (×)	Image Scale (μm/px)
2.5	4.246
5	2.136
20	0.5300
50	0.2123
100	0.1062

Table C.1. Image scale for digital photographs (1300 × 1000 px resolution) taken on the particular Zeiss Axioplan 2 microscope used for this thesis work (see footnote).

C.2 Laser Diffraction

Laser diffraction is a way of "physically" computing the FT of a periodically ordered feature that is capable of diffracting light. Passing coherent laser light (632.8 nm wavelength) through a PEM film undergoing buckling leads to prominent diffraction peaks on a screen placed behind the film. Assuming the laser light is incident normally on the buckled film, measuring the center to 1st-order peak distance (d) and the distance from the sample to the diffraction screen (S) yields the buckling wavelength (λ) using Equation C.2.

Equation C.2

$$\lambda = \frac{S}{d} \cdot (632.8\,nm).$$

An alternative method to employing the absolute distances is to measure d as a function of the relative distance to the screen, S_{rel}. This technique is particularly useful if, for example, the sample is positioned on an optical rail (as described in Section 5.3), along which very precise *relative* distance measurements can be made. For reasonably small diffraction

* This microscope is located, at the time of writing this thesis, on the 4th floor of Building 13 at MIT.

angles, the independent variable d increases linearly with the dependent variable S_{rel} and the slope of the regression line can be used in to calculate the buckling wavelength using Equation C.3.

Equation C.3

$$\lambda = \frac{1}{\frac{d(d)}{dS_{rel}}} \cdot (632.8\,nm).$$

More information about this technique can be found in Section 5.3.

Appendix D
AFM Images of Salt-Etched Films

The following two figures are AFM images of $(PAH7.5/PAA3.5)_{20.5}$ films that were assembled on PDMS and etched for 3 min in NaCl solution at the indicated concentrations. In Figure D.1 a slight decrease in roughness was observed for the films etched at 3 M, 4 M, and 5 M concentrations. A large increase in roughness was observed for the film that was etched in concentrated ($\approx$ 6 M) NaCl. Deep pocketing and loss of film material suggests that the PEM is able to undergo phase separation on the PDMS substrate at concentrations of NaCl greater than 5 M.

The 6 M film appears to contain craters that reach all the way to the PDMS substrate, as indicated by the difference between the 5 M and 6 M phase images in Figure D.2.

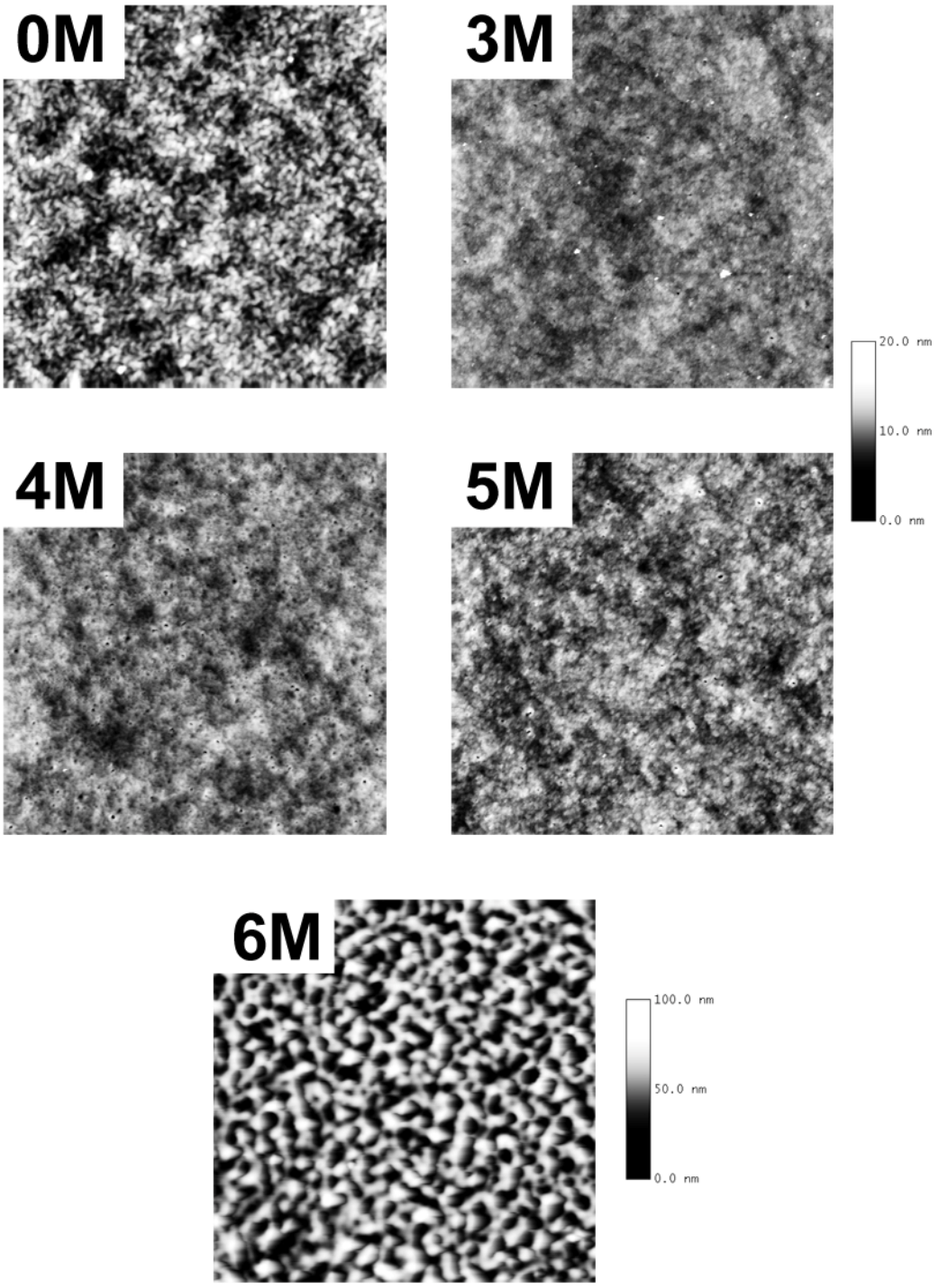

Figure D.1. AFM height images of $(PAH7.5/PAA3.5)_{20.5}$ films following 3 min NaCl etch steps at the indicated concentrations. Image scales are 10 × 10 μm. The height scale for the 0, 3, 4, and 5 M films is 20 nm, and that of the 6 M film is 100 nm. RMS surface roughness values (in nm) are as follows: 0 M: 2.00; 3 M: 1.04; 4 M: 1.16; 5 M: 1.38; 6 M: 12.7.

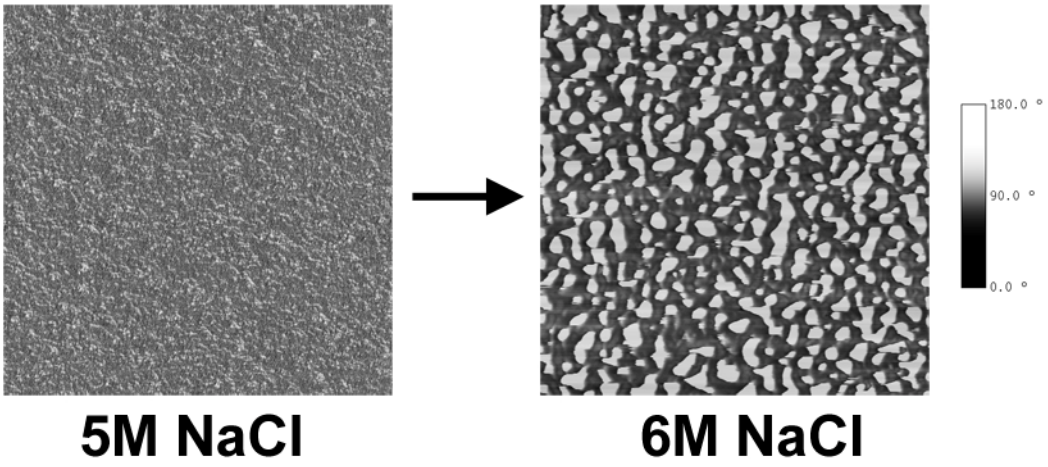

Figure D.2. AFM phase images of the 5 M and 6 M films from Figure D.2. The phase scale for both images is 180°.

Appendix E
MATLAB® Source Code

This appendix contains the source code for the MATLAB® programs that were composed as part of this thesis work. Each program's source code is introduced by a brief description.

E.1 Photonic Calculations

E.1.1 The *Photonic Calculator* : photonic_calc60()

This is the source code for the program described in Section A.3.

```
%***          1-D PHOTONIC CALCULATOR     v 6.01 ***
%***          Adam Nolte, February 2002          ***
%
%This function uses the matrix method to calculate the reflectivity,
%transmission, and absorptance of a 1-D optically stratified medium.
%
%USAGE:  "[R,T,A] =
photonic_calc60(theta0,P,lambda,d,n,n0,ns,Rplot,Tplot,Aplot,plot_choice,su
bstrate_account,xlimits,ylimits)"

%1.01 outputs "lambda" in nm, rather than m (ver 1.0), so that if the
program statement is
%run as above (USAGE) the value of lambda stays constant

%1.02 puts the incidence angle in the title of the graphs

%1.03 corrected a mistake in calculating R_TM where the conjugate being
taken was
%of r_TE

%1.04 corrected an error in the calculation of r t for the TM polarization
%state.  The difference in calculating r_TE and t_TE versus r_TM and t_TM
is
%subtle and is not mentioned in Hecht, pg. 428.  Besides accounting for
the different
%Y's, one must multiply the r_TM equation by a factor of -1, and the t_TM
equation by
%a factor of cos(theta0)/cos(thetas).

%1.05 changed name of T from "Transmission" to the correct "Transmittance"

%3.0 incorporates an option whereas there is an eleventh pass variable,
whose
%value can be true (1) or false (0).  For true values R, T, and A are
calculated
%and plotted (if desired) versus wavelength.  For false values, R, T, and
A are
```

```
%calculated and plotted (if desired) versus angular frequency.  Version
3.0 also
%places a semicolon after the conversion of lambda back to nanometers
(line 215)
%to prevent lambda from being written to the screen every time the program
is
%executed.

%3.01 added "real" to R,T, and A calculations

%4.0 added the option of including back-substrate reflection (with
absorptance)

%4.1 added the ability to set axis limits.  Axis limits are simply
commented out if not desired.

%4.2 (hopefully) resolved an error in how substrate_account handled
imaginary refractive indices.  the exponentials were assuming
%n+ki notation, and other stuff used n-ki.  Now either way will generate
absorption in the substrate.

%4.21 changed substrate thickness so that the user enters mm, and the
%program changes it to nm.  Also, the final computations of R, T, and A
%have real() in them.  Imaginary parts (zero, but still displayed) were
%sneaking into R, T, and A somehow.  In addition, the decision on whether
%or not to use graph limits is set as a variable by the user in the code
as
%"graph_limit".  graph_limit=1 implies limits will be used, graph_limit=0
%implies automatic limit setting by MATLAB.  In addition, the final
%calculation of "A" was changed to its present form from "1-R-T" which is
no
%longer true with an absorbing substrate

%4.3 found problem with exponentials in the substrate account section--
%units on lambda and sub_thick didn't match up (lambda was in m at that
%point, sub_thick in nm).  sub_thick is now put into m after the function
%declaration, instead of nm.  4.3 also changed the R's, T's, and A's in
the
%substrate account section into R_xn's, because R_TE, for example was
being
%redefined and then called again in later expressions where the orginal
R_x
%was needed.  Also added tic and toc and moved the setting of the graph
%axis limits inside the graphing if statement.

%4.31 moved the location of the plot limits to the program's beginning

%5.0 put the plot limits into the call statement

%6.01 changed instructions on plot limits to indicate for that automatic
%limit-setting xlimits,ylimits must be [0 0], not just 0, which returns an
%error
```

```
%This function [photonic_calc40()] takes as inputs the following
%entries in this particular order:

% 1. The angle of incidence, measured in degrees from the normal.

% 2. The degree of polarization of the light, expressed as a number
between
%    0 and 1, where "0" represents completely TE light, and "1" represents
%    completely TM light (i.e. natural light = 0.5).

% 3. A column vector (lambda) containing the wavelengths of interest,
measured
%    in nm (i.e. approx [400:700] for the visible spectrum).

% 4. A # by 2 matrix containing in the first column the thicknesses
%    of each layer from incidence
%    to transmission side, measured in nm.  The second column should
%    contain a number for each respective layer which tells the
%    program which column of the index of refraction matrix contains the
%    lambda dependent index of refraction data for that layer.

% 5. The index of refraction matrix, a matrix containing as
%    columns the lambda dependent index of refraction data.  It should
%    have as many rows as there are elements in the lambda vector, and
%    as many columns as there are different materials in the photonic
stack.
%
%    v 1.0 and above incorporate an option whereas if a row vector of
refractive indices
%    is given in place of a full matrix, the program will assume the given
refractive
%    index is constant over all wavelengths

% 6. The refractive index of the incidence medium, a column
%    vector with wavelength dependence.  (if v 1.0 or above, a constant
value
%    assumes constant refractive index over all wavelengths)

% 7. The refractive index of the transmission medium, a column
%    vector with wavelength dependence.  (if v 1.0 or above, a constant
value
%    assumes constant refractive index over all wavelengths)

% 8. A "1" if a plot of the %Reflectance is desired, a "0" if not.

% 9. A "1" if a plot of the %Transmission is desired, a "0" if not.

% 10. A "1" if a plot of the %Absorbance is desired, a "0" if not.

% 11. A "1" if a plots should be versus wavelength, a "0" if versus
angular frequency.
```

```
% 12. A "1" if the plot should take substrate back-reflectance into
% account, a "0" if not.  New to version 6.0 is the option of putting a
% "2".  This calculates the spectral response assuming a filter on each
% side of the substrate.  It assumes mirror symmetry through a plane
% cutting the substrate in half.

% 13. The abscissa limits expressed as a two-element vector [xlow xhigh].
% An entry of "[0 0]" specifies auto-set limits.

% 14. The ordinate limits expressed as a two-element vector [ylow yhigh].
% An entry of "[0 0]" specifies auto-set limits.

% This function returns as output a column vector of associated
% % reflectance, a column vector of associated % transmittance,
% and a column vector of associated % absorptance.


function [R,T,A] =
photonic_calc60(theta0,P,lambda,d,n,n0,ns,Rplot,Tplot,Aplot,plot_choice,su
bstrate_account,xlimits,ylimits);

%tic;


%Using x and y graph limits?
graph_limitx = 0;
graph_limity = 0;

if xlimits(1) | xlimits(2)
    graph_limitx = 1;
end

if ylimits(1) | ylimits(2)
    graph_limity = 1;
end


%Set Substrate Thickness (mm)
sub_thick = 1.09; %units of mm.  glass substrate usually ~1.09mm
sub_thick = sub_thick*10^-3;  %convert to m

% Calculate angular frequency vector
omega0 = (2 * pi * 3.00E8)./(lambda*10^-9);
central_wavelength = 1000; %Set central wavelength for k/k0 plots (units
of nm)
omega0_center = (2 * pi * 3.00E8)/(central_wavelength*10^-9);

% Convert angle to a string to place in the graph titles
angle0 = num2str(theta0);
```

```
%ditto for central wavelength
cen_wave = num2str(central_wavelength);

%convert theta0 to radians
theta0=theta0*pi/180;

%define needed constant of the square root of epsilon 0 over mu 0
emu = 2.65442E-3;

%convert "lambda" and "d" vectors to meters
lambda = lambda*10^-9;
d(:,1) = d(:,1)*10^-9;

% Find the number of layers we're dealing with
numlayers = size(d);
numlayers = numlayers(1);

% Find the number of wavelengths we're scanning
numwaves = size(lambda);
numwaves = numwaves(1);

% Find min and max lambda

lami = lambda(1);
lamf = lambda(numwaves);

%this section converts constant entries (for the refractive indices) into
vectors
size_n0 = size(n0);
size_n0 = size_n0(1);
if size_n0 == 1
    n0 = n0 * ones(numwaves,1);
end

size_ns = size(ns);
size_ns = size_ns(1);
if size_ns == 1
    ns = ns * ones(numwaves,1);
end

size_n = size(n);
dec_n = size_n(1);
num_n = size_n(2);
if dec_n == 1
    for I = 1 : num_n,
        new_n(:,I) = n(1,I) * ones(numwaves,1);
    end
    n = new_n;
end

% Begin creating a matrix of entry angles of light into each layer
% based on Snell's Law.  Each column represents a layer-- each row
```

```
% the angles at a given wavelength

theta = asin( n0 .* sin(theta0) ./ n(:,d(1,2)) );

if numlayers > 1
   for I = 2 : numlayers,
      theta(:,I)= asin( (n0).*sin(theta0)./n(:,d(I,2)) );
   end
end


% Now create thetas as the transmitted angles
thetas = asin( n0.*sin(theta0)./ns );


% Loop over wavelengths and create and multiply transfer matrices
% for TE polarization case

for I = 1 : numwaves,
   % Create unity matrix M1
   M1 = [1 0;0 1];
   k0 = 2*pi/lambda(I);
   Y0 = emu * n0(I) * cos(theta0);
   Ys = emu * ns(I) * cos(thetas(I));

   for J = 1 : numlayers,
      h = n(I,d(J,2))*d(J,1) * cos(theta(I,J));
      Y = emu * n(I,d(J,2)) * cos(theta(I,J));
      M2 = M1 * [cos(k0*h) i*sin(k0*h)/Y; Y*i*sin(k0*h) cos(k0*h)];
      M1 = M2;
  end

   %Calculate amplitude reflection and transmission coefficients
   r_TE(I,1) = (Y0*M1(1,1) + Y0*Ys*M1(1,2) - M1(2,1) -
Ys*M1(2,2))/(Y0*M1(1,1) + Y0*Ys*M1(1,2) + M1(2,1) + Ys*M1(2,2));

   t_TE(I,1) = 2*Y0/(Y0*M1(1,1) + Y0*Ys*M1(1,2) + M1(2,1) + Ys*M1(2,2));
   if substrate_account
       %Calculate reverse amplitude reflection and transmission
coefficients (M1(1,1)-> M1(2,2) and vice versa for reverse stack)
       rRev_TE(I,1) = (Ys*M1(2,2) + Ys*Y0*M1(1,2) - M1(2,1) -
Y0*M1(1,1))/(Ys*M1(2,2) + Ys*Y0*M1(1,2) + M1(2,1) + Y0*M1(1,1));

       tRev_TE(I,1) = 2*Ys/(Ys*M1(2,2) + Ys*Y0*M1(1,2) + M1(2,1) +
Y0*M1(1,1));
   end
end

% Loop over wavelengths and create and multiply transfer matrices
% for TM polarization case

for I = 1 : numwaves,
```

```
   % Create unity matrix M1
   M1 = [1 0;0 1];
   k0 = 2*pi/lambda(I);
   Y0 = emu * n0(I) / cos(theta0);
   Ys = emu * ns(I) / cos(thetas(I));

   for J = 1 : numlayers,
      h = n(I,d(J,2))*d(J,1) * cos(theta(I,J));
      Y = emu * n(I,d(J,2)) / cos(theta(I,J));
      M2 = M1 * [cos(k0*h) i*sin(k0*h)/Y; Y*i*sin(k0*h) cos(k0*h)];
      M1 = M2;
   end

   %Calculate amplitude reflection and transmission coefficients
   %Note: these equations are different from the TE case
   r_TM(I,1) = -(Y0*M1(1,1) + Y0*Ys*M1(1,2) - M1(2,1) -
Ys*M1(2,2))/(Y0*M1(1,1) + Y0*Ys*M1(1,2) + M1(2,1) + Ys*M1(2,2));

   t_TM(I,1) = 2*Y0*(cos(theta0)/cos(thetas(I)))/(Y0*M1(1,1) +
Y0*Ys*M1(1,2) + M1(2,1) + Ys*M1(2,2));

   if substrate_account
       %Calculate reverse amplitude reflection and transmission
coefficients (M1(1,1)-> M1(2,2) and vice versa for reverse stack)
       rRev_TM(I,1) = -(Ys*M1(2,2) + Ys*Y0*M1(1,2) - M1(2,1) -
Y0*M1(1,1))/(Ys*M1(2,2) + Ys*Y0*M1(1,2) + M1(2,1) + Y0*M1(1,1));

       tRev_TM(I,1) = 2*Ys*(cos(thetas(I))/cos(theta0))/(Ys*M1(2,2) +
Ys*Y0*M1(1,2) + M1(2,1) + Y0*M1(1,1));
   end

end

% Find reflectance (R), transmittance (T), and absorptance (A)
% for each polarization case


R_TE = r_TE .* conj(r_TE);
T_TE = ((real(ns) .* cos(real(thetas)))./(real(n0) .* cos(real(theta0))))
.* t_TE .* conj(t_TE);
A_TE = 1 - R_TE - T_TE;

R_TM = r_TM .* conj(r_TM);
T_TM = ((real(ns) .* cos(real(thetas)))./(real(n0) .* cos(real(theta0))))
.* t_TM .* conj(t_TM);
A_TM = 1 - R_TM - T_TM;

if substrate_account
    % Find rev reflectance/transmittance
    Rrev_TE = rRev_TE .* conj(rRev_TE);
    Trev_TE = ((n0 .* cos(theta0))./(ns .* cos(thetas))) .* tRev_TE .*
conj(tRev_TE);
```

```
    Arev_TE =  1 - Rrev_TE - Trev_TE;

    Rrev_TM = rRev_TM .* conj(rRev_TM);
    Trev_TM = ((n0 .* cos(theta0))./(ns .* cos(thetas))) .* tRev_TM .*
conj(tRev_TM);
    Arev_TM =  1 - Rrev_TM - Trev_TM;

    % Find Reflectance of back-surface interface with Fresnel equations--
    % either air or reverse film
    if substrate_account == 1;
        psi_TE = ((ns.*cos(thetas)-
n0.*cos(theta0))./(ns.*cos(thetas)+n0.*cos(theta0))) .*
conj((ns.*cos(thetas)-
n0.*cos(theta0))./(ns.*cos(thetas)+n0.*cos(theta0)));
        psi_TM = ((n0.*cos(thetas)-
ns.*cos(theta0))./(ns.*cos(theta0)+n0.*cos(thetas))) .*
conj((n0.*cos(thetas)-
ns.*cos(theta0))./(ns.*cos(theta0)+n0.*cos(thetas)));
        phi_TE = 1 - psi_TE;
        phi_TM = 1 - psi_TM;
        abs_TE = phi_TE * 0;
        abs_TM = phi_TM * 0;
    elseif substrate_account == 2;
        psi_TE = Rrev_TE;
        psi_TM = Rrev_TM;
        phi_TE = Trev_TE;
        phi_TM = Trev_TM;
        abs_TE = Arev_TE;
        abs_TM = Arev_TM;
    end

    % Recalculate reflectance/transmittance/absorptance with substrate
effect.  R+T+A no longer = 1 with absorbing substrate!
    % This assumes imaginary RI, no matter what the sign convention, are
meant to assume absorption.

    for I = 1 : numwaves,
        R_TEn(I,1) = R_TE(I,1) + (T_TE(I,1) * Trev_TE(I,1) * psi_TE(I,1) *
exp(-2*4*pi*abs(imag(ns(I,1)))*sub_thick/lambda(I)))/(1-
Rrev_TE(I,1)*psi_TE(I,1)*exp(-
2*4*pi*abs(imag(ns(I,1)))*sub_thick/lambda(I)));
        R_TMn(I,1) = R_TM(I,1) + (T_TM(I,1) * Trev_TM(I,1) * psi_TM(I,1) *
exp(-2*4*pi*abs(imag(ns(I,1)))*sub_thick/lambda(I)))/(1-
Rrev_TM(I,1)*psi_TM(I,1)*exp(-
2*4*pi*abs(imag(ns(I,1)))*sub_thick/lambda(I)));

        T_TEn(I,1) = (phi_TE(I,1) * T_TE(I,1) * exp(-
4*pi*abs(imag(ns(I,1)))*sub_thick/lambda(I)))/(1-
Rrev_TE(I,1)*psi_TE(I,1)*exp(-
2*4*pi*abs(imag(ns(I,1)))*sub_thick/lambda(I)));
        T_TMn(I,1) = (phi_TM(I,1) * T_TM(I,1) * exp(-
4*pi*abs(imag(ns(I,1)))*sub_thick/lambda(I)))/(1-
```

```
Rrev_TM(I,1)*psi_TM(I,1)*exp(-
2*4*pi*abs(imag(ns(I,1)))*sub_thick/lambda(I)));

        A_TEn(I,1) = A_TE(I,1) + (T_TE(I,1) * exp(-
4*pi*abs(imag(ns(I,1)))*sub_thick/lambda(I)) * (abs_TE(I,1) + psi_TE(I,1)
* exp(-4*pi*abs(imag(ns(I,1)))*sub_thick/lambda(I)) * Arev_TE(I,1))/(1-
Rrev_TE(I,1)*psi_TE(I,1)*exp(-
2*4*pi*abs(imag(ns(I,1)))*sub_thick/lambda(I))));
        A_TMn(I,1) = A_TM(I,1) + (T_TM(I,1) * exp(-
4*pi*abs(imag(ns(I,1)))*sub_thick/lambda(I)) * (abs_TM(I,1) + psi_TM(I,1)
* exp(-4*pi*abs(imag(ns(I,1)))*sub_thick/lambda(I)) * Arev_TM(I,1))/(1-
Rrev_TM(I,1)*psi_TM(I,1)*exp(-
2*4*pi*abs(imag(ns(I,1)))*sub_thick/lambda(I))));

    end

    R_TE = R_TEn;
    R_TM = R_TMn;
    T_TE = T_TEn;
    T_TM = T_TMn;
    A_TE = A_TEn;
    A_TM = A_TMn;
end

% Create R, T, and A given the polarization of the light
R = (1-P)*R_TE + P*R_TM;
T = (1-P)*T_TE + P*T_TM;
A = (1-P)*A_TE + P*A_TM;


R=real(R);
T=real(T);
A=real(A);

%Convert lambda back to nm
lambda = lambda * 10^9;

%toc;

% Plot R, T, and A
if plot_choice

if Rplot == 1
   figure('color','white');
   plot(lambda,100*R);
   title(strcat('Reflectance vs. Wavelength',' (theta=',angle0,')'));
   xlabel('Wavelength (nm)');
   ylabel('Reflectance (%)');

   if graph_limitx
       xlim(xlimits);
   end
```

```
    if graph_limity
        ylim(ylimits);
    end
end

if Tplot == 1
    figure('color','white');
    plot(lambda,100*T);
    title(strcat('Transmittance vs. Wavelength',' (theta = ',angle0,')'));
    xlabel('Wavelength (nm)');
    ylabel('Transmission (%)');

    if graph_limitx
        xlim(xlimits);
    end

    if graph_limity
        ylim(ylimits);
    end

end

if Aplot == 1
    figure('color','white');
    plot(lambda,100*A);
    title(strcat('Absorptance vs. Wavelength',' (theta = ',angle0,')'));
    xlabel('Wavelength (nm)');
    ylabel('Absorbance (%)');

    if graph_limitx
        xlim(xlimits);
    end

    if graph_limity
        ylim(ylimits);
    end

end

else

    if Rplot == 1
    figure('color','white');
    plot(omega0/omega0_center,100*R);
    title(strcat('Reflectance vs. Dimensionless Wavenumber','
(theta=',angle0,')'));
    xlabel(strcat('k/k0, lambda0=',cen_wave,' nm'));
    ylabel('Reflectance (%)');

    if graph_limitx
        xlim(xlimits);
```

```
    end

    if graph_limity
        ylim(ylimits);
    end

end

if Tplot == 1
    figure('color','white');
    plot(omega0/omega0_center,100*T);
    title(strcat('Transmittance vs. vs. Dimensionless Wavenumber',' (theta
= ',angle0,')'));
    xlabel(strcat('k/k0, lambda0=',cen_wave,' nm'));
    ylabel('Transmission (%)');

    if graph_limitx
        xlim(xlimits);
    end

    if graph_limity
        ylim(ylimits);
    end

end

if Aplot == 1
    figure('color','white');
    plot(omega0/omega0_center,100*A);
    title(strcat('Absorptance vs. vs. Dimensionless Wavenumber',' (theta =
',angle0,')'));
    xlabel(strcat('k/k0, lambda0=',cen_wave,' nm'));
    ylabel('Absorbance (%)');

    if graph_limitx
        xlim(xlimits);
    end

    if graph_limity
        ylim(ylimits);
    end

end

end
```

E.1.2 Apodized Rugate Function: odefun()

This function defines the apodized rugate profile given in Figure 2.5a. It was called by an initial-value differential equation solver in MATLAB® to solve the Riccati equation governing reflection from a film with a continuously varying refractive index profile (see Section A.2). Wavelengths and distances are measured in nm.

```
function dydx = odefun(x,y);

global LAMBDA;

nh=2;
nl=1.55;
na=(nh+nl)/2;
lambda0 = 1000;
T = lambda0/(2*na);
A = 1;  %Linear apodization constant

if x < A*T;
    n = na + .5*(nh-nl)*sin(2*pi*x/T)*x/(2.5*T);  %Note:  This 2.5 was
kept as 2.5 for RUG2.  Better behavior if it had been "A"
    dndx = (.2/T)*(nh-nl)*(sin(2*pi*x/T)+(2*pi*x/T)*cos(2*pi*x/T));
elseif x > A*T & x <= 3.25*T;
    n = na + .5*(nh-nl)*sin(2*pi*x/T);
    dndx = (pi/T)*(nh-nl)*cos(2*pi*x/T);
else
    n = na + .5*(nh-nl)*sin(2*pi*(6.5*T-x)/(2.5*T));
    dndx = -(.2/T)*(nh-nl)*(sin(2*pi*(6.5*T-x)/T)+(2*pi*(6.5*T-
x)/T)*cos(2*pi*(6.5*T-x)/T));
end

%n = na + .5*(nh-nl)*sin(2*pi*x/T);
%dndx = (nh-nl)*pi/T*cos(2*pi*x/T);

%nl = 1;
%nh = 1.5;
%na = (nh+nl)/2;
%n = na + .5*(nh-nl)*tanh((x-500)/5);
%dndx = .5*(nh-nl)/5*(sech((x-500)/5))^2;


dydx = .5*(1/n)*dndx*(1-y.^2)-4*pi*n*y*i./LAMBDA;
```

E.2 Fourier Transform Functions

The following two functions were used to compute fast Fourier transforms (FFTs) on optical microscopy images. The first function, imageFFT(), is the "engine". The second function uses the first to take the FFT of every file in a specified directory.

E.2.1 Fast Fourier Transform Engine: imageFFT()

```
function imageFFT(filename);

%USAGE: imageFFT('path\filename')
%
%This function saves the fft image of
%the 1024 x 1024 black and white .tif image with name "filename" in the
%same directory as "filenameF"

%July 6th, 2005.  AJN.

filename = strrep(filename,'.tif','');

rawimage = imread(filename,'tif');

fftimage = fft2(single(rawimage));

power = abs(fftimage);

R = max(max(power));

oldmatrix = 255 - uint8(255/log(1+R)*log(1+power));

newmatrix(1:512,1:512) = oldmatrix(513:1024,513:1024);
newmatrix(513:1024,1:512) = oldmatrix(1:512,513:1024);
newmatrix(1:512,513:1024) = oldmatrix(513:1024,1:512);
newmatrix(513:1024,513:1024) = oldmatrix(1:512,1:512);

newfilename = strcat(filename,'F','.tif');

imwrite(newmatrix,newfilename,'tif');
```

E.2.2 Directory Tool for Fourier Transforms: dirFFT()

```
%dirFFT program
%Author: Adam Nolte
%Fall 2005

function dirFFT(path);

%USAGE: dirFFT('path\directory_name')
%
%dirFFT attempts to take the FFT of every file with a .tif extension in
the directory named
%"directory_name" and take its FFT, adding an "F" to the end of the
%filename.  It calls the the function imageFFT.

%July 7th, 2005.  AJN.

files = dir(strcat(path,'\*.tif'));
numfiles = size(files);

for I = 1:numfiles(1),

    disp(strcat(path,'\',files(I).name))

    imageFFT(strcat(path,'\',files(I).name));

end
```

References

1. Freund, L. B.; Suresh, S., *Thin Film Materials*. Cambridge University Press: Cambridge, U.K., 2003.

2. Li, H.; Iga, K., *Vertical-cavity surface-emitting laser devices*. Springer: Berlin; New York, 2003; Vol. 6.

3. Sargent, R. B.; O'Brien, N. A., Dielectric materials for thin-film-based optical communications filters. *MRS Bulletin* **2003,** 28, (5), 372-376.

4. Suresh, S., Graded materials for resistance to contact deformation and damage. *Science* **2001,** 292, (5526), 2447-2451.

5. Pavoor, P. V.; Gearing, B. P.; Bellare, A.; Cohen, R. E., Tribological characteristics of polyelectrolyte multilayers. *Wear* **2004,** 256, (11-12), 1196-1207.

6. Whitesides, G. M.; Ostuni, E.; Takayama, S.; Jiang, X. Y.; Ingber, D. E., Soft lithography in biology and biochemistry. *Annual Review of Biomedical Engineering* **2001,** 3, 335-373.

7. Thompson, M. T.; Berg, M. C.; Tobias, I. S.; Rubner, M. F.; Van Vliet, K. J., Tuning compliance of nanoscale polyelectrolyte multilayers to modulate cell adhesion. *Biomaterials* **2005,** 26, (34), 6836-6845.

8. Yang, S. Y.; Mendelsohn, J. D.; Rubner, M. F., New class of ultrathin, highly cell-adhesion-resistant polyelectrolyte multilayers with micropatterning capabilities. *Biomacromolecules* **2003,** 4, (4), 987-994.

9. Yang, S. Y.; Lee, D.; Cohen, R. E.; Rubner, M. F., Bioinert solution-cross-linked hydrogen-bonded multilayers on colloidal particles. *Langmuir* **2004,** 20, (14), 5978-5981.

10. Macleod, H. A., *Thin-Film Optical Filters*. 3 ed.; Institute of Physics Publishing: London, 2001.

11. Kumar, S.; Nann, T., Shape control of II-VI semiconductor nanomateriats. *Small* **2006,** 2, (3), 316-329.

12. Gross, M.; Muller, D. C.; Nothofer, H. G.; Scherf, U.; Neher, D.; Brauchle, C.; Meerholz, K., Improving the performance of doped pi-conjugated polymers for use in organic light-emitting diodes. *Nature* **2000,** 405, (6787), 661-665.

13. Iler, R. K., Multilayers of colloidal particles. *Journal of Colloid and Interface Science* **1966,** 21, 569-594.

14. Decher, G.; Hong, J. D., Buildup of Ultrathin Multilayer Films By a Self-Assembly Process .1. Consecutive Adsorption of Anionic and Cationic Bipolar Amphiphiles On Charged Surfaces. *Makromolekulare Chemie-Macromolecular Symposia* **1991,** 46, 321-327.

15. Decher, G.; Hong, J. D., Buildup of Ultrathin Multilayer Films By a Self-Assembly Process .2. Consecutive Adsorption of Anionic and Cationic Bipolar Amphiphiles and Polyelectrolytes On Charged Surfaces. *Berichte Der Bunsen-Gesellschaft-Physical Chemistry Chemical Physics* **1991,** 95, (11), 1430-1434.

16. Decher, G.; Hong, J. D.; Schmitt, J., Buildup of ultrathin multilayer films by a self-assembly process. 3. Consecutively alternating adsorption of anionic and cationic polyelectrolytes on charged surfaces. *Thin Solid Films* **1992,** 210, (1-2), 831-835.

17. Decher, G., Fuzzy nanoassemblies: Toward layered polymeric multicomposites. *Science* **1997,** 277, (5330), 1232-1237.

18. Caruso, F.; Caruso, R. A.; Mohwald, H., Nanoengineering of inorganic and hybrid hollow spheres by colloidal templating. *Science* **1998,** 282, (5391), 1111-1114.

19. Lee, D.; Cohen, R. E.; Rubner, M. F., Heterostructured Magnetic Nanotubes. *Langmuir* **2006,** ASAP.

20. Ostrander, J. W.; Mamedov, A. A.; Kotov, N. A., Two modes of linear layer-by-layer growth of nanoparticle-polylectrolyte multilayers and different interactions in the layer-by-layer deposition. *Journal of the American Chemical Society* **2001,** 123, (6), 1101-1110.

21. Mamedov, A. A.; Kotov, N. A., Free-standing layer-by-layer assembled films of magnetite nanoparticles. *Langmuir* **2000,** 16, (13), 5530-5533.

22. Mamedov, A.; Ostrander, J.; Aliev, F.; Kotov, N. A., Stratified assemblies of magnetite nanoparticles and montmorillonite prepared by the layer-by-layer assembly. *Langmuir* **2000,** 16, (8), 3941-3949.

23. Pastoriza-Santos, I.; Koktysh, D. S.; Mamedov, A. A.; Giersig, M.; Kotov, N. A.; Liz-Marzan, L. M., One-pot synthesis of Ag@TiO2 core-shell nanoparticles and their layer-by-layer assembly. *Langmuir* **2000,** 16, (6), 2731-2735.

24. Aliev, F. G.; Correa-Duarte, M. A.; Mamedov, A.; Ostrander, J. W.; Giersig, M.; Liz-Marzan, L. M.; Kotov, N. A., Layer-by-layer assembly of core-shell magnetite nanoparticles: Effect of silica coating on interparticle interactions and magnetic properties. *Advanced Materials* **1999,** 11, (12), 1006-1010.

25. Kotov, N. A.; Dekany, I.; Fendler, J. H., Layer-by-Layer Self-Assembly of Polyelectrolyte-Semiconductor Nanoparticle Composite Films. *Journal of Physical Chemistry* **1995,** 99, (35), 13065-13069.

26. Keller, S. W.; Kim, H. N.; Mallouk, T. E., Layer-by-Layer Assembly of Intercalation Compounds and Heterostructures on Surfaces - toward Molecular Beaker Epitaxy. *Journal of the American Chemical Society* **1994,** 116, (19), 8817-8818.

27. Mamedov, A. A.; Kotov, N. A.; Prato, M.; Guldi, D. M.; Wicksted, J. P.; Hirsch, A., Molecular design of strong single-wall carbon nanotube/polyelectrolyte multilayer composites. *Nature Materials* **2002,** 1, (3), 190-194.

28. Mamedov, A. A.; Belov, A.; Giersig, M.; Mamedova, N. N.; Kotov, N. A., Nanorainbows: Graded semiconductor films from quantum dots. *Journal of the American Chemical Society* **2001,** 123, (31), 7738-7739.

29. Tang, Z. Y.; Kotov, N. A.; Magonov, S.; Ozturk, B., Nanostructured artificial nacre. *Nature Materials* **2003,** 2, (6), 413-418.

30. Yoo, D.; Wu, A. P.; Lee, J.; Rubner, M. F., New electro-active self-assembled multilayer thin films based on alternately adsorbed layers of polyelectrolytes and functional dye molecules. *Synthetic Metals* **1997,** 85, (1-3), 1425-1426.

31. Jiang, C. Y.; Singamaneni, S.; Merrick, E.; Tsukruk, V. V., Complex buckling instability patterns of nanomembranes with encapsulated gold nanoparticle arrays. *Nano Letters* **2006,** 6, (10), 2254-2259.

32. Stockton, W. B.; Rubner, M. F., Molecular-level processing of conjugated polymers .4. Layer-by- layer manipulation of polyaniline via hydrogen-bonding interactions. *Macromolecules* **1997,** 30, (9), 2717-2725.

33. Wang, L. Y.; Wang, Z. Q.; Zhang, X.; Shen, J. C.; Chi, L. F.; Fuchs, H., A new approach for the fabrication of an alternating multilayer film of poly(4-vinylpyridine) and poly(acrylic acid) based on hydrogen bonding. *Macromolecular Rapid Communications* **1997,** 18, (6), 509-514.

34. Wang, L. Y.; Fu, Y.; Wang, Z. Q.; Fan, Y. G.; Zhang, X., Investigation into an alternating multilayer film of poly(4-vinylpyridine) and poly(acrylic acid) based on hydrogen bonding. *Langmuir* **1999,** 15, (4), 1360-1363.

35. Sukhishvili, S. A.; Granick, S., Layered, erasable, ultrathin polymer films. *Journal of the American Chemical Society* **2000,** 122, (39), 9550-9551.

36. Yang, S. Y.; Rubner, M. F., Micropatterning of polymer thin films with pH-sensitive and cross-linkable hydrogen-bonded polyelectrolyte multilayers. *Journal of the American Chemical Society* **2002,** 124, (10), 2100-2101.

37. Yoo, D.; Shiratori, S. S.; Rubner, M. F., Controlling bilayer composition and surface wettability of sequentially adsorbed multilayers of weak polyelectrolytes. *Macromolecules* **1998,** 31, (13), 4309-4318.

38. Shiratori, S. S.; Rubner, M. F., pH-dependent thickness behavior of sequentially adsorbed layers of weak polyelectrolytes. *Macromolecules* **2000,** 33, (11), 4213-4219.

39. Choi, J.; Rubner, M. F., Influence of the degree of ionization on weak polyelectrolyte multilayer assembly. *Macromolecules* **2005,** 38, (1), 116-124.

40. Schlenoff, J. B.; Dubas, S. T.; Farhat, T., Sprayed polyelectrolyte multilayers. *Langmuir* **2000,** 16, (26), 9968-9969.

41. Izquierdo, A.; Ono, S. S.; Voegel, J. C.; Schaaff, P.; Decher, G., Dipping versus spraying: Exploring the deposition conditions for speeding up layer-by-layer assembly. *Langmuir* **2005,** 21, (16), 7558-7567.

42. Fujita, S.; Fujimoto, K.; Naka, T.; Shiratori, S., Anti reflection films fabricated by roll-to-roll layer-by-layer adsorption process. *Ieice Transactions on Electronics* **2004,** E87C, (12), 2064-2070.

43. Fujimoto, K.; Fujita, S.; Ding, B.; Shiratori, S., Fabrication of layer-by-layer self-assembly films using roll-to-roll process. *Japanese Journal of Applied Physics Part 2-Letters & Express Letters* **2005,** 44, (1-7), L126-L128.

44. Bucur, C. B.; Sui, Z. J.; Schlenoff, J. B., Ideal mixing in polyelectrolyte complexes and multilayers: entropy driven assembly. *Journal of the American Chemical Society* **2006,** 128, (42), 13690-13691.

45. Mendelsohn, J. D.; Barrett, C. J.; Chan, V. V.; Pal, A. J.; Mayes, A. M.; Rubner, M. F., Fabrication of microporous thin films from polyelectrolyte multilayers. *Langmuir* **2000,** 16, (11), 5017-5023.

46. Choi, J. Y.; Rubner, M. F., Selective adsorption of amphiphilic block copolymers on weak polyelectrolyte multilayers. *Journal of Macromolecular Science-Pure and Applied Chemistry* **2001,** 38, (12), 1191-1206.

47. Mendelsohn, J. D.; Yang, S. Y.; Hiller, J.; Hochbaum, A. I.; Rubner, M. F., Rational design of cytophilic and cytophobic polyelectrolyte multilayer thin films. *Biomacromolecules* **2003,** 4, (1), 96-106.

48. Dante, S.; Hou, Z. Z.; Risbud, S.; Stroeve, P., Nucleation of iron oxy-hydroxide nanoparticles by layer-by- layer polyionic assemblies. *Langmuir* **1999,** 15, (6), 2176-2182.

49. Jiang, M.; Wang, E. B.; Kang, Z. H.; Lian, S. Y.; Wu, A. G.; Li, Z., In situ controllable synthesis of polyoxometalate nanoparticles in polyelectrolyte multilayers. *Journal of Materials Chemistry* **2003,** 13, (4), 647-649.

50. Joly, S.; Kane, R.; Radzilowski, L.; Wang, T.; Wu, A.; Cohen, R. E.; Thomas, E. L.; Rubner, M. F., Multilayer nanoreactors for metallic and semiconducting particles. *Langmuir* **2000,** 16, (3), 1354-1359.

51. Wang, T. C.; Rubner, M. F.; Cohen, R. E., Polyelectrolyte multilayer nanoreactors for preparing silver nanoparticle composites: Controlling metal concentration and nanoparticle size. *Langmuir* **2002,** 18, (8), 3370-3375.

52. Wang, D. Y.; Caruso, F., Polyelectrolyte-coated colloid spheres as templates for sol-gel reactions. *Chemistry of Materials* **2002,** 14, (5), 1909-1913.

53. Wang, D. Y.; Caruso, R. A.; Caruso, F., Synthesis of macroporous titania and inorganic composite materials from coated colloidal spheres - A novel route to tune pore morphology. *Chemistry of Materials* **2001,** 13, (2), 364-371.

54. Kramer, E.; Forster, S.; Goltner, C.; Antonietti, M., Synthesis of nanoporous silica with new pore morphologies by templating the assemblies of ionic block copolymers. *Langmuir* **1998,** 14, (8), 2027-2031.

55. Mayya, K. S.; Gittins, D. I.; Caruso, F., Gold-titania core-shell nanoparticles by polyelectrolyte complexation with a titania precursor. *Chemistry of Materials* **2001,** 13, (11), 3833-3836.

56. Wang, T. C.; Chen, B.; Rubner, M. F.; Cohen, R. E., Selective electroless nickel plating on polyelectrolyte multilayer platforms. *Langmuir* **2001,** 17, (21), 6610-6615.

57. Wang, T. C.; Rubner, M. F.; Cohen, R. E., Manipulating nanoparticle size within polyelectrolyte multilayers via electroless nickel deposition. *Chemistry of Materials* **2003,** 15, (1), 299-304.

58. Hiller, J. A.; Mendelsohn, J. D.; Rubner, M. F., Reversibly erasable nanoporous anti-reflection coatings from polyelectrolyte multilayers. *Nature Materials* **2002,** 1, (1), 59-63.

59. Zhai, L.; Nolte, A. J.; Cohen, R. E.; Rubner, M. F., pH-gated porosity transitions of polyelectrolyte multilayers in confined geometries and their application as tunable Bragg reflectors. *Macromolecules* **2004,** 37, (16), 6113-6123.

60. Zhai, L.; Cebeci, F. C.; Cohen, R. E.; Rubner, M. F., Stable superhydrophobic coatings from polyelectrolyte multilayers. *Nano Letters* **2004,** 4, (7), 1349-1353.

61. Zhai, L.; Berg, M. C.; Cebeci, F. C.; Kim, Y.; Milwid, J. M.; Rubner, M. F.; Cohen, R. E., Patterned superhydrophobic surfaces: Toward a synthetic mimic of the Namib Desert beetle. *Nano Letters* **2006,** 6, (6), 1213-1217.

62. Wang, T. C.; Cohen, R. E.; Rubner, M. F., Metallodielectric photonic structures based on polyelectrolyte multilayers. *Advanced Materials* **2002,** 14, (21), 1534-1537.

63. Wang, T. C. Polyelectrolyte Multilayers as Nanostructured Templates for Inorganic Synthesis. *Doctoral Thesis*, Massachusetts Institute of Technology, Cambridge, MA, 2002.

64. Cohen, R. E., Block copolymers as templates for functional materials. *Current Opinion in Solid State & Materials Science* **1999,** 4, (6), 587-590.

65. Kane, R. S.; Cohen, R. E.; Silbey, R., Semiconductor nanocluster growth within polymer films. *Langmuir* **1999,** 15, (1), 39-43.

66. Kane, R. S.; Cohen, R. E.; Silbey, R., Synthesis of doped ZnS nanoclusters within block copolymer nanoreactors. *Chemistry of Materials* **1999,** 11, (1), 90-93.

67. Kreibig, U.; Vollmer, M., *Optical Properties of Metal Clusters*. Springer-Verlag: Berlin, 1995.

68. Born, M.; Wolf, E., *Principles of Optics*. 6 ed.; Pergamon Press Inc.: Oxford, 1980.

69. Nolte, A. J.; Rubner, M. F.; Cohen, R. E., Creating effective refractive index gradients within polyelectrolyte multilayer films: Molecularly assembled rugate filters. *Langmuir* **2004,** 20, (8), 3304-3310.

70. Ibanescu, M.; Fink, Y.; Fan, S.; Thomas, E. L.; Joannopoulos, J. D., An all-dielectric coaxial waveguide. *Science* **2000,** 289, (5478), 415-419.

71. Baumeister, P.; Pincus, G., Optical interference coatings. *Scientific American* **1970,** 223, (6), 59-68,74-75.

72. Cunin, F.; Schmedake, T. A.; Link, J. R.; Li, Y. Y.; Koh, J.; Bhatia, S. N.; Sailor, M. J., Biomolecular screening with encoded porous-silicon photonic crystals. *Nature Materials* **2002,** 1, (1), 39-41.

73. Li, Y. Y.; Cunin, F.; Link, J. R.; Gao, T.; Betts, R. E.; Reiver, S. H.; Chin, V.; Bhatia, S. N.; Sailor, M. J., Polymer replicas of photonic porous silicon for sensing and drug delivery applications. *Science* **2003,** 299, (5615), 2045-2047.

74. Joannopoulos, J. D.; Meade, R. D.; Winn, J. N., *Photonic Crystals*. Princeton University Press: Princeton, 1995.

75. Fujita, S.; Shiratori, S., The optical properties of ultra-thin films fabricated by layer-by-layer adsorption process depending on dipping time. *Thin Solid Films* **2006,** 499, (1-2), 54-60.

76. Hattori, H., Anti-reflection surface with particle coating deposited by electrostatic attraction. *Advanced Materials* **2001,** 13, (1), 51-54.

77. Koo, H. Y.; Yi, D. K.; Yoo, S. J.; Kim, D. Y., A snowman-like array of colloidal dimers for antireflecting surfaces. *Advanced Materials* **2004,** 16, (3), 274-277.

78. Cebeci, F. C.; Wu, Z. Z.; Zhai, L.; Cohen, R. E.; Rubner, M. F., Nanoporosity-driven superhydrophilicity: A means to create multifunctional antifogging coatings. *Langmuir* **2006,** 22, (6), 2856-2862.

79. Wu, Z.; Walish, J.; Nolte, A.; Zhai, L.; Cohen, R. E.; Rubner, M. F., Deformable antireflection coatings from polymer and nanoparticle multilayers. *Advanced Materials* **2006,** 18, (20), 2699-2702.

80. Lee, D.; Rubner, M. F.; Cohen, R. E., All-Nanoparticle thin-film coatings. *Nano Letters* **2006,** 6, (10), 2305-2312.

81. Zhang, X. T.; Sato, O.; Taguchi, M.; Einaga, Y.; Murakami, T.; Fujishima, A., Self-cleaning particle coating with antireflection properties. *Chemistry of Materials* **2005,** 17, (3), 696-700.

82. Ahn, J. S.; Hammond, P. T.; Rubner, M. F.; Lee, I., Self-assembled particle monolayers on polyelectrolyte multilayers: particle size effects on formation, structure, and optical properties. *Colloids and Surfaces a-Physicochemical and Engineering Aspects* **2005,** 259, (1-3), 45-53.

83. Yancey, S. E.; Zhong, W.; Heflin, J. R.; Ritter, A. L., The influence of void space on antireflection coatings of silica nanoparticle self-assembled films. *Journal of Applied Physics* **2006,** 99, (3).

84. Jacobsson, R. In *A review of the optical properties of inhomogeneous thin films*, Inhomogeneous and quasi-inhomogeneous optical coatings, Quebec, Canada, 1993, 1993; SPIE: Quebec, Canada, 1993; pp 2-8.

85. Jacobsson, R., Optical properties of a class of inhomogeneous thin films. *Optica Acta* **1963,** 10, 309-323.

86. Jacobsson, R., *Light reflection from films of continuously varying refractive index*. North-Holland: Amsterdam, 1965; Vol. 5.

87. Jacobsson, R.; Martensson, J. O., Evaporated inhomogeneous thin films. *Applied Optics* **1965,** 5, (1), 29-34.

88. Jacobsson, R., *Inhomogeneous and coevaporated homogeneous films for optical applications*. Academic: New York, 1975; Vol. 8.

89. Gunning, W. J.; Hall, R. L.; Woodberry, F. J.; Southwell, W. H.; Gluck, N. S., Codeposition of continuous composition rugate filters. *Applied Optics* **1989,** 28, (14), 2945-2948.

90. Allen, J.; Herrington, B. In *Digitized rugate filters for laser rejection*, Inhomogeneous and quasi-inhomogeneous optical coatings, 1993, 1993; SPIE: 1993; pp 126-131.

91. Poitras, D.; Larouche, S.; Martinu, L., Design and plasma deposition of dispersion-corrected multiband rugate filters. *Applied Optics* **2002,** 41, (25), 5249-5255.

92. Linkens, D. A.; Abbod, M. F.; Metcalfe, J.; Nichols, B., Modeling and fabrication of optical interference rugate filters. *Isa Transactions* **2001,** 40, (1), 3-16.

93. Baumeister, P., Simulation of a rugate filter via a stepped-index dielectric multilayer. *Applied Optics* **1986,** 25, (16), 2644-2645.

94. Tikhonravov, A. V.; Trubetskov, M. K.; Hrdina, J.; Sobota, J., Characterization of quasi-rugate filters using ellipsometric measurements. *Thin Solid Films* **1996,** 277, (1-2), 83-89.

95. Abusafia, H. A.; Alsharif, A. I.; Abualjarayesh, I. O., Rugate Filter Sidelobe Suppression Using Half-Apodization. *Applied Optics* **1993,** 32, (25), 4831-4835.

96. Bataineh, M.; Asfar, O. R., Application of multiple scales analysis and the fundamental matrix method to rugate filters: Initial-value and two-point boundary problem formulations. *Journal of Lightwave Technology* **2000,** 18, (12), 2217-2223.

97. Bovard, B. G., Rugate Filter Theory - an Overview. *Applied Optics* **1993,** 32, (28), 5427-5442.

98. Bovard, B.; Vanmilligen, F. J.; Messerly, M. J.; Saxe, S. G.; Macleod, H. A., Optical-Constants Derivation For an Inhomogeneous Thin-Film From Insitu Transmission Measurements. *Applied Optics* **1985,** 24, (12), 1803-1807.

99. Bovard, B. G., Derivation of a New Matrix For an Inhomogeneous Dielectric Thin-Film. *Journal of the Optical Society of America A-Optics, Image Science, and Vision* **1986,** 3, (13), P7-P7.

100. Bovard, B. G., Derivation of a Matrix Describing a Rugate Dielectric Thin-Film. *Applied Optics* **1988,** 27, (10), 1998-2005.

101. Bovard, B. G., Rugate Filter Design - the Modified Fourier-Transform Technique. *Applied Optics* **1990,** 29, (1), 24-30.

102. Fabricius, H., Gradient-Index Filters - Designing Filters With Steep Skirts, High Reflection, and Quintic Matching Layers. *Applied Optics* **1992,** 31, (25), 5191-5196.

103. Johnson, W. E.; Crane, R. L. In *Introduction to rugate filter technology*, Proceedings of SPIE, 1993, 1993; SPIE: 1993; pp 88-108.

104. Perelman, N.; Averbukh, I., Rugate filter design: An analytical approach using uniform WKB solutions. *Journal of Applied Physics* **1996,** 79, (6), 2839-2845.

105. Rahmlow, T. D.; Tirri, B. A. In *Graded period rugates*, Proceedings of SPIE, 1993, 1993; SPIE: 1993; pp 147-153.

106. Rouxel, Y. In *Analytical approach of rugate filter properties using Mathieu functions*, Proceedings of SPIE, 1994, 1994; SPIE: 1994; pp 59-72.

107. Southwell, W. H., Spectral Response Calculations of Rugate Filters Using Coupled- Wave Theory. *Journal of the Optical Society of America a-Optics Image Science and Vision* **1988,** 5, (9), 1558-1563.

108. Southwell, W. H., Using apodization functions to reduce sidelobes in rugate filters. *Applied Optics* **1989,** 28, (23), 5091-5094.

109. Southwell, W. H., Extended-bandwidth reflector designs by using wavelets. *Applied Optics* **1997,** 36, (1), 314-318.

110. Southwell, W. H.; Hall, R. L., Rugate Filter Sidelobe Suppression Using Quintic and Rugated Quintic Matching Layers. *Applied Optics* **1989,** 28, (14), 2949-2951.

111. Tikhonravov, A. V., Some Theoretical Aspects of Thin-Film Optics and Their Applications. *Applied Optics* **1993,** 32, (28), 5417-5426.

112. Tikhonravov, A. V. In *Mathematical aspects of the synthesis of inhomogeneous coatings*, Proceedings of SPIE, 1993, 1993; SPIE: 1993; pp 18-29.

113. Willey, R. R. In *Rugate broadband antireflection coating design*, Current developments in optical engineering and commerical optics, San Diego, 1989; SPIE: San Diego, 1989; pp 224-228.

114. Willey, R. R. In *Basic nature and properties of inhomogeneous antireflection coatings*, Proceedings of SPIE, 1993, 1993; SPIE: 1993; pp 69-77.

115. Verly, P. G. In *Multiple solutions to the synthesis of graded index optical coatings*, Proceedings of SPIE, 1993, 1993; SPIE: 1993; pp 9-16.

116. Verly, P. G., Fourier-Transform Technique With Frequency Filtering For Optical Thin-Film Design. *Applied Optics* **1995,** 34, (4), 688-694.

117. Verly, P. G.; Dobrowolski, J. A.; Wild, W. J.; Burton, R. L., Synthesis of High Rejection Filters With the Fourier-Transform Method. *Applied Optics* **1989,** 28, (14), 2864-2875.

118. Baumeister, P., Multilayer reflectors with absent higher-order reflectance bands. *Applied Optics* **1996,** 35, (25), 4978-4981.

119. Gunning, W. In *Gradient-index thin films: an emerging optical coating technology*, Thin film technologies III, Hamburg, Germany, 1989, 1989; SPIE: Hamburg, Germany, 1989; pp 204-210.

120. Southwell, W. H., Gradient-Index Anti-Reflection Coatings. *Optics Letters* **1983,** 8, (11), 584-586.

121. Southwell, W. H., Use of Gradient Index For Spectral Filters. *Proceedings of the Society of Photo-Optical Instrumentation Engineers* **1984,** 464, 110-114.

122. Southwell, W. H., Coating design using very thin high-index and low-index layers. *Applied Optics* **1985,** 24, (4), 457-460.

123. Sankur, H.; Southwell, W. H., Broad-band gradient-index antireflection coating for ZnSe. *Applied Optics* **1984,** 23, (16), 2770-2773.

124. Greenewalt, C. H.; Brandt, W.; Friel, D. D., Iridescent colors of hummingbird feathers. *Journal of the Optical Society of America* **1960,** 50, (10), 1005-1013.

125. Delano, E., Fourier synthesis of multilayer filters. *Journal of the Optical Society of America* **1967,** 57, (12), 1529-1533.

126. Vincent, G., Optical properties of porous silicon superlattices. *Applied Physics Letters* **1994,** 64, (18), 2367-2369.

127. Kaminska, K.; Brown, T.; Beydaghyan, G.; Robbie, K., Vacuum evaporated porous silicon photonic interference filters. *Applied Optics* **2003,** 42, (20), 4212-4219.

128. Wang, X.; Masumoto, H.; Someno, Y.; Hirai, T., Design and experimental approach of optical reflection filters with graded refractive index profiles. *Journal of Vacuum Science & Technology a-Vacuum Surfaces and Films* **1999,** 17, (1), 206-211.

129. Wang, X. R.; Masumoto, H.; Someno, Y.; Chen, L. D.; Hirai, T., Fabrication of a 33-layer optical reflection filter with stepwise graded refractive index profiles. *Journal of Materials Research* **2000,** 15, (2), 274-277.

130. Herpin, A., Calcul du pouvoir reflecteur d'un systeme stratifie quelconque. *Comptes Rendus Academie des Sciences* **1947,** 225, 182-183.

131. Epstein, L. I., The design of optical filters. *Journal of the Optical Society of America* **1952,** 42, (11), 806-810.

132. Berning, P. H., Use of equivalent films in the design of infrared multilayer antireflection coatings. *Journal of the Optical Society of America* **1962,** 52, (4), 431-436.

133. Carr, N.; Goodwin, M. J.; Harrison, K. J.; Lewis, K. L., The design and fabrication of optical filters using organic materials. *Thin Solid Films* **1993,** 230, (1), 59-64.

134. Goodwin, M. J.; Carr, N.; Harrison, K.; Lewis, K., Organic quarter-wave stack filter fabricated by Langmuir- Blodgett deposition. *Optics Letters* **1991,** 16, (10), 699-701.

135. Jessel, N.; Atalar, F.; Lavalle, P.; Mutterer, J.; Decher, G.; Schaaf, P.; Voegel, J. C.; Ogier, J., Bioactive coatings based on a polyelectrolyte multilayer architecture functionalized by embedded proteins. *Advanced Materials* **2003,** 15, (9), 692-695.

136. Lavalle, P.; Gergely, C.; Cuisinier, F. J. G.; Decher, G.; Schaaf, P.; Voegel, J. C.; Picart, C., Comparison of the structure of polyelectrolyte multilayer films exhibiting a linear and an exponential growth regime: An in situ atomic force microscopy study. *Macromolecules* **2002,** 35, (11), 4458-4465.

137. Nolte, A. J.; Rubner, M. F.; Cohen, R. E., Determining the young's modulus of polyelectrolyte multilayer films via stress-induced mechanical buckling instabilities. *Macromolecules* **2005,** 38, (13), 5367-5370.

138. Thompson, M. T.; Berg, M. C.; Tobias, I. S.; Lichter, J. A.; Rubner, M. F.; Van Vliet, K. J., Biochemical functionalization of polymeric cell substrata can alter mechanical compliance. *Biomacromolecules* **2006,** 7, (6), 1990-1995.

139. Baumler, H.; Artmann, G.; Voigt, A.; Mitlohner, R.; Neu, B.; Kiesewetter, H., Plastic behaviour of polyelectrolyte microcapsules derived from colloid templates. *Journal of Microencapsulation* **2000,** 17, (5), 651-655.

140. Collin, D.; Lavalle, P.; Garza, J. M.; Voegel, J. C.; Schaaf, P.; Martinoty, P., Mechanical properties of cross-linked hyaluronic acid/poly-(L-lysine) multilayer films. *Macromolecules* **2004,** 37, (26), 10195-10198.

141. Dubreuil, F.; Elsner, N.; Fery, A., Elastic properties of polyelectrolyte capsules studied by atomic-force microscopy and RICM. *European Physical Journal E* **2003,** 12, (2), 215-221.

142. Dubreuil, F.; Shchukin, D. G.; Sukhorukov, G. B.; Fery, A., Polyelectrolyte capsules modified with YF3 nanoparticles: An AFM study. *Macromolecular Rapid Communications* **2004,** 25, (11), 1078-1081.

143. Engler, A. J.; Richert, L.; Wong, J. Y.; Picart, C.; Discher, D. E., Surface probe measurements of the elasticity of sectioned tissue, thin gels and polyelectrolyte multilayer films: Correlations between substrate stiffness and cell adhesion. *Surface Science* **2004,** 570, (1-2), 142-154.

144. Fan, X. W.; Park, M. K.; Xia, C. J.; Advincula, R., Surface structural characterization and mechanical testing by nanoindentation measurements of hybrid polymer/clay nanostructured multilayer films. *Journal of Materials Research* **2002,** 17, (7), 1622-1633.

145. Fery, A.; Dubreuil, F.; Mohwald, H., Mechanics of artificial microcapsules. *New Journal of Physics* **2004,** 6, 1-13.

146. Gao, C.; Donath, E.; Moya, S.; Dudnik, V.; Mohwald, H., Elasticity of hollow polyelectrolyte capsules prepared by the layer-by-layer technique. *European Physical Journal E* **2001,** 5, (1), 21-27.

147. Gao, C. Y.; Leporatti, S.; Moya, S.; Donath, E.; Mohwald, H., Stability and mechanical properties of polyelectrolyte capsules obtained by stepwise assembly of poly(styrenesulfonate sodium salt) and poly(diallyldimethyl ammonium) chloride onto melamine resin particles. *Langmuir* **2001,** 17, (11), 3491-3495.

148. Hsieh, M. C. Polyelectrolyte multilayer assemblies. *Thesis*, University of Massachusetts, Amherst, 1999.

149. Hsieh, M. C.; Farris, R. J.; McCarthy, T. J., Mechanical properties of layer-by-layer-deposited polyelectrolyte assemblies. *Abstracts of Papers of the American Chemical Society* **1999,** 218, U620-U620.

150. Jiang, C. Y.; Markutsya, S.; Pikus, Y.; Tsukruk, V. V., Freely suspended nanocomposite membranes as highly sensitive sensors. *Nature Materials* **2004,** 3, (10), 721-728.

151. Jiang, C. Y.; Markutsya, S.; Tsukruk, V. V., Compliant, robust, and truly nanoscale free-standing multilayer films fabricated using spin-assisted layer-by-layer assembly. *Advanced Materials* **2004,** 16, (2), 157-161.

152. Kim, B. S.; Vinogradova, O. I., pH-Controlled swelling of polyelectrolyte multilayer microcapsules. *Journal of Physical Chemistry B* **2004,** 108, (24), 8161-8165.

153. Lebedeva, O. V.; Kim, L. S.; Vinogradova, O. I., Mechanical properties of polyelectrolyte-filled multilayer microcapsules studied by atomic force and confocal microscopy. *Langmuir* **2004,** 20, (24), 10685-10690.

154. Lulevich, V. V.; Andrienko, D.; Vinogradova, O. I., Elasticity of polyelectrolyte multilayer microcapsules. *Journal of Chemical Physics* **2004,** 120, (8), 3822-3826.

155. Lulevich, V. V.; Nordschild, S.; Vinogradova, O. I., Investigation of molecular weight and aging effects on the stiffness of polyelectrolyte multilayer microcapsules. *Macromolecules* **2004,** 37, (20), 7736-7741.

156. Lulevich, V. V.; Radtchenko, I. L.; Sukhorukov, G. B.; Vinogradova, O. I., Mechanical properties of polyelectrolyte microcapsules filled with a neutral polymer. *Macromolecules* **2003,** 36, (8), 2832-2837.

157. Lulevich, V. V.; Radtchenko, I. L.; Sukhorukov, G. B.; Vinogradova, O. I., Deformation properties of nonadhesive polyelectrolyte microcapsules studied with the atomic force microscope. *Journal of Physical Chemistry B* **2003,** 107, (12), 2735-2740.

158. Lulevich, V. V.; Vinogradova, O. I., Effect of pH and salt on the stiffness of polyelectrolyte multilayer microcapsules. *Langmuir* **2004,** 20, (7), 2874-2878.

159. Mermut, O.; Lefebvre, J.; Gray, D. G.; Barrett, C. J., Structural and mechanical properties of polyelectrolyte multilayer films studied by AFM. *Macromolecules* **2003,** 36, (23), 8819-8824.

160. Pavoor, P. V.; Bellare, A.; Strom, A.; Yang, D. H.; Cohen, R. E., Mechanical characterization of polyelectrolyte multilayers using quasi-static nanoindentation. *Macromolecules* **2004,** 37, (13), 4865-4871.

161. Pavoor, P. V.; Gearing, B. P.; Gorga, R. E.; Bellare, A.; Cohen, R. E., Engineering the friction-and-wear behavior of polyelectrolyte multilayer nanoassemblies through block copolymer surface capping, metallic nanoparticles, and multiwall carbon nanotubes. *Journal of Applied Polymer Science* **2004,** 92, (1), 439-448.

162. Richert, L.; Engler, A. J.; Discher, D. E.; Picart, C., Elasticity of native and cross-linked polyelectrolyte multilayer films. *Biomacromolecules* **2004,** 5, (5), 1908-1916.

163. Salomaki, M.; Laiho, T.; Kankare, J., Counteranion-controlled properties of polyelectrolyte multilayers. *Macromolecules* **2004,** 37, (25), 9585-9590.

164. Salomaki, M.; Loikas, K.; Kankare, J., Effect of polyelectrolyte multilayers on the response of a quartz crystal microbalance. *Analytical Chemistry* **2003,** 75, (21), 5895-5904.

165. Vinogradova, O. I., Mechanical properties of polyelectrolyte multilayer microcapsules. *Journal of Physics-Condensed Matter* **2004,** 16, (32), R1105-R1134.

166. Vinogradova, O. I.; Andrienko, D.; Lulevich, V. V.; Nordschild, S.; Sukhorukov, G. B., Young's modulus of polyelectrolyte multilayers from microcapsule swelling. *Macromolecules* **2004,** 37, (3), 1113-1117.

167. Heuvingh, J.; Zappa, M.; Fery, A., Salt softening of polyelectrolyte multilayer capsules. *Langmuir* **2005,** 21, (7), 3165-3171.

168. Stafford, C. M.; Harrison, C.; Beers, K. L.; Karim, A.; Amis, E. J.; Vanlandingham, M. R.; Kim, H. C.; Volksen, W.; Miller, R. D.; Simonyi, E. E., A buckling-based metrology for measuring the elastic moduli of polymeric thin films. *Nature Materials* **2004,** 3, (8), 545-550.

169. Berg, M. C.; Yang, S. Y.; Hammond, P. T.; Rubner, M. F., Controlling mammalian cell interactions on patterned polyelectrolyte multilayer surfaces. *Langmuir* **2004,** 20, (4), 1362-1368.

170. Boura, C.; Kerdjoudj, H.; Moby, V.; Vautier, D.; Dumas, D.; Schaaf, P.; Voegel, J. C.; Stoltz, J. F.; Menu, P., Initial adhesion of endothelial cells on polyelectrolyte multilayer films. *Bio-Medical Materials and Engineering* **2006,** 16, (S4), S115-S121.

171. Boura, C.; Muller, S.; Vautier, D.; Dumas, D.; Schaaf, P.; Voegel, J. C.; Stoltz, J. F.; Menu, P., Endothelial cell - interactions with polyelectrolyte multilayer films. *Biomaterials* **2005,** 26, (22), 4568-4575.

172. Boura, C.; Muller, S.; Voegel, J. C.; Schaaf, P.; Stoltz, J. F.; Menu, P., Behaviour of endothelial cells seeded on thin polyelectrolyte multilayered films: A new biological scaffold. *Clinical Hemorheology and Microcirculation* **2005,** 33, (3), 269-275.

173. Etienne, O.; Gasnier, C.; Taddei, C.; Voegel, J. C.; Aunis, D.; Schaaf, P.; Metz-Boutigue, M. H.; Bolcato-Bellemin, A. L.; Egles, C., Antifungal coating by biofunctionalized polyelectrolyte multilayered films. *Biomaterials* **2005,** 26, (33), 6704-6712.

174. Georges, P. C.; Janmey, P. A., Cell type-specific response to growth on soft materials. *Journal of Applied Physiology* **2005,** 98, (S4), 1547-1553.

175. Kerdjoudj, H.; Boura, C.; Marchal, L.; Dumas, D.; Schaff, P.; Voegel, J. C.; Stoltz, J. F.; Menu, P., Decellularized umbilical artery treated with thin polyelectrolyte multilayer films: Potential use in vascular engineering. *Bio-Medical Materials and Engineering* **2006,** 16, (4), S123-S129.

176. Mhamdi, L.; Picart, C.; Lagneau, C.; Othmane, A.; Grosgogeat, B.; Jaffrezic-Renault, N.; Ponsonnet, L., Study of the polyelectrolyte multilayer thin films' properties and correlation with the behavior of the human gingival fibroblasts. *Materials Science & Engineering C-Biomimetic and Supramolecular Systems* **2006,** 26, (2-3), 273-281.

177. Ngankam, A. P.; Mao, G. Z.; Van Tassel, P. R., Fibronectin adsorption onto polyelectrolyte multilayer films. *Langmuir* **2004,** 20, (8), 3362-3370.

178. Olenych, S. G.; Moussallem, M. D.; Salloum, D. S.; Schlenoff, J. B.; Keller, T. C. S., Fibronectin and cell attachment to cell and protein resistant polyelectrolyte surfaces. *Biomacromolecules* **2005,** 6, (6), 3252-3258.

179. Picart, C.; Elkaim, R.; Richert, L.; Audoin, T.; Arntz, Y.; Cardoso, M. D.; Schaaf, P.; Voegel, J. C.; Frisch, B., Primary cell adhesion on RGD-functionalized and covalently crosslinked thin polyelectrolyte multilayer films. *Advanced Functional Materials* **2005,** 15, (1), 83-94.

180. Richert, L.; Arntz, Y.; Schaaf, P.; Voegel, J. C.; Picart, C., pH dependent growth of poly(L-lysine)/poly(L-glutamic) acid multilayer films and their cell adhesion properties. *Surface Science* **2004,** 570, (1-2), 13-29.

181. Richert, L.; Boulmedais, F.; Lavalle, P.; Mutterer, J.; Ferreux, E.; Decher, G.; Schaaf, P.; Voegel, J. C.; Picart, C., Improvement of stability and cell adhesion properties of polyelectrolyte multilayer films by chemical cross-linking. *Biomacromolecules* **2004,** 5, (2), 284-294.

182. Richert, L.; Lavalle, P.; Vautier, D.; Senger, B.; Stoltz, J. F.; Schaaf, P.; Voegel, J. C.; Picart, C., Cell interactions with polyelectrolyte multilayer films. *Biomacromolecules* **2002,** 3, (6), 1170-1178.

183. Richert, L.; Schneider, A.; Vautier, D.; Vodouhe, C.; Jessel, N.; Payan, E.; Schaaf, P.; Voegel, J. C.; Picart, C., Imaging cell interactions with native and crosslinked polyelectrolyte multilayers. *Cell Biochemistry and Biophysics* **2006,** 44, (2), 273-285.

184. Schneider, A.; Francius, G.; Obeid, R.; Schwinte, P.; Hemmerle, J.; Frisch, B.; Schaaf, P.; Voegel, J. C.; Senger, B.; Picart, C., Polyelectrolyte multilayers with a tunable Young's modulus: Influence of film stiffness on cell adhesion. *Langmuir* **2006,** 22, (3), 1193-1200.

185. Schoeler, B.; Delorme, N.; Doench, I.; Sukhorukov, G. B.; Fery, A.; Glinel, K., Polyelectrolyte films based on polysaccharides of different conformations: Effects on multilayer structure and mechanical properties. *Biomacromolecules* **2006,** 7, (6), 2065-2071.

186. Dubas, S. T.; Schlenoff, J. B., Swelling and smoothing of polyelectrolyte multilayers by salt. *Langmuir* **2001,** 17, (25), 7725-7727.

187. Jomaa, H. W.; Schlenoff, J. B., Salt-induced polyelectrolyte interdiffusion in multilayered films: A neutron reflectivity study. *Macromolecules* **2005,** 38, (20), 8473-8480.

188. Kovacevic, D.; van der Burgh, S.; de Keizer, A.; Stuart, M. A. C., Kinetics of formation and dissolution of weak polyelectrolyte multilayers: Role of salt and free polyions. *Langmuir* **2002,** 18, (14), 5607-5612.

189. Lebedeva, O. V.; Kim, B. S.; Vasilev, K.; Vinogradova, O. I., Salt softening of polyelectrolyte multilayer microcapsules. *Journal of Colloid and Interface Science* **2005,** 284, (2), 455-462.

190. McAloney, R. A.; Dudnik, V.; Goh, M. C., Kinetics of salt-induced annealing of a polyelectrolyte multilayer film morphology. *Langmuir* **2003,** 19, (9), 3947-3952.

191. Ren, K. F.; Wang, Y. X.; Ji, J.; Lin, Q. K.; Shen, J. C., Construction and deconstruction of PLL/DNA multilayered films for DNA delivery: Effect of ionic strength. *Colloids and Surfaces B-Biointerfaces* **2005,** 46, (2), 63-69.

192. Rmaile, H. H.; Schlenoff, J. B., "Internal pK(a)'s" in polyelectrolyte multilayers: Coupling protons and salt. *Langmuir* **2002,** 18, (22), 8263-8265.

193. Fischer-Cripps, A. C., *Nanoindentation*. Springer-Verlag, Inc.: New York, 2002.

194. Jaber, J. A.; Schlenoff, J. B., Mechanical properties of reversibly cross-linked ultrathin polyelectrolyte complexes. *Journal of the American Chemical Society* **2006,** 128, (9), 2940-2947.

195. Jaber, J. A.; Schlenoff, J. B., Dynamic viscoelasticity in polyelectrolyte multilayers: Nanodamping. *Chemistry of Materials* **2006,** ASAP.

196. Volynskii, A. L.; Bazhenov, S.; Lebedeva, O. V.; Bakeev, N. F., Mechanical buckling instability of thin coatings deposited on soft polymer substrates. *Journal of Materials Science* **2000,** 35, (3), 547-554.

197. Biot, M. A., Bending of an infinite beam on an elastic foundation. *Journal of Applied Mechanics* **1937,** 4, A1-A7.

198. Harrison, C.; Stafford, C. M.; Zhang, W. H.; Karim, A., Sinusoidal phase grating created by a tunably buckled surface. *Applied Physics Letters* **2004,** 85, (18), 4016-4018.

199. "Propagation of uncertainty." (23 September 2006). In *Wikipedia.* Retrieved October 17, 2006, from http://en.wikipedia.org/w/index.php?title=Propagation_of_uncertainty&oldid=77380983.

200. Taylor, B. N.; Kuyatt, C. E., *Guidelines for Evaluating and Expressing the Uncertainty of NIST Measurement Results (NIST Technical Note 1297, 1994 ed.)*. U.S. Government Printing Office: Washington, 1994.

201. Urbach, F., The long-wavelength edge of photographic sensitivity and of the electronic absorption of solids. *Physical Review* **1953,** 92, (5), 1324.

202. Ladam, G.; Schaad, P.; Voegel, J. C.; Schaaf, P.; Decher, G.; Cuisinier, F., In situ determination of the structural properties of initially deposited polyelectrolyte multilayers. *Langmuir* **2000,** 16, (3), 1249-1255.

203. Itano, K.; Choi, J.; Rubner, M. F., Mechanism of the pH-induced discontinuous swelling/deswelling transitions of poly(allylamine hydrochloride)-containing polyelectrolyte multilayer films. *Macromolecules* **2005,** 38, (8), 3450-3460.

204. Hiller, J.; Rubner, M. F., Reversible molecular memory and pH-switchable swelling transitions in polyelectrolyte multilayers. *Macromolecules* **2003,** 36, (11), 4078-4083.

205. Nolte, A. J.; Cohen, R. E.; Rubner, M. F., A two-plate buckling technique for thin film modulus measurements: Applications to polyelectrolyte multilayers. *Macromolecules* **2006,** 39, (14), 4841-4847.

206. Park, J.; Hammond, P. T., Polyelectrolyte multilayer formation on neutral hydrophobic surfaces. *Macromolecules* **2005,** 38, (25), 10542-10550.

207. Hillborg, H.; Tomczak, N.; Olah, A.; Schonherr, H.; Vancso, G. J., Nanoscale hydrophobic recovery: A chemical force microscopy study of UV/ozone-treated cross-linked poly(dimethylsiloxane). *Langmuir* **2004,** 20, (3), 785-794.

208. Olah, A.; Hillborg, H.; Vancso, G. J., Hydrophobic recovery of UV/ozone treated poly(dimethylsiloxane): adhesion studies by contact mechanics and mechanism of surface modification. *Applied Surface Science* **2005,** 239, (3-4), 410-423.

209. Hillborg, H.; Gedde, U. W., Hydrophobicity recovery of polydimethylsiloxane after exposure to corona discharges. *Polymer* **1998,** 39, (10), 1991-1998.

210. Chua, D. B. H.; Ng, H. T.; Li, S. F. Y., Spontaneous formation of complex and ordered structures on oxygen-plasma-treated elastomeric polydimethylsiloxane. *Applied Physics Letters* **2000,** 76, (6), 721-723.

211. Stafford, C. M.; Guo, S.; Harrison, C.; Chiang, M. Y. M., Combinatorial and high-throughput measurements of the modulus of thin polymer films. *Review of Scientific Instruments* **2005,** 76, (6), 062207.

212. Beer, F. P.; E. Russel Johnston, J., *Mechanics of Materials*. 2 ed.; McGraw-Hill, Inc.: New York, 1992.

213. Allen, H. G., *Analysis and Design of Structural Sandwich Panels*. Pergamon Press Ltd.: Oxford, 1969.

214. Jiang, C. Y.; Kommireddy, D. S.; Tsukruk, V. V., Gradient array of freely suspended nanomembranes. *Advanced Functional Materials* **2006,** 16, (1), 27-32.

215. Li, J. W.; Oh, K. H.; Yu, H., Surface rearrangements of oxygen plasma treated polystyrene: Surface dynamics and humidity effect. *Chinese Journal of Polymer Science* **2005,** 23, (2), 187-196.

216. Bonaccurso, E.; Cappella, B.; Graf, K., Local mechanical properties of plasma treated polystyrene surfaces. *Journal of Physical Chemistry B* **2006,** 110, (36), 17918-17924.

217. Muratoglu, O. K.; Argon, A. S.; Cohen, R. E.; Weinberg, M., Microstructural Processes of Fracture of Rubber-Modified Polyamides. *Polymer* **1995,** 36, (25), 4771-4786.

218. Hollaway, L., *Handbook of polymer composites for engineers*. Woodhead Publishing Ltd.: Cambridge, England, 1994.

219. Ye, S. Q.; Wang, C. Y.; Liu, X. X.; Tong, Z.; Ren, B.; Zeng, F., New loading process and release properties of insulin from polysaccharide microcapsules fabricated through layer-by-layer assembly. *Journal of Controlled Release* **2006,** 112, (1), 79-87.

220. Berg, M. C.; Zhai, L.; Cohen, R. E.; Rubner, M. F., Controlled drug release from porous polyelectrolyte multilayers. *Biomacromolecules* **2006,** 7, (1), 357-364.

221. Barry, R. A.; Wiltzius, P., Humidity-sensing inverse opal hydrogels. *Langmuir* **2006,** 22, (3), 1369-1374.

222. Arregui, F. J.; Ciaurriz, Z.; Oneca, M.; Matias, I. R., An experimental study about hydrogels for the fabrication of optical fiber humidity sensors. *Sensors and Actuators B-Chemical* **2003,** 96, (1-2), 165-172.

223. Annaka, M.; Tanaka, T., Multiple Phases of Polymer Gels. *Nature* **1992,** 355, (6359), 430-432.

224. Higbie, J., Uncertainty in the Linear-Regression Slope. *American Journal of Physics* **1991,** 59, (2), 184-185.

225. Wong, J. E.; Rehfeldt, F.; Hanni, P.; Tanaka, M.; Klitzing, R. V., Swelling behavior of polyelectrolyte multilayers in saturated water vapor. *Macromolecules* **2004,** 37, (19), 7285-7289.

226. Kugler, R.; Schmitt, J.; Knoll, W., The swelling Behavior of polyelectrolyte multilayers in air of different relative humidity and in water. *Macromolecular Chemistry and Physics* **2002,** 203, (2), 413-419.

227. Halthur, T. J.; Claesson, P. M.; Elofsson, U. M., Stability of polypeptide multilayers as studied by in situ ellipsometry: Effects of drying and post-buildup changes in temperature and pH. *Journal of the American Chemical Society* **2004,** 126, (51), 17009-17015.

228. Blasi, P.; D'Souza, S. S.; Selmin, F.; DeLuca, P. P., Plasticizing effect of water on poly(lactide-co-glycolide). *Journal of Controlled Release* **2005,** 108, (1), 1-9.

229. Hsieh, M. C.; Farris, R. J.; McCarthy, T. J., Surface "priming" for layer-by-layer deposition: Polyelectrolyte multilayer formation on allylamine plasma-modified poly(tetrafluoroethylene). *Macromolecules* **1997,** 30, (26), 8453-8458.

230. Zawodzinski, T. A.; Derouin, C.; Radzinski, S.; Sherman, R. J.; Smith, V. T.; Springer, T. E.; Gottesfeld, S., Water-Uptake by and Transport through Nafion(R) 117 Membranes. *Journal of the Electrochemical Society* **1993,** 140, (4), 1041-1047.

231. Laporta, M.; Pegoraro, M.; Zanderighi, L., Perfluorosulfonated membrane (Nafion): FT-IR study of the state of water with increasing humidity. *Physical Chemistry Chemical Physics* **1999,** 1, (19), 4619-4628.

232. Bauer, F.; Denneler, S.; Willert-Porada, M., Influence of temperature and humidity on the mechanical properties of Nafion (R) 117 polymer electrolyte membrane. *Journal of Polymer Science Part B-Polymer Physics* **2005,** 43, (7), 786-795.

233. Izumrudov, V.; Sukhishvili, S. A., Ionization-controlled stability of polyelectrolyte multilayers in salt solutions. *Langmuir* **2003,** 19, (13), 5188-5191.

234. Kovacevic, D.; van der Burgh, S.; de Keizer, A.; Stuart, M. A. C., Specific ionic effects on weak polyelectrolyte multilayer formation. *Journal of Physical Chemistry B* **2003,** 107, (32), 7998-8002.

235. Kharlampieva, E.; Sukhishvili, S. A., Ionization and pH stability of multilayers formed by self-assembly of weak polyelectrolytes. *Langmuir* **2003,** 19, (4), 1235-1243.

236. Sukhishvili, S. A.; Granick, S., Layered, erasable polymer multilayers formed by hydrogen-bonded sequential self-assembly. *Macromolecules* **2002,** 35, (1), 301-310.

237. Dubas, S. T.; Schlenoff, J. B., Polyelectrolyte multilayers containing a weak polyacid: Construction and deconstruction. *Macromolecules* **2001,** 34, (11), 3736-3740.

238. Sui, Z. J.; Salloum, D.; Schlenoff, J. B., Effect of molecular weight on the construction of polyelectrolyte multilayers: Stripping versus sticking. *Langmuir* **2003,** 19, (6), 2491-2495.

239. Sui, Z. J.; Schlenoff, J. B., Phase separations in pH-responsive polyelectrolyte multilayers: Charge extrusion versus charge expulsion. *Langmuir* **2004,** 20, (14), 6026-6031.

240. Kabanov, V. A., Physicochemical basis and the prospects of using soluble interpolyelectrolyte complexes (review). *Polymer Science* **1994,** 36, (2), 143-156.

241. Biesheuvel, P. M.; Stuart, M. A. C., Cylindrical cell model for the electrostatic free energy of polyelectrolyte complexes. *Langmuir* **2004,** 20, (11), 4764-4770.

242. Biesheuvel, P. M.; Stuart, M. A. C., Electrostatic free energy of weakly charged macromolecules in solution and intermacromolecular complexes consisting of oppositely charged polymers. *Langmuir* **2004,** 20, (7), 2785-2791.

243. Sui, Z. J.; Jaber, J. A.; Schlenoff, J. B., Polyelectrolyte complexes with pH-tunable solubility. *Macromolecules* **2006,** 39, (23), 8145-8152.

244. Schlenoff, J. B.; Ly, H.; Li, M., Charge and mass balance in polyelectrolyte multilayers. *Journal of the American Chemical Society* **1998,** 120, (30), 7626-7634.

245. Izumrudov, V.; Kharlampieva, E.; Sukhishvili, S. A., Salt-induced multilayer growth: Correlation with phase separation in solution. *Macromolecules* **2004,** 37, (22), 8400-8406.

246. Douglas, J. F.; Johnson, H. E.; Granick, S., A Simple Kinetic-Model of Polymer Adsorption and Desorption. *Science* **1993,** 262, (5142), 2010-2012.

247. Tanchak, O. M.; Barrett, C. J., Swelling dynamics of multilayer films of weak polyelectrolytes. *Chemistry of Materials* **2004,** 16, (14), 2734-2739.

248. Tanchak, O. M.; Yager, K. G.; Fritzsche, H.; Harroun, T.; Katsaras, J.; Barrett, C. J., Water distribution in multilayers of weak polyelectrolytes. *Langmuir* **2006,** 22, (11), 5137-5143.

249. Yu, H. H.; Yao, L.; Wang, L. X.; Hu, W. B.; Jiang, D. S., Fiber optic humidity sensor based on self-assembled polyelectrolyte multilayers. *Journal of Wuhan University of Technology-Materials Science Edition* **2001,** 16, (3), 65-69.

250. Yu, H. H.; Jiang, D. S., Ionic self-assembly and humidity sensitivity of polyelectrolyte multilayers. *Chinese Journal of Polymer Science* **2002,** 20, (1), 1-7.

251. Wilder, E. A.; Guo, S.; Lin-Gibson, S.; Fasolka, M. J.; Stafford, C. M., Measuring the modulus of soft polymer networks via a buckling-based metrology. *Macromolecules* **2006,** 39, (12), 4138-4143.

252. Wilder, E. A.; Guo, S.; Lin-Gibson, S.; Fasolka, M. J.; Stafford, C. M., Measuring the modulus of soft polymer networks via a buckling-based metrology (vol 39, pg 4138, 2006). *Macromolecules* **2006,** 39, (17), 5956-5956.

253. Mathur, A.; Brown, A. D.; Erlebacher, J., Self-ordering of colloidal particles in shallow nanoscale surface corrugations. *Langmuir* **2006,** 22, (2), 582-589.

254. Takane, N., *Unpublished results.*

255. Hecht, E., *Optics*. 4th ed.; Pearson Addison Wesley: Reading, MA, 2001.

256. Chew, W. C., *Waves and Fields in Inhomogeneous Media*. IEEE Press: Piscataway, 1995.

257. Boyce, W. E.; DiPrima, R. C., *Elementary Differential Equations and Boundary Value Problems*. 8 ed.; John Wiley & Sons, Inc.: Hoboken, 2005.

258. Bowden, N.; Brittain, S.; Evans, A. G.; Hutchinson, J. W.; Whitesides, G. M., Spontaneous formation of ordered structures in thin films of metals supported on an elastomeric polymer. *Nature* **1998,** 393, (6681), 146-149.

259. Bowden, N.; Huck, W. T. S.; Paul, K. E.; Whitesides, G. M., The controlled formation of ordered, sinusoidal structures by plasma oxidation of an elastomeric polymer. *Applied Physics Letters* **1999,** 75, (17), 2557-2559.